CRANFIELD UNIVERSITY

LEON KOCJANČIČ

MULTIBEAM RADAR SYSTEM BASED ON WAVEFORM DIVERSITY FOR RF SEEKER APPLICATIONS

CRANFIELD DEFENCE AND SECURITY
Centre for Electronic Warfare, Information and Cyber

PhD
Academic Year: 2016–2019

Supervisors: Dr A Balleri, Prof M A Richardson
October 2019

CRANFIELD UNIVERSITY

CRANFIELD DEFENCE AND SECURITY
Centre for Electronic Warfare, Information and Cyber

PhD

Academic Year: 2016–2019

LEON KOCJANČIČ

Multibeam Radar System Based on Waveform Diversity for RF Seeker Applications

Supervisors: Dr A Balleri, Prof M A Richardson
October 2019

This thesis is submitted in partial fulfilment of the requirements for the degree of PhD.

Abstract

Existing radiofrequency (RF) seekers use mechanically steerable antennas. In order to improve the robustness and performance of the missile seeker, current research is investigating the replacement of mechanical 2D antennas with active electronically controlled 3D antenna arrays capable of steering much faster and more accurately than existing solutions. 3D antenna arrays provide increased radar coverage, as a result of the conformal shape and flexible beam steering in all directions. Therefore, additional degrees of freedom can be exploited to develop a multifunctional seeker, a very sophisticated sensor that can perform multiple simultaneous tasks and meet spectral allocation requirements.

This thesis presents a novel radar configuration, named multibeam radar (MBR), to generate multiple beams in transmission by means of waveform diversity. MBR systems based on waveform diversity require a set of orthogonal waveforms in order to generate multiple channels in transmission and extract them efficiently at the receiver with digital signal processing. The advantage is that MBR transmit differently designed waveforms in arbitrary directions so that waveforms can be selected to provide multiple radar functions and better manage the available resources.

An analytical model of an MBR is derived to analyse the relationship between individual channels and their performance in terms of isolation and phase steering effects. Combinations of linear frequency modulated (LFM) waveforms are investigated and the analytical expressions of the isolation between adjacent channels are presented for rectangular and Gaussian amplitude modulated LFM signals with different bandwidths, slopes and frequency offsets. The theoretical results have been tested experimentally to corroborate the isolation properties of the proposed waveforms. In addition, the practical feasibility of the MBR concept has been proved with a radar test bed with two orthogonal channels simultaneously detecting a moving target.

Keywords

Multibeam radar, MBR, orthogonal waveforms, semi-orthogonal waveforms, channel isolation, multiple-input multiple-output radars, MIMO, linear frequency modulation, LFM, piecewise linear frequency modulation, PLFM, waveform diversity, RF seekers.

Contents

Abstract **v**

Contents **vii**

List of Figures **ix**

List of Tables **xiii**

List of Abbreviations **xv**

List of Symbols **xix**

Acknowledgements **xxi**

1 Introduction **1**
1.1 Preface 1
1.2 Motivation and Objectives 3
1.3 Research Contributions 4
1.4 Thesis Outline 5
1.5 Publications 6

2 Literature Review **9**
2.1 Introduction 9
2.2 MIMO Radars 10
2.3 Multifunction Radars 21
2.4 Waveform Design 27
2.5 Summary 36

3 Radar Signal Processing **37**
3.1 Introduction 37
3.2 Operating Principles 37
3.3 Waveform Representation 42
3.4 Radar Range Equation 46
3.5 Matched Filter 49
3.6 Pulse Compression Waveforms 56
3.7 Summary 67

4 Multibeam Radar **69**
4.1 Introduction 69
4.2 Phased Arrays 69
4.3 MBR Signal Model 77

4.4 Channel Isolation . . . 80
4.5 MBR Advantages and Potential Applications . . . 85
4.6 Summary . . . 86

5 Frequency Modulated Waveforms 87
5.1 Introduction . . . 87
5.2 Rectangular LFM Waveforms . . . 87
5.3 Asymptotic Approximation of Fresnel Integral . . . 101
5.4 Gaussian LFM Orthogonality . . . 107
5.5 Time-Frequency Approach to Orthogonality . . . 116
5.6 Summary . . . 127

6 Experimental Work 129
6.1 Introduction . . . 129
6.2 Static Waveform Isolation . . . 129
6.3 Isolation Performance with Induced Doppler Shift . . . 141
6.4 Summary . . . 154

7 Conclusion and Future Work 155
7.1 Conclusion . . . 155
7.2 Future Work . . . 157

A Mathematical Derivations 159
A.1 Cauchy-Schwarz Inequality . . . 159
A.2 Parceval's Theorem . . . 161

B Piecewise Linear Frequency Modulation 163
B.1 Introduction . . . 163
B.2 Waveform Design . . . 164
B.3 Numerical Simulations . . . 165
B.4 Summary . . . 172

References 173

List of Figures

2.1 Spatial decorrelation of MIMO radar with transmitting and receiving antenna arrays . . . 11
2.2 Formation of virtual arrays on the evenly spaced grid . . . 18
2.3 Scanning difference of phased array radar with high gain and narrower beam swath and coherent MIMO radar with lower main beam gain and wider swath 22
2.4 Time-frequency modulation scheme of a two-portion PLFM waveform . . . 29
2.5 Two quasi-orthogonal waveforms implemented by OFDM chirp waveform diversity . . . 31

3.1 Pulsed radar transmission diagram . . . 38
3.2 Radar range resolution between two closely spaced targets . . . 39
3.3 Simplified block diagram of a radar system . . . 40
3.4 Radar receiving chain of a dual conversion superheterodyne receiver . . . 42
3.5 Radar receiving chain of a dual conversion superheterodyne receiver . . . 42
3.6 Block diagrams for obtaining in-phase and quadrature components from the initial signal and for obtaining real signal from components of the complex envelope . . . 46
3.7 Power densities of the radar pointing towards a target . . . 47
3.8 Block diagram of the matched filter . . . 52
3.9 Radar range resolution between two closely spaced targets . . . 57
3.10 Normalised pulse compression output of an LFM waveform . . . 59
3.11 Examples of two binary matrices for Costas code generation . . . 61
3.12 Compressed pulse of a five step Barker code . . . 63
3.13 Normalised ambiguity function for a pulse signal with no modulation . . . 67

4.1 Radar receiving chain of a dual conversion superheterodyne receiver . . . 70
4.2 Antenna array factor for different number of antennas and fixed antenna spacing . . . 72
4.3 Normalised directivity of a linear antenna array with 20 elements and for two inter-element spacing configurations . . . 76
4.4 Schematic of a transmitting part of a multibeam radar . . . 79
4.5 Schematic of the receiving part of a multibeam radar . . . 80
4.6 An example of MBR, based on an air platform that incorporates multiple functions . . . 85

5.1 Surface plot of the normalised ambiguity function of a rectangular LFM signal 88
5.2 Plot of the normalised ambiguity function of a rectangular LFM signal . . . 89
5.3 Matched filter mismatch caused by the Doppler shift . . . 90
5.4 Frequency modulation diagram of the LFM waveforms as used for the analytical derivation . . . 91

5.5 Isolation values of a rectangular up-chirp and a rectangular down-chirp . . . 93
5.6 Frequency modulation diagram of the LFM waveforms as used for the analytical derivation . . . 94
5.7 Isolation performance of two LFM waveforms as a function of bandwidth difference . . . 98
5.8 Cross-correlation functions of two up-chirps with the parametrised bandwidth difference . . . 99
5.9 Cross-correlation functions of two up-chirps with the parametrised starting frequency . . . 100
5.10 Isolation values showing starting frequency tolerance with bandwidth difference set as a parameter. . . . 100
5.11 Integration path of the complex Fresnel integral in the complex plane . . . 102
5.12 Asymptotic expansion of Fresnel cosine integral . . . 105
5.13 Asymptotic expansion of Fresnel sine integral . . . 106
5.14 Isolation values of a Gaussian up-chirp and a Gaussian down-chirp . . . 111
5.15 Integration path of the Gaussian integral in the complex plane . . . 112
5.16 Cross-correlation functions of two Gaussian amplitude modulated up-chirps with parametrised bandwidth difference . . . 114
5.17 Cross-correlation functions of two Gaussian amplitude modulated up-chirps with parametrised starting frequency . . . 114
5.18 Comparison of cross-correlation functions of rectangular and Gaussian amplitude modulation . . . 116
5.19 Wigner-Ville distribution of an infinite chirp . . . 120
5.20 Wigner-Ville distribution of a cross-correlation function for a fixed time delay 121
5.21 Wigner-Ville distribution of an up-chirp signal with finite rectangular envelope 123
5.22 Product of an up-chirp WVD and a down-chirp WVD for a zero time delay 124
5.23 Wigner-Ville distribution of an up-chirp signal with infinite Gaussian envelope 125
5.24 Wigner-Ville distribution of an up-chirp signal with infinite Gaussian envelope 126

6.1 Experimental setup for isolation measurements consisting of a USRP-2943 and horn antennas Narda 642 . . . 131
6.2 Photo of the experimental RF link for stationary channel isolation measurements . . . 131
6.3 Measured cross-correlation responses of an up-chirp and a secondary up-chirp with varying bandwidth difference . . . 132
6.4 Measured cross-correlation responses of an up-chirp and a secondary down-chirp with varying bandwidth difference . . . 132
6.5 Measured matched filter responses of two up-chirp signals with different bandwidths when transmitted simultaneously . . . 134
6.6 Measured matched filter responses of an up-chirp and a down-chirp with different bandwidths when transmitted simultaneously . . . 135
6.7 Measured matched filter responses of two up-chirp signals with different bandwidths and offset starting frequency when transmitted simultaneously 136
6.8 Measured suppression responses of simultaneously transmitted varying chirp and a fixed up-chirp by a filter matched to the fixed down-chirp . . . 137
6.9 Measured cross-correlation responses of rectangular and Gaussian AM waveforms of different BT-products with the bandwidth fixed . . . 138
6.10 Comparison of measured and simulated isolation obtained by LFM waveforms with the same bandwidth and opposite frequency rate as a function of BT-product . . . 139

6.11 Comparison of amplitude spectra of rectangular and Gaussian AM waveforms 140
6.12 Measured isolation values of waveforms with different bandwidths for rectangular and Gaussian AM of different frequency rates 141
6.13 Measured and normalised cross-correlation functions of waveform combinations with rectangular and Gaussian AM 142
6.14 Experimental setup for measuring isolation performance in presence of a rotating target 143
6.15 Photo of the laboratory setup using a rotating target 144
6.16 A measurement of the background noise with the noise floor with non-rotating target 145
6.17 Measured range-Doppler maps of a rotating target for rectangular and Gaussian AM for a set of up-chirp and down-chirp signals with the same bandwidth 146
6.18 Measured range-Doppler maps of a rotating target for rectangular and Gaussian AM for a set of an up-chirp and a down-chirp with the bandwidth difference 147
6.19 Measured micro-Doppler signatures of a rotating target for a two-channel MBR with the same bandwidth 149
6.20 Experimental setup for measuring isolation performance in the presence of a moving target 150
6.21 A measurement of the background noise when no moving target was present 151
6.22 Measured range-Doppler maps of a moving target for rectangular and Gaussian AM for a set of up-chirp and down-chirp signals with the same bandwidth 152
6.23 Statistical analysis of PRIs, showing mean and variance of a fitted normal distribution 153
6.24 Photo of the experimental setup using the MBR and a moving target 154

B.1 Optimisation results for the set 2 with parametrised bandwidths 167
B.2 Optimisation results for the waveform set 3 as a function of two frequency offsets 168
B.3 Optimisation results for the waveform set 4 as a function of two delay times 169
B.4 Optimisation results for the waveform set 5 as a function of two delay times 170
B.5 Frequency modulation, cross-correlation values, and Doppler shift effects for the optimised waveforms 171

List of Tables

3.1 Table of all the known binary Barker codes 62
3.2 Sidelobe suppression of binary minimum peak sidelobe codes 63

5.1 Simulated isolation values of up-chirp and down-chirp signal pairs 115

6.1 Measured and simulated isolation values of the rectangular LFM waveforms 133
6.2 Measured isolation properties of two rectangular waveforms when transmitted simultaneously 135
6.3 Measured isolation properties of two simultaneously transmitted rectangular waveforms when suppressed by a third waveform 136
6.4 Measured and simulated isolation between LFM waveforms with the same bandwidth 139
6.5 Measured isolation comparison of rectangular and Gaussian AM for varying bandwidth difference 143

B.1 Waveform parameters and isolation figures for the proposed waveform sets. 170

List of Abbreviations

2D	Two Dimensional
3D	Three Dimensional
ADC	Analog-to-Digital Converter
AESA	Active Electronically Steered Array
AF	Ambiguity Function
AM	Amplitude Modulation
AOA	Angle of Arrival
APE	Amplitude Phase Estimation
ASIC	Application-Specific Integrated Circuit
ATD	Advanced Technology Demonstrator
BPF	Band-Pass Filter
BPSK	Binary Phase Shift Keying
CAN	Cycle Algorithm New
CPL	Cross-correlation Peak Level
CPM	Continuous Phase Modulation
CPU	Central Processing Unit
CW	Continuous Wave
DBS	Doppler Beam Sharpening
DFCCW	Discrete Frequency and Chirp-rate Coding Waveform
ECCM	Electronic Counter-Countermeasure
EM	Electromagnetic
FAA	Federal Aviation Administration
FDM	frequency Division Multiplexing

FFT	Fast Fourier Transform
FH	Frequency Hopping
FM	Frequency Modulation
FPGA	Field-Programmable Gate Array
FRFT	Fractional Fourier Transform
GLRT	Generalised Likelihood Ratio Test
GMTI	Ground Moving Target Indication
GPU	Graphics Processing Unit
HPBW	Half-Power Beamwidth
IF	Intermediate Frequency
IPP	Interpulse Period
ISL	Integrated Sidelobe Level
LFM	Linear Frequency Modulation
LHS	Left-Hand Side
LNA	Low-Noise Amplifier
LO	Local Oscillator
LTI	Linear Time-Invariant
MA	Matched Filter
MBR	Multibeam Radar
MF	Matched Filter
MIMO	Multiple-Input Multiple-Output
MM	Majorisation-Minimisation
MMIC	Monolithic Microwave Integrated Circuitry
MPAR	Multifunction Phased Array Radar
MSE	Mean Square Error
MTI	Moving Target Indicator
NOAA	National Oceanic and Atmospheric Administration
OFDM	Orthogonal Frequency Division Multiplexing
ONRS	Orthogonal Netted Radar Systems
PA	Power Amplifier
PAPR	Peak to Average Power Ratio

PLFM	Piecewise Linear Frequency Modulated Waveforms
PPLFM	Polyphase Piecewise Linear Frequency Modulated Waveforms
PRF	Pulse Repetition Frequency
PRI	Pulse Repetition Interval
PSK	Phase Shift Keying
PSL	Peak Sidelobe Level
QCQP	Quadratically Constrained Quadratic Programming
RCS	Radar Cross Section
RF	Radio Frequency
RF	Radiofrequency
RHS	Right-Hand Side
RSR	Random Signal Radars
SAR	Synthetic Aperture Radar
SDP	Semidefinite Programming
SIAR	Synthetic Impulse and Aperture Radar
SIMO	Single-Input Multiple-Output
SINR	Signal to Interference plus Noise Ratio
SNR	Signal to Noise Ratio
SNR	Signal to Noise Ratio
STAP	Space-Time Adaptive Processing
STFT	Short-Time Fourier Transform
TDM	Time Division Multiplexing
TWT	Travelling Wave Tube
ULA	Uniform Linear Array
WD	Waveform Diversity
WSS	Wide-Sense Stationary

List of Symbols

a	Scalar number
$\mathbf{a}$	Vector
$\mathbf{A}$	Matrix
$C(\cdot)$	Cosine Fresnel integral
$S(\cdot)$	Sine Fresnel integral
$F(\cdot)$	Complex Fresnel integral
$\delta(\cdot)$	Delta function
$\text{rect}(\cdot)$	Rectangular function
$\text{sinc}(\cdot)$	Sinc function
$\mathcal{F}[\cdot]$	Fourier transform
$\mathcal{F}^{-1}[\cdot]$	Inverse Fourier transform
$\mathcal{H}[\cdot]$	Hilbert transform
$\mathcal{A}[\cdot]$	Analytic function transform
$\mathcal{O}(\cdot)$	Asymptotic notation
$\Re[\cdot]$	Real component of a number
$\Im[\cdot]$	Imaginary component of a number
$\text{E}[\cdot]$	Estimation operator
$W_s(\cdot,\cdot)$	Wigner-Ville distribution of a signal
$S_s(\cdot,\cdot)$	Spectrogram of a signal
$\chi(\cdot,\cdot)$	Ambiguity function
$\chi_{i,j}(\cdot,\cdot)$	Cross-ambiguity function
$R_{i,j}(\cdot)$	Cross-correlation function
$I_i(\cdot)$	Isolation function

$\lvert \cdot \rvert$	Absolute value
$\mathbb{N}$	The set of natural numbers
$\mathbb{Z}$	The set of integers
$\mathbb{R}$	The set of real numbers
$\mathbb{C}$	The set of complex numbers
$\int_a^b$	Definite integral
$\oint_\xi$	Closed contour integral
$\sum_n^N$	Summation symbol
$(\cdot)^T$	Transpose operator
$(\cdot)^*$	Complex conjugate operator
$(\cdot)^H$	Conjugate transpose operator
$\in$	Is element of
$\mapsto$	Maps to
$\approx$	Is approximately
$\sim$	Is asymptotic to

Acknowledgements

It is hard to appreciate all the people that supported me throughout this journey, but above all, I would like to express my deep gratitude to my supervisor Dr Alessio Balleri, whose dedication and support have made this work possible.

I am also grateful to Prof Mark A Richardson, director of research at the time, Dr David B James, and Amanda Marlow, who contributed a lot towards research activities undergone at Cranfield in Shrivenham. I also wish to sincerely thank Dr Annie Maddison-Warren and Bea Kingdom for all their support offered to PhD students in the most difficult of times.

The contributions of this work would not have been possible without the efforts of Dr Thomas Merlet and his splendid team at Thales in Elancourt, who continue their involvement in outstanding research activities.

I would also like to express my appreciation to all my radar colleagues for their support, interesting discussions, and joyful moments. In particular, I am thankful to Krasin Georgiev, Ioannis Vagias, Gareth Frazer, and Luc Fourtinon. I owe special thanks to my office mates Michał Szulik, Samuel Westlake, Alix Leroy, and Amélie Grenier for all the great memories. I will always remain grateful to Carole Belloni for being the best conference travelling companion and Axel Beauvisage to push my sporting endeavours to the limit.

I owe a great deal of gratitude to my fellow villagers Akhil Kallepalli, Nasyitah Ghazalli, Mengjia Ding, and Sarah Skoropa, who have all made my stay in Shrivenham full of pleasant memories and were always there when I needed them.

Nazadnje bi se rad v največji meri zahvalil svojim staršem, ki me neumorno podpirajo na moji življenjski poti. To delo bi rad posvetil Veri, Maksu in Urši.

Chapter 1

Introduction

1.1 Preface

Radiofrequency (RF) spectrum is a limited resource and is therefore strictly regulated to allow for efficient exploitation by telecommunication, radionavigation and sensing applications. Improvement of the related technologies has been a constant driver for researchers in academic and industry sectors, focusing on hardware development, advances in the underlying signal processing and data fusion.

Specifically, information throughput and time latency are being constantly improved in telecommunications, more reliable and accurate positioning systems have been deployed to meet the modern navigation requirements, and radar technology has made significant advances as well. The advances in radar systems are twofold. In terms of hardware, the miniaturisation and sampling frequency increase of transmit and receive integrated circuit modules have improved phased array radars when it comes to their ability to select and transmit suitable waveforms, continuously adapt the waveform parameters to the environment, and increase robustness to failure of individual modules. In the context of signal processing, new concepts in waveform design and diversity have emerged to advance cooperative and non-cooperative radar networks [Gini et al., 2012]. Multiple input-multiple output (MIMO) radars are the most notable cooperative radar technology, that has yet to be successfully implemented in practical applications. Non-cooperative radars and RF systems, in general, pose a more common challenge as every new RF device should interfere as little as possible with the existing systems.

The positive and negative aspects of MIMO radars in monostatic configurations have been investigated analytically in great detail [Li and Stoica, 2009]. Performance improvements of such implementations are increased angle resolution due to virtual antenna aperture, more accurate moving target indication modes, and a wider swath of illumination. However, the main challenge remains with waveform design as it must account for the waveform orthogonality in order to enable sufficient channel isolation. Similar orthogonality constraints apply to waveforms of non-cooperative radar networks and multistatic MIMO radars, which exploit spatial diversity of a target cross-section to improve operational performance. Orthogonal waveforms, therefore, remain crucial in providing sufficient channel separation and extraction on receive.

Different approaches can be adopted to implement waveforms with orthogonal properties. Time-division multiplexing (TDM) and spatial filtering in the sense of phase steering are very effective methods, which provide sufficient separation of signals. However, time synchronisation is not always possible among different systems to utilise TDM and often systems operate in the same space domain, which makes spatial filtering infeasible. Both approaches can be implemented jointly to form space-time adaptive techniques (STAP), mainly used to suppress ground clutter. Separation of signals is also possible in frequency domain, known as frequency division multiplexing (FDM), which provides optimal orthogonal properties. The pertinent drawback is the separation of the available frequency spectrum into multiple bands, resulting in limited bandwidth available per channel, which ultimately impacts upon radar resolution. In addition, spectrum utilisation becomes less efficient in this case as each additional channel necessitates more frequency bands.

A more comprehensive approach to designing radar signals is waveform diversity (WD) [Antonik and Wicks, 2007]. The concept is based on the idea to fully exploit all available degrees of freedom, and therefore utilise spatial beamforming, time domain, frequency domain, as well as coding and polarisation of the signals [Blunt and Mokole, 2016]. Different approaches can be undertaken to implement WD, depending on the design criteria and whether the waveforms are defined in continuous or discrete form. Applying different frequency and amplitude modulation schemes is one of the most straightforward approaches that exhibits good results and extends the signal representation in the joint time-frequency domain. Such techniques are mainly used for continuous signals, while discretely defined

signals are mostly derived by the means of an optimisation process. Relating to the nature of the problem, the solutions to the optimisations can be locally or globally optimal. In many cases, problems have to be relaxed to obtain tractability.

1.2 Motivation and Objectives

Sensor proliferation, most notably in the RF domain, has increased the demands for efficient exploitation of the limited spectrum allocations. Furthermore, sensor fusion and industry drive to push costs of the sensor suits down can be addressed by introducing multifunctional devices, that are capable of carrying out multiple tasks simultaneously. An airborne platform, whether it is a reconnaissance vehicle, missile or an autonomous aircraft, is typically equipped with a range of different RF sensors. The sensors can be dedicated to communication links, radio altimetry, target seeking, environment sensing, proximity activation, and radar imaging. By appropriate hardware design with the implementation of suitable processing techniques, some of the aforementioned sensors can be combined to form a single device. As the proposed device is intended to facilitate multiple sensing channels, waveform design becomes a crucial aspect to obtain optimal performance of the entire system.

Fusing RF sensing functionalities is directly applicable to RF missile seekers, which function as a dedicated radar system in the nose of a missile. The latest achievements in antenna design have made three dimensional antennas possible for seeker applications, which has inevitably made the mechanical antenna gimbals obsolete as they can be completely replaced by active electronically controlled arrays. Additionally, the implementation of a three dimensional antenna widens the front field of view of a missile and makes the case for multiple simultaneous beams, acting as separate sensing channels. Each beam can therefore carry out a dedicated functionality without affecting the performance of adjacent beams if sufficient isolation is achieved. An optimal waveform can be preselected for each independent channel with the respect to specific requirements of a channel. The main challenge remains to select and design the waveforms that fully utilise the available bandwidth, reduce channel interference, and retain good detecting properties for fast targets.

The main research aim of this work is to investigate possible implementations of orthogonal or quasi-orthogonal waveforms, that would be suitable for simultaneous operation. As the intended use is primarily for radar systems and RF missile seekers more specifically, the proposed waveforms should exhibit good compression properties, low range sidelobes, and a sufficient amount of isolation when being transmitted simultaneously. An additional and very restrictive condition is related to the detection of fast targets, which produce high Doppler shifts of the returned signals. This requires high Doppler tolerant waveforms, in particular when the potential targets can have stealthy attributes and a bank of Doppler filters is to be avoided for reasons of computational complexity.

The objectives of this study envisage a proposal for a set of waveforms, that meets the above-stated criteria. The analytical derivation of isolation properties and ambiguity function should be undertaken where possible to demonstrate the feasibility of the proposed waveforms. To corroborate the analytical results and applicability of the waveforms an experimental work should be conducted.

1.3 Research Contributions

Research contributions of this work fall mainly in the domain of waveform diversity and radar signal design. In the context of Doppler tolerance properties, which pose a strict limitation to waveform design, the research is mainly concentrated on the linear frequency modulated (LFM) waveforms. The main contributions of this work are stated below.

- A novel radar configuration is proposed to address the requirement of multiple independent channels. Multibeam radar (MBR), as the new configuration is named, employs orthogonal waveforms together with spatial filtering to sufficiently separate independent channels. An analytical MBR model is presented that confirms the implementation of beam steering in conjunction with an arbitrary set of orthogonal waveforms to achieve channel isolation.

- A set of LFM waveforms with rectangular amplitude modulation with frequency rate diversity is proposed for an MBR application. Isolation between two arbitrary LFM waveforms is analytically derived in a form of the cross-ambiguity function to account for arbitrary time delays and Doppler shifts.

- Analytically derived lower bound on the isolation is demonstrated for two rectangular LFM signals, corroborating the fact that the isolation improves with the increasing time-bandwidth product.

- A set of LFM waveforms with Gaussian amplitude modulation is found to have a closed-form isolation expression for an up-chirp and a down-chirp of the same bandwidth. Additionally, cross-ambiguity function for a general case with different frequency rates is derived.

- Waveform isolation based on chirp rate diversity is investigated in the time-frequency domain by utilising Wigner-Ville distribution (WVD). The source of leakage energy between channels is demonstrated numerically for the rectangular LFM and analytically for the Gaussian LFM.

- Isolation figures of the proposed waveforms are experimentally corroborated with an indoor direct RF link setup.

- An experimental demonstration of a two-channel MBR is conducted using rectangular and Gaussian amplitude modulated LFM waveforms. The suppression of the adjacent channel is shown to be comparable to the noise level.

1.4 Thesis Outline

This thesis consists of seven chapters and two appendices. The remainder of the content is organised as follows.

Chapter 2 gives a comprehensive literature review of statistical and coherent MIMO radars, which can be related to the MBR concept. Existing multifunction radar systems are examined, concentrating on applications in weather monitoring, air control, and defence environments. A further survey of joint radar and communication systems is conducted.

Chapter 3 is dedicated to the well documented radar theory and signal processing. The topics covering radar configurations, internal block design, range equation, and matched filtering are discussed. Further theory is given on pulse compression, different modulations, and ambiguity function.

Chapter 4 is devoted to the theory of linear phased arrays, different definitions of channel isolation are formally introduced, and novel signal model representing MBR is explained.

Chapter 5 introduces the proposed LFM waveforms. The analytical treatment of rectangular LFM is presented first and the supporting theory of Fresnel integrals is presented thereafter. Gaussian amplitude modulated LFM are discussed next and simulations of both modulation proposed are compared. Finally, WVD is introduced to investigate waveform diversity in the time-frequency domain.

Chapter 6 presents the experimental work that was carried out in the scope of the proposed waveforms. The first section is devoted to the measurement of isolation performance in the static environment without the Doppler shift. The second section conveys the results of more realistic scenarios with rotating and moving targets.

Chapter 7 discusses the concluding remarks and presents possibilities for future work, related to analytical and experimental research.

Appendix A gives additional mathematical derivations, while Appendix B is dedicated to the more complex waveforms, consisting of piecewise linear frequency modulated chirps.

1.5 Publications

The publications listed below are a direct result of the work conducted within the scope of the PhD research.

Journal Papers

- L. Kocjancic, A. Balleri, and T. Merlet, "Multibeam Radar Based on Linear Frequency Modulated Waveform Diversity," *IET Radar, Sonar Navigation*, vol. 12, no. 11, pp. 1320–1329, 2018.

Conference Papers

- L. Kocjancic, A. Balleri, and T. Merlet, "Study of the Frequency Slope Effect on the Chirp Waveform Orthogonality," in *International Conference on Radar Systems (Radar 2017)*, pp. 1–6, October 2017, Belfast, UK.

- L. Kocjancic, A. Balleri, and T. Merlet, "Experiments of Quasi-Orthogonal Linear Frequency Modulated Waveforms for Multibeam Radar," in *2019 IEEE Radar Conference (RadarConf)*, pp. 1–6, April 2019, Boston, US.

- L. Kocjancic, A. Balleri, and T. Merlet, "Numerical Characterisation of Quasi-Orthogonal Piecewise Linear Frequency Modulated Waveforms," in *2019 Sensor Signal Processing for Defence Conference (SSPD)*, pp. 1–5, May 2019, Brighton, UK.

- L. Kocjancic, A. Balleri, and T. Merlet, "STFT Target Analysis with Quasi-Orthogonal LFM Waveforms," in *2019 International Conference on RADAR Systems*, September 2019, Toulon, France.

Invited Talks

- L. Kocjancic, "Overview of MIMO Radar Systems and Their Advantages," in *23 Seminar on Radio Communications*, February 2018, Ljubljana, Slovenia.

Chapter 2

Literature Review

2.1 Introduction

In this chapter, the major advances and contributions to the field of MIMO and multifunctional radars in different configurations are presented together with a comprehensive review of advanced radar waveforms and their design. The emphasis is on the waveforms that are designed for radar spectrum sharing, MIMO radars, netted radar systems and radars with multifunctional operation that can be used for multiple tasks simultaneously and therefore improve performance aspects of a sensing system.

In the past two decades, with the advances of microprocessors [Tuzlukov, 2017] and graphics processing units (GPU) [Bernaschi et al., 2012] that have brought about increased computational capabilities, lower costs and more compact dimensions, the capabilities of radar systems have improved significantly. Fast developments of monolithic microwave integrated circuitry (MMIC) [Brookner, 2003] and field-programmable gate arrays (FPGA) [Li and Wang, 2012, Khan et al., 2018] have enabled high throughput processing of real-time data. That made complex radar systems feasible in practice and allowed for their adoption by the academia and commercialisation by the industry. Consequently, novel algorithms and more advanced processing techniques have emerged to address the requirements of MIMO radars [Li and Stoica, 2009], cognitive radars [Farina et al., 2017], multifunctional radars [Brandfass et al., 2018] and data fusion with other sensors [Liggins et al., 2017]. All aforementioned radar systems and techniques potentially require orthogonal or quasi-orthogonal waveforms that exhibit predefined isolation properties.

Generally speaking, multiple approaches can be followed to design radar waveforms with specific properties while meeting the requirements of low interference levels, orthogonality or decorrelation. Different approaches related to diverse radar configurations will be discussed in the following sections.

2.2 MIMO Radars

Phased array radar systems were extensively developed during the 1960s and 1970s, and have now become a mature technology that is successfully in use for many different sensing applications. In the following decades, advances in digital signal processing in combination with the fabrication improvements of more efficient microprocessors enabled adaptive array processing that has evolved into modern radar systems in use today [Brookner, 2003].

Phased array radars are able to steer multiple beams in desired directions by utilising arrays of smaller antennas that transmit identical waveforms with different phase shifts. The beams can be quickly steered in different directions through electronic scanning in order to cohere energy in specified directions. Despite the fact that a phased array uses multiple antenna elements on transmit, the waveforms, when transmitted, are perfectly correlated and therefore do not provide additional degrees of freedom. It is possible to look at the distinction between phased array and MIMO radar systems from the system perspective [Davis et al., 2014]. Therefore, if the environment is considered to be a system, with sensing waveforms being inputs and target echoes outputs, then the phased array can be classified as a single-input multiple-output (SIMO) system. Single-inputs, in this case, are perfectly correlated waveforms that are forming a beam and illuminating a particular range-azimuth cell. Since the inputs to the phased array can be arbitrarily steered to any direction in post processing, the outputs of the environment can be seen as multiple spatially diverse outputs of the system, hence the SIMO designation. A similar comparison of SIMO and MIMO radar systems was given in the context of array manifolds, described by differential geometry, where a monostatic configuration was assumed with no assumptions on the transmitted waveforms [Commin and Manikas, 2012].

In the case of a MIMO radar, the transmitted waveforms are decorrelated, which requires a different processing approach at the receive and has an effect on the key perfor-

mance figures, depending on the antenna array configuration. The key idea, that defines MIMO radars, is the ability to transmit independent waveforms from each antenna separately and to jointly process them on receive. As the beams from the transmitting antennas are not correlated, there is no constructive interference in the direction of transmission, which causes the beampatterns to be more omnidirectional [Li and Stoica, 2009, Chapter 2]. Furthermore, the independence of waveforms opens up additional possibilities to design waveform sets with specific radiations patterns, interference and clutter rejection properties that are controlled through the optimisation of a waveform correlation matrix [Ahmed and Alouini, 2014, Grossi et al., 2011].

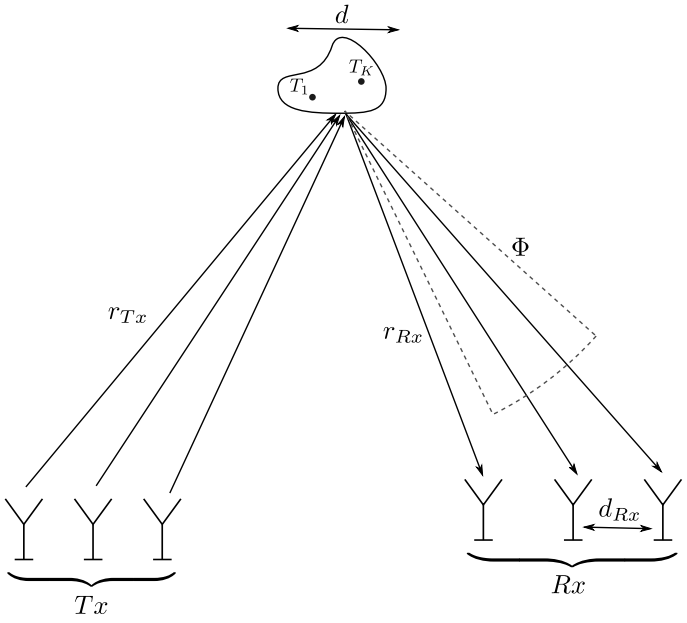

Figure 2.1: Spatial decorrelation of MIMO radar with transmitting and receiving antenna arrays, where r_{Tx} and r_{Rx} are distances from transmitting antennas to target and receiving antennas to target, respectively. Target is considered to be an antenna with aperture size d and radiation beam $\Phi = \lambda/d$.

Two configurations of MIMO radars are considered in general, one with the antenna elements collocated and a second with the antennas widely separated. Another classification is based on the coherency between signal transmission and reception. Since MIMO radars with collocated antennas operate in a coherent mode, they are widely referred to as the coherent MIMO radars. Contrarily, the MIMO radars with widely separated antennas usually operate in a non-coherent mode, hence their statistical MIMO designation. In which mode a radar can operate is mainly dependant on the geometrical position of the

transmitting antennas, receiving antennas and the target, as can be seen in Figure 2.1. The spread target, that is shown in the figure and is in general formed by many point scatterers $T_1, ..., T_K$, can be considered as an antenna with a radiation beam with an angle of $\Phi = \lambda/d$, where λ is the wavelength and d is the antenna aperture [Haimovich, 2008]. Therefore, the radar can operate in a statistical MIMO regime if the beam of the target cannot illuminate two receiving antennas simultaneously. According to Figure 2.1, this condition is true when the distances between the receiving antennas are greater than the arc of the beam pattern $d_{Rx} > r_{Rx}\lambda/d$. If the same condition holds for the transmitting antennas as well, the radar system is able to fully exploit the radar cross-section (RCS) diversity of a target and therefore spatial decorrelation is possible. Contrarily, coherent MIMO is possible when a single beam covers all the receiving antennas and the scattering response is the same for all possible combinations of transmitting and receiving antennas [Li and Stoica, 2009]. This configuration, for example, is particularly suitable for air surveillance radars where targets are well isolated from the clutter.

A way to describe relations between transmitting antenna elements, reflectivity of a target, and receiving antennas is through the MIMO channel matrix that relates all possible signal propagation channels of a radar system [Fishler et al., 2004]. In the case of M transmitting antennas and N receiving antennas, this is an $N \times M$ matrix that describes the geometry of the propagation channel and the target scattering properties. Elements of the matrix are decorrelated if the conditions for the RCS diversity hold and, additionally, if M transmitted waveforms are perfectly orthogonal and can be separated at the receiver [Haimovich et al., 2008]. Possibilities for the waveform design will be reviewed in Section 2.4. The number of antenna elements and the operating principle of a radar affect the number of spatial degrees of freedom [Bliss and Forsythe, 2004]. SIMO radars steer only on receive and can, therefore, operate with N degrees of freedom. If the transmitting antennas are adaptive as well, $N + M$ degrees are possible. For a MIMO radar with shared antennas for transmission and reception, which is an equivalent of the monostatic radar, the maximum possible degrees of freedom is $N(N + 1)/2$. In the case of decorrelated channel matrix, the channel diversity is fully exploited with MN degrees of freedom.

Parallels can be drawn between MIMO radar systems and MIMO communication sys-

tems, from which the ideas proliferated into the radar field [Fishler et al., 2004]. In MIMO communications, spatial multiplexing is a widely used technique that exploits multipath to increase information throughput or improves the reliability of a channel. The performance of a link improves with the increasing number of uncoupled parallel channels, which can be numerically determined with the diversity gain [Hampton, 2013, Chapter 1]. In the radar case, consecutive measurements of target echoes can be considered as multiple channels that provide diversity gain. Wider separation of the transmitting and receiving antennas is, on the other hand, providing spatial decorrelation, that can potentially improve detection, parameter estimation, and classification [Haimovich, 2008].

2.2.1 Statistical MIMO Radar

As discussed earlier, statistical MIMO radars employ widely separated antennas or transmitting and receiving antenna arrays in order to achieve spatial decorrelation. The geometrical arrangement of the antennas makes them similar to bistatic and multistatic radars, which have been extensively researched in the literature [Willis, 2004, Cherniakov, 2008]. The terminology in use reflects the common aspects of the two types of radar. The distance between the receiver and transmitter is usually referred to as the bistatic baseline. The angle that is subtended between the transmitter, target and receiver is called the bistatic angle [Willis and Griffiths, 2007]. Both parameters define the working characteristics of a bistatic radar and by extending the bistatic angle or increasing the baseline, the RCS diversity of a target can be more effectively exploited, which is true for a statistical MIMO radar as well.

One of the earliest examples of a MIMO radar system, that operated in the statistical regime, was a synthetic impulse and aperture radar (SIAR). It was conceived by [Dorey et al., 1984] at the French Aerospace Lab ONERA in the late 1970s under the acronym of RIAS and effectively paved the way for MIMO radar techniques [Dorey, J. and Garnier, G. and Auvray, G., 1989]. The main goal of the project was to develop and demonstrate the surveillance and tracking capabilities of the RIAS radar that was operating in the VHF band [Lesturgie, 2011]. The main requirement was to improve the angular resolution of radars in this band. The demonstrator consisted of two concentric antenna arrays with only one array dedicated to the transmission of orthogonal waveforms with different fre-

quency carriers. The antennas radiated isotropically and therefore reduced the probability of interception by a third party. Waveform orthogonality ensured that separate processing was possible at the receiver and improvement in angular resolution was achieved. Following successful trials, the concept was later adopted by the company THOMSON-CSF to improve measurements of radar coverage in range and elevation, target localisation accuracy and target discrimination [Luce et al., 1992]. A thorough examination of SIAR was thereafter conducted by [Chen Baixiao et al., 2001], in particular, to counter targets with low RCS values and radar stealth capabilities [Chen Baixiao et al., 2002, Chen, 2014]. Most of the research that followed was a continuation of RIAS ideas but the designation of the technology changed to either MIMO radar with widely separated antennas or statistical MIMO radar.

Spatial diversity and effects on detection performance related to phased array radars, MISO radars, and statistical MIMO radars were thoroughly investigated in [Fishler et al., 2006]. The authors introduced a more accurate statistical representation of a distributed Swerling-1 target composed of a finite number of scatterers. The Swerling-1 denotes a target in slow motion, therefore the RCS fluctuations are fixed during a scan and vary independently on a scan to scan basis. The representation of a target is important to accurately model the radar channel matrix in order to derive optimal detectors. The comparison of SNR figures after the detection process, denoted by β, was given for two cases, with input signals of high and low SNR, denoted by σ. It was shown that for high SNR, the MIMO detector outperforms a phased array. For M transmitters and N receivers, the statistical MIMO radar acts as MN independent radar systems, which average out fluctuations of the target RCS. The phased array, with the coherent processing mode, is more affected by the RCS variations. In this case, the SNR after the detector can be approximately given as $\beta_{MIMO} \approx 2NM$, $\beta_{MISO} \approx 2M$ and $\beta_{PA} \approx 2$, under the assumption that the waveforms are perfectly orthogonal. In the case of a low SNR of the impinging signals, the coherent processing of the phased array has an advantage over the statistical MIMO system, especially in instances of fading RCS, as the instantaneous SNR is higher than the averaged value. The SNR output of the optimal detectors can in this case be approximated as $\beta_{MIMO} \approx \sigma^2 N/M$, $\beta_{MISO} \approx 2M$ and $\beta_{PA} \approx \sigma^2 N^2 M^2$.

In [Lehmann et al., 2007], the authors investigated the performance of statistical MIMO

radars in terms of angle of arrival (AOA) estimation. The system under investigation had widely separated antennas in transmit and a uniform linear array (ULA) with closely spaced antennas on receive. This configuration allowed for spatial decorrelation of the channel matrix, hence reducing the fluctuation of RCS, and, at the same, perform direction finding measurements with the receiving ULA. The performance of AOA estimation was analysed by deriving the Cramer-Rao bound (CRB), which gives a lower bound on the variance of an unbiased estimator. The CRB conditioned on the channel matrix coefficients was calculated and its average value was found by estimating the mean value of channel coefficients, described by the chi-squared distribution. In addition, the correlation between the elements of the channel matrix was explored, to represent a more realistic scenario. The correlation effects are due to the interference of adjacent aspect angles of a multicomponent target. It was demonstrated by simulations that small correlation factors are negligible when estimating AOA and a statistical MIMO configuration of antenna elements offers significant improvements in high correlation cases. Although the correlation effects, which were caused by physical attributes of the target, were taken into account, the effects of waveform interference were neglected.

Target velocity estimation using statistical MIMO radar configuration was investigated by [He et al., 2010a]. The analysis was focusing on minimising the CRB of velocity estimation by optimising the transmit and receive antenna locations. The authors introduced the concept of geometry gain, which improves the estimation performance by observing a target from different aspect angles and therefore reduces the possibility of a target moving perpendicularly to the sensor placements with a resulting small Doppler shift. With strong assumptions, namely perfect signal orthogonality, a single isotropic scatterer and equidistant antenna locations from the target, it was theoretically shown that the symmetrical placement of receive and transmit antennas is optimal. Nevertheless, a frequency spread technique to separate independent channels was proposed that could potentially mitigate the strong assumption of orthogonality.

The exploitation of polarimetric diversity in statistical MIMO radars was introduced by [Gogineni and Nehorai, 2010]. Different polarisations of transmitting and receiving signals introduce additional degrees of freedom, which amount to the product of the numbers of receiving and transmitting antennas. It was shown that, for point-like targets

with known reflectivity and polarisation reflections, described by the scattering matrix, significant improvements over the conventional MIMO radar with fixed horizontal or vertical polarisations can be achieved. The elements of the scattering matrix were modelled as complex Gaussian random variables in order to design a detector for the binary hypothesis problem. Numerical results of an optimised system, under the assumption of perfectly decorrelated waveforms, showed improvements in the probability of detection. Furthermore, the improvements were more significant at lower values of SNR.

In [Godrich et al., 2011], the authors investigated power allocation strategies for target location estimation. The analysis is given for a single target, with predetermined positions of antennas and an assumed perfect orthogonality of the transmitted waveforms. Two optimisation algorithms are described, one to minimise the total transmitted power constrained by the power limits and predetermined localisation mean square error (MSE). The second one to maximise accuracy by minimising the MSE for a given power budget. Nonconvex optimisation problems are solved by implementing relaxation and domain decomposition methods. It is numerically demonstrated that uniform power allocation is not necessarily the optimal solution and depends on the geometrical spread of the antennas and spatial diversity of the RCS.

Detection of multiple individual isotropic targets by a statistical MIMO system was explored by [Gogineni and Nehorai, 2011]. The authors introduced sparse modelling as the target state vectors, which were defined by location and velocity, had to be recovered from observations and target state space matrix. The number of the possible state spaces is significantly greater than the number of targets, which requires implementation of sparse recovery algorithms. Two methods were introduced, namely the basis pursuit, which is an unconstrained minimisation problem, and the block-matching pursuit, which is an iterative algorithm. Although, the adopted assumption of perfectly orthogonal waveforms makes the proposed techniques hard to implement in practice.

Moving target detection in homogeneous clutter by MIMO radars with widely spaced antennas was investigated by [He et al., 2010b]. The theory was developed under the assumptions of perfectly orthogonal waveforms, homogeneous clutter with complex Gaussian distribution and a known covariance matrix. A phased array was compared with two statistical MIMO processing implementations, namely centralised and distributed MIMO

moving target detectors. The former has a central processor that conducts a joint estimate of the target velocity based on the generalised likelihood ratio test (GLRT) of the datapoints received by all the antennas. In the latter case, the detectors at each receiving element processes the received data independently and send a local GLRT decision to a central unit. It was shown that the centralised processing achieves higher probability of detection but with additional computational cost. A phased array is seen as an advantage only in circumstances with very low SNR.

As discussed in the foregoing publications, statistical MIMO radar configurations enable the exploitation of geometrical and spatial diversity, which improves detection and target tracking performance. It has to be noted that the majority of publications rely on strong assumptions of perfectly orthogonal waveforms, which renders the techniques questionable for practical applications. The impact of limited orthogonality on processing will be discussed in Section 4.3.

2.2.2 Coherent MIMO Radars

Coherent MIMO radar is a generalisation of a monostatic phased array radar, which is now a mature technology and thoroughly understood [Fenn, 2007]. The main difference is that the phased array acts as a MISO system, whereas the coherent MIMO radar has the ability to steer on transmit after reception, form a virtual array of antennas and control the radiation pattern through the waveform correlation matrix. Steering on transmit and receive after reception is possible when the orthogonal waveforms can be perfectly decorrelated with matched filtering and therefore arbitrary phase shifts can be applied to the transmitted waveforms individually. Virtual arrays are formed under the same orthogonality condition of the waveforms and MN virtual phase centres are formed on receive if arrays of M transmit and N receive elements are used. The radiation beam of coherent MIMO radars can be controlled by designing a waveform correlation matrix, which is often defined as an optimisation problem with a specific objective function.

Virtual array formation for coherent MIMO radars was discussed in [Davis et al., 2014] and [Li and Stoica, 2009, Chapter 2], but it has to be pointed out that the same phenomenon can be exploited in statistical MIMO configurations. The virtual array can be explained with the channel matrix $\mathbf{H}(\tau)$ at the specific delay $\tau = \tau_T$, corresponding to

the range bin containing a target. If only the propagating paths are considered, omitting the effects of target reflectivity and signal attenuation, an element of $\mathbf{H}(\tau_T)$ can be written as

$$[\mathbf{H}(\tau_T)]_{n,m} = ke^{j2\pi\mathbf{u}^T(\mathbf{r}_{T,m}+\mathbf{r}_{R,n})/\lambda} \tag{2.1}$$

where k is the proportional factor, $\mathbf{u}$ is the target direction in the far field and $\mathbf{r}_{T,m}$, $\mathbf{r}_{R,n}$ are positions of the transmitting and receiving antennas, respectively. Therefore, the mth transmitted waveform, received by the nth antenna has a corresponding relative path of $\mathbf{u}^T(\mathbf{r}_{T,m} + \mathbf{r}_{R,n})$, which, in the case of perfectly orthogonal waveforms, amounts to MN virtual receiving antennas. In an idealised linear antenna array [Li and Stoica, 2009] with an inter element spacing of half-wavelength, $\lambda/2$, the positions of the antennas can be given by a vector $[1, 1, 1]$, where each entry represents an antenna, located on the linear grid. A possible configuration is depicted in Figure 2.2a, where the receiving and transmitting antenna arrays occupy the same location with the elements positioned at $[-\lambda/2, 0, \lambda/2]$. A virtual array on receive is formed with the elements positioned at $[-\lambda, -\lambda/2, 0, \lambda/2, \lambda]$. As can be observed, the virtual aperture is bigger than the physical one and some of the virtual locations correspond to multiple received signals. This situation can be avoided by introducing sparse arrays, as seen in Figure 2.2b, which, by appropriately distributing the antenna elements, can result in contiguous virtual antenna arrays. The resulting virtual arrays can be mathematically defined by convolving the vectors of physical positions.

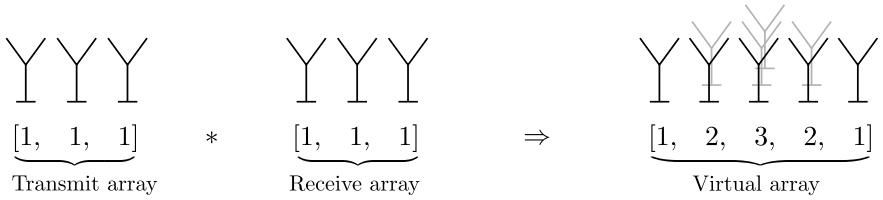

(a) Non-Contiguous Virtual Array

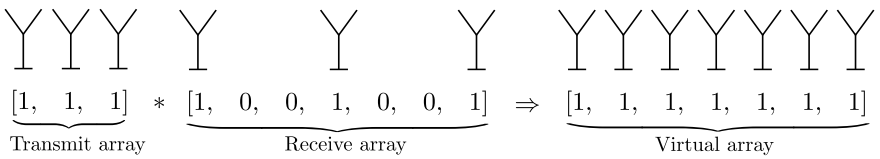

(b) Contiguous Virtual Array

Figure 2.2: Formation of virtual arrays on the $\lambda/2$ evenly spaced grid. (a) Densely represented transmit and receive arrays result in the virtual array with multiple signals at some locations. (b) If one of the physical arrays is sparsely defined, the resulting virtual array has contiguous virtual phase centres on the receive.

An overview of a MIMO radar systems with collocated antennas was given in [Li and Stoica, 2007], where the authors presented an overview of the main advantages of such a configuration. It was pointed out that significantly improved parameter identifiability, direct applicability of arrays for target detection and parameter estimation, as well as increased flexibility for transmit pattern design, can be achieved. It was established that the maximum number of uniquely identifiable targets by the MIMO processing technique can be up to M times greater than the phased array equivalent, where M is the number of transmitting antennas. The authors argued that the CRB performance of target azimuth estimation is much lower in the MIMO case and is less affected when additional targets are introduced. An algorithm was proposed to form beampatterns, as the MIMO configurations offer more degrees of freedom. The optimisation algorithm had $M^2 - M$ degrees of freedom, compared to $M - 1$ in the phased array case.

Beampattern design for coherent MIMO systems was investigated by [Fuhrmann and San Antonio, 2008]. The phased arrays transmit waveforms that are equal to each other and the resulting narrowly focused beampattern can be steered by applying phase shifts. Consequently, the cross-correlation matrix of the transmitted signals is a rank-one matrix and there are no degrees of freedom to optimise the beampattern. In comparison, the orthogonal waveforms have a corresponding cross-correlation matrix, which is a multiple of the identity matrix and ρ in (2.2) is equal to zero. The off-diagonal elements ρ can be relaxed, which makes the optimisation of the cross-correlation matrix possible. This principle is known by the name correlated MIMO radar.

$$\mathbf{R} = \begin{bmatrix} 1 & \rho & \rho^2 & \cdots & \rho^{M-1} \\ \rho & 1 & \rho & & \\ \rho^2 & \rho & 1 & & \vdots \\ \vdots & & & \ddots & \rho \\ \rho^{M-1} & & \cdots & \rho & 1 \end{bmatrix} \tag{2.2}$$

As the authors showed, the emitted power density of the electrical field is related to the cross-correlation matrix, which can be optimised to achieve a desired radiation pattern. Two convex optimisation methods were proposed for this purpose. A squared error opti-

misation technique with the barrier method to account for the feasible region and minimax optimisation of the error function, where the maximum values are minimised. To keep the analysis tractable, the authors proposed a finite alphabet of symbols that constituted each waveform. Binary phase shift keying (BPSK) waveforms were used in simulations to numerically design the optimised beampatterns.

A comparison of signal to interference plus noise ratios (SINR) for different radar operating modes was given by [Ahmed and Alouini, 2014]. The analysis was presented for phased array radars, MIMO radars, phased MIMO radars and correlated MIMO radars. A phased MIMO radar is a combination of phased array and MIMO radar, where M transmit antennas are divided into K uniform subarrays and the antennas in each subarray transmit coherently. It was shown that the SINR of a MIMO radar mode can achieve the optimal value of $SINR = MN/\sigma_n^2$, where N is the number of receiving antennas and interference terms were omitted for clarity. A phased array radar is able to achieve better performance with $SINR = MN^2/\sigma_n^2$ and a phase MIMO radar is a compromise between the two with $SINR = MN(M-K+1)/\sigma_n^2$. A correlated MIMO configuration with waveforms related to the correlation matrix (2.2) achieves the optimal SINR of

$$SINR = \frac{MN}{\sigma_n^2} + \frac{2N\rho}{\sigma_n^2(1-\rho)}\left(M - \frac{1-\rho^M}{1-\rho}\right) \tag{2.3}$$

It can be shown that the expression above is always greater than SINR in the MIMO case for $\rho \in (0,1)$ and as $\rho \to 1$, it approaches to the SINR of a phased array. The authors proposed an improvement to replace the value ρ with cosine functions, which improved the SINR in (2.3) and pushes down the sidelobe levels.

In [Xu et al., 2008], the authors analysed the behaviour of several detection and parameter estimation techniques for collocated MIMO radars in the case of multiple targets. It was shown that the Capon beamformer provides accurate estimates of the locations of multiple targets, whereas amplitude response estimations were found to be below actual values. The amplitude and phase estimation (APES) algorithm provided more accurate amplitude estimates, but with a lower angular resolution and hence lower localisation accuracy. A combined method of both approaches, referred to as CAPES, was tested, where in the first step the Capon approach was used for target localisation and in the

second step, the amplitude estimates at the target locations were performed with APES. Additionally, a novel technique was introduced to counteract the issue of array calibration errors.

In [Davis et al., 2014] a coherent MIMO signal model was presented and the effects of MIMO processing were introduced as if they were a part of antenna subsystem. In this way the MIMO flexibility in waveform generation is incorporated in the antenna gain patterns and a direct comparison of three quantities between MIMO and phased array is possible. The quantities are steered responses, which quantify the ability to digitally resteer the beam, the beam pattern, which quantifies the spatial spread of energy as well as signal rejection from undesired angles, and point spread function, which gives the ability to resolve closely spaced targets. The transmit gain of a phased array is $G = \frac{1}{M}\left|\mathbf{a}(\tilde{\theta}_T)^H\mathbf{a}(\theta)\right|^2$ and of the coherent MIMO radar $G = \frac{1}{M^2}\left|\mathbf{a}(\theta_T)^H\mathbf{a}(\theta)\right|^2$, where θ_T is the target location and $\tilde{\theta}_T$ signifies the fact that the phased array steering is fixed after transmission. As demonstrated, the phased array has a gain M times higher in the desired direction, but both patterns still retain the same beampattern shape. As both configurations can resteer after reception, the receiving gain patterns are the same $G = \frac{1}{N}\left|\mathbf{b}(\theta_T)^H\mathbf{b}(\theta)\right|^2$. It is worth considering the search rates for a radar system in scanning mode. The SNR of a single dwell time is M times higher in the case of a phased array when compared to the radar with orthogonal waveforms, but the latter produces a broader beam that is able to illuminate an area M times the size, as can be observed in Figure 2.3. Consequently, the coherent processing interval is M times longer for all of the simultaneous beams and the MIMO radar can obtain equivalent SNR performance.

2.3 Multifunction Radars

Multifunction radars are not a recent idea, but the progress of microprocessing technology and availability of commercial-off-the-shelf components have made the approach tractable for defence [Conn et al., 2004], industry [Schikorr et al., 2016] and research institutions [Huizing, 2008]. The main driver for multifunction radars in the industry has been the tendency to unify the air traffic control radars with weather surveillance radars [Galati and Pavan, 2009]. By merging the two capabilities into a single device, operational costs could

be significantly reduced and the logistics of running a network of surveillance radars would be simplified, further improving the availability of the entire network and maintenance expenses. Defence applications require advanced sensor fusion and effective surveillance of the surroundings so the main driver for functionality is the performance of systems, which can be on air, space or naval platforms.

2.3.1 Weather and Air Control Surveillance

One of the first attempts to achieve this was initiated by the National Oceanic and Atmospheric Administration (NOAA) and the Federal Aviation Administration (FAA), both governmental agencies of the United States. A joint project named Multifunction Phased Array Radar (MPAR) was proposed in 2003 with three main goals: affordability, multifunctionality and dual polarisation [Stailey and Hondl, 2016]. Some radars at that time incorporated multiple functions, mainly in defence applications related to point targets, that conducted missile and aircraft surveillance with tracking and targeting. But the requirements for MPAR delegated the radar system to perform both weather and aircraft surveillance as primary tasks. The required flexibility was provided by a phased array, which enabled quick scanning and effective switching between the operating modes. An additional novelty was the introduction of dual polarisation to an active antenna ar-

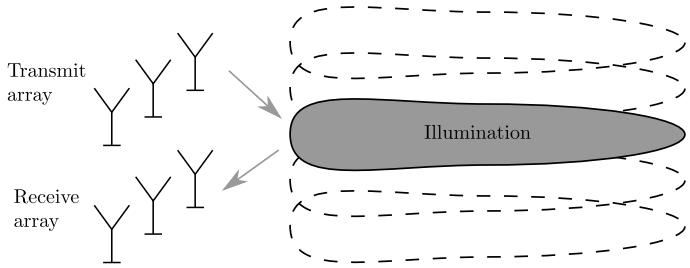

(a) Phased Array Radar

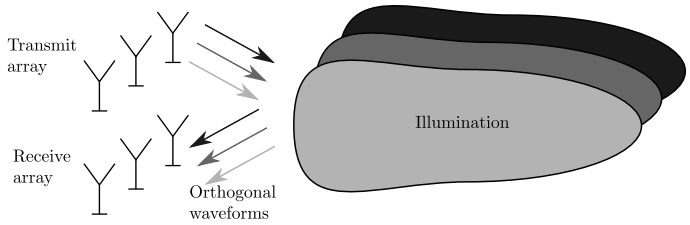

(b) Coherent MIMO Radar

Figure 2.3: Scanning difference of (a) phased array radar with high gain and narrower beam swath and (b) coherent MIMO radar with lower main beam gain and wider swath.

ray system, as different surveillance missions require different polarisation modes. For aircraft surveillance, linear polarisation is preferred and, in the case of heavy precipitation, the polarisation is switched to circular in order to mitigate polarisation losses. Weather surveillance usually exploits differential reflectivity, differential phase, and cross-correlation coefficients to determine the reflectivity characteristics of rain and hail, which all requires dual simultaneous polarisation transmission [Herd et al., 2010]. Time scheduling of surveillance was optimised by adopting simultaneous multibeam clusters in a way that the search volume was divided into different areas with dedicated scanning beams. It was found that broadening the illuminating beam and receiving with multiple narrower beams significantly accelerated the volume search rate.

Additionally, MPAR incorporated adaptive weather scanning that allowed for continuous adaptation of running parameters. The compromises have to be taken into account when determining a scanning strategy which is defined by update time, spatial sampling, and data quality, which involves the variance of meteorological variables, absence of artefacts, and sampling ambiguities [Torres et al., 2014].

The MPAR test bed was active until 2016 and successfully demonstrated the suitability of a phased array for weather monitoring. In addition, faster volume scans techniques were developed, wind profiling was demonstrated, and more comprehensive thunderstorm characterisations were available, all while the simultaneous tracking of aircraft was conducted. The successor of MPAR is in development under the name of Advanced Technology Demonstrator (ATD) [Conway et al., 2018].

2.3.2 Defence Applications

Multifunction radar systems are widely used in defence applications, where they have to meet complex scenarios in increasingly contested environments. The main challenges are adversaries with low RCS platforms, low speed platforms masked with clutter, and high speed hypersonic and ballistic targets. Furthermore, access to the electromagnetic spectrum could be actively denied by jamming and effective countermeasures have to be adopted in such scenarios. Fielded phased array systems nowadays allow for multiple concurrent functionalities, for example volume searching, tracking, non-cooperative target recognition and communication uplinks. Multiple tasks therefore require effective resource

management in terms of time, energy and frequency budgets in order to optimise the performance of a radar system in a contested environment [Labreuche et al., 2017].

The amount of RF sensors on naval vessels has increased significantly in the last three decades, which inevitability contributed towards higher levels of interference, more complex onboard processing and centralised information systems. The additional aerials and radar equipment increased the RCS of naval vessels, which made them more vulnerable in contested environments. To address this problem multifunction RF systems have been investigated, based on phased arrays, also called active electronically steered arrays (AESA), that can support all the operational requirements, such as radar sensing, communications and electronic warfare functionalities, which would include electronic attack and electronic support [Moo and DiFilippo, 2018]. AESA technology with the quick scanning ability and possibility to divide the antenna array into multiple subarrays is a suitable technology to enable multifunctionality and it has been extensively deployed on all modern naval vessels. The separation of transmit and receive AESA subarrays from scalability point of view is further investigated in [Huizing, 2008].

Multifunction systems based on AESA technology have been deployed on airborne platforms as well, where they are additionally constrained by weight and limited space. Joining multiple functionalities in one sensor therefore enables more efficient integration of the sensor and opens up the possibility to more effectively processing the acquired signals in terms of data fusion. In [Winter and Lupinski, 2006], the authors investigated the problem of scheduling the dwell times of a multifunction radar system. The timing optimisation was recast as a linear programming problem, which can be efficiently solved in polynomial time.

Airborne ground surveillance platforms are affected by ground clutter interference and the usual approach to mitigate this is to apply space-time adaptive processing (STAP). In [Burger and Nickel, 2008], an advanced STAP algorithm was applied to a multifunction radar with subbarayed planar antenna structures intended for ground moving target indication (GMTI). A solution was presented to effectively combine the STAP method with adaptive target detection algorithms.

Although multifunction and MIMO radar systems are of great interest to the defence sector, much of the research and technology is classified.

2.3.3 Joint Radar and Communication Systems

One of the research areas related to multifunction radar systems is investigating a possibility to simultaneously conduct radar sensing and communication activities. The main benefits of such an application are common hardware usage and more optimal spectral utilisation. This would in turn ease the spectrum competition and enhance the functionality of cognitive radio and radar systems [Hassanien et al., 2016]. Two possible approaches have been adopted by the research community. One treats radar and communication systems as separate entities, where each system is designed in a way that the mutual interference is reduced, for example by employing dynamic spectral sensing or adaptive cancellation. The second approach concentrates on co-designing a single system with two functionalities that exploit waveform diversity to enable coexistence of all the transmitted waveforms.

Although the approach of joint radar and communication can be applied to an MBR, separation of the combined functionalities is not possible. Therefore, it can be only used to augment a single MBR channel rather than implement two or more separate channels.

An approach to co-designing simultaneous radar and communications emissions from the same antenna array with the same spectral support was presented in [McCormick et al., 2017]. The approach is similar to the space-division multiple-access, as the algorithm seeks to produce a radar beam in one spatial direction and the communication beam in another spatial direction, where both are determined in the far field by phase steering. The radar functionality is designed as a primary task, but it still suffers from power degradation that has to be allocated to the communication channel, which inevitably reduces the SNR and therefore the radar sensitivity. In order to keep the emitting power constant, so that the waveforms can be transmitted by a power amplifier in the saturated mode, a null space of the steering matrix is used to form the waveform matrix. The waveform matrix is therefore a summation of two orthogonal matrices, where one contains the information about the waveforms and the other is used to level up the transmission power without affecting the two waveforms, which are steered in a predefined direction.

In [Hassanien et al., 2016], phase modulation based dual function radar and communication system was proposed. The authors proposed a bank of beamforming weight vectors on transmit that satisfied a predefined radiation pattern and can be slightly modified for

each radar pulse in order to convey the embedded communication information towards the receiver. The bank of weights can be determined by solving an optimisation problem and it was noted that reflecting each weight against the unit circle in complex plane preserved the magnitude of beampattern. For an $M \times 1$ vector 2^{M-1} possible weight vectors can be determined, each with the same radiation pattern and a different phase shift. Therefore each phase shift, corresponding to a communication symbol, has to be matched with the appropriate vector of weights by a minimisation criterion. Three communication strategies are proposed. Coherent phase modulation requires only one transmission waveform but synchronisation mismatches can cause performance degradation. Non-coherent modulation requires two orthogonal waveforms pointing in one direction, which are simultaneously transmitted, such that the information can be embedded in the phase difference, whereas the third strategy, non-coherent broadcasting mode, transmits in all directions.

In [Hassanien et al., 2017], the authors also designed dual function radar communications codes specifically for MIMO systems. The proposed MIMO radar uses frequency hopping (FH) codes [Han and Nehorai, 2016] and it is assumed that communication embedding is a secondary function, prioritising the optimisation of FH codes. The information embedding is implemented by phase shift keying (PSK), where each of the P frequency hops in one pulse is phase modulated according to the constellation diagram. As the MIMO radar transmits an orthogonal waveform from each of its M antennas, the number of transmitted communication symbols per radar pulse equals MP.

The waveform diversity of LFM chirps signals to design coexisting radar and communication systems was exploited by Kota et al. [Kota et al., 2016]. The authors envisaged a multiuser scenario, with each user using an LFM waveform with different chirp rate. The information intended for each user was embedded in each LFM signal by PSK modulation, where all of the signals were in time synchronisation. Mutual interference between communication channels was minimised by defining the chirp rates via stochastic optimisation. Additional optimisation was performed to reduce mutual interference between the radar chirp waveform and the set of communication signals. As noted, both optimisation problems do not have a joint optimal design, therefore a multi-objective Pareto optimisation was considered to highlight the performance trade-offs.

A dual function radar and communication system was proposed in [Hassanien et al.,

2015], where sidelobe control and waveform diversity were utilised to achieve both functionalities. It was assumed that the radar transmits Q orthogonal waveforms from each antenna in the array and all the waveforms are time synchronised. Two weight vectors were designed for each orthogonal waveform such that the mainlobe pattern was preserved and sidelobes pointing in the direction of communication links possessed two distinct magnitude levels. The transmitter could therefore transmit Q-bit of information per each radar pulse. The receiver matched to one waveform had to estimate which weight vector the received signal belonged to. The drawback of the demonstrated technique is that it can only transmit information in one or multiple directions outside the mainlobe.

Another possibility to separate communications and radar signals is to use OFDM. In this case the frequency separation of waveforms is ensuring low interference levels. In [Sturm et al., 2009], the PSK modulation was used in conjunction with OFDM so that the simultaneous operation of both systems was achieved, whereas in [Kangrun Chen et al., 2015] the fractional Fourier transform (FRFT) was utilised as modulation scheme of OFDM signals.

2.4 Waveform Design

Waveform design is an important aspect of every radar system that defines radar sensing characteristics and its performance. It plays an especially important role in MIMO radar systems since all the signal models presented in Section 2.2.1 assume little or no interference between the waveforms, whereas the waveforms in Section 2.2.2 have to conform to exact correlation constraints in order to perform as intended.

Multiple approaches have been followed by the research community to design suitable MIMO radar waveforms. The available degrees of freedom, e.g. time, space, frequency and waveform diversity, can be exploited to optimise a waveform according to a predefined criterion or multiple criteria, sequentially or at the same time. Objective functions in the optimisation problems are used to optimise selected aspects of waveforms, for example increasing the detectability of a target, suppressing clutter or interference sources, improving the radar map quality of the surroundings, increasing spatial resolution, reducing searching time or decreasing sidelobes in rage and Doppler domains [Li and Stoica, 2009,

Chapter 6].

The waveforms can be classified in different groups and as presented herein, they are grouped according to whether they are based on LFM, whether they are presented in discrete form for optimisation techniques or whether they can be treated as chaotic or noise-like signals. The biggest emphasis is given on the review of LFM waveforms, which are the main subject of this research and are presented in more detail in Section 2.4.1.

2.4.1 Waveforms Based on LFM

Orthogonality of waveforms may be imposed in time domain, frequency domain or in signal space, which is usually referred to as waveform diversity. In [Galati and Pavan, 2011a, Galati and Pavan, 2011b] the feasibility of LFM to implement two orthogonal channels by exploiting up-chirp and down-chirp diversity is demonstrated. Further research, published in [Galati and Pavan, 2013] compared orthogonality of LFM waveforms to Costas codes [Levanon, 2004] and established the fact that the isolation is improving with time-bandwidth product of the LFM waveforms. Amplitude modulation (AM) has an impact on waveform performance from the isolation point of view as well and more thorough investigation is reported in Chapter 5.

One of the main advantages of LFM waveforms is their Doppler tolerance that is generally exploited in most fielded radar systems. This property, though, prevents the LFM waveforms to detect and estimate Doppler shifts and the train of pulses is needed to achieve this. To adapt LFM for Doppler sensitivity, a triangular FM waveform can be adopted, or more generally, piecewise linear frequency modulated (PLFM) waveforms.

PLFM waveforms were investigated in [Qazi and Fam, 2012], where three different modulations are presented in terms of numerical simulations. To improve the Doppler tolerance, an extended matched filter was introduced by widening the chirp modulations in time-frequency domain. The resulting behaviour improved Doppler tolerance at the expense of lowering the SNR and slightly increasing cross-correlation values of a set of waveforms. The authors extended their work in [Qazi and Fam, 2014, Qazi and Fam, 2015] to prove the behaviour of the extended matched filter and demonstrated the extraction of target range and radial velocity. The PLFM is substituted by chirplike polyphase codes P3 and P4 that possess quadratic phase dependence and therefore preserve Doppler tolerance

[Levanon, 2004]. The phases of P3 and P4 codes for any length M are defined as

$$\Phi_{P3}(m) = \frac{2\pi}{M}\frac{(m-1)^2}{2} \tag{2.4}$$

$$\Phi_{P4}(m) = \frac{2\pi}{M}(m-1)\left(\frac{m-1-M}{2}\right) \tag{2.5}$$

where m is a phase index. The resulting sets of waveforms were named polyphase PLFM (PPLFM) and it is shown that they inherit good correlation and Doppler properties of PLFM. An example of PLFM is depicted in Figure 2.4 where the waveform modulations are shown in black and extended matched filter modifications are shown in dashed black colour. The extended matched filter on receive is decomposed into two parts, each one matched to one of the LFM waveforms and processed jointly for detection.

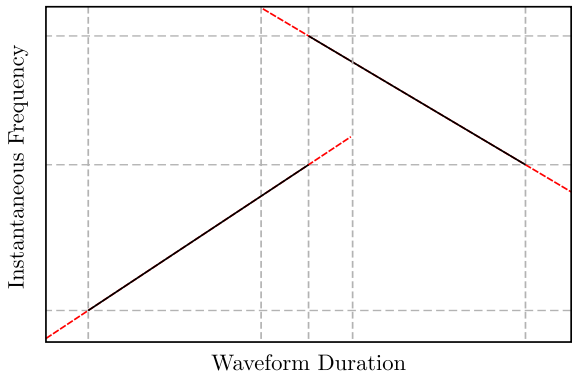

Figure 2.4: Time-frequency modulation scheme of a two-portion PLFM waveform, shown in black. The extended matched filter additions are shown in red.

A similar approach to PLFM design was presented by [Gao et al., 2016], wherein the waveforms were divided in PLFM subpulses, which consisted of three linear parts. The definition of PLFM modulation allows for six degrees of freedom with the bounded bandwidth and pulse repetition interval (PRI). For M waveforms with each containing N subpulses, the total amount of degrees of freedom is $6NM$, which were utilised in an optimisation routine, based on genetic search algorithm. By keeping the time duration and bandwidth fixed, $4NM$ degrees of freedom were used to optimise cross-correlation values and sidelobes of the autocorrelation function.

In [Chang et al., 2018], the authors introduced another method to design a set of PLFM waveforms, named discrete frequency and chirp-rate coding waveform (DFCCW). Each waveform, designed for the proposed MIMO radar, is composed of M subpulses that

are LFM. The analytical expressions for ambiguity and cross-ambiguity functions were provided so that relative time delays and Doppler shifts were taken into account. Each LFM subpulse has two variable parameters that define frequency offset and chirp rate, which were tuned during the optimisation. The optimisation was set as a multi-objective problem, where the authors employed a differential genetic algorithm to determine Pareto optimal boundaries according to four criteria, ambiguity sidelobe peak, ambiguity main-lobe volume, cross-ambiguity peak and cross-ambiguity volume. As the final cost function was not defined as a weighted sum and the solution was presented in a Pareto optimal fashion, an optimal waveform could be selected based on the importance of the underlying criterium functions.

Synthetic aperture radar (SAR) is a well-understood radar imaging technique, however, new operational requirements have demanded an increased resolution and wider swath scanning performance. One of the more recent solutions to this problem was presented by [Wang and Cai, 2012], where a MIMO SAR system is proposed. In a conventional SAR system a narrower beam and higher pulse repetition frequency (PRF) are needed to improve azimuth resolution, but increasing PRF inevitably increases ambiguous range and therefore decreases swath width. The proposed idea is to place a MIMO antenna array in cross-track direction to form multiple independent beams, each beam belonging to a particular subaperture, i.e. antenna subarray. The waveforms used by different subapertures should be orthogonal, with a high time-bandwidth product and constant transmit power, therefore the authors proposed an OFDM chirp waveform to meet the required criteria. The waveform was in essence a concatenation of multiple short chirp signals covering only a portion of the entire bandwidth. The number of time and frequency steps could be different and it depended on how many orthogonal waveforms were required in a set. An example of two non optimised OFDM chirp waveforms is shown in Figure 2.5.

Further improvement of the proposed waveforms was done in [Wang, 2015], where the author exploited time delays and frequency shifts of chirps to decorrelate the waveforms. The design of the waveforms was done by implementing a random matrix modulation routine that took into account the reduction of the peak-to-average ratios in time and frequency domains. Despite improvements in resolution and swath size, the method suffers

from decreased SNR as the proposed waveforms are not perfectly orthogonal.

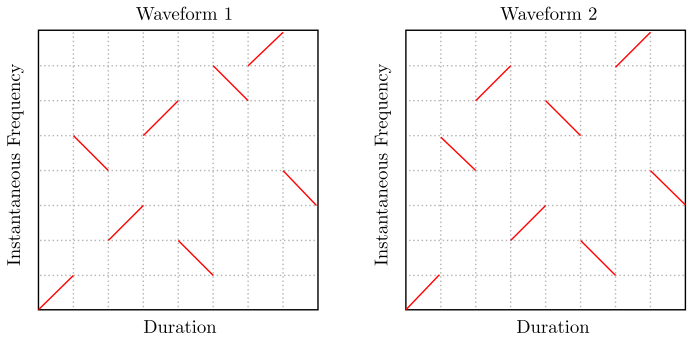

Figure 2.5: Two quasi-orthogonal waveforms implemented by OFDM chirp waveform diversity. The optimisation routine tries to minimise the difference of chirp appearances in each row and each column.

It was noted in [Krieger, 2014], where OFDM chirp waveforms were tested on SAR images, that waveform orthogonality in practice may not suffice and additional time or spatial separation of received signals may be needed. Further details on waveform orthogonality are covered in Chapter 5.

In recent work, further relaxation of additional degrees of freedom related to OFDM chirp waveforms was proposed by [Li et al., 2017]. It was shown that the usage of the same subpulses, i.e. chirps with the same frequency offset and the same bandwidth, causes increased peak sidelobe levels (PSL) and cross-correlation peak levels (CPL). To improve the PSL optimisation metric different chirp rates were used by arbitrarily varying time duration or bandwidth of subpulses. An improved performance is reported with numerical simulations.

2.4.2 Polyphase Waveforms Based on Heuristics

In this section, a review and latest achievements in design of binary and polyphase codes based on heuristic optimisation methods are given. The size of a set defining phase constellation can vary from two elements to a continuous interval of length 2π and the design methods have to be adapted accordingly. The phase coding principle and different generating techniques have been a subject of research for several decades and an extensive review of the most known codes is given in [Levanon, 2004, Chapter 6]. The discrete nature of polyphase codes makes them suitable for different optimisation techniques, e.g. genetic algorithms [Liu et al., 2006], simulated annealing [Deng, 2004], particle swarm

optimisation [Zeng et al., 2011], tabu search [Liu et al., 2012], and others.

It has to be noted that the instantaneous phase changes between consecutive phase codes cause spectral leakage, which is not passed through an operational radar transmitting chain. This effect, including the nonlinearity of the power amplifier, causes a distortion of the transmitted waveform that affects reception performance. In [Blunt et al., 2014b, Blunt et al., 2014a] this issues are addressed by proposing continuous phase modulation (CPM), which is spectrally contained, power efficient because of the constant envelope, and can be implemented by frequency modulation.

In [Deng, 2004] a technique was demonstrated to design polyphase codes for a statistical MIMO radar system, named orthogonal netted radar systems (ONRS). A simulated annealing algorithm was used to optimise cost function that quantifies energy in the autocorrelation sidelobes and cross-correlation functions. The numerical results were reported for multiple sets of waveforms and it was shown that the average cross-correlation peaks decrease at the rate of $1/\sqrt{N}$, where N was the length of the code. The autocorrelation properties of the proposed polyphase codes were worse than the well known Frank and Golomb codes [Levanon, 2004].

A similar approach to polyphase code design was followed by [Khan et al., 2006], where the resilience to Doppler shifts was addressed and further improvements to the optimisation algorithm were done to take into account cross entropy between the waveforms. For signals with the length of 128 samples, mean cross-correlation reached $-25.8\,\mathrm{dB}$.

Another technique was demonstrated by [Yang et al., 2013], where polyphase codes were optimised with an adaptive clonal selection algorithm. The autocorrelation and cross-correlation levels of comparable codes with the length of 40 samples were similar to the codes proposed by [Deng, 2004, Khan et al., 2006], while the orthogonality deterioration due to Doppler effect was significantly smaller as the Doppler effect was accounted for in the cost function.

In [Petrolati et al., 2012], the authors proposed a technique to generate piecewise linear polyphase codes that improved on peak to side-peak ratio and sidelobe energy when compared to Frank and Px codes [Levanon, 2004]. To design the codes, the authors relied on the Fourier transform duality property when a flat spectrum corresponds to sharp peak in autocorrelation function. The codes, named PAT, were generated by a simple recursive

formula, which made them easy to implement for arbitrary lengths.

In [Ren et al., 2019] an improved genetic algorithm MA-GCS was presented that was divided in two steps in order to improve on exploration and exploitation properties of a code search. In general, evolutionary algorithms are employed to improve on exploration ability, which is related to searching for new potential solutions on a global level. Whereas greedy code searches are more powerful locally and are implemented to improve the accuracy of a solution. Numerical simulations showed the orthogonality levels of 20.8 dB for a length of 200, 24.2 dB for 512, and 25.4 dB for 2046.

For more information on heuristically optimised waveforms, the reader is referred to [Ren et al., 2019] and the references therein.

2.4.3 Polyphase Waveforms Based on Numerical Optimisation

This section gives an overview of the numerically optimised polyphase codes that rely on gradient descent algorithms. Multiple approaches to an optimisation problem exist and they mostly depend on whether an objective function, together with the possible constraints, can be recognised as convex, can be relaxed to a convex problem or can be majorised by a convex problem (in the case of minimisation). All of the listed techniques, which require convexity assumptions, are sufficient to find an optimal solution, but often enough convexity is not met and the resort to conventional methods is needed. A plethora of numerical optimisation methods is available [Jorge Nocedal, 2006], such as linear search methods, trust-region methods, conjugate gradient methods, quasi-Newton methods, etc.

An extensive work related to the computation of cyclic algorithms was presented by [He et al., 2012] with possible applications to MIMO waveform design [He et al., 2009]. Proposed cyclic algorithm-new (CAN) was designed to minimise integrated sidelobe level (ISL) metric in frequency space and could therefore be used for very long codes $N \approx 10^6$. Weighting can be applied to the ISL metric to improve the correlation sidelobes and a weighted CAN (WeCAN) algorithm was developed for this purpose. It was additionally shown that quantisation of phase space reduces performance and ISL was increased in this case. An extension to the CAN was performed to design aperiodic sequence sets that can be used as MIMO waveforms. The cost function was extended to account for the auto-correlation sidelobes and cross-correlation levels, which were converted to frequency space

for optimisation. Resulting Multi-CAN and Multi-WeCAN algorithms could suppress the cross-correlation peaks to $-18.9\,\mathrm{dB}$ and $-29.1\,\mathrm{dB}$, respectively, for a set of $M = 4$ codes, length of $N = 256$ and $P = 50$ correlation lags. The drawback is that the Multi-CAN algorithms are useful for a predetermined amount of correlation lags.

It is well known that the complementary codes of a corresponding set, e.g. Golay codes, have autocorrelation functions that sum to zero for every out-of-phase lag. This property can be exploited to reduce the sidelobes, whereby code separation at receive has to be ensured. In [Searle et al., 2008], the authors proposed separating the square-complimentary codes in frequency space for multiple MIMO channels and [Soltanalian et al., 2013] provided an efficient CAN algorithm to design such codes. The complexity was reduced by employing fast Fourier transform (FFT) rather than eigenvalue decomposition technique. Another method to calculate complementary sets of sequences was proposed, which concentrated on minimising ISL under multiple constraints [Wu et al., 2019]. A majorisation function was found that was successfully implemented in a majorisation-minimisation (MM) algorithm.

In [Aubry et al., 2014], the authors addressed the problem of spectral coexistence between licensed electromagnetic radiators and newly added radar systems. The optimised figure of merit was SINR, while an additional constraint ensured that the interference energy on the occupied spectral bands was minimised and a similarity constraint enforced the properties of a targeted waveform to be inherited, in this case range-Doppler resolution, signal amplitude variations and PSL. The problem was found to be nonconvex quadratically constrained quadratic programming (QCQP), which was relaxed to the convex semidefinite programming (SDP) problem that could be solved in polynomial time.

2.4.4 Chaotic and Random Waveforms

Transmitting chaotic, noise or pseudo-random waveforms is not a novel idea and the topic has been extensively researched in the past [Liu Guosui et al., 1999]. The first paper on noise modulation appeared in 1959 by [Horton, 1959] to implement a range-measuring radar. Random signal radars (RSR) utilise such waveforms, which do not suffer from range or Doppler ambiguity, have low peak power, and can effectively share the same environment with other electromagnetic devices [Kulpa, 2013]. Low peak power makes them suitable

as an electronic counter-countermeasure (ECCM) technique and the random nature of generation simplifies generation of multiple waveforms. They have been used in a wide range of applications, e.g. surveillance, interferometric SAR, SAR, altimetry, collision warning, subsurface profiling [Axelsson, 2003].

In [Willsey et al., 2011a] quasi orthogonal wideband waveforms were proposed, that were based on the Lorenz chaotic system. It was shown that the resulting waveforms possessed a contained spectrum, low range sidelobes and a small variation of amplitude. The waveforms were an output of a deterministic system and can therefore be specified by a small number of parameters. Additional properties of the Lorenz-based waveforms were given in [Willsey et al., 2011b], where the relation between parameters and bandwidth scaling is shown.

MIMO waveform generation with Chebyshev chaotic maps was investigated by [Esmaeili Najafabadi et al., 2017] wherein the proposed waveforms were compared to Lorenz-based and Multi-CAN waveforms. It was shown through simulations that the Chebyshev waveforms perform better in terms of cross-correlation peaks when generating a set of $M = 40$ waveforms of length in the range from $N = 10$ to $N = 1000$. Additionally, it was statistically demonstrated that the cross-correlation peak and autocorrelation sidelobe ratios with respect to the autocorrelation peak tend to $-\infty$ when $N \to \infty$.

A different approach, utilising chaotic behaviour, was taken by [Jin et al., 2013]. Four chaotic systems were used (Bernoulli, Logistic, Tent, and Quadratic mapping) to generate arbitrarily long sequences, for which complementary codes were found by implementing a genetic algorithm. It was shown that the resulting codes exhibit lower autocorrelation sidelobes due to interference from complimentary codes when compared to Deng codes and, additionally, the sidelobe levels remained suppressed when Doppler shift was applied, as a Doppler penalty function had been incorporated in the optimisation procedure.

The utilisation of noise as a random signal was proposed and tested by [Lai and Narayanan, 2010]. A digital noise radar system was used to detect and track humans behind building walls by correlating signal echoes with the digitally stored replica of the transmitted noise signal.

In [Axelsson, 2003], the author investigated Gaussian random noise waveforms for range-Doppler estimation and digital beamforming. The possible use of low-bit analog-to-

digital converters (ADC) was demonstrated when fast signal processing was needed due to receiver correlating over multiple range gates and fine resolution Doppler filtering. It was shown that injecting an extra noise signal before ADC conversion additionally suppresses the sidelobes.

Noise waveforms were also used in [Xu and Shi, 2018] to mitigate interference for automotive radars. The Wiener-Khinchin relations were utilised to improve sidelobes by applying an optimised Kaiser window to the noise spectrum and phase retrieval algorithm was used to obtain the final noise signal to be transmitted.

MIMO noise radars were discussed in [Gray and Capria, 2008], where two possible configurations are noted, namely element space and beam space. In the element space mode, each omnidirectional antenna transmitted an independent instance of noise, whereas in the beam space mode, each independent noise source was used to illuminate a partial field of view. It was shown that in the element space mode, the radar possesses typical MIMO radar advantages, but the related matched filter has a large statistical variability and the receiving signal needs longer averaging.

2.5 Summary

This chapter discussed the advances in MIMO and multifunction radar systems. Although MIMO radar is a different concept when compared to a multifunctional phased array system, many similarities and key concepts are shared in waveform design, that is suitable for a particular type of radar. Many advantages of MIMO radars were pointed out, such as spatial decorrelation, improved resolution, and detection, but it has to be mentioned that most of the conclusions rely on the fact that suitable perfectly orthogonal waveforms can be generated. In practice, this is not the case and further research should focus on the effects of the non-perfectly orthogonal waveforms on the performance on MIMO systems. One of the major challenges in the field of MIMO radar therefore remains the waveform design. All possible approaches to the design were demonstrated, but the given list of references is by no means exhaustive. As this thesis mainly studies the LFM waveforms, mostly the references in Section 2.4.1 are relevant for Chapter 3.

Chapter 3

Radar Signal Processing

3.1 Introduction

In this chapter, basic radar principles will be presented, explaining how a pulsed radar system works and the physical principles that determine its performance. A mathematical definition of waveform representation will be discussed, along with simple models of signal upconversion and downconversion. Additionally, the most common waveforms and their basic properties will be presented. The ambiguity function, as a very important tool to analyse radar waveforms, concludes the chapter.

3.2 Operating Principles

Radar systems are electrical devices that utilise electromagnetic (EM) waves in the radiofrequency (RF) spectrum to sense the surrounding environment. The name radar originates from its historical designation, when it was used as an acronym for radio detection and ranging. Nowadays, radars have a wide scope of applications and can be utilised as ranging, detection, imaging or energy delivery systems.

3.2.1 Radar Configurations and Modes of Operation

In this section, a basic overview of different radar configurations and operating modes will be given. In terms of antenna placements, monostatic, bistatic, and multistatic configurations of a radar system are possible. The monostatic layout is the most basic configuration

in which, most commonly, the receiver and the transmitter share the same antenna. This configuration simplifies the mechanical structure of a radar system and makes it more compact but introduces additional challenges, such as providing sufficient isolation between the transmitting and receiving chain. Monostatic operation is also considered in the case when the transmitting and receiving antennas are placed closely together so that both antenna beams cover the same spatial angle and illuminate the same aspect angle of a target. A bistatic configuration has already been discussed in Section 2.2.1 in the context of statistical MIMO radars, which share similar geometrical relationships between the positions of antennas. Longer separation between the antenna locations allows for spatial decorrelation and can improve the detectability of targets. Additionally, better isolation between transmitter and receiver is achieved. Bistatic notion can be naturally extended to multiple antennas, which results in a network of radar systems, cooperating with each other to improve detection statistics [Deng, 2004] or cover a wider search area.

Another distinction is based on the transmission mode, as radars can be divided in two categories, namely continuous wave (CW) and pulsed radars [Richards et al., 2009]. CW radars continuously transmit without interruptions and continuously receive as well, which requires the transmitter and receiver to be separated in order to reduce the mutual interference. The pulsed radars only transmit for very short periods and then switch to the receiving or listening mode, during which only the receiving chain is active. The combined time of transmitting and listening mode is called pulse repetition interval (PRI) or interpulse period (IPP), as depicted in Figure 3.1. The number of transmitting cycles per second is called pulse repetition frequency (PRF) and it is determined as $PRF = 1/PRI$. The ratio between the transmitting time T_{tr} and PRI is called the duty cycle

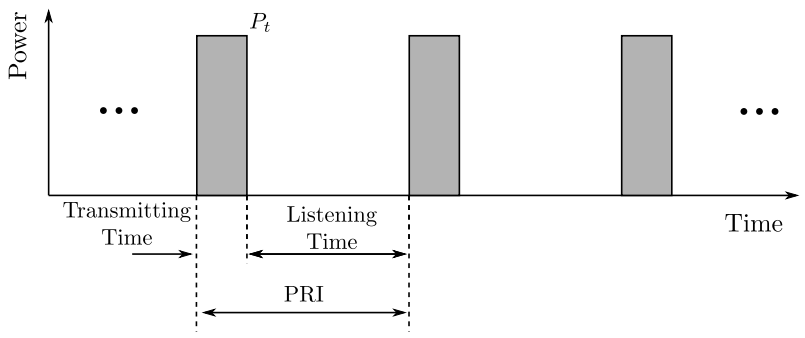

Figure 3.1: Pulsed radar transmission diagram.

d_t and defined as $d_t = T_{tr}/PRI$. It is related to the average transmitting power as $P_{avg} = P_t d_t$, where P_t is transmitting power. The length of PRI is conditioned by the range measurement ambiguity. The travel time of an EM wave is determined as $T_t = 2R/c$, where R is range to the target and c is the speed of light. If the echo signal is not received before the next pulse is transmitted, the range ambiguity will appear, since the radar will associate the echo with the wrong transmitted pulse. In order to avoid such ambiguities, PRI should satisfy the following $PRI > 2R_{max}/c$, where R_{max} is the maximum range that a radar system can detect unambiguously. Another disadvantage related to the monostatic radar is its blind range. Because the monostatic radar cannot be receiving during transmission, the minimum detectable range is determined by the transmission time $R_{min} = cT_{tr}/2$.

Radars can operate as noncoherent or coherent systems. While the noncoherent radars detect only the amplitude, the coherent ones detect both amplitude and phase. Coherent radars, which are prevalent nowadays, can determine the phase on a pulse to pulse basis and can therefore be utilised for motion measurements and imaging. A relative motion between the target and the radar will cause a change in frequency. This change or Doppler shift can be approximately determined as $f_D = 2v/\lambda$, where v is the radial speed of the target in relation to the radar. As the pulsed radar is sampling the Doppler shift at the rate of PRF, sampling has to be done at double the rate of expected frequency shift to satisfy the Nyquist condition. In other words, the maximum unambiguous Doppler shift that can be detected is $f_{D,max} = \pm PRF/2$. Doppler shift can be utilised in many applications, such as Doppler beam sharpening (DBS), cross-range resolution in SAR, and stationary clutter rejection in moving target indication (MTI) radars.

Resolution is a property of a radar system that describes its ability to resolve two closely spaced targets. Figure 3.2 shows signal returns from four targets as received by

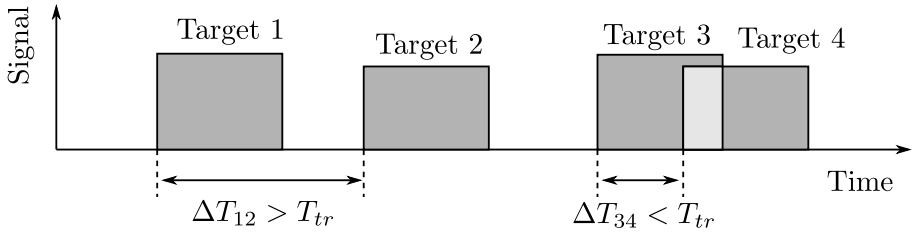

Figure 3.2: Radar range resolution between two closely spaced targets.

a receiver. The time delay between the first two targets is $\Delta T_{12} = 2\Delta R_{12}/c$, which is long enough to distinguish between the targets as the delay is longer than the pulse width $\Delta T_{12} > T_{tr}$. The opposite is true in the second case, where the condition is not met. Range resolution can be improved by pulse compression, which is further discussed in Section 3.6.

3.2.2 Radar Components

A typical radar block diagram is presented in Figure 3.3, which shows a simplified version of a pulsed radar, operating as an MTI radar system [Skolnik, 2008, Chapter 2.2]. The

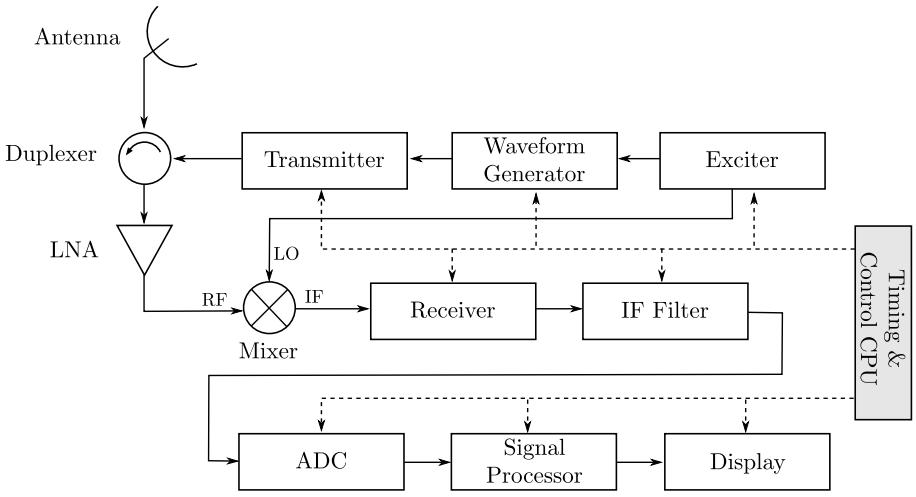

Figure 3.3: Simplified block diagram of a radar system.

integral block is the timing and control central processing unit (CPU), which is a general-purpose computer that controls all aspects of the radar, schedules timing operations, and ensures proper functioning of all subcomponents. The transmitting chain starts with the exciter, which acts as a source of continuous and very stable low-power signal. The reference frequency is then passed on to the waveform generator, which selects a suitable waveform and modulates it to the carrier. After this stage, the signal needs to be amplified to a suitable level by a power amplifier (PA) or a travelling wave tube (TWT) in order to be transmitted into the propagating medium by an antenna. In a pulsed radar, the transmitting and receiving chains are both connected to the same antenna via a simple switch or a duplexer, which provides separation between powerful transmitted signals and sensitive receiver components. Antennas can exist in many different forms, but their main

function is to act as a transitional structure between a guiding device (e.g. coaxial cable, waveguide) and the free space. Assuming that the antenna is pointing towards a target, the signal is echoed back and received by the same antenna. The signal is then amplified due to antenna gain and conveyed through the duplexer to the low-noise amplifier (LNA). Thereafter, the RF signal is down-converted to the intermediate frequency (IF), which is a difference between RF frequency and local oscillator (LO) frequency in the case of low-side injection, and supplied to the IF filter before it is passed on to the analog-to-digital converter (ADC). The digitised signal is read by the signal processor, which is a digital computer handling the received signals, arranging the data into the range bins, additionally applying target detection and clutter rejection algorithms, if needed. The processed information is then shown on a display.

A more detailed representation of a receiver block chain is shown in Figure 3.4. It depicts a dual conversion superheterodyne receiver as the RF frequency is down-converted twice to obtain two IF, in order to apply band-pass filtering progressively. The signal that arrives from the duplexer is first filtered by a band-pass filter (BPF) to remove any frequencies outside the channel of operation and is then amplified by the LNA. The next stage is the high IF stage mixer. Using higher IF frequency for Mixer 1 permits for a wider frequency separation between the signal and its image, which are $2f_{IF,1}$ apart, and therefore allows for a better image suppression by the BPF 2. Signal is then further filtered by the channel rejection filter BPF 3 and amplified by the IF amplifier before it is passed to the low IF stage. At this stage, another image rejection filter, BPF 4, is used before the signal is down-converted to $f_{IF,2}$. The final filtering is applied by BPF 5, which can be very effective at rejecting close interference signals in the same channel, as it is operating at a lower frequency. Finally, the signal can be further amplified by the second IF amplifier before it is passed to the demodulator and ADC. A demodulator is sometimes referred to as video detector and it produces I and Q components of the received signal, as will be discussed in Section 3.3. Actual receivers tend to have more complex structures and the reader is referred to [Drentea, 2010] for further insight.

The signal processing block that is shown in Figure 3.3 is discussed hereafter in more detail. It is assumed that the ADC converter provides both I and Q components and that the radar operates in the MTI mode [Stimson, 2014]. The data that is provided by the

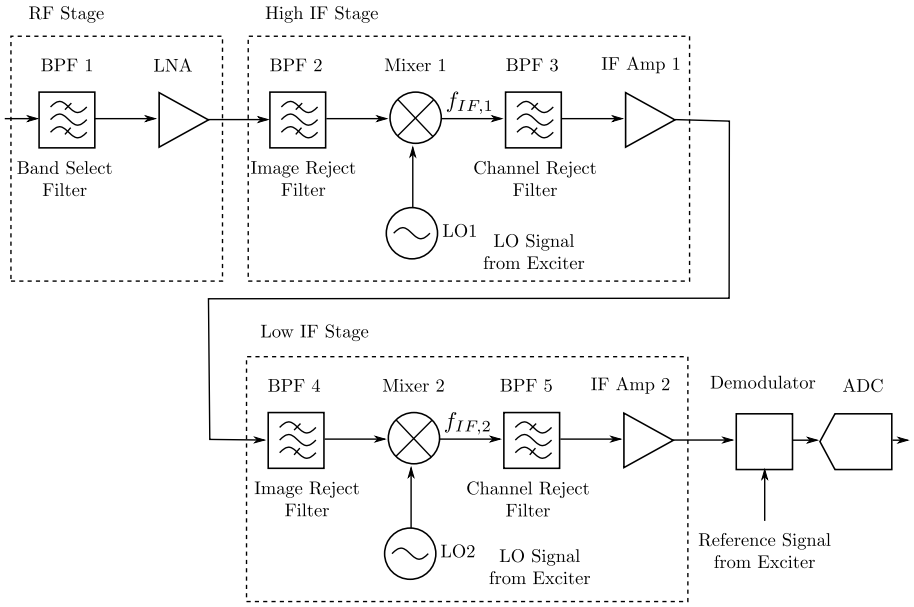

Figure 3.4: Radar receiving chain of a dual conversion superheterodyne receiver.

ADC is rearranged according to the time of arrival into consecutive range bins. Then clutter filtering is applied to remove any strong stationary signals that do not exhibit Doppler shifts. After that, each range bin is processed by a bank of Doppler filters and echoes in each bin are integrated in time to increase the energy return from targets with the same velocity. the threshold detector then applies predefined criteria related to the SNR and effects of the clutter returns to determine a threshold, above which an echo is recognised as a target. The detection is related to the the scan position so that the elevation and azimuth of the target can be determined and information is passed on to the display or for further data processing.

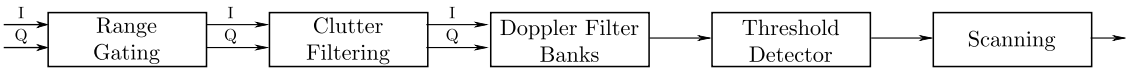

Figure 3.5: Radar receiving chain of a dual conversion superheterodyne receiver.

3.3 Waveform Representation

This section will introduce the Hilbert transformation of the signals, which is used throughout this work. Additionally, in-phase and quadrature components will be introduced along with the narrowband assumption of the signals, that is generally applied herein.

3.3.1 Analytic Signals and Hilbert Transform

Real signals $x(t) \in \mathbb{R}$ have a symmetric energy density spectrum $|X(\omega)|^2$, such that $X(-\omega) = X^*(\omega)$. In order to derive the analytic[1] signal $y(t)$ corresponding to $x(t)$, its real component should be equal to $x(t)$ and its spectrum should be equal to the positive part of $X(\omega)$. Therefore, $x(t) = \Re[y(t)]$ and $Y(\omega) = X_+(\omega)$, where

$$X_+(\omega) = \begin{cases} X(\omega), \omega \geq 0 \\ 0, \omega < 0 \end{cases} \tag{3.1}$$

The analytic signal can now be expressed [Cohen, 1994] with an inverse Fourier transform of $X_+(\omega)$ as

$$y(t) = 2\frac{1}{\sqrt{2\pi}} \int_{-\infty}^{\infty} X_+(\omega) e^{j\omega t} d\omega \tag{3.2}$$

$$= 2\frac{1}{\sqrt{2\pi}} \int_{0}^{\infty} X(\omega) e^{j\omega t} d\omega \tag{3.3}$$

where the factor 2 is added to equalise the energy content. The Fourier transform of $x(t)$, defined as

$$X(\omega) = \frac{1}{\sqrt{2\pi}} \int_{-\infty}^{\infty} s(t) e^{-j\omega t} dt \tag{3.4}$$

can be inserted in (3.3) to obtain

$$y(t) = \frac{1}{\pi} \int_{0}^{\infty} \int_{-\infty}^{\infty} x(t') e^{j\omega(t-t')} dt' d\omega \tag{3.5}$$

The first integral in (3.5) is equivalent to the inverse Fourier transform of the unit step function in frequency domain

$$\mathcal{F}^{-1}[\mathrm{u}(\omega)] = \frac{1}{\sqrt{2\pi}} \int_{0}^{\infty} e^{j\omega\xi} \, d\omega \tag{3.6}$$

$$= \frac{1}{\sqrt{2\pi}} \left[\pi\delta(\xi) + \frac{j}{\xi} \right] \tag{3.7}$$

[1]The word analytic comes from complex analysis, where it is reserved for the signals that are differentiable in the complex plane and therefore satisfy Cauchy-Riemann conditions.

where the unit step function is

$$\mathrm{u}(t) = \begin{cases} 0, t < 0 \\ 1/2, t = 0 \\ 1, t > 0 \end{cases} \tag{3.8}$$

Inserting (3.7) into (3.5) leads to

$$y(t) = \frac{1}{\pi} \int_{-\infty}^{\infty} x(t') \left[\pi\delta(t - t') + \frac{j}{t - t'} \right] dt' \tag{3.9}$$

The analytic signal of $x(t)$ is then

$$\mathcal{A}[x(t)] = y(t) = x(t) + j \int_{-\infty}^{\infty} \frac{x(t')}{\pi(t - t')} dt' \tag{3.10}$$

where the sifting property of δ function was used for the first term, while the second term can be recognised as the Hilbert transform of $x(t)$.

3.3.2 Hilbert Transform

As was derived in the previous section, the Hilbert transform plays an integral part when defining an analytic signal. According to (3.10) it is defined as

$$\mathcal{H}[x(t)] = \frac{1}{\pi} \int_{-\infty}^{\infty} \frac{x(t')}{t - t'} dt' \tag{3.11}$$

and an analytic signal of function $x(t)$ can be written shortly as

$$\mathcal{A}[x(t)] = x(t) + j\mathcal{H}[x(t)] \tag{3.12}$$

It can be seen from the definition (3.11), that the Hilbert transform can be interpreted as the convolution between the functions $x(t)$ and $1/(\pi t)$. As convolving two functions in the time domain is equivalent to multiplying their Fourier transforms in the frequency domain, further insight can be gained in the frequency space, where $\omega = 2\pi f$. The Fourier

transformation pair

$$\mathcal{F}\left[\frac{1}{\pi t}\right] = -j\,\mathrm{sgn}(f) \tag{3.13}$$

where the signum function is defined as

$$\mathrm{sgn}(f) = \begin{cases} -1, f < 0 \\ 0, f = 0 \\ 1, t > 0 \end{cases} \tag{3.14}$$

can be used to express the Fourier transform of the Hilbert transformed function, which is

$$\mathcal{F}\,[\,\mathcal{H}[x(t)]\,] = -j\,\mathrm{sgn}(f)X(f) \tag{3.15}$$

It follows from the equation above, that the Hilbert transform causes phase shifts of $\pi/2$ for all the negative frequencies and $-\pi/2$ for all the positive frequencies, without altering their amplitude. The spectrum of an analytic signal is then

$$\mathcal{F}[\,\mathcal{A}[x(t)]\,] = X(f) + j\big(-j\,\mathrm{sgn}(f)\big)X(f) \tag{3.16}$$

which is, as noted before, zero for all negative frequencies as they cancel out.

3.3.3 In-Phase and Quadrature Components

The analytic signal, defined as (3.10), is also called a pre-envelope of $x(t)$ and denoted as $\tilde{x}(t)$ [Haykin, 1994]. In communication systems, such signals often have a small bandwidth B in comparison to their carrier frequency f_c and are therefore called band-pass signals. They can be expressed as a product

$$\tilde{x}(t) = \hat{x}(t)e^{j2\pi f_c t} \tag{3.17}$$

where $\hat{x}(t)$ is a newly defined signal, referred to as a complex envelope, and an exponential function is a frequency shift of the carrier signal. The complex envelope can be split into two real-value components, named in-phase and quadrature which are low-pass signals, so

that

$$\hat{x}(t) = x_I(t) + jx_Q(t) \tag{3.18}$$

and the initial signal can be determined as

$$x(t) = \Re[\hat{x}(t)e^{j2\pi f_c t}] \tag{3.19}$$

$$= x_I(t)\cos(2\pi f_c t) - x_Q(t)\sin(2\pi f_c t) \tag{3.20}$$

The process of manipulating the complex envelope is depicted in Figure 3.6 for down-conversion (a) and upconversion (b). The derivations in this work refer to the complex envelope signals, unless stated otherwise.

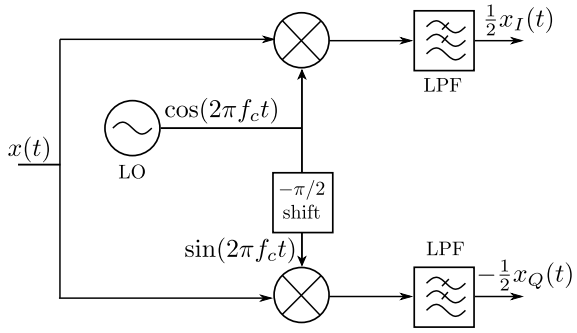

(a) Obtaining In-Phase and Quadrature Signals

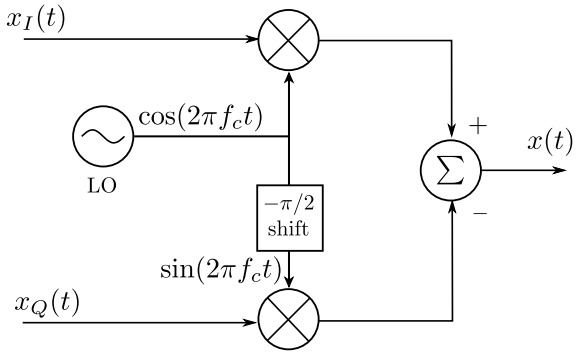

(b) Obtaining Bandpass Signal

Figure 3.6: Block diagrams (a) for obtaining in-phase and quadrature components from the initial signal and (b) for obtaining real signal from components of the complex envelope.

3.4 Radar Range Equation

The radar range equation is an important tool for evaluating radar systems in terms of power transmission. It relates the basic radar parameters that give an insight in power

budgeting decisions when designing a radar system for a particular application. Multiple factors will inevitably affect the performance. Among the most important ones are frequency of operation, antenna size, receiver dynamic range, detection range of expected targets and losses.

3.4.1 Range Equation Derivation

The range equation can be derived based on a simple scenario, where a radar with the power P_t and antenna gain G_t is pointed towards a target at a distance R, as depicted in Figure 3.7.

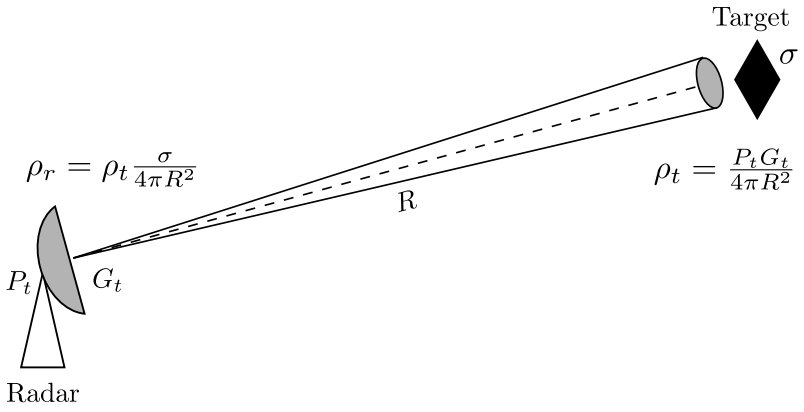

Figure 3.7: Radar with the transmitting power P_t and antenna gain G_t is pointing towards a target at a distance R and RCS σ. The power density at the range of the target is ρ_t and ρ_r when reflected back and received by the radar.

The power density of the transmitted signal impinging on the target is therefore

$$\rho_t = \frac{P_t G_t}{4\pi R^2} \tag{3.21}$$

Part of the energy is reflected by the target back towards the transmitting antenna, where the power density is

$$\rho_r = \rho_t \frac{\sigma}{4\pi R^2} \tag{3.22}$$

and σ is RCS, which defines the size of the target as seen by the radar. The received power is proportional to the antenna effective area $A_{e,r}$, which is related to antenna gain as

$$G_r = \frac{4\pi A_{e,r}}{\lambda^2} = \frac{4\pi \eta_{a,r} A_r}{\lambda^2} \tag{3.23}$$

where A_r is the receiving antenna physical area and $\eta_{a,r}$ is antenna efficiency. The received power is then

$$P_r = \rho_r A_{e,r} = \frac{P_t G_t G_r \lambda^2 \sigma}{(4\pi)^3 R^4} \tag{3.24}$$

3.4.2 Noise and Losses Affecting Detection in Range

It is informative to include the effects of noise and losses in the range equation, which can significantly reduce the receiving performance. There are two sources of noise; external, that is received through antenna and internal, also called thermal or Johnson noise, that is usually dominant. Thermal noise, assumed to be white, is proportional to the receiver temperature T_0 and its bandwidth B, expressed as $N_0 = k_B T_0 B G_s$, where k_B is Boltzmann constant and G_s is the gain of the entire receiver chain [Richards, 2005, Chapter 2]. In practice, the noise power at the output is higher than the ideal noise power N_0 due to additional losses in the antenna and a nonideal receiver chain. The additional noise is described by the effective temperature T_e and the total noise is

$$N = k_B T_0 B G_s + k_B T_e B G_s \tag{3.25}$$

which can be alternatively described with the noise figure F_n, stating the ratio between actual and theoretical minimum of noise power as

$$F_n = \frac{N}{k_B T_0 B G_s} \tag{3.26}$$

The output SNR is then the ratio between output power $P_o = G_s P_r$ and output noise $N_o = k_B T_0 B F_n G_s$ given as

$$SNR = \frac{P_o}{N_o} = \frac{P_t G_t G_r \lambda^2 \sigma}{(4\pi)^3 R^4} \frac{1}{k_B T_0 B F_n G_s} \tag{3.27}$$

which can be simplified, and a losses term L can be added to obtain

$$SNR = \frac{P_t G_t G_r \lambda^2 \sigma}{(4\pi)^3 R^4 k_B T_0 F_n B L} \tag{3.28}$$

Multiple losses can affect the power of the received signal and $L = L_t L_a L_r L_{sp}$ is a factor of multiple contributions, caused by transmit losses, atmospheric losses, receiver losses and signal processing losses, respectively [Richards et al., 2009, Chapter 2].

Assuming a minimum SNR, that still allows for the signal detection, is known, the maximum detection range is

$$R_{max} = \sqrt[4]{\frac{P_t G_t G_r \lambda^2 \sigma}{(4\pi)^3 k_B T_0 F_n SNR_{min} BL}} \tag{3.29}$$

3.5 Matched Filter

Signal compression in radar systems is achieved with the use of matched filter (MF) that has been a standard technique in the field. MF is derived in Section 3.5.2 in the context of random processes, introduced in the next section. Signal compression will be explained in Section 3.6.

3.5.1 Random Processes

In this section, the basic underlying theory is presented that is necessary to understand the derivation of the matched filter. More detailed treatment of the topic is available in [Haykin, 1994, Page 218]. The returned signals at the receiver can be interpreted as they were random processes with specific properties. Consider a random process $X(t)$ with the mean value

$$\mu_X(t) = \mathrm{E}\left[X(t)\right] \tag{3.30}$$

$$= \int_{-\infty}^{\infty} x f_{X(t)}(x) dx \tag{3.31}$$

where $f_{X(t)}$ is the probability density function of the process. The autocorrelation function of the random process is defined as a product of two random variables, $X(t_1)$ and $X(t_2)$, that are obtained at two time instances

$$R_{X,X}(t_1, t_2) = \mathrm{E}[X(t_1)X(t_2)] \tag{3.32}$$

$$= \int_{-\infty}^{\infty} \int_{-\infty}^{\infty} x_1 x_2 f_{X(t_1),X(t_2)}(x_1, x_2) dx_1 dx_2 \tag{3.33}$$

where $f_{X(t_1),X(t_2)}(x_1, x_2)$ is the joint probability density function. If the autocorrelation function depends only on the time difference

$$R_{X,X}(t_1, t_2) = R_{X,X}(t_2 - t_1), \quad \forall t_1, \forall t_2 \tag{3.34}$$

and the mean of a random process is constant

$$\mu_X(t) = \mu_X \tag{3.35}$$

then the process is considered to be wide-sense stationary (WSS). The autocorrelation is then simplified to

$$R_{X,X}(\tau) = \mathrm{E}[X(t+\tau)X(t)] \tag{3.36}$$

Suppose that we have a linear time-invariant filter (LTI) with an impulse response function $h(t)$ and with a WSS random process $X(t)$ present as an input. In this case, the mean value of the output is the expected value of the convolution integral

$$\begin{aligned} \mu_Y &= \mathrm{E}[Y(t)] && (3.37)\\ &= \mathrm{E}\left[\int_{-\infty}^{\infty} h(\tau)X(t-\tau)d\tau\right] && (3.38)\\ &= \int_{-\infty}^{\infty} h(\tau)\mathrm{E}[X(t-\tau)]d\tau && (3.39)\\ &= \mu_X \int_{-\infty}^{\infty} h(\tau)d\tau && (3.40) \end{aligned}$$

According to (3.32), the autocorrelation function of the output process can be established as

$$R_{Y,Y}(t_1, t_2) = \mathrm{E}\left[\int_{-\infty}^{\infty} h(\tau_1)X(t_1-\tau_1)d\tau_1 \int_{-\infty}^{\infty} h(\tau_2)X(t_2-\tau_2)d\tau_2\right] \tag{3.41}$$

and assuming that the filter is LTI, expectation operation can be brought inside integration as

$$R_{Y,Y}(t_1, t_2) = \int_{-\infty}^{\infty}\int_{-\infty}^{\infty} h(\tau_1)h(\tau_2)\mathrm{E}\left[X(t_1-\tau_1)X(t_2-\tau_2)\right]d\tau_1 d\tau_2 \tag{3.42}$$

at this point we consider (3.32) and (3.34), to obtain the final expression

$$R_{Y,Y}(t_1,t_2)=\int_{-\infty}^{\infty}\int_{-\infty}^{\infty}h(\tau_1)h(\tau_2)R_{X,X}(\tau-\tau_1+\tau_2)d\tau_1 d\tau_2 \tag{3.43}$$

where $\tau=t_1-t_2$.

The time domain analysis can now be considered to derive random process filtering in the frequency domain. The time and frequency relations are connected by the Wiener-Khinchin theorems

$$S_{X,X}(\omega)=\int_{-\infty}^{\infty}R_{X,X}(\tau)e^{-j\omega\tau}d\tau \tag{3.44}$$

$$R_{X,X}(\tau)=\frac{1}{2\pi}\int_{-\infty}^{\infty}S_{X,X}(\omega)e^{j\omega\tau}d\omega \tag{3.45}$$

where $S_{X,X}(\omega)$ is the power spectral density of the random process $X(t)$. The Fourier transform of filter impulse response

$$h(\tau_1)=\frac{1}{2\pi}\int_{-\infty}^{\infty}H(\omega)e^{j\omega\tau_1}d\omega \tag{3.46}$$

can be inserted in (3.43) for $\tau=0$ to obtain $R_{Y,Y}(0)=\mathrm{E}[Y^2(t)]$ that can be expressed as

$$\mathrm{E}[Y^2(t)]=\frac{1}{2\pi}\int_{-\infty}^{\infty}\int_{-\infty}^{\infty}\left[\int_{-\infty}^{\infty}H(\omega)e^{j\omega\tau_1}d\omega\right]h(\tau_2)R_{X,X}(\tau_2-\tau_1)d\tau_1 d\tau_2 \tag{3.47}$$

A new variable $\tau_3=\tau_2-\tau_1$ and the differential $d\tau_3=-d\tau_1$ can be introduced to obtain

$$\mathrm{E}[Y^2(t)]=\frac{1}{2\pi}\int_{-\infty}^{\infty}H(\omega)d\omega\int_{-\infty}^{\infty}h(\tau_2)e^{j\omega\tau_2}d\tau_2\int_{-\infty}^{\infty}R_{X,X}(\tau_3)e^{-j\omega\tau_3}d\tau_3 \tag{3.48}$$

where the second integral equals $H^*(\omega)$ and the last one corresponds to the power spectral density (3.44), so the final expression for the mean square value of the filter output is

$$\mathrm{E}[Y^2(t)]=\frac{1}{2\pi}\int_{-\infty}^{\infty}|H(\omega)|^2S_{X,X}(\omega)d\omega \tag{3.49}$$

3.5.2 Matched Filter Derivation

Herein the filter is derived for a received continuous-time[2] deterministic signal corrupted by the white Gaussian noise, as shown in Figure 3.8. The input signal to the matched filter is $x(t) = s(t) + w(t)$, where $s(t)$ is the known deterministic signal and $w(t)$ is stationary white Gaussian noise. The output signal after filtering is a convolution of linear filter

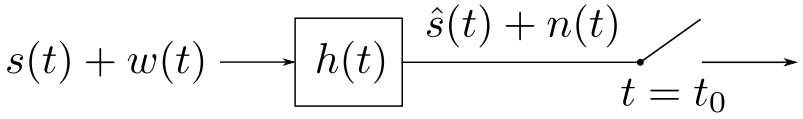

Figure 3.8: Block diagram of the matched filter.

impulse response $h(t)$ and input signal $x(t)$

$$y(t) = x(t) * h(t) \tag{3.50}$$

$$= \int_{-\infty}^{\infty} s(\tau) g(t-\tau) d\tau \tag{3.51}$$

$$= \hat{s}(t) + n(t) \tag{3.52}$$

The aim of the filter design is to maximise the signal to noise ratio (SNR) at $t = t_0$. The SNR at the input is the ratio between signal power and noise power and it is assumed to be WSS. The input SNR is indicated as SNR_i and equals to

$$SNR_i = \frac{E_s}{\mathrm{E}\left[|n(t)|^2\right]} \tag{3.53}$$

$$= \frac{E_s}{R_{n,n}(0)} \tag{3.54}$$

$$= \frac{\int_0^T |s(t)|^2 dt}{\frac{1}{2\pi}\int_{-\infty}^{\infty} S_{n,n}(\omega) d\omega} \tag{3.55}$$

where the Wiener-Khinchin relation (3.45) was used together with its zero correlation property

$$R_{X,X}(0) = \mathrm{E}\left[X^2(t)\right] \tag{3.56}$$

[2]Derivation of matched filter for discrete signals is also possible and relies on Schwartz inequality as does the development presented herein. For further details see [Richards et al., 2009].

The output SNR can be expressed as a ratio between the power of output signal at $t = t_0$ and the expected value of noise power. Noise power can be expressed by an autocorrelation function property (3.56) and ultimately by the filter transfer function (3.49) as

$$SNR_o = \frac{|\hat{s}(t_0)|^2}{\mathrm{E}\left[|w(t)|^2\right]} \tag{3.57}$$

$$= \frac{|\hat{s}(t_0)|^2}{R_{w,w}(0)} \tag{3.58}$$

$$= \frac{\left|\frac{1}{2\pi}\int_{-\infty}^{\infty} S(\omega)H(\omega)e^{jwt_0}d\omega\right|^2}{\frac{1}{2\pi}\int_{-\infty}^{\infty} S_{n,n}(\omega)|H(\omega)|^2 d\omega} \tag{3.59}$$

and accounting for the constant power spectral density of the white noise $S_{w,w}(\omega) = \sigma^2$, the SNR is

$$SNR_o = \frac{1}{2\pi\sigma^2}\frac{\left|\int_{-\infty}^{\infty}(S^*(\omega)e^{-jwt_0})^* H(\omega)d\omega\right|^2}{\int_{-\infty}^{\infty}|H(\omega)|^2 d\omega} \tag{3.60}$$

$$\leq \frac{1}{2\pi\sigma^2}\frac{\int_{-\infty}^{\infty}|S(\omega)e^{j\omega t_0}|^2 d\omega \int_{-\infty}^{\infty}|H(\omega)|^2 d\omega}{\int_{-\infty}^{\infty}|H(\omega)|^2 d\omega} \tag{3.61}$$

where the Cauchy-Schwarz expression (A.3) was used to establish the inequality. The RHS of the inequality represents the maximal achievable SNR and, with the use of Parceval's energy equivalence theorem, we can write

$$SNR_{o,max} = \frac{1}{2\pi\sigma^2}\int_{-\infty}^{\infty}|S(\omega)|^2 d\omega \tag{3.62}$$

$$= \frac{1}{\sigma^2}\int_0^T |S(t)|^2 dt \tag{3.63}$$

$$= \frac{E_s}{\sigma^2} \tag{3.64}$$

To obtain the maximum value of SNR_o, the equality in (3.61) must hold, which is conditioned by (A.15) and therefore

$$H(\omega) = \eta S^*(\omega)e^{-j\omega t_0} \tag{3.65}$$

with η being a factor of proportionality. With the following Fourier pairs

$$\mathcal{F}[s(-t)] = S(-\omega) \tag{3.66}$$

$$\mathcal{F}[s^*(t)] = S^*(-\omega) \tag{3.67}$$

$$\mathcal{F}[s(t-t_0)] = S(\omega)e^{-j\omega t_0} \tag{3.68}$$

the matched filter can be transformed in the time domain as

$$h(t) = \eta s^*(t_0 - t) \tag{3.69}$$

where η is a proportional factor.

3.5.3 Matched Filter Equivalence to Cross-Correlation

The filtering process is expressed with a convolution integral and, in the case of matched filter (3.69), it can be written as

$$y(t) = s(t) * h(t) \tag{3.70}$$

$$= \int_{-\infty}^{\infty} s(\tau)\eta s^*(-(t-\tau-t_0))d\tau \tag{3.71}$$

With a simple substitution of variables $\tau' = \tau - t + t_0$ and $d\tau' = d\tau$, the filter output is

$$y(t) = \eta \int_{-\infty}^{\infty} s^*(\tau')s(\tau' + (t-t_0))d\tau' \tag{3.72}$$

which is an autocorrelation function. The filter output is maximised at $t = t_0$ and the peak energy is then proportional to the energy of the waveform $s(t)$ as

$$y(t_0) = \eta \int_{-\infty}^{\infty} |s(\tau')|^2 d\tau' \tag{3.73}$$

The time delay t_0 corresponds to the distance between the radar and target at which the filter output reaches maximum. The resulting response is called pulse compression as it compresses waveform energy at one time instance. The overview of waveform used for pulse compression is discussed in Section 3.6. Related to equation (3.72), cross-correlation

will be used throughout this thesis instead of convolution with a matched filter and will be denoted without a proportional factor and slightly changed variables as

$$y(\tau) = R_{i,j}(\tau) = \int_{-\infty}^{\infty} s_i^*(t) s_j(t+\tau) dt \tag{3.74}$$

3.5.4 Discrete Signals and Straddle Loss

Before transmission and after reception, the signals are sampled by an ADC. Discretised waveforms with a sampling rate of $f_s = 1/T_s$ have to be processed by a discrete autocorrelation or cross-correlation functions. Presenting filtering output (3.72) in a discrete form leads to

$$y[k] = \eta \sum_{-\infty}^{\infty} s^*(nT_s + \delta) s((n+k)T_s + \delta) \tag{3.75}$$

$$= \eta \sum_{-\infty}^{\infty} s^*[n] s[n+k] \tag{3.76}$$

where δ signifies the fact that a shift within one sampling period is going to be introduced when the signal passed through ADC for transmission purposes. On reception, the samples may not perfectly correspond to the transmitted ones and the mismatch causes straddle losses. The losses are caused by an additional sampling mismatch $\sigma \in [-T_s/2, T_s/2]$ within the sampling period so that the output signal is now a cross-correlation

$$y(k, \sigma) = \eta \sum_{-\infty}^{\infty} s^*(nT_s + \delta) s((n+k)T_s + \delta + \sigma) \tag{3.77}$$

The straddle losses are highest when the received signal is sampled halfway between the sampled points of the transmitted waveforms. The losses can be quantified as [Richards et al., 2009, Chapter 20.4]

$$L_{straddle} = 20 \log_{10} \left| \frac{y(0, T_s/2)}{y(0,0)} \right| \tag{3.78}$$

Straddle losses are bigger for signals with sharper roll-off if the sampling frequency is the same.

3.6 Pulse Compression Waveforms

Radar systems that employ single tone unmodulated waveforms exhibit a limitation as a compromise has to be made between SNR and range resolution. As discussed in Section 3.2.1, good range resolution requires small pulse widths, while improving SNR relates to increasing the transmitted energy and therefore, extending the pulse width. The two waveform properties can be decoupled by using amplitude, frequency or phase modulated waveforms in conjunction with the matched filter to achieve pulse compression. The technique is very effective because the SNR of the filtered signal depends on transmitted signal energy and not only on its amplitude, as derived in (3.64). This allows for much more energy to be transmitted towards a target for a given range resolution and fixed peak power of a transmission module.

3.6.1 Range Resolution after Compression

Range resolution is defined as a distance at which two closely spaced targets can be still resolved in range. The resolution of a pulse compression waveform is mainly affected by the shape of the mainlobe after matched filtering. Two possible resolution metrics can be defined [Richards et al., 2009]. The Rayleigh criterion defines the resolution as the distance between the peak and the first null of a compressed signal, while the second definition is based on the characterisation of the mainlobe. It is determined as the width of the mainlobe at a specific level belowthe maximum, e.g. $-3\,\mathrm{dB}$ point.

A simple example of signal compression is a single frequency pulse. With amplitude A and pulse width T it is defined as

$$s(t) = A \,\mathrm{rect}\left(\frac{t}{T}\right) \tag{3.79}$$

where

$$\mathrm{rect}\,(t) = \begin{cases} 1, -\frac{1}{2} < t < \frac{1}{2} \\ 0, \mathrm{elsewhere} \end{cases} \tag{3.80}$$

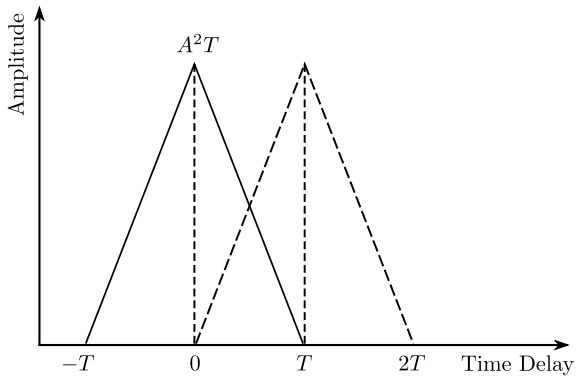

Figure 3.9: Radar range resolution between two closely spaced targets.

The pulse compression after matched filtering is therefore

$$y(t) = \begin{cases} A^2(t+T), -T \leq t \leq 0 \\ A^2(T-t), 0 < t \leq T \\ 0, \text{elesewhere} \end{cases} \tag{3.81}$$

which is shown in Figure 3.9 for two closely spaced targets at a Rayleigh distance, defined previously. The range resolution in this case is

$$\Delta R = \frac{cT}{2} \tag{3.82}$$

as the signals travel a two-way path and c is the speed of light. Range resolution can be related to the bandwidth of a signal. The relationship is related to the properties of Fourier transform pairs. A measure of signal width in time or frequency domains can be defined as [Papoulis, 1962, Cohen, 1994]

$$D_t^2 = \int_{-\infty}^{\infty} (t - t_{avg})^2 |s(t)|^2 dt \tag{3.83}$$

$$D_\omega^2 = \int_{-\infty}^{\infty} (\omega - \omega_{avg})^2 |S(\omega)|^2 dw \tag{3.84}$$

where $|s(t)|^2$ is considered as a density of the signal in time and $|S(\omega)|^2$ is the energy density spectrum of $S(\omega) = \mathcal{F}[s(t)]$. Unit energy is assumed for simplicity as

$$\int_{-\infty}^{\infty} |f(t)|^2 dt = \frac{1}{2\pi} \int_{-\infty}^{\infty} |S(\omega)|^2 d\omega = 1 \tag{3.85}$$

and the average values, as used above, are defined as

$$t_{avg} = \int_{-\infty}^{\infty} t|s(t)|^2 dt \tag{3.86}$$

$$\omega_{avg} = \int_{-\infty}^{\infty} \omega|S(\omega)|^2 d\omega \tag{3.87}$$

The Fourier transform uncertainty principle is then defined as

$$D_t D_\omega \geq \sqrt{\frac{\pi}{2}} \tag{3.88}$$

which implies that time and frequency widths of a signal are in an inversely proportional relation. This property can be related to the pulse signal and its Fourier transform

$$\mathcal{F}\left[A \text{ rect}\left(\frac{\text{t}}{\text{T}}\right)\right] = AT \text{ sinc}\left(\omega\frac{T}{2}\right) \tag{3.89}$$

where the sinc function is unnormalised. The mainlobe width of the sinc function at -4 dB points corresponds to bandwidth $B = 1/T$ and the range resolution of a pulse, given in (3.82), can be expressed as

$$\Delta R = \frac{c}{2B} \tag{3.90}$$

which proves that increasing the bandwidth will increase resolution. The relation above holds in general, i.e. for different modulation types.

3.6.2 Linear Frequency Modulated Waveforms

Linear frequency modulated (LFM) waveforms or chirp signals are the most commonly used pulse compression signals and have been in use since 1940s. They are Doppler tolerant and exhibit range-Doppler coupling, which makes them suitable for detection but not for Doppler frequency estimation. Constant modulus, ease of phase generation and spectral containment are properties that allowed for an early adoption of this waveform. Properties of LFM and nonlinear waveforms are discussed in Chapter 5 in more details.

The complex envelope of a chirp signal with a time width T and bandwidth B is defined as

$$s(t) = A \text{ rect}\left(\frac{t}{T}\right) \; e^{j\pi\mu t^2} \tag{3.91}$$

where μ is the chirp rate

$$\mu = \frac{B}{T} \tag{3.92}$$

The phase is a quadratic function, defined as $\phi(t) = \pi\mu t^2$ and the frequency modulation $f(t)$ expressed in hertz is its first derivative

$$f(t) = \frac{1}{2\pi}\frac{d\phi(t)}{dt} = \mu t \tag{3.93}$$

Pulse compression of a LFM waveform can be determined by using the cross-correlation function (3.72) where the filter normalising factor is chosen such that $y(0) = 1$, i.e. $\eta = 1/(A^2T)$. The filter output response is in this case [Richards et al., 2009, Chapter 20]

$$y(t) = \left(1 - \frac{|t|}{T}\right)\frac{\sin\big((B - \mu|t|)\pi t\big)}{\big(B - \mu|t|\big)\pi t},\ |t| \leq T \tag{3.94}$$

which is a sinc function, multiplied by a triangular function and $\mu = B/T$. The response of a chirp signal with $B = 20\,\text{MHz}$ and $T = 2.0\,\mu\text{s}$ is shown in Figure 3.10 where the typical sidelobe level of $-13.4\,\text{dB}$ can be observed. The plot is showing the power output of the complex envelope. When $|t| \ll T$, the expression (3.94) closely resembles the sinc

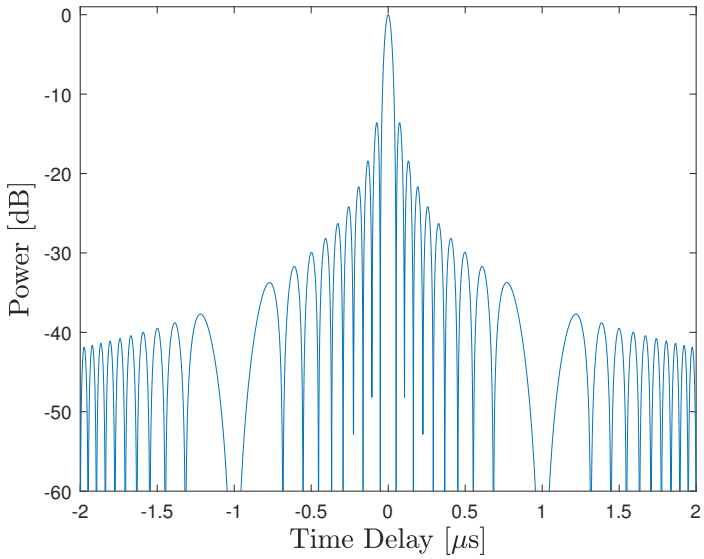

Figure 3.10: Normalised pulse compression output of an LFM waveform with $B = 20\,\text{MHz}$ and $T = 2.0\,\mu\text{s}$.

function as the quadratic term t^2 vanishes

$$\frac{\sin\big((B-\mu|t|)\pi t\big)}{\big(B-\mu|t|\big)\pi t} \approx \frac{\sin\big(\pi B t\big)}{\pi B t} \tag{3.95}$$

It is interesting to notice that the Rayleigh resolution, as defined previously, is in accordance with $\Delta R = c/(2B)$. The resolution equation follows from the fact that the first nulls appear approximately at the positions $t \approx \pm 1/B$ for $BT > 10$, as stated in [Richards et al., 2009].

To improve the sidelobe levels below the typical levels and therefore eliminate possibilities for target masking, different weighting functions can be employed in either the time or frequency domain. Sidelobe shaping can be implemented by using different windows, such as Taylor, Tuckey, Hann or Hamming windows [Levanon, 2004].

3.6.3 Frequency Modulated Waveforms

Although LFM is the most widespread pulse in use by radar systems, different frequency modulation schemes exist as well. One such example are Costas codes that are generated in discrete frequency steps using binary matrices, where each frequency occupies a unique discrete time interval. For a square $M \times M$ binary matrix, $M!$ possible permutations can be constructed; two of them are shown in Figure 3.11. The energy of the waveform is therefore distributed in a time-frequency matrix, where only one non-zero element can exist in each row and each column. Time delays of pulse compression are equivalent to the products of two shifting binary matrices in horizontal direction. The peak would therefore occur at the zero time delay and no energy would result from other delays. The LFM waveform can be constructed by reducing the time step $T_s = T/M$ and populating the binary matrix diagonally.

The Costas waveforms are defined as [Levanon, 2004, Chapter 7]

$$s(t) = \frac{1}{\sqrt{MT_s}} \sum_{m=1}^{M} s_m(t-(m-1)T_s) \tag{3.96}$$

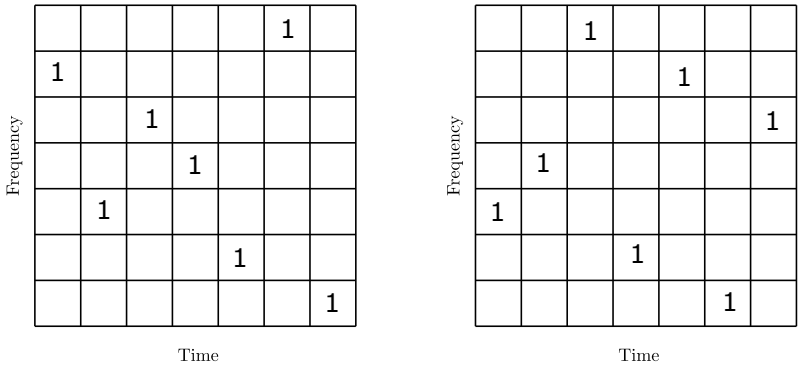

Figure 3.11: Examples of two 7×7 binary matrices for Costas code generation.

where the subsignals are constant frequency chips defined as

$$s_m(t) = \begin{cases} e^{j2\pi f_m t}, 0 \leq t \leq T_s \\ 0, \text{elesewhere} \end{cases} \tag{3.97}$$

and frequencies are calculated from the Costas hopping sequence $\mathbf{a} = [a_1, ..., a_M]$ as

$$f_m = \frac{a_m}{T_s} \tag{3.98}$$

so that the frequency steps are equivalent to $1/T_s$. The definition of the hopping sequence and, equivalently, binary matrix is an optimisation problem that can be solved in multiple ways and an exhaustive search can be implemented for smaller problems. For further details refer to [Levanon, 2004] and references therein.

Another possibility for constructing signals is by employing the nonlinear frequency modulation. This approach is most commonly used when windowing in time or frequency domain is to be avoided and sidelobe energy distribution is controlled by FM. The main advantage of this method over amplitude windowing is that it preserves the constant amplitude of the waveform and allows for the transmission amplifiers to operate in optimal conditions. The approach to design such waveforms was introduced in [Cook and Bernfeld, 1993].

Table 3.1: Table of all the known binary Barker codes.

Length	Sequence	PSL [dB]
2	$+-, ++$	-6.0
3	$++-$	-9.5
4	$++-+, +++-$	-12.0
5	$+++-+$	-14.0
7	$+++--+-$	-16.9
11	$+++---+--+-$	-20.8
13	$+++++--++-+-+$	-22.3

3.6.4 Phase Coded Waveforms

Phase coded waveforms constitute multiple discrete subpulses, where each one is phase modulated to produce a different sequence. A waveform with M subpulses, each being $T_s = T/M$ long, is defined as

$$s(t) = \frac{1}{\sqrt{T}} \sum_{m=1}^{M} e^{j\phi_m} \text{ rect}\left(\frac{t-(m-1)T_s}{T_s}\right) \tag{3.99}$$

where $\phi = [\phi_1, ..., \phi_M]$ is a vector of phases that defines a particular waveform and finding the vector is a subject of phase generation rules and algorithms. The criteria for determining the set of phases are the ambiguity function properties, range-Doppler resolution, frequency spectrum spillage, sidelobe levels and ease of implementation. The advantage when designing new phase coded waveforms is that cross-correlation functions have to be examined only at the discrete steps $t = nT_s$ as intermediate values can be extrapolated with linear interpolation in a complex plane [Levanon, 2004].

The biphase Barker codes exhibit the lowest sidelobe to peak ratio for a given length. The relative sidelobe level for a sequence of length M is $1/M$ and the relative peak sidelobe levels (PSL) for all the known Barker codes are given in Table 3.1. The match filtered response of a five step Barker code is shown in Figure 3.12 where it can be observed that the PSL of unnormalised signal is one, which is true for all lengths of Barker codes, regardless of the amplitude of the main lobe.

The Barker codes are optimal in terms of sidelobes as suppression ratios of $1/M$ are achieved, but their length is often a limitation when transmitting longer pulses. To address this, different minimum peak sidelobe (MPS) codes were proposed in the literature

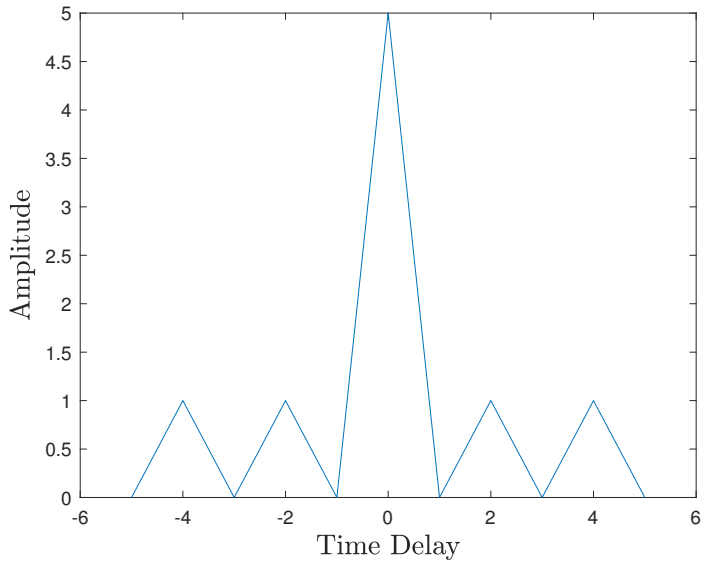

Figure 3.12: Compressed pulse of a five step Barker code with PSL equal to 14 dB.

[Levanon, 2004]. Biphase MPS codes with up to 40 steps can achieve PSL suppression ratios of $2/M$ and $3/M$. While the ratios achieved are the best possible for a given code length, they are still suboptimal in the sense of Barker codes. A summary of the binary MPS codes is given in Table 3.2 [Richards et al., 2009].

Table 3.2: Sidelobe suppression of binary MPS codes.

Code Length	PSL (Amplitude)
2-5, 7, 11, 13	1
6, 8-10, 12, 14-21, 25, 28	2
22-24, 26, 27, 29-40, 41-48, 51	3
49, 50, 52-70, 71-82	4
83-105	5

Another set of biphase codes are maximal length sequences that are generated using shift registers and irreducible primitive polynomials. Binary coefficients of such waveforms can be found in literature and the derivation is based on the theory of Galois fields. It is noted in [Richards et al., 2009] that PSL ratio approaches the value of $20\log_{10}(1/M)$ in the dB scale.

Polyphase codes are an extension of biphase codes and possess more degrees of freedom for optimisation purposes. Polyphase Barker codes have been found that comply with the sidelobe criteria for PSL. More common are Frank, Px, P1 and P2 codes, which are defined

by explicit formulas. The Frank code is defined for sequences of a square length $M = L^2$ and is determined as

$$\phi_{(n-1)L+k} = \frac{2\pi}{L}(n-1)(k-1) \tag{3.100}$$

where $1 \leq n \leq L$ and $1 \leq k \leq L$. The PSL ratio in dB is $-20\log_{10}(M\sin(\pi/L))$ when N is even and $-20\log_{10}(2M\sin(\pi/2L))$ when N is odd. Frank codes are Doppler intolerant as high sidelobes appear in the presence of small Doppler shifts. Additionally, they are sensitive to band-limiting, which causes an increase of the peak sidelobes and a widening of the mainlobe. To counteract band-limiting effects Px, P1 and P2 codes were developed. The zero frequency term in this case is the middle of the code, while in the Barker code it appears at the beginning. All the codes are defined for lengths $M = L^2$ and Px is expressed as

$$\phi_{(n-1)L+k} = \begin{cases} \frac{2\pi}{L}\left(\frac{L+1}{2}-k\right)\left(\frac{L+1}{2}-n\right), L \text{ is even} \\ \frac{2\pi}{L}\left(\frac{L}{2}-k\right)\left(\frac{L+1}{2}-n\right), L \text{ is odd} \end{cases} \tag{3.101}$$

where k and n are defined as for the Frank code. The P1 code is defined as

$$\phi_{(n-1)L+k} = \frac{2\pi}{L}\left(\frac{L+1}{2}-n\right)\big((n-1)L+(k-1)\big) \tag{3.102}$$

and the P2 code is defined as Px code for even L. P3 and P4 are similar codes with Doppler tolerant properties and were previously given with (2.4) and (2.5). Both can be obtained by sampling the phase function of an LFM waveform. The generalised expressions of P3 and P4 are Chu and Zadoff codes, respectively. The Zadoff code is defined as

$$\phi_m = \frac{2\pi}{m}(m-1)\left(r\frac{M-1-m}{2}-q\right) \tag{3.103}$$

where m, q are integers in the ranges of $1 \leq m \leq M$ and $0 \leq q \leq M$, respectively. Code length M can be of arbitrary length, while r and M should be relatively prime. The P4 code can be obtained from (3.103) by requiring $r = -1$ and $q = 1$. The Chu code is defined as

$$\phi_m = \begin{cases} \frac{2\pi}{M} r\frac{(m-1)^2}{2}, M \text{ is even} \\ \frac{2\pi}{M} r\frac{(m-1)m}{2}, M \text{ is odd} \end{cases} \tag{3.104}$$

for $1 \leq m \leq M$ and r is relatively prime to M. The P3 code is derived from the Chu code for even M by setting $r = 1$. All the previously defined codes are used to construct radar waveforms by employing (3.99).

3.6.5 Ambiguity Function and Its Properties

The response of the matched filter is an important aspect of waveform evaluation. As was noted in Section 3.5.3, the match filtering is mathematically equivalent to the cross-correlation function. This process gives information of waveform sidelobes for specific delays and waveform resolution, which depends on the size and shape of the mainlobe, but it does not provide any information on how the Doppler shift affects the filtering process. The ambiguity function (AF) is a quadratic transform that accounts for different time delays and different Doppler shifts to determine the matched filter response. The AF is defined as

$$\chi(\tau, f_D) = \int_{-\infty}^{\infty} s^*(t)s(t+\tau)e^{j2\pi f_D t}dt \tag{3.105}$$

where τ is time delay of the waveform and f_D is the radial Doppler shift. For no Doppler shifts, $f_D = 0$, the AF reduces to the cross-correlation function. The cross-correlation function is also equivalent to the zero-Doppler cut of AF, determined as $\chi(\tau, 0)$. Similarly, the zero-delay cut for $\tau = 0$ is defined as

$$\chi(0, f_D) = \int_{-\infty}^{\infty} |s(t)|^2 e^{j2\pi f_D t}dt \tag{3.106}$$

which is equivalent to the Fourier transform of squared amplitude, therefore the zero-delay cut is not affected by the frequency or phase modulation.

The AF possesses some important properties as described below. The maximum value of the AF is at its origin point and it is equivalent to the waveform energy

$$|\chi(\tau, f_D)| \leq |\chi(0, 0)| = E \tag{3.107}$$

The AF is symmetrical with respect to the origin

$$|\chi(\tau, f_D)| = |\chi(-\tau, -f_D)| \tag{3.108}$$

and its volume remains constant for all waveforms with energy E so that

$$\int_{-\infty}^{\infty}\int_{-\infty}^{\infty}|\chi(\tau,f_D)|^2 d\tau df_D = E^2 \tag{3.109}$$

which implies that changing properties of a waveform will only redistribute the volume of the AF, e.g. narrowing the mainlobe will cause the volume of the sidelobes in time-Doppler plane to increase. A waveform with an ideal range and Doppler resolution would possess a thumbtack shape, but such a shape is not physically realisable as all the energy would have to be located at the origin of the delay-Doppler plane. Similarly, an ideal Doppler tolerant waveform would require an ambiguity function in the shape of vertical plane with zero volume, aligned along $\tau = 0$. Such a shape would violate (3.109) and the best approximate, found in practice, is the LFM waveform.

As an example, the AF of a single pulse, defined as (3.79), can be determined as [Richards et al., 2009]

$$|\chi(\tau,f_D)| = \left| A^2 T\left(1-\frac{|\tau|}{T}\right)\frac{\sin\left(\pi f_D T\left(1-\frac{|\tau|}{T}\right)\right)}{\pi f_D T\left(1-\frac{|\tau|}{T}\right)}\right| \tag{3.110}$$

for $|\tau \leq T|$. The normalised ambiguity function for $A = 1/\sqrt{T}$ is shown in Figure 3.13. The time delay is normalised with respect to pulse width T and Doppler frequency with respect to $1/T$. It can be seen that the maximum is achieved at $|\chi(0,0)|$ where the filter is perfectly matched to the waveform. As was already demonstrated in (3.81), the zero-Doppler cut at $f_D = 0$ is a triangular function

$$|\chi(\tau,0)| = A^2 T\left(1-\frac{|\tau|}{T}\right),\ |\tau| \leq T \tag{3.111}$$

and zero-delay cut is a sinc function of Doppler shift, defined as

$$|\chi(0,f_D)| = A^2 T\left|\frac{\sin(\pi T f_D)}{\pi T f_D}\right|,\ |\tau| \leq T \tag{3.112}$$

Therefore, the filter response quickly tapers off with increasing Doppler mismatch and the zeros appear at frequencies k/T, where $k \in \mathbb{Z}$.

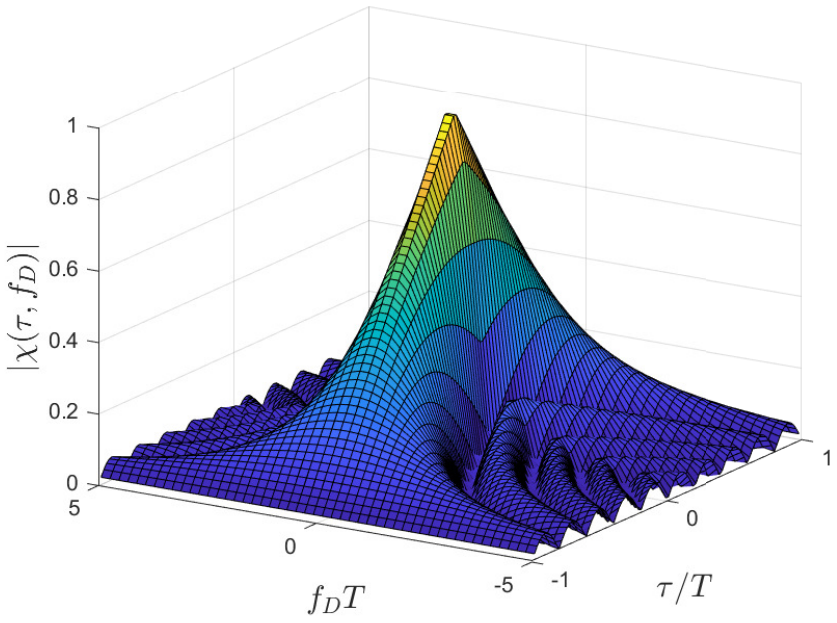

Figure 3.13: Normalised ambiguity function for a pulse signal with no modulation. The pulse width was set to $T = 10\,\mu s$ and Doppler frequency range $f_D = \pm 5/T$.

3.7 Summary

This chapter was devoted to the basic signal processing techniques and operating modes. Firstly, basic operating principles were discussed and a radar block diagram was presented. The motivation for a waveform representation was given for in-phase and quadrature components. An overview of the radar range equation was presented, which is an important aspect when designing a radar system from the SNR point of view. A matched filter was then derived from the first principles and an introduction to the pulse compression was given. The most common pulse compression waveforms were presented and further details on FM waveforms will follow in Chapter 5. An introduction was made to the ambiguity function and its most important properties as it remains one of the most important tools to analyse radar signals.

Chapter 4

Multibeam Radar

4.1 Introduction

A multibeam radar (MBR) system, a novel contribution of this work, can be seen as a subclass of MIMO radars because they both require an orthogonal set of waveforms to function as intended. The operational characteristics of MBR make it more similar to the conventional phased array radar rather than the MIMO system. A single channel MBR is equivalent to the phased array radar, while adding additional orthogonal channels would potentially make it capable of multitasking and simultaneously tracking multiple targets, which is usually the primary functionality of an RF seeker.

As the MBR heavily relies on the phased array steering, this topic is presented first. Then the MBR signal model is presented before commonly agreed measures for orthogonality are introduced. Finally, possible applications and advantages of implementing such a system are discussed.

4.2 Phased Arrays

Phased arrays have become an indispensable technology when it comes to modern radar systems as their flexibility, fast inertialess beam steering and robustness to failures of individual transmit and receive modules have made them superior to the traditional mechanically driven radar antennas. In this section, the underlying theory of phased antennas will be introduced, focusing on linear configuration arrays. More advanced topics, such as

planar and conformal phased arrays are a subject of great interest in current research and can be found in [Wirth, 2013, Hansen, 2009], amongst others.

4.2.1 Phased Array Factor

A linear antenna array with equidistant elements will be presented herein. It is assumed that the antennas are perfect isotropic radiators, emitting energy evenly in all spherical directions. The arrangement of the antenna elements can be seen in Figure 4.1, where an array of $2N + 1$ antennas with an inter-element distance of d is shown. On receive, the phased array radiation pattern depends on the geometrical position of the antennas and signal wavelength. In the case of a linear array, a linear wavefront from a target positioned at θ from boresight will cause the signals at neighbouring antennas to have a phase difference of ϕ, defined below with (4.1). All the signals are then summed together before passing on for further processing.

On transmit, EM waves spread out in concentric circles from each antenna and form a wavefront in the far-field. Wavefront direction can be controlled by adjusting delays or phases of phase shifters, which are shown in Figure 4.1.

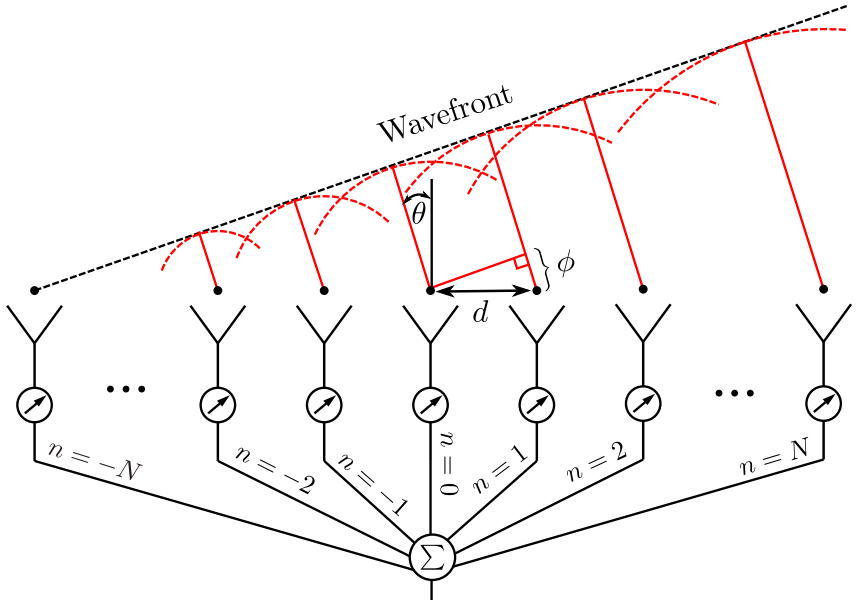

Figure 4.1: Radar receiving chain of a dual conversion superheterodyne receiver.

To derive the phased array factor, as presented in [Wirth, 2013, Chapter 4], the phase shift between adjacent antenna elements is determined from the right triangle, defined by

θ and d in Figure 4.1 as

$$\phi = 2\pi \frac{d}{\lambda} \sin\theta \tag{4.1}$$

where λ is the signal wavelength. The central antenna is indexed as $n = 0$ with zero relative phase shift and all the adjacent antenna elements have relative shifts of $n\phi$. The array factor $F(\theta)$ is now determined as a summation of all the phase shifts relative to the central element as

$$F(\theta) = \sum_{n=-N}^{N} e^{jn\phi} \tag{4.2}$$

In the boresight direction, $\theta = 0$, the array factor has a peak amounting to $F(0) = 2N+1$. The array factor expression can be simplified by forming

$$e^{j\phi} F(\theta) = \sum_{n=-N}^{N} e^{j(n+1)\phi} \tag{4.3}$$

and subtracting it from the array factor leads to

$$F(\theta) - e^{j\phi} F(\theta) = \sum_{n=-N}^{N} e^{jn\phi} - \sum_{n=-N+1}^{N+1} e^{jn\phi} \tag{4.4}$$

$$= e^{-jN\phi} - e^{j(N+1)\phi} \tag{4.5}$$

and the array factor is further derived as

$$F(\theta) = \frac{e^{-jN\phi} - e^{j(N+1)\phi}}{1 - e^{j\phi}} \tag{4.6}$$

$$= \frac{e^{-jN\phi} - e^{j(N+1)\phi}}{1 - e^{j\phi}} \frac{1 - e^{-j\phi}}{1 - e^{-j\phi}} \tag{4.7}$$

$$= \frac{e^{-jN\phi} - e^{j(N+1)\phi} - e^{-j(N+1)\phi} + e^{jN\phi}}{2 - e^{j\phi} - e^{-j\phi}} \tag{4.8}$$

$$= \frac{2\cos N\phi - 2\cos(N+1)\phi}{2 - 2\cos\phi} \tag{4.9}$$

Using the trigonometric equalities

$$\cos\alpha - \cos\beta = -2\sin\frac{\alpha+\beta}{2} \sin\frac{\alpha-\beta}{2} \tag{4.10}$$

$$1 - \cos 2\alpha = 2\sin^2\alpha \tag{4.11}$$

simplifies (4.9) to

$$F(\theta) = \frac{\sin\frac{(2N+1)\phi}{2}\sin\frac{\phi}{2}}{\sin^2\frac{\phi}{2}} \tag{4.12}$$

Taking into account (4.1) and (4.12) leads to the final expression of the array factor

$$F(\theta) = (2N+1)\frac{\sin\left((2N+1)\pi\frac{d}{\lambda}\sin\theta\right)}{(2N+1)\sin\left(\pi\frac{d}{\lambda}\sin\theta\right)} \tag{4.13}$$

Array factor for antenna arrays of sizes $N = 5$, $N = 10$, $N = 20$ and for $d = \lambda/2$ is

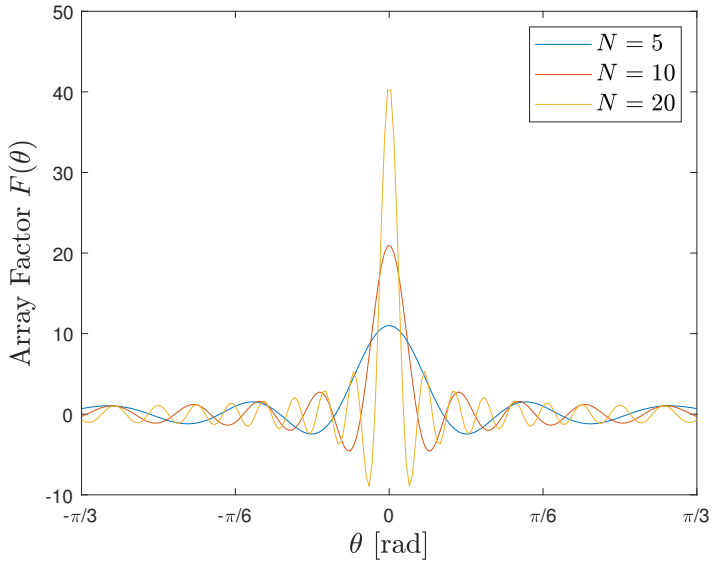

Figure 4.2: Antenna array factor for number of antennas $N = 5$, $N = 10$, $N = 20$, carrier frequency $f_c = 4.0\,\text{GHz}$ and element spacing of $d = \lambda/2$.

depicted in Figure 4.2. It can be seen that extending the size of the array L narrows the mainlobe, whereas the increase of antenna elements increases maximum energy collected. To simplify expression (4.13), a new variable is introduced

$$\xi = (2N+1)\pi\frac{d}{\lambda}\sin\theta \tag{4.14}$$

and approximating $\sin(\pi\frac{d}{\lambda}\sin\theta) \approx \pi\frac{d}{\lambda}\sin\theta$ for small arguments of the sine function, the approximate array factor can be written with a sinc function

$$F(\theta) \approx (2N+1)\frac{\sin\xi}{\xi} = (2N+1)\text{sinc}\,\xi \tag{4.15}$$

Steering is implemented by adjusting the phase shifters so that the mainlobe is pointed in a specified direction. If the selected steering direction is θ_S, the array should reach its peak at $\theta = \theta_S$ and therefore, according to (4.2), the steering equation is

$$F(\theta, \theta_S) = \sum_{n=-N}^{N} e^{2\pi j \frac{d}{\lambda}(\sin\theta - \sin\theta_S)n} \tag{4.16}$$

and the phase values can be extracted as

$$\phi_n = -2\pi \frac{d}{\lambda} n \sin\theta_S, \quad n = -N, -N+1, ..., N \tag{4.17}$$

The antenna elements usually exhibit some directivity, described by the radiation pattern of a single element $E(\theta)$. The antenna array radiation pattern consisting of such directional elements can therefore be determined as

$$E_{PA}(\theta) = F(\theta)E(\theta) \tag{4.18}$$

where the coupling effects between the neighbouring elements were omitted and different radiation patterns of the edge elements were not accounted for. For a more accurate pattern prediction a full-wave EM solver has to be used.

4.2.2 Half-Power Beamwidth

Half-power beamwidth (HPBW) is affecting the angular resolution of a radar system and is determined as the angle between two half power points of the mainlobe. The array factor amplitude is therefore decreased by the factor $1/\sqrt{2}$ at the angle θ_{HP} so that

$$F(\theta_{HP}) = \frac{2N+1}{\sqrt{2}} \tag{4.19}$$

In the case of beam steering to the direction θ_S, the difference from the half-power angle θ_{HP} and the beam peak follows from (4.15) and (4.14)

$$\sin\theta_{HP} - \sin\theta_S = \operatorname{arcsinc}\left(\frac{1}{\sqrt{2}}\right) \frac{\lambda}{\pi(2N+1)d} \tag{4.20}$$

where arcsinc(·) is the inverse sinc function. Alternatively, the difference can be written as [Wirth, 2013]

$$\sin\theta_{HP} - \sin\theta_S = 2\cos\left(\frac{\theta_{HP}+\theta_S}{2}\right)\sin\left(\frac{\theta_{HP}-\theta_S}{2}\right) \tag{4.21}$$

$$\approx (\theta_{HP} - \theta_S)\cos\theta_S \tag{4.22}$$

where it was assumed that the mainlobe is narrow, pencil-like, so that θ_{HP} and θ_S are of comparable size and the approximation $\sin x \approx x$ can be made. The HPBW can be expressed as $\theta_{HPBW} = 2(\theta_{HP} - \theta_S)$ and by joining (4.20) with (4.22) it is rewritten as

$$\theta_{HPBW} \approx \frac{1}{\cos\theta_S}\text{arcsinc}\left(\frac{1}{\sqrt{2}}\right)\frac{2\lambda}{\pi(2N+1)d} \tag{4.23}$$

With the approximation $\text{arcsinc}\left(1/\sqrt{2}\right) \approx 1.39$ and considering the length of array as $L = (2N+1)d$, the simplified formula becomes

$$\theta_{HPBW} \approx \frac{1.39}{\pi}\frac{\lambda}{L\cos\theta_S} \tag{4.24}$$

which demonstrates that the array length L is projected in the steering direction and the main beam broadens as a result.

4.2.3 Phase Steering Limitations

Beam steering that is implemented with time delay shifters is not affected by the frequency of operation. Due to hardware limitations and cost efficiency, phase steering is usually achieved with phase shifters. Similarly as was defined in (4.16), the array factor, that now depends on the frequency of the signal, is

$$F(\theta, f) = \sum_{n=-N}^{N} e^{j\left(\frac{2\pi f d}{c}\sin\theta - \frac{2\pi f_S d}{c}\sin\theta_S\right)n} \tag{4.25}$$

where the second term in the exponential defines the steering phase needed for direction θ_S and fixed for the frequency f_S. As the frequency of the signal f changes , the frequency related to the phase shifter f_S is fixed, which affects the array factor and shifts the mainlobe. The peak of the mainlobe is achieved when the exponent in (4.25) reaches zero so

that

$$f \sin\theta = f_S \sin\theta_S \tag{4.26}$$

$$(f_S + \Delta f)\sin(\theta_S + \Delta\theta) = f_S \sin\theta_S \tag{4.27}$$

Using the trigonometric equality below and approximating it for $\Delta\theta \ll 1$ as follows

$$\sin(\theta_S + \Delta\theta) = \sin\theta_S \cos\Delta\theta + \sin\Delta\theta \cos\theta_S \tag{4.28}$$

$$\approx \sin\theta_S + \Delta\theta \cos\theta_S \tag{4.29}$$

and combining it with (4.27) leads to the final expression for the mainlobe shift

$$\Delta\theta = -\frac{\Delta f}{f} \tan\theta_S \tag{4.30}$$

The mainlobe peak is therefore tilting towards the boresight with increasing frequency.

4.2.4 Grating Lobes

Narrowing the beamwidth requires extending the distance between the consecutive antenna elements as much as possible but this can be done only to a certain extent, because additional grating lobes appear otherwise. Grating lobes are undesirable since they can cause angular ambiguities and increase interference from undesired directions. The array factor

$$F(\theta, \theta_S) = \sum_{n=-N}^{N} e^{2\pi j n \frac{d}{\lambda}(\sin\theta - \sin\theta_S)} \tag{4.31}$$

achieves maximum values when the exponential arguments are integer multiples of $2\pi jn$ so peaks appear whenever

$$\frac{d}{\lambda}|\sin\theta_P - \sin\theta_S| = 0, \pm 1, \pm 2, ... \tag{4.32}$$

It can be seen from the equation above that the grating lobes are periodic and move with the applied steering θ_S. Grating lobes have a period of λ/d in the sine space, i.e. peaks appear every time $\sin\theta$ reaches a multiple of λ/d. Decreasing d pushes grating lobes

apart, which can be seen in Figure 4.3. If the angles of interest are $\theta \in [-\pi/2, \pi/2]$ or $\sin\theta \in [-1, 1]$ in the sine space and θ_S is the maximum steering angle, the period of the array factor should exceed $1 + \sin\theta_S$ so that

$$\frac{\lambda}{d} > 1 + |\sin\theta_S| \tag{4.33}$$

and inter-element spacing should be

$$d < \frac{\lambda}{1 + |\sin\theta_S|} \tag{4.34}$$

The element spacing of $\lambda/2$ is commonly used, which is adequate for scanning angles ranging in $\pm 60°$, according to (4.34). Such an example is depicted in Figure 4.3, where the antenna directivities of two antenna element spacings are compared and the mainlobe is steered to $\theta_S = \pi/3$. As can be seen, the grating lobe periodicity is 1 and 2 for $d = \lambda, \lambda/2$, respectively.

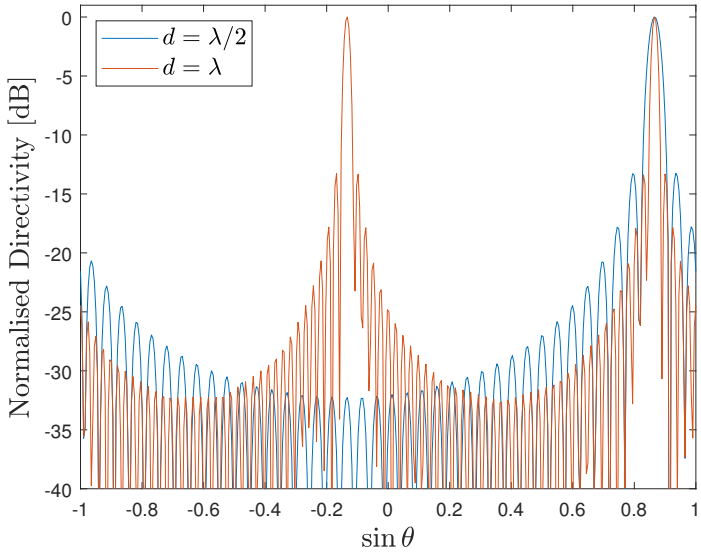

Figure 4.3: Normalised directivity of a linear antenna array with $N = 20$ elements and for two inter-element spacing configurations, $d = \lambda/2, \lambda$.

4.3 MBR Signal Model

The MBR presented herein is a monostatic pulsed radar system with the transmitting elements arranged in a linear phased array. It transmits multiple simultaneous beams, where each beam forms an independent channel to conduct a designated functionality. Beams are associated with a set of unique orthogonal or quasi-orthogonal waveforms to further isolate the channels. The signal model is a novel contribution and is derived below, as in [Kocjancic et al., 2018]. The model does not assume any specific type of waveforms.

Let us assume a linear antenna array of K elements, each one transmitting a narrow-band sum of waveforms $s_k(t)$, as is depicted in Figure 4.4. The transmitted signals are arranged in a vector

$$\mathbf{s}(t) = [s_1(t), ..., s_k(t), ..., s_K(t)]^T \tag{4.35}$$

where each element represents an independent channel. Now let us consider an ideal point target at a distance R from the array in a direction θ from the boresight. The signal impinging on the target is a superposition of phase-shifted delayed replicas of the waveforms $s_k(t)$ and can be written as

$$\hat{s}(t) = \mathbf{a}^T(\theta) s\left(t - \frac{R}{c}\right) e^{-j2\pi f_c \frac{R}{c}} \tag{4.36}$$

where c is the speed of light, f_c is the carrier frequency and $\mathbf{a}$ is a phase vector, pointing towards the target and defined as

$$\mathbf{a}(\theta) = \frac{1}{\sqrt{K}}[a_1(\theta), ..., a_k(\theta), ..., a_K(\theta)]^T \tag{4.37}$$

with each element, as given in (4.1), defining a phase shift as

$$a_k(\theta) = e^{\frac{j2\pi f_c}{c}(k-1)d\sin\theta} \tag{4.38}$$

with d being the spacing between antenna elements. On receive, each antenna element receives a phase shifted copy of $\hat{s}(t)$. The signal received by the kth element is

$$y_k(t) = \frac{1}{\sqrt{K}} e^{j\frac{2\pi f_c}{c}(k-1)d\sin\theta}\ \hat{s}\left(t - \frac{R}{c}\right) e^{-j2\pi f_c \frac{R}{c}} \tag{4.39}$$

Expanding $\hat{s}(t)$ and taking into account a two-way propagation path yields

$$y_k(t) = \frac{1}{\sqrt{K}} e^{j\frac{2\pi f_c}{c}(k-1)d\sin\theta}\, \mathbf{a}^T(\theta)\mathbf{s}\left(t - \frac{2R}{c}\right) e^{-j2\pi f_c \frac{2R}{c}} \tag{4.40}$$

The received signals can be gathered in the vector

$$\mathbf{y} = [y_1(t), ..., y_k(t), ..., y_K(t)]^T \tag{4.41}$$

that can be expressed as

$$\mathbf{y}(t) = \gamma_1 \mathbf{b}(\theta)\mathbf{a}^T(\theta)\mathbf{s}(t-\tau)e^{-j2\pi f_c \tau} \tag{4.42}$$

where γ_1 is the reflectivity of target T_1, $\tau = 2R/c$ is the echo time delay and $\mathbf{b}(\theta)$ is the phase shifting vector on receive, defined as

$$\mathbf{b}(\theta) = \frac{1}{\sqrt{K}}[b_1(\theta), ..., b_k(\theta), ..., b_K(\theta)]^T \tag{4.43}$$

For a monostatic system, the phase shifting vectors are the same

$$b_k(\theta) = a_k(\theta) = e^{j\frac{2\pi f_c}{c}(k-1)d\sin\theta} \tag{4.44}$$

Each antenna element transmits a linear combination of M orthogonal waveforms that are stacked in the vector

$$\mathbf{x}(t) = [x_1(t, ..., x_m(t), ..., x_M(t)]^T \tag{4.45}$$

as depicted in Figure 4.4. The vector of all the signals transmitted by each antenna can be expressed as

$$\mathbf{s}(t) = \mathbf{W}\mathbf{x}(t) \tag{4.46}$$

where $\mathbf{W}$ is a $K \times M$ steering matrix

$$\mathbf{W} = [\mathbf{a}(\bar{\theta}_1), ..., \mathbf{a}(\bar{\theta}_m), ..., \mathbf{a}(\bar{\theta}_M)] \tag{4.47}$$

where the mth column is a phase steering vector pointing in the direction $\bar{\theta}_m$. Each element

$w_{k,m}$ therefore applies a phase shift to the kth transmitting antenna towards direction $\bar{\theta}_m$. If the mth channel is steered towards the direction of the target θ, then the mth column of $\mathbf{W}$ corresponds to $\mathbf{a}(\bar{\theta}_m) = \mathbf{a}^*(\theta)$.

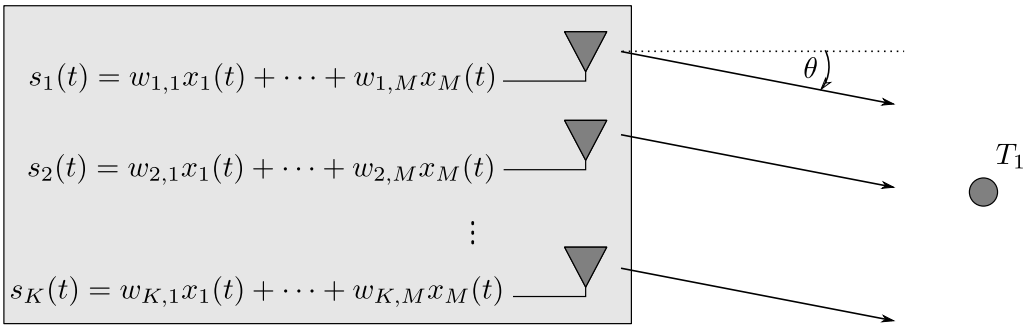

Figure 4.4: Schematic of a transmitting part of the MBR, where $s_k(t)$ is the signal transmitted from the kth antenna, $x_m(t)$ is an orthogonal waveform and $w_{k,m}$ is a phase factor. Antennas form a linear array with inter-element spacing d and target T_1 in the farfield at angle θ from boresight.

The receiving array is the same as the transmitting array in the case of a monostatic configuration and all the signals received are arranged in

$$\mathbf{y}(t) = \alpha \mathbf{b}(\theta)\mathbf{a}^T(\theta)\mathbf{W}\mathbf{x}(t-\tau) \tag{4.48}$$

where $\alpha = \gamma\ e^{-j2\pi f_c \tau}$. The receiver consists of a bank of matched filter, as is shown in Figure 4.5. To extract the mth channel from the received signals, the signal from each antenna element is match filtered to $x_m(t)$ before the beam steering on receive is applied as

$$z_m(t) = \mathbf{b}^T(\bar{\theta}_m)\big[\mathbf{y}(t) * x_m^*(-t)\big] \tag{4.49}$$

where $*$ denotes the convolution. Inserting (4.48) in the equation above yields

$$z_m(t) = \alpha \mathbf{b}^T(\bar{\theta}_m)\mathbf{b}(\theta)\mathbf{a}^T(\theta)\big[\mathbf{W}\mathbf{x}(t-\tau) * x_m^*(-t)\big] \tag{4.50}$$

$$= \alpha \mathbf{b}^T(\bar{\theta}_m)\mathbf{b}(\theta)\mathbf{a}^T(\theta)\left[\sum_{k=1}^{K} \mathbf{a}(\bar{\theta}_k)x_k(t-\tau) * x_m^*(-t)\right] \tag{4.51}$$

$$= \alpha \mathbf{b}^T(\bar{\theta}_m)\mathbf{b}(\theta)\mathbf{a}^T(\theta)\left[\sum_{k=1}^{K} \mathbf{a}(\bar{\theta}_k)R_{k,m}(t-\tau)\right] \tag{4.52}$$

where $\mathbf{R}_{k,m}(t)$ is a cross-correlation function between $x_k(t)$ and $x_m(t)$. Equation (4.52)

can be split in the co-channel and adjacent channel response as

$$z_m(t) = \alpha \mathbf{b}^T(\bar{\theta}_m)\mathbf{b}(\theta)\mathbf{a}^T(\theta)\mathbf{a}(\bar{\theta}_m)R_{m,m}(t-\tau) + \alpha \mathbf{b}^T(\bar{\theta}_m)\mathbf{b}(\theta)\mathbf{a}^T(\theta)\left[\sum_{k\neq m}^{K} \mathbf{a}(\bar{\theta}_k)R_{k,m}(t-\tau)\right] \quad (4.53)$$

where the first part can be interpreted as the response of pulse compression and the second part as the suppression of the adjacent channels. If the waveforms are orthogonal, resulting in low cross-correlation values $R_{k,m}(t)$, the equation above can be simplified to

$$z_m(t) = \alpha \mathbf{b}^T(\bar{\theta}_m)\mathbf{b}(\theta)\mathbf{a}^T(\theta)\mathbf{a}(\bar{\theta}_m)R_{m,m}(t-\tau) \quad (4.54)$$

which is a typical output of the phased array.

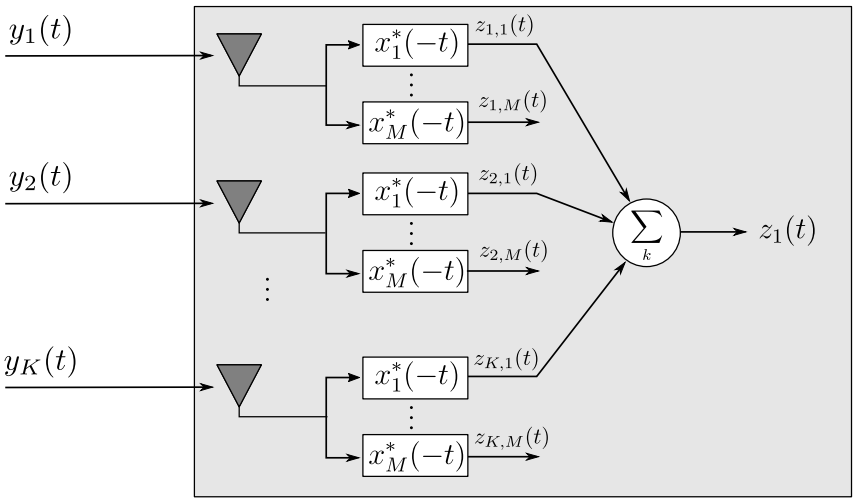

Figure 4.5: Schematic of the receiving part of the MBR, where each antenna is connected to a bank of filters, in this case the $x_1(t)$ is being extracted.

4.4 Channel Isolation

In this section the definition of isolation between different channels of an MBR is given. Channel isolation, as defined for an MBR system, is equivalent to the orthogonality criterion defined for MIMO communication and MIMO radar systems. The aim of the proposed metrics is to define a measure for separation between orthogonal or quasi-orthogonal waveforms after filtering. The resulting measure will serve as an important tool to quantify the

performance of the waveforms under investigation as well as an optimisation cost function, whenever the mutual interference between the waveforms is to be minimised.

4.4.1 Definitions

The most common definition of orthogonality, used in mathematics, is defined for two signals $s_i(t)$ and $s_j(t)$ as

$$\langle s_i(t), s_j(t) \rangle = \int_{-\infty}^{\infty} w(t) s_i^*(t)\ s_j(t) dt = 0 \tag{4.55}$$

which is an inner product of the two signals and $w(t)$ is a weight function. Many sets of functions that exhibit this property exist, such as Jacobi polynomials, Laguerre polynomials, Hermite polynomials, and Chebyshev polynomials. In engineering applications the condition above simplifies to the cross-correlation function, defined in (3.74) and evaluated at time delay $\tau = 0$ with $w(t) = 1$ so that the orthogonality requirement is

$$R_{i,j}(0) = \int_{-\infty}^{\infty} s_i^*(t) s(t) dt = 0 \tag{4.56}$$

or similarly for quasi-orthogonal signals, the condition is relaxed to

$$|R_{i,j}(0)| = \left| \int_{-\infty}^{\infty} s_i^*(t) s_j(t) dt \right| < \delta \tag{4.57}$$

where $\delta > 0$ is an arbitrary small number $\delta \ll 1$. The choice for δ would depend on the application and the ratio with the signal energy, δ/E, can range from $-10\,\text{dB}$ to $-100\,\text{dB}$ and smaller. Condition (4.57) is only sufficient for the point targets in the case of simultaneous channel transmission and to account for the distributed targets with arbitrary delays between transmissions, the condition has to hold for all possible delays

$$|R_{i,j}(\tau)| = \left| \int_{-\infty}^{\infty} s_i^*(t) s_j(t+\tau) dt \right| < \delta, \forall \tau \tag{4.58}$$

In some cases, where the spatial distribution of a target is known or in remote sensing applications, where the proximity of targets within one swath can be predicted [Krieger, 2014], orthogonality can be required only for specific time shifts $\forall \tau \in [-\Delta\tau, \Delta\tau]$. For

the high speed targets that would cause significant Doppler shifts, the cross-ambiguity function has to be considered to determine the level of orthogonality as

$$|\chi_{i,j}(\tau, f_D| = \left| \int_{-\infty}^{\infty} s_i^*(t) s_j(t+\tau) e^{j2\pi f_D t} dt \right| < \delta, \ \forall\tau, \forall f_D \tag{4.59}$$

where the relation has to hold for all Doppler shifts f_D or for a specific range $\forall f_D \in [-\Delta f, \Delta f]$.

Signal orthogonality is closely related to the isolation between two or more waveforms. The isolation between two waveforms is defined as a ratio between the compressed signal peak and the cross-correlation function. If the energy of the waveforms is the same, the isolation is defined as

$$I(\tau) = \left| \frac{R_{i,i}(0)}{R_{i,j}(\tau)} \right| = \left| \frac{R_{j,j}(0)}{R_{j,i}^*(\tau)} \right| \tag{4.60}$$

where $R_{i,j}(\tau)$ is a cross-correlation defined with (3.74). The minimum isolation can therefore be formulated as

$$I = \frac{|R_{i,i}(0)|}{\max_\tau |R_{i,j}(\tau)|} = \frac{|R_{j,j}(0)|}{\max_\tau |R_{j,i}(\tau)|} \tag{4.61}$$

where the conjugation can be omitted. It could be omitted in (4.61) but it was kept to maintain consistency. Isolation between the ith waveform in a set with J other waveforms can be determined by extending (4.60) as

$$I_i(\tau_1, ..., \tau_J) = \left| \frac{R_{i,i}(0)}{\sum_{j\neq i} R_{i,j}(\tau_j)} \right| \tag{4.62}$$

$$\geq \frac{|R_{i,i}(0)|}{\sum_{j\neq i} |R_{i,j}(\tau_j)|} \tag{4.63}$$

where τ_j is time delay affiliated with each jth waveform. If the absolute values of cross-correlations are determined for pairs of waveforms, only a lower bound on the isolation can be determined. The expression above can be simplified for a point target and simultaneous transmission $\tau_i = \tau_j = \cdots = \tau_J = \tau$ as

$$I_i(\tau) = \left| \frac{R_{i,i}(0)}{\sum_{j\neq i} R_{i,j}(\tau)} \right| \tag{4.64}$$

A more convenient way of expressing the isolation performance of a set of waveforms is

to establish the maximum value of pairwise isolation figures of all possible combinations. Therefore

$$I_{i,min} = \frac{|R_{i,i}(0)|}{\max\limits_{j,\tau}|R_{i,j}(\tau)|} \tag{4.65}$$

is the worst possible isolation value of a given set of waveforms.

To account for the Doppler shift, the cross-correlation in the isolation definition is replaced by the cross-ambiguity function to obtain

$$I(\tau, f_D) = \left|\frac{\chi_{i,i}(0,0)}{\chi_{i,j}(\tau, f_D)}\right| = \left|\frac{\chi_{j,j}(0,0)}{\chi^*_{j,i}(\tau, f_D)}\right| \tag{4.66}$$

and similarly for a set of waveforms

$$I_i(\tau_1, ..., \tau_J, f_{D,1}, ..., f_{D,J}) = \left|\frac{\chi_{i,i}(0,0)}{\sum_{j\neq i}\chi_{i,j}(\tau_j, f_{D,j})}\right| \tag{4.67}$$

$$\geq \frac{|\chi_{i,i}(0,0)|}{\sum_{j\neq i}|\chi_{i,j}(\tau_j, f_{D,j})|} \tag{4.68}$$

The minimum isolation figure for all possible combinations and accounting for different τ, f_D is

$$I_{i,min} = \frac{|\chi_{i,i}(0,0)|}{\max\limits_{j,\tau,f_D}|\chi_{i,j}(\tau_j, f_{D,j})|} \tag{4.69}$$

which is a single figure, that can be expressed in dB as a power of the signal from the matched filter. Since the expression is always positive, the value is $20\log_{10}(I_{i,min})$.

4.4.2 Orthogonality in Frequency Domain

Waveforms that share the same frequency support and radars that rely on waveform diversity (WD) to achieve orthogonality are considered in this section. Two waveforms $s_i(t)$ and $s_j(t)$ of the same length $T_i = T_j$, bandwidth $B_i = B_j$, and energy $R_{i,i}(0) = R_{j,j}(0)$ are taken into account. Consider a scenario where two waveforms are transmitted simultaneously and are reflected from a point target. The return signal is

$$s(t) = s_i(t-\tau) + s_j(t-\tau) \tag{4.70}$$

where τ is the two-way propagation delay and all the attenuation factors were omitted. Matched filtering is then applied and cross-correlation can be done with each signal separately as the operation is linear. The filter output is therefore

$$y(t) = \int_{-\infty}^{\infty} s_i(\tau' + t - \tau) s_i^*(\tau') d\tau' + \int_{-\infty}^{\infty} s_j(\tau' + t - \tau) s_i^*(\tau') d\tau' \tag{4.71}$$

where the first integral corresponds to the delayed compressed signal, while the second integral represents an interference due to the second waveform. The second integral is a cross-correlation function

$$R_{i,j}(t) = \int_{-\infty}^{\infty} s_i^*(\tau') s_j(\tau' + t - \tau) d\tau' \tag{4.72}$$

with energy, determined as

$$E = \int_{-\infty}^{\infty} R_{i,j}(t) R_{i,j}^*(t) dt \tag{4.73}$$

which can be determined in the frequency domain according to the Parceval's theorem (A.23) as

$$E = \int_{-\infty}^{\infty} \mathcal{F}[R_{i,j}(t)] \mathcal{F}[R_{i,j}^*(t)] df \tag{4.74}$$

Cross-correlation is equivalent to a product in the frequency domain as

$$\mathcal{F}[R_{i,j}(t)] = \mathcal{F}^*[s_i(t)] \; \mathcal{F}[s_j(t - \tau)] \tag{4.75}$$

$$= S_i^*(f) \; S_j(f) e^{-j2\pi f \tau} \tag{4.76}$$

where $S_i(f), S_j(f)$ are the Fourier pairs of $s_i(t), s_j(t)$. Inserting (4.76) in (4.74) and considering $\mathcal{F}[s^*(t)] = S^*(f)$ reveals the energy of the interfering signal

$$E = \int_{-\infty}^{\infty} |S_i(f)|^2 \; |S_j(f)|^2 df \tag{4.77}$$

which depends on the spectral overlapping of the interfering signal and the matched filter. This phenomenon was noted in [Krieger, 2014] where it is shown that the interfering energy from a secondary channel can cause image interference in SAR radars with multiple channels. As shown with (4.77), signals with the same frequency support will cause the

same energy leakage between channels. The aim is therefore not to reduce energy but to reduce the maximum power or maximum amplitude of the suppressed signal. It is therefore necessary to account for frequency as well as time distribution when designing waveforms. This will be looked at in Chapter 5.

4.5 MBR Advantages and Potential Applications

Modern radar systems employ antenna arrays where each antenna has its own transmission and reception module. This allows for more flexibility as phased arrays, MIMO radars and MBR systems can be realised with the same hardware and different processing. A radar system can also be designed in a way that allows for seamless transition between the modes, depending on the current operational requirements.

With the proliferation of sensors required for autonomous platforms, sensor fusion and interoperability will become crucial to reduce the hardware costs. MBR can, in this respect, provide for different functionalities implemented in a single device. The main advantage of MBR is that it can transmit different waveform designs in different directions simultaneously. Waveforms can therefore be designed and the bandwidth of each channel allocated to best suit the purpose, taking into account target RCS, range, clutter rejection and interferences from adjacent channels and other RF devices operating in the same spectrum.

Making RF sensors compact is especially important for air platforms, where the cross-section of the sensor payload must conform to the shape of the platform, whether it is

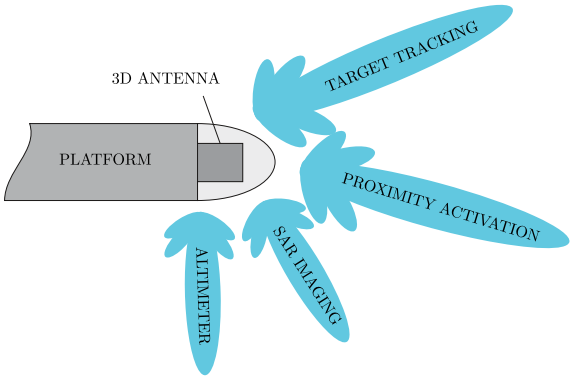

Figure 4.6: An example of MBR, based on an air platform that incorporates multiple functions, in this case target tracking, proximity activation, SAR imaging, and altimetry.

an aeroplane, an autonomous drone or a missile, as depicted in Figure 4.6. Sensor fusion based on MBR can reduce the payload size by employing a three-dimensional conformal antenna and joining multiple functionalities, such as target tracking, proximity activation, SAR imaging, and altimetry.

Adjacent channel rejection can be improved by jointly applying waveform diversity and spatial filtering, which can compensate for lack of orthogonality between the waveforms. Additionally, if an MBR is tracking two independent targets, the waveforms of the secondary channel can be intercepted by the sidelobes of the primary channel and therefore cause false detection in the direction of primary channel. This effect can be mitigated by employing orthogonal or quasi-orthogonal waveforms so that the effect is reduced by the amount of isolation between the waveforms.

Note that the simultaneous transmission of two or more FM signals with constant amplitude results in amplitude modulated waveforms at each element. In this case, the amplifier in transmission cannot operate in saturation and has to operate in the linear region. To retain the optimal transmission conditions and operate in saturation mode, waveforms have to be transmitted consecutively, or alternatively, each waveform would require its own channel amplification module.

4.6 Summary

This chapter discussed the background theory of phased array antennas and the derivation of the phased array factor, as phase steering is an important aspect of MBR. Limitations and properties of a phased array were introduced. Although the array was introduced as a linear antenna group, similar conclusions hold for rectangular planar arrays that are in use. Section 4.3 introduced the novel MBR signal model with the aim to distinguish it from the standard MIMO radar, as presented in Section 2.2.2. One of the important aspects of an MBR, as it was shown, is that waveform diversity and spatial steering can jointly achieve better channel separation. Section 4.4 discussed waveform orthogonality and channel isolation definitions, both of which will be used in the subsequent chapters to analyse the performance of waveforms. Lastly, the advantages and possible applications of MBR were discussed.

Chapter 5

Frequency Modulated Waveforms

5.1 Introduction

In this chapter, the orthogonal properties of frequency modulated waveforms will be investigated. Such signals are very common in radar, sonar and laser signal processing as the design of modulation allows for different requirements and properties of the waveforms to be met. The proposed waveforms are meant to be used by an MBR but wider usage is possible for MIMO radars or MIMO communication systems.

5.2 Rectangular LFM Waveforms

Rectangular LFM waveforms, or chirp signals, are the most widely used waveforms for radar applications. As was already discussed in Section 3.6.2, LFM have good compression properties and a matched filter output as given in (3.94). In this chapter, frequency shift f_s will be introduced, which determines the modulation frequency offset at $t = 0$. The chirp equation (3.91) is therefore extended to

$$s(t) = A \text{ rect}\left(\frac{t}{T}\right) e^{j2\pi\left(f_s t + \frac{1}{2}\mu t^2\right)} \tag{5.1}$$

where the chirp rate is defined by (3.92) and the rectangular function by (3.80).

5.2.1 Range-Doppler Coupling

Properties of a rectangular LFM can be analysed by examining its ambiguity function. By using (5.1) in conjunction with (3.105), it can be derived as

$$\chi(\tau, f_D) = A^2 T \left(1 - \frac{|\tau|}{T}\right) \frac{\sin\left(\pi T \left(1 - \frac{|\tau|}{T}\right)(f_D + f_s + \mu\tau)\right)}{\pi T \left(1 - \frac{|\tau|}{T}\right)(f_D + f_s + \mu\tau)} \tag{5.2}$$

for $|\tau| < T$ and zero elsewhere. The zero-Doppler cut, similar to (3.94), is

$$\chi(\tau, 0) = A^2 T \left(1 - \frac{|\tau|}{T}\right) \frac{\sin\left(\pi T \left(1 - \frac{|\tau|}{T}\right)(f_s + \mu\tau)\right)}{\pi T \left(1 - \frac{|\tau|}{T}\right)(f_s + \mu\tau)} \tag{5.3}$$

Figure 5.1 depicts the absolute value of the ambiguity function for $A = 1/\sqrt{T}$, $f_s = 0$ and the time-bandwidth product of $BT = 10$. The range Doppler coupling is clearly visible as the ridge in the surface plot. The consequence of this property is Doppler tolerance as the targets with significant Doppler shift can be detected with a certain range mismatch and a negligible drop of amplitude for realistic targets.

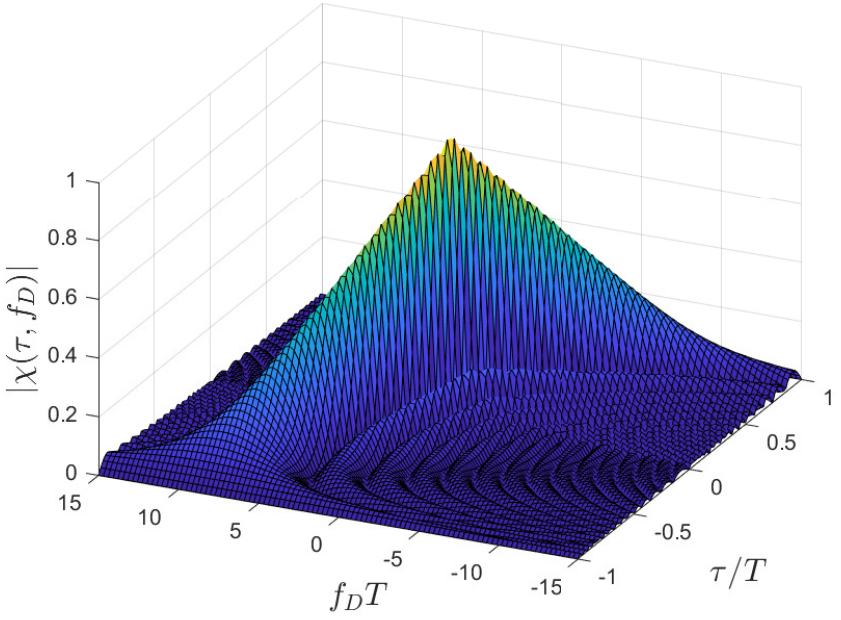

Figure 5.1: Surface plot of the normalised ambiguity function of a rectangular LFM signal. The pulse width was set to $T = 2\,\mu\text{s}$, bandwidth to $B = 5\,\text{MHz}$ and Doppler frequency range $f_D = \pm 15/T$.

Range Doppler coupling is more visible in Figure 5.2, from which the mismatch between true and perceived range is apparent. For positive Doppler shifts and positive chirp rates the targets appear closer to the source. According to (5.2) the delay mismatch is obtained by comparing the arguments of the sine function and it equals

$$\Delta\tau = \frac{f_D T}{B} \tag{5.4}$$

which can be neglected for the majority of applications. Additionally, the peak response is reduced and near the origin for $f_s = 0$ it amounts to [Levanon, 2004, Chapter 4]

$$|\chi(\tau_{max}, f_D)| = 1 - \left|\frac{f_D}{\mu T}\right| = 1 - \left|\frac{f_D}{B}\right| \tag{5.5}$$

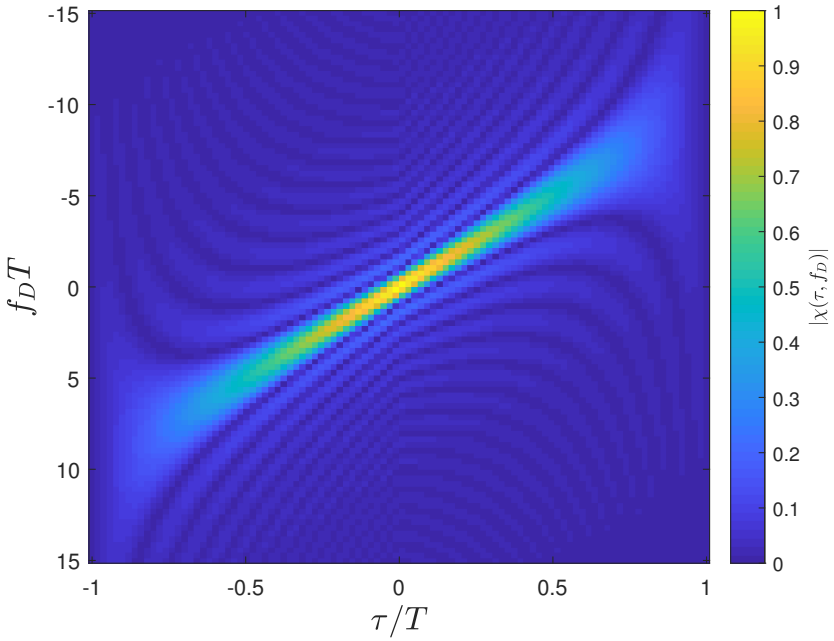

Figure 5.2: Plot of the normalised ambiguity function of a rectangular LFM signal. The pulse width was set to $T = 2\,\mu s$, bandwidth to $B = 5\,MHz$ and Doppler frequency range $f_D = \pm 15/T$.

The Doppler filter mismatch is analysed and presented in Figure 5.3. For each Doppler shift, a maximum value of the ambiguity function is found. The bandwidth of the test signal is fixed to 5.0 MHz and time-bandwidth product of the waveform is changed by extending time duration. It can be seen that the maximum amplitude response decreases

linearly with increasing normalised Doppler shift, defined as f_D/B, up to half of the chirp bandwidth, where the amplitude drops to approximately one half. The waveforms with greater BT-products are more affected by the Doppler mismatch, although Doppler values comparable to bandwidth are not common in radar applications.

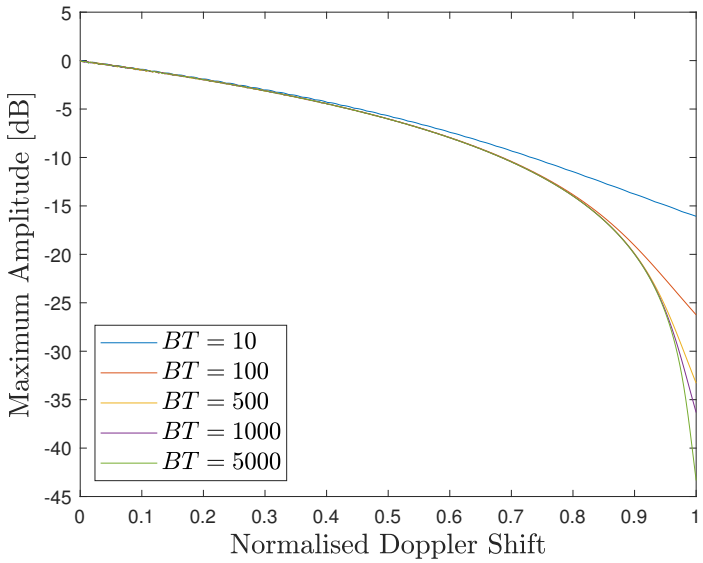

Figure 5.3: Matched filter mismatch caused by the Doppler shift, normalised to the waveform bandwidth $B = 5.0\,\text{MHz}$.

5.2.2 Isolation of Up-Chirp and Down-Chirp

It is known that a combination of an up-chirp and a down-chirp shows some degree of orthogonality [Davis et al., 2014] and it has already been used in an experimental setup to form a multichannel radar system [Frankford, 2011]. In this section a simple case of cross-correlation is presented to investigate the suppression performance of the proposed combination of waveforms. The frequency modulation is shown in Figure 5.4 where it is established that the waveforms have the same pulse width T, same bandwidth B and opposite chirp rate $\mu_i = -\mu_j$. Both waveforms are defined according to (5.1) as

$$s_i(t) = A \,\text{rect}\left(\frac{t}{T}\right) e^{j\pi\mu t^2} \tag{5.6}$$

$$s_j(t) = A \,\text{rect}\left(\frac{t}{T}\right) e^{-j\pi\mu t^2} \tag{5.7}$$

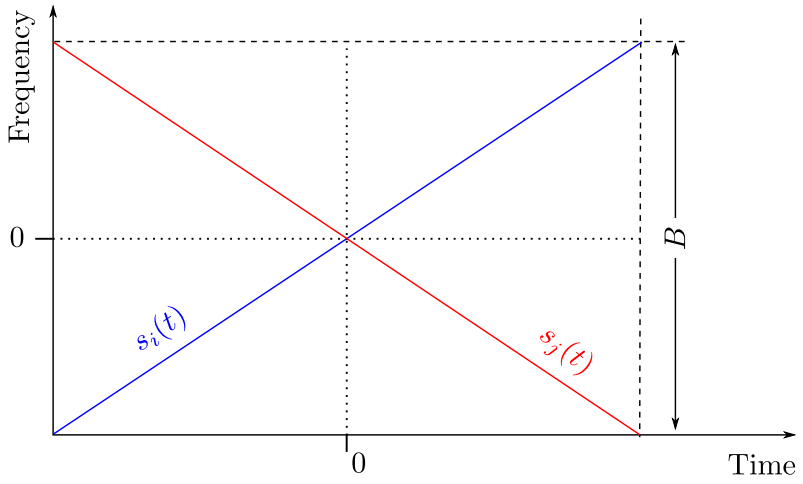

Figure 5.4: Frequency modulation diagram of the LFM waveforms $s_i(t)$ and $s_j(t)$ as used for the analytical derivation of the chirp rate diversity.

where the rectangular function is defined as (3.80) and $\mu = B/T$. After replacing function definitions in (4.58), omitting the absolute value and calculating for $\tau \geq 0$ leads to

$$R_{i,j}(\tau) = A^2 \int_{-T/2}^{T/2-\tau} e^{-j\pi\mu t^2} e^{-j\pi\mu(t+\tau)^2} dt \tag{5.8}$$

Introducing a new variable $\xi = 2\sqrt{\mu}(t + \tau/2)$ allows the expression to be simplified to

$$R_{i,j}(\tau) = \frac{A^2}{2\sqrt{\mu}} e^{-j\frac{\pi\mu\tau^2}{2}} \int_{-\alpha}^{\alpha} e^{j\frac{\pi}{2}\xi^2} d\xi \tag{5.9}$$

where $\alpha = 2\sqrt{\mu}(T/2 - \tau/2)$ is the new integration limit. Expanding the exponential function into trigonometric functions while considering the fact that the integrated functions are even to simplify the integration bounds leads to

$$R_{i,j}(\tau) = \frac{A^2}{2\sqrt{\mu}} e^{-j\frac{\pi\mu\tau^2}{2}} \left[2\int_0^{\alpha} \cos\frac{\pi\xi^2}{2} d\xi - 2j\int_0^{\alpha} \sin\frac{\pi\xi^2}{2} d\xi \right] \tag{5.10}$$

where the integrals are recognised as Fresnel integrals, defined as[1]

$$S(\alpha) = \int_0^{\alpha} \sin\frac{\pi\xi^2}{2} d\xi \tag{5.11}$$

$$C(\alpha) = \int_0^{\alpha} \cos\frac{\pi\xi^2}{2} d\xi \tag{5.12}$$

[1]Fresnel integrals can be defined in different ways. In this text the definition of Abramowitz and Stegun is adopted [Abramowitz and Stegun, 1965, Page 295].

The integrals are depicted in Figures 5.12 and 5.13 for positive values only as they are odd functions, satisfying equalities $S(\alpha) = -S(-\alpha)$ and $C(\alpha) = -C(-\alpha)$. A complex form of Fresnel integral is defined as

$$F(\alpha) = C(\alpha) + jS(\alpha) \tag{5.13}$$

and the absolute value of cross-correlation (5.10) for $\tau \geq 0$ can therefore be simplified to

$$|R_{i,j}(\tau)| = \frac{A^2}{\sqrt{\mu}} \left| F\left(\sqrt{\mu}(T-\tau)\right) \right| \tag{5.14}$$

After inserting the value of μ and calculating for $-T < \tau < T$ one obtains

$$|R_{i,j}(\tau)| = A^2 \sqrt{\frac{T}{B}} \left| F\left(\sqrt{BT}\left(1 - \frac{|\tau|}{T}\right)\right) \right| \tag{5.15}$$

The expression above can be inserted in (4.60) to obtain a limit value for channel isolation when $BT \to \infty$ as

$$\lim_{BT\to\infty} I_{i,j}(\tau) = \frac{A^2 T}{\lim_{BT\to\infty} |R_{i,j}(\tau)|} = \sqrt{2TB} \tag{5.16}$$

where the limit value of the complex Fresnel integral $\lim_{BT\to\infty} F(\alpha) = 1/\sqrt{2}$ was utilised. The limit value derivation is given in Section 5.3.1. The isolation can be approximated as

$$I_{i,j} \approx \sqrt{2BT},\ BT \gg 1 \tag{5.17}$$

which proves that for the big time-bandwidth products the isolation depends solely on on the time duration of the signal and its bandwidth. Practical implementation of such waveforms pair would pose some limitations, since the bandwidth is limited by the technical characteristics of the system and also the large time duration of the waveform can cause eclipsing.

The isolation values as a function of time delay and parametrised BT-product are depicted in Figure 5.5. The figure relates to up-chirp and down-chirp waveforms with pulse width 10.0 µs and variable bandwidth. The effective isolation is considered to be the minimum value of isolation defined in (4.60).

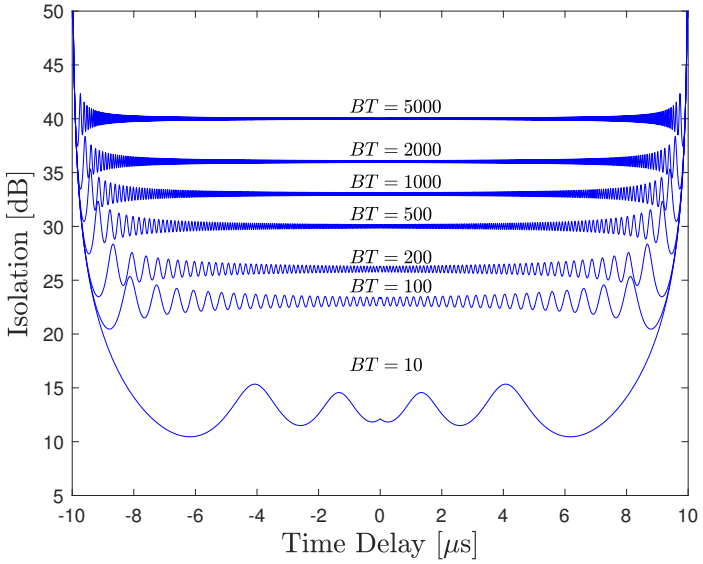

Figure 5.5: Isolation values of a rectangular up-chirp and a rectangular down-chirp with $T = 10.0\,\mu s$ and the same bandwidth, varying from 1.0 MHz to 500.0 MHz.

5.2.3 Isolation of Chirp Rate Diverse LFM

In this section an analytic derivation of the isolation of the square envelope LFM waveforms is extended to waveforms with different bandwidths with induced Doppler shift, as was demonstrated in [Kocjancic et al., 2018], which is a novel contribution as the chirp rate diversity and Doppler shift are included in the derivation. Two LFM waveforms $s_i(t)$ and $s_j(t)$ are defined as

$$s_i(t) = A \text{ rect}\left(\frac{t}{T}\right) \exp\left(2\pi j(f_{s,i}t + \frac{\mu_i t^2}{2})\right) \tag{5.18}$$

$$s_j(t) = A \text{ rect}\left(\frac{t}{T}\right) \exp\left(2\pi j(f_{s,j}t + \frac{\mu_j t^2}{2})\right) \tag{5.19}$$

where $\mu_i = B_i/T$, $\mu_j = B_j/T$ and the rectangular function is given as (3.80). As seen from the frequency modulation diagrams in Figure 5.6, both waveforms have the same duration T and the same amplitude A, hence the energy is the same $E = A^2T$. It is assumed, without loss of generality, that $\mu_j > \mu_i$, $\mu_j > 0$ and therefore $s_j(t)$ occupies greater bandwidth and can be treated as the main channel of an MBR. The starting frequency offsets $f_{s,i}$ and $f_{s,j}$ are arbitrary, where the waveform $s_i(t)$ is allowed to be additionally shifted by the Doppler frequency f_D.

The equations (5.18) and (5.19) are used in conjunction with the cross-ambiguity

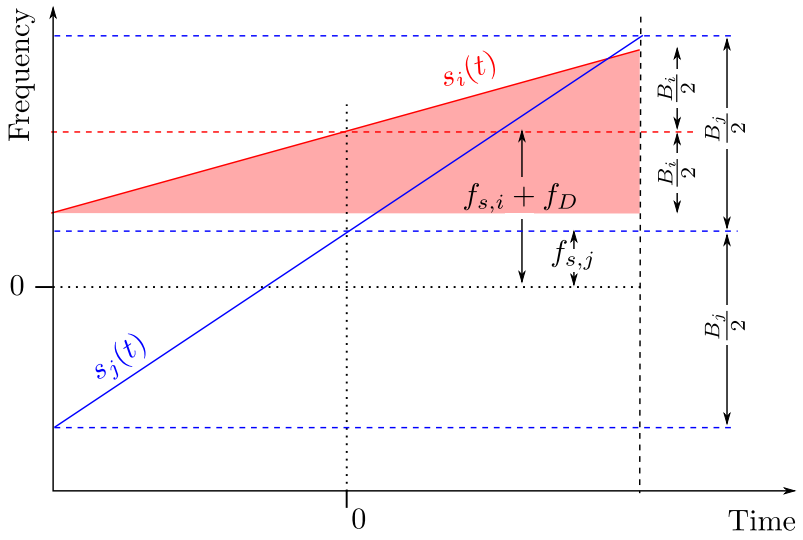

Figure 5.6: Frequency modulation diagram of the LFM waveforms $s_i(t)$ and $s_j(t)$ as used for the analytical derivation of the chirp rate diversity.

function (4.59) to obtain

$$\chi_{i,j}(\tau, f_D) = A^2 \exp\left(j2\pi(f_{s,j}\tau + \frac{1}{2}\mu_j\tau^2 - \frac{(f_{s,j} - f_{s,i} - f_D + \mu_j\tau)^2}{2(\mu_j - \mu_i)})\right) \times \int_{\eta_1}^{\eta_2} \exp\left(j\pi(\mu_j - \mu_i)(t + \frac{f_{s,j} - f_{s,i} - f_D + \mu_j\tau}{\mu_j - \mu_i})^2\right) dt \quad (5.20)$$

where the integration limits are

$$\eta_1 = -T/2 \quad (5.21)$$

$$\eta_2 = T/2 - \tau \quad (5.22)$$

if $0 \geq \tau \geq T$ and

$$\eta_1 = -T/2 - \tau \quad (5.23)$$

$$\eta_2 = T/2 \quad (5.24)$$

if $-T \geq \tau < 0$. The equation (5.20) can be further simplified with the change of variables

$$\xi = \sqrt{2(\mu_j - \mu_i)}\left(t + \frac{f_{s,j} - f_{s,i} - f_D + \mu_j\tau}{\mu_j - \mu_i}\right) \quad (5.25)$$

$$d\xi = \sqrt{2(\mu_j - \mu_i)}\, dt \quad (5.26)$$

that leads to

$$\chi_{i,j}(\tau, f_D) = A^2 K(\tau, f_D) \int_{\xi(\eta_1)}^{\xi(\eta_2)} \exp\left(j\frac{\pi}{2}\xi^2\right) d\xi \tag{5.27}$$

where

$$K(\tau, f_D) = \frac{\exp\left(j\pi\left(2f_{s,j}\tau + \mu_j\tau^2 - \frac{(f_{s,j}-f_{s,i}-f_D+\mu_j\tau)^2}{\mu_j-\mu_i}\right)\right)}{\sqrt{2(\mu_j-\mu_i)}} \tag{5.28}$$

The integral in the cross-ambiguity function (5.27) can be rewritten as the difference of two complex Fresnel integrals to simplify the expression as

$$\chi_{i,j}(\tau, f_D) = A^2 K(\tau, f_D)\Big(F(\xi(\eta_2)) - F(\xi(\eta_1))\Big) \tag{5.29}$$

and after expanding the complex Fresnel integral

$$\chi_{i,j}(\tau, f_D) = A^2 K(\tau, f_D)\Big[C(\xi(\eta_2)) + jS(\xi(\eta_2)) - C(\xi(\eta_1)) - S(\xi(\eta_1))\Big] \tag{5.30}$$

The arguments of the Fresnel integral in the equation above are defined as follows. For $0 < \tau < T$

$$\xi(\eta_1) = \sqrt{2(\mu_j-\mu_i)}\left(-\frac{T}{2} + \frac{f_{s,j}-f_{s,i}-f_D}{\mu_j-\mu_i} + \frac{\mu_j\tau}{\mu_j-\mu_i}\right) \tag{5.31}$$

$$\xi(\eta_2) = \sqrt{2(\mu_j-\mu_i)}\left(\frac{T}{2} + \frac{f_{s,j}-f_{s,i}-f_D}{\mu_j-\mu_i} + \frac{\mu_i\tau}{\mu_j-\mu_i}\right) \tag{5.32}$$

and for $-T < \tau < 0$ as

$$\xi(\eta_1) = \sqrt{2(\mu_j-\mu_i)}\left(-\frac{T}{2} + \frac{f_{s,j}-f_{s,i}-f_D}{\mu_j-\mu_i} + \frac{\mu_i\tau}{\mu_j-\mu_i}\right) \tag{5.33}$$

$$\xi(\eta_2) = \sqrt{2(\mu_j-\mu_i)}\left(\frac{T}{2} + \frac{f_{s,j}-f_{s,i}-f_D}{\mu_j-\mu_i} + \frac{\mu_j\tau}{\mu_j-\mu_i}\right) \tag{5.34}$$

The isolation expression can now be obtained by replacing (5.29) in (4.66). The bandwidth difference is defined as $\Delta B = B_j - B_i$, it is assumed that $f_{s,i} = 0$ and that the total energy is $E = \chi_{i,i}(0,0) = A^2T$. The waveform isolation for $|\tau| < T$ when $\tau < 0$ can be

found to be

$$I_{i,j}(\tau, f_D)\Big|_{\tau<0} = \sqrt{2T\Delta B}\left|F\left(\sqrt{\frac{2\Delta B}{T}}\left(\frac{T}{2}+\frac{B_j\tau - T(f_{s,i}+f_D)}{\Delta B}\right)\right)\right.$$
$$\left. - F\left(\sqrt{\frac{2\Delta B}{T}}\left(-\frac{T}{2}+\frac{B_i\tau - T(f_{s,i}+f_D)}{\Delta B}\right)\right)\right|^{-1} \quad (5.35)$$

and when $\tau > 0$ as

$$I_{i,j}(\tau, f_D)\Big|_{\tau>0} = \sqrt{2T\Delta B}\left|F\left(\sqrt{\frac{2\Delta B}{T}}\left(-\frac{T}{2}+\frac{B_j\tau - T(f_{s,i}+f_D)}{\Delta B}\right)\right)\right.$$
$$\left. - F\left(\sqrt{\frac{2\Delta B}{T}}\left(\frac{T}{2}+\frac{B_i\tau - T(f_{s,i}+f_D)}{\Delta B}\right)\right)\right|^{-1} \quad (5.36)$$

Note that for the up-chirps $B_i > 0$ and for the down-chirps $B_i < 0$ so that ΔB changes accordingly. The results obtained herein are in agreement with those presented in [Kocjancic et al., 2017], wherein the Doppler shift was omitted.

The isolation expression can be further simplified by fixing $f_{s,i} = 0$, $f_{s,j} = 0$ and $f_D = 0$. The simplification, which holds for $|\tau| < T$, yields

$$I_{ij}(\tau, 0) = \sqrt{2T\Delta B}\left|F\left(\sqrt{\frac{2\Delta B}{T}}\left(-\frac{T}{2}+\frac{B_j|\tau|}{\Delta B}\right)\right)\right.$$
$$\left. - F\left(\sqrt{\frac{2\Delta B}{T}}\left(\frac{T}{2}+\frac{B_i|\tau|}{\Delta B}\right)\right)\right|^{-1} \quad (5.37)$$

5.2.4 Rectangular LFM Isolation Bound

An isolation bound on the isolation can be established by considering the maximum value of Fresnel integrals, which allows for the lower bound on the isolation to be obtained.

To obtain the bound on the cross-ambiguity function (5.30) we note that its amplitude can be expressed as a function of the amplitude of the difference between two Fresnel integrals as

$$|\chi_{i,j}(\tau, f_D)| = \sqrt{\frac{T}{2\Delta B}}A^2\left|C(\xi(\eta_2)) + jS(\xi(\eta_2)) - C(\xi(\eta_1)) - jS(\xi(\eta_1))\right| \quad (5.38)$$

where $C(\cdot)$ and $S(\cdot)$ are the real and imaginary parts of $F(\cdot)$. Now the upper bound can

be established by applying a triangular inequality to obtain

$$|\chi_{i,j}(\tau, f_D)| \leq \sqrt{\frac{T}{2\Delta B}} A^2 \left[\left| C(\xi(\eta_2)) + jS(\xi(\eta_2)) \right| + \left| C(\xi(\eta_1)) + jS(\xi(\eta_1)) \right| \right] \tag{5.39}$$

Noting that the absolute value of complex Fresnel integral is a bounded function, satisfying the relation $F(\xi) \leq F_{max} \approx 0.9491$, the inequality can be further simplified

$$|\chi_{i,j}(\tau, f_D)| \leq \sqrt{\frac{T}{2\Delta B}} A^2 [F_{max} + F_{max}] \tag{5.40}$$

and the isolation is therefore determined as

$$I_{i,j}(\tau, f_D) = \left| \frac{\chi_{i,i}(0,0)}{\chi_{i,j}(\tau, f_D)} \right| \tag{5.41}$$

$$\geq \frac{A^2 T}{2A^2 F_{max} \sqrt{\frac{T}{2\Delta B}}} \tag{5.42}$$

$$> \sqrt{\frac{T\Delta B}{2}} \tag{5.43}$$

The inequality (5.43) is an important equation as it establishes the fact that the lower bound on the isolation is proportional to the square root of the pulse width and the bandwidth difference so that

$$I_{i,j,min} \propto \sqrt{T\Delta B} \tag{5.44}$$

To corroborate the isolation bounds derived above a simulation was performed with two LFM waveforms, with a bandwidth $B_j = 50.0\,\text{MHz}$ and $B_i = B_j - \Delta B$. The jth signal was fixed as an up-chirp and the ith signal varied as up-chirp and down-chirp. Figure 5.7 depicts the amount of isolation as a function of ΔB, where the lower bound is calculated according to (5.42) and the simplified lower bound according to (5.43). It can be observed that the lower bound and its simplified expression for bandwidth differences above 15 % of the bandwidth are approximately 1.0 dB and 1.5 dB off the true values, respectively.

Additionally, Figure 5.7 shows the isolation performance of chirp signals with variable slope rate. As was explained previously, the waveform $s_j(t)$ is fixed with $B_j = 50.0\,\text{MHz}$ and $T = 10.0\,\mu\text{s}$, while $s_i(t)$ is changing, as shown in Figure 5.6. It has to be noted that the bandwidth difference referred to in the figure is calculated as $\Delta B = |B_j| - |B_i|$, but in the

calculations $\Delta B = B_j - B_i$ is used. By convention the sign of the bandwidth is positive for up-chirps, $B_i > 0$, and negative for down-chirps, $B_i < 0$. This fact explains the difference in isolation when comparing a set of waveforms with opposite sign of the chirp rate to the set with the same sign of the chirp rate. Waveforms with different opposite chirp rates, e.g. a combination of up-chirp and down-chirp, reach higher effective bandwidth difference $|\Delta B|$, which results in higher isolation values. This phenomenon can be observed in Figure 5.7, where the best isolation is achieved for up-chirp and down-chirp with $\Delta B = 0\,\text{MHz}$. Therefore the entire bandwidth is exploited and maximum BT-product is achieved.

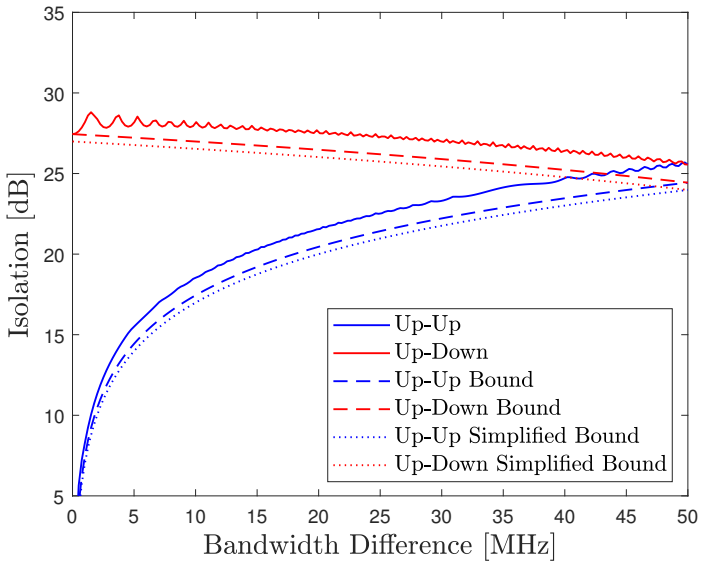

Figure 5.7: Isolation performance of two LFM waveforms as a function of bandwidth difference ΔB. The isolation lower bounds are determined according to (5.42) and (5.43).

5.2.5 Numerical Simulations

This section presents numerical simulations of two up-chirp waveforms with frequency modulation defined in Figure 5.6. The waveforms $s_i(t)$ and $s_j(t)$ are defined in the same way as presented in Section 5.2.4. The result of the first simulation is shown in Figure 5.8, which is a cross-correlation between the two waveforms $R_{i,j}(\tau)$, also showing a zero-Doppler cut of the ambiguity function. The fixed parameters are $B_j = 50.0\,\text{MHz}$, $f_{s,i} = f_{s,j} = 0\,\text{Hz}$ and $T = 10.0\,\mu\text{s}$, while the bandwidth B_i is changing according to ΔB. Both waveforms are centrally aligned in frequency, hence the symmetry of the cross-correlation functions, as shown in Figure 5.8. It can be observed in the figure that bigger bandwidth

differences produce better isolation, hence the suppression of the secondary channel is more effective. By increasing ΔB, the sidelobes of the cross-correlation functions are extended symmetrically in positive and negative delays. The behaviour of the sidelobes, as defined with (5.35) and (5.36), can be explained by observing Figure 5.6. When the time delays τ are positive $x_i(t)$ moves to the left in the-time frequency plot and the presence of the sidelobes can be observed until there is no more overlapping between the linear curves. The drop of sidelobes coincides with delays of non-overlapping LFM. The minimum isolation values as a function of ΔB are depicted in Figure 5.7.

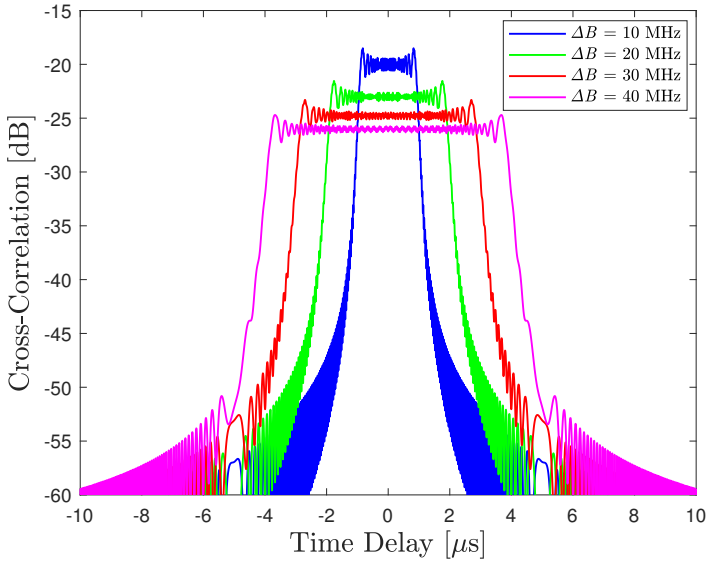

Figure 5.8: Cross-correlation functions of two up-chirps with the parametrised bandwidth difference ΔB.

The effect of changing the starting frequency $f_{s,i}$ is investigated next. In this case the bandwidths were fixed as $B_i = 10.0\,\text{MHz}$ and $B_j = 50.0\,\text{MHz}$ so that the chirp $x_i(t)$ could be shifted within the bandwidth of the jth waveform. The offset frequency $f_{s,i}$ was varied for the specific set of values shown, in Figure 5.9. The results show that the isolation is invariant to the starting frequency shifts, which can be deduced from the time-frequency plots in Figure 5.6. Changes of the starting frequency will result in modulation curve movement in a vertical direction. Therefore, increasing the starting frequency of the ith waveform has the effect of moving the cross-correlation function to positive delays τ while preserving the ΔB. The starting frequency invariance is further tested with simulations and results plotted in Figure 5.10, where the isolation is shown as a function of $f_{s,i}$. The

isolation values are plotted according to (4.61) and show that the increase of ΔB from 20 MHz to 40 MHz results in isolation improvement from 21.5 dB to 24.6 dB. The variation of isolation values with changing $f_{s,i}$ is, as expected, minimal.

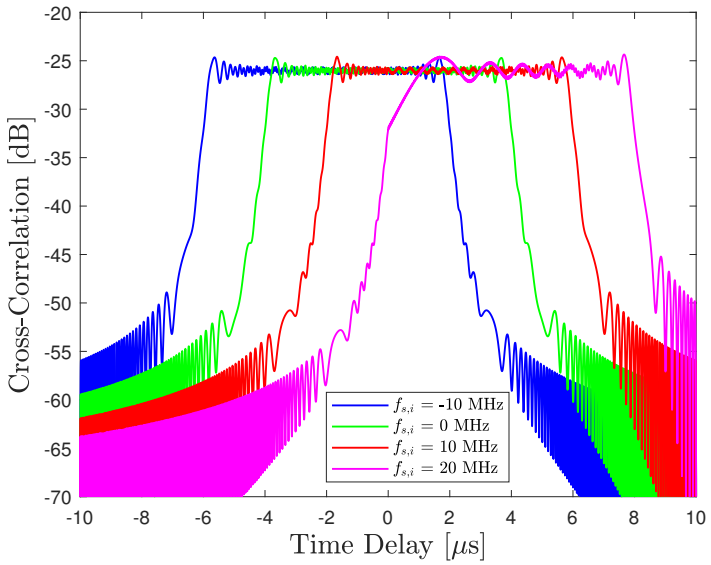

Figure 5.9: Cross-correlation functions of two up-chirps with the parametrised starting frequency $f_{s,i}$.

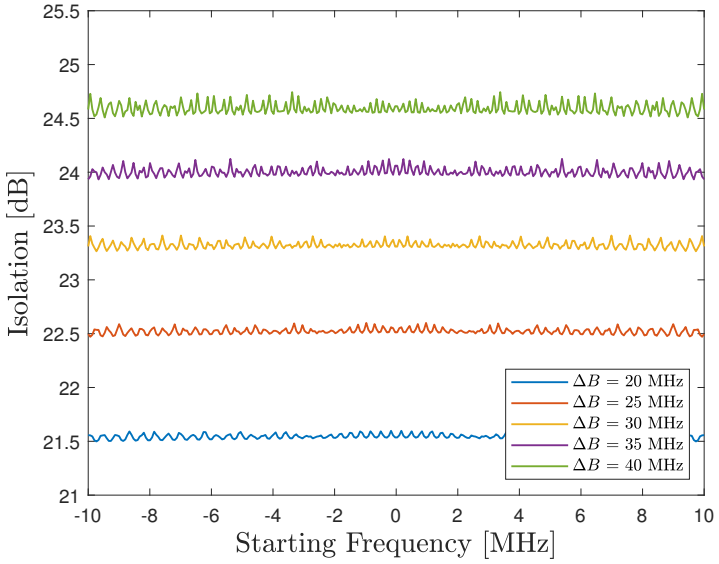

Figure 5.10: Isolation values showing starting frequency ($f_{s,i}$) tolerance with bandwidth difference set as a parameter.

5.3 Asymptotic Approximation of Fresnel Integral

Two functions $f(x)$ and $g(x)$ are asymptotic to each other if and only if the ratio $g(x)/f(x)$ approaches one as $x \to \infty$ [Bender and Orszag, 1999, Chapter 3.4], [Chapling, 2016]. Therefore the relative error between $f(x)$ and $g(x)$ goes to zero. We can write the asymptotic relation as

$$g(x) \sim f(x) \iff \lim_{x\to\infty} \frac{g(x)}{f(x)} = 1 \tag{5.45}$$

The big-$\mathcal{O}$ notation of the form

$$g(x) = \mathcal{O}\big(h(x)\big), \quad x \in \mathcal{A} \tag{5.46}$$

is used to describe the residual terms in an expansion. The notation (5.46) holds when for an arbitrary constant $M > 0$ the inequality $|g(x)| \leq M|h(x)|$ is true for all $x \in \mathcal{A}$.

5.3.1 Limit Value of Fresnel Integral

We first solve the Fresnel integrals, defined as (5.11) and (5.12), in the limit when $x \to \infty$ by integrating the complex function $f(z) = e^{-\frac{\pi}{2}z^2}$ along the contour $\xi(R)$ in the complex plane. As the function in question is analytic, Cauchy's integral theorem applies

$$\oint_{\xi(R)} f(z)dz = \int_{\xi_1(R)} f(z)dz + \int_{\xi_2(R)} f(z)dz + \int_{\xi_3(R)} f(z)dz = 0 \tag{5.47}$$

where $\xi_1(R)$, $\xi_2(R)$ and $\xi_3(R)$ are parts of the anticlockwise integration contour, depicted in Figure 5.11. The first contribution is integrated along the real line and in the limit as $R \to \infty$ it converges to the Gaussian integral (5.109) with a known solution

$$\lim_{R\to\infty} \int_{\xi_1(R)} f(z)dz = \int_0^\infty e^{-\frac{\pi}{2}x^2} dx = \frac{1}{\sqrt{2}} \tag{5.48}$$

Rewriting a complex number in polar form as $z = re^{j\theta}$ and its differential as

$$dz = dx + idy = e^{j\theta}dr + jre^{j\theta}d\theta \tag{5.49}$$

it can be shown that the second contribution is

$$\lim_{R\to\infty}\int_{\xi_2(R)} f(z)dz = \lim_{R\to\infty}\int_0^{\pi/4} e^{-\frac{\pi}{2}R^2e^{2j\theta}} jRe^{j\theta}d\theta = 0 \tag{5.50}$$

To prove it, we show that the integral converges absolutely to 0 as $R\to\infty$

$$\begin{aligned}
\lim_{R\to\infty}\left|\int_{\xi_2(R)} f(z)dz\right| &\le \lim_{R\to\infty}\int_{\xi_2(R)} |f(z)|\,dz && (5.51)\\
&= \lim_{R\to\infty} R\int_0^{\pi/4}\left|e^{-\frac{\pi}{2}R^2(\cos 2\theta + j\sin 2\theta)}\right| d\theta && (5.52)\\
&= \lim_{R\to\infty} R\int_0^{\pi/4} e^{-\frac{\pi}{2}R^2\cos 2\theta}d\theta && (5.53)\\
&\le \lim_{R\to\infty} R\int_0^{\pi/4} e^{-\frac{\pi}{2}R^2(1-\frac{4}{\pi}\theta)}d\theta && (5.54)\\
&= \lim_{R\to\infty} Re^{-\frac{\pi}{2}R^2}\int_0^{\pi/4} e^{2R^2\theta}d\theta && (5.55)\\
&= \lim_{R\to\infty}\frac{1}{2R}\left[1-e^{-\frac{\pi}{2}R^2}\right] && (5.56)
\end{aligned}$$

which clearly converges to 0. In (5.53), the modified Jordan's inequality for cosine functions was used that is valid within the interval $\alpha\in[0,\pi/2]$

$$1-\frac{2}{\pi}\alpha \le \cos\alpha \le -\alpha+\frac{\pi}{2} \tag{5.57}$$

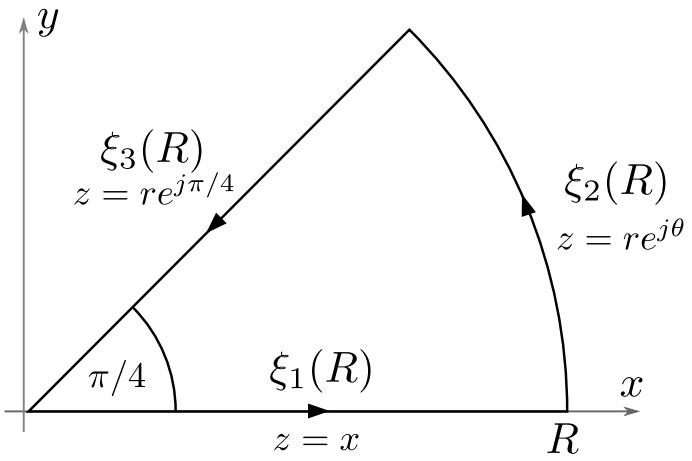

Figure 5.11: Integration path $\xi(R)$ of the complex Fresnel integral in the complex plane with x being the real axis and y the imaginary axis.

The integral along $\xi_3(R)$ can be transformed in polar form (5.49) and integrated in the radial direction only

$$\int_{\xi_3(R)} f(z)dz = \int_{\infty}^{0} e^{-\frac{\pi}{2}\left(re^{j\pi/4}\right)^2} e^{j\pi/4} dr \tag{5.58}$$

$$= \frac{\sqrt{2}(1+j)}{2} \int_{\infty}^{0} e^{-j\frac{\pi}{2}r^2} dr \tag{5.59}$$

$$= \frac{\sqrt{2}}{2} \int_{\infty}^{0} (1+j)\left(\cos\frac{\pi r^2}{2} - j\sin\frac{\pi r^2}{2}\right) dr \tag{5.60}$$

$$= \frac{\sqrt{2}}{2} \int_{\infty}^{0} \left(\cos\frac{\pi r^2}{2} + \sin\frac{\pi r^2}{2}\right) + j\left(\cos\frac{\pi r^2}{2} - \sin\frac{\pi r^2}{2}\right) dr \tag{5.61}$$

Taking into account (5.47), (5.48) and the fact that $\int_{\xi(R)} f(z)dz = 0$, we can write

$$-\int_{\xi_3(R)} f(z)dz = \frac{1}{\sqrt{2}} \tag{5.62}$$

Therefore two set of equations for real and imaginary part can be obtained

$$\int_{0}^{\infty} \cos\frac{\pi r^2}{2} dr + \int_{0}^{\infty} \sin\frac{\pi r^2}{2} dr = 1 \tag{5.63}$$

$$C(\infty) + S(\infty) = 1 \tag{5.64}$$

and

$$\int_{0}^{\infty} \cos\frac{\pi r^2}{2} dr - \int_{0}^{\infty} \sin\frac{\pi r^2}{2} dr = 0 \tag{5.65}$$

$$C(\infty) = S(\infty) \tag{5.66}$$

which implies

$$C(\infty) = S(\infty) = \frac{1}{2} \tag{5.67}$$

From the definition of integrals, it follows that

$$C(-\infty) = S(-\infty) = -\frac{1}{2} \tag{5.68}$$

and the absolute value of the asymptotic expansion of complex Fresnel integral is therefore

$$|F(\infty)| = |C(\infty) + jS(\infty)| = \frac{1}{\sqrt{2}} \tag{5.69}$$

5.3.2 Asymptotic Expansion of the Fresnel Integral

To find the asymptotic expansion of the Fresnel sine integral, we write the integral as a difference between its limit value as $x \to \infty$ and the remaining integral as

$$S(x) = \int_0^x \sin\frac{\pi t^2}{2} dt = \frac{1}{2} - \int_x^\infty \sin\frac{\pi t^2}{2} dt \tag{5.70}$$

After introducing a new variable $u = \pi t^2/2$ and $dt = du/\sqrt{2\pi u}$, we have

$$S(x) = \frac{1}{2} - \frac{1}{\sqrt{2\pi}} \int_{\xi(x)}^\infty \frac{\sin u}{u^{1/2}} du \tag{5.71}$$

where $\xi = \xi(x) = \pi x^2/2$ is the new integration limit. Integrating (5.71) by parts multiple times results in the asymptotic expansion

$$\int_\xi^\infty \frac{\sin u}{u^{1/2}} du = -\frac{\cos u}{u^{1/2}}\bigg|_\xi^\infty - \frac{1}{2}\int_\xi^\infty \frac{\cos u}{u^{3/2}} du \tag{5.72}$$

$$= \frac{\cos\xi}{\xi^{1/2}} - \frac{1}{2}\left[\frac{\sin u}{u^{3/2}}\bigg|_\xi^\infty + \frac{3}{2}\int_\xi^\infty \frac{\sin u}{u^{5/2}} du\right] \tag{5.73}$$

$$= \frac{\cos\xi}{\xi^{1/2}} + \frac{1}{2}\frac{\sin\xi}{\xi^{3/2}} - \frac{3}{4}\left[-\frac{\cos u}{u^{5/2}}\bigg|_\xi^\infty - \frac{5}{2}\int_\xi^\infty \frac{\cos u}{u^{7/2}} du\right] \tag{5.74}$$

$$= \frac{\cos\xi}{\xi^{1/2}} + \frac{1}{2}\frac{\sin\xi}{\xi^{3/2}} - \frac{3}{4}\frac{\cos\xi}{\xi^{5/2}} + \frac{15}{8}\left[\frac{\sin u}{u^{7/2}}\bigg|_\xi^\infty + \frac{7}{2}\int_\xi^\infty \frac{\sin u}{u^{9/2}} du\right] \tag{5.75}$$

$$= \frac{\cos\xi}{\xi^{1/2}} + \frac{1}{2}\frac{\sin\xi}{\xi^{3/2}} - \frac{3}{4}\frac{\cos\xi}{\xi^{5/2}} - \frac{15}{8}\frac{\sin\xi}{\xi^{7/2}} + \frac{105}{16}\int_\xi^\infty \frac{\sin u}{u^{9/2}} du \tag{5.76}$$

where the fact that the limit value approaches 0 as $u \to \infty$ was used

$$\frac{\cos u}{u^{1/2}}\bigg|_\xi^\infty = \lim_{u\to\infty}\frac{\cos u}{u^{1/2}} - \frac{\cos\xi}{\xi^{1/2}} = -\frac{\cos\xi}{\xi^{1/2}} \tag{5.77}$$

and similarly holds for the subsequent terms. Inserting (5.76) in (5.71) and replacing ξ leads to the asymptotic expansion

$$S(x) \sim \frac{1}{2} - \frac{\cos\frac{\pi x^2}{2}}{\pi x} - \frac{\sin\frac{\pi x^2}{2}}{\pi^2 x^3} + 3\frac{\cos\frac{\pi x^2}{2}}{\pi^3 x^5} + 15\frac{\sin\frac{\pi x^2}{2}}{\pi^4 x^7} + \mathcal{O}\left(x^{-9}\right) \tag{5.78}$$

Asymptotic expansion of Fresnel cosine for different numbers of terms is shown in Figure 5.12.

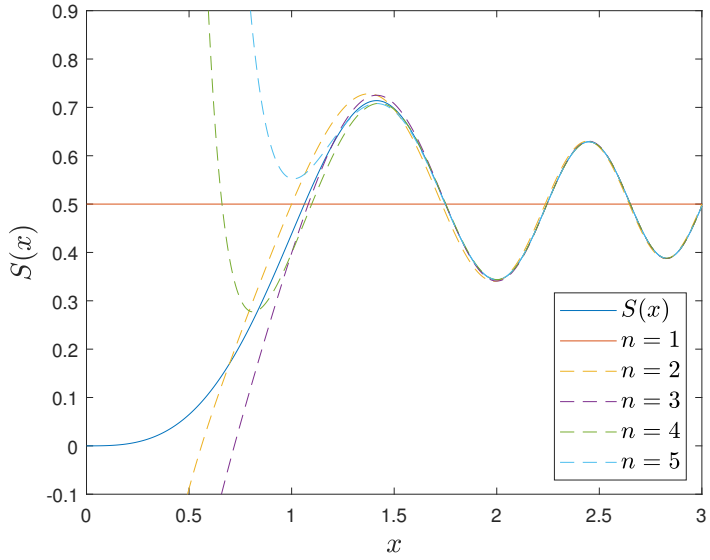

Figure 5.12: Asymptotic expansion of Fresnel cosine integral for n number of terms.

Similarly, we write for the Fresnel cosine integral

$$C(x) = \frac{1}{2} - \frac{1}{\sqrt{2\pi}} \int_{\xi(x)}^{\infty} \frac{\cos u}{u^{1/2}} du \tag{5.79}$$

with the same variable substitution as in (5.70). Employing multiple steps of integration

by parts leads to

$$\int_{\xi}^{\infty} \frac{\cos u}{u^{1/2}} du = \frac{\sin u}{u^{1/2}}\bigg|_{\xi}^{\infty} + \frac{1}{2}\int_{\xi}^{\infty} \frac{\sin u}{u^{3/2}} du \tag{5.80}$$

$$= -\frac{\sin \xi}{\xi^{1/2}} + \frac{1}{2}\left[-\frac{\cos u}{u^{3/2}}\bigg|_{\xi}^{\infty} - \frac{3}{2}\int_{\xi}^{\infty} \frac{\cos u}{u^{5/2}} du\right] \tag{5.81}$$

$$= -\frac{\sin \xi}{\xi^{1/2}} + \frac{1}{2}\frac{\cos \xi}{\xi^{3/2}} - \frac{3}{4}\left[\frac{\sin u}{u^{5/2}}\bigg|_{\xi}^{\infty} + \frac{5}{2}\int_{\xi}^{\infty} \frac{\sin u}{u^{7/2}} du\right] \tag{5.82}$$

$$= -\frac{\sin \xi}{\xi^{1/2}} + \frac{1}{2}\frac{\cos \xi}{\xi^{3/2}} + \frac{3}{4}\frac{\sin \xi}{\xi^{5/2}} - \frac{15}{8}\left[-\frac{\cos u}{u^{7/2}}\bigg|_{\xi}^{\infty} - \frac{7}{2}\int_{\xi}^{\infty} \frac{\cos u}{u^{9/2}} du\right] \tag{5.83}$$

$$= -\frac{\sin \xi}{\xi^{1/2}} + \frac{1}{2}\frac{\cos \xi}{\xi^{3/2}} + \frac{3}{4}\frac{\sin \xi}{\xi^{5/2}} - \frac{15}{8}\frac{\cos \xi}{\xi^{7/2}} + \frac{105}{16}\int_{\xi}^{\infty} \frac{\cos u}{u^{9/2}} du \tag{5.84}$$

and after inserting (5.84) in (5.79) and accounting for $\xi = \pi x^2/2$, the final asymptotic expansion equals to

$$C(x) \sim \frac{1}{2} + \frac{\sin \frac{\pi x^2}{2}}{\pi x} - \frac{\cos \frac{\pi x^2}{2}}{\pi^2 x^3} - 3\frac{\sin \frac{\pi x^2}{2}}{\pi^3 x^5} + 15\frac{\cos \frac{\pi x^2}{2}}{\pi^4 x^7} + \mathcal{O}\left(x^{-9}\right) \tag{5.85}$$

Plots of asymptotic expansions of Fresnel sine integral are shown in Figure 5.13 for different number of terms.

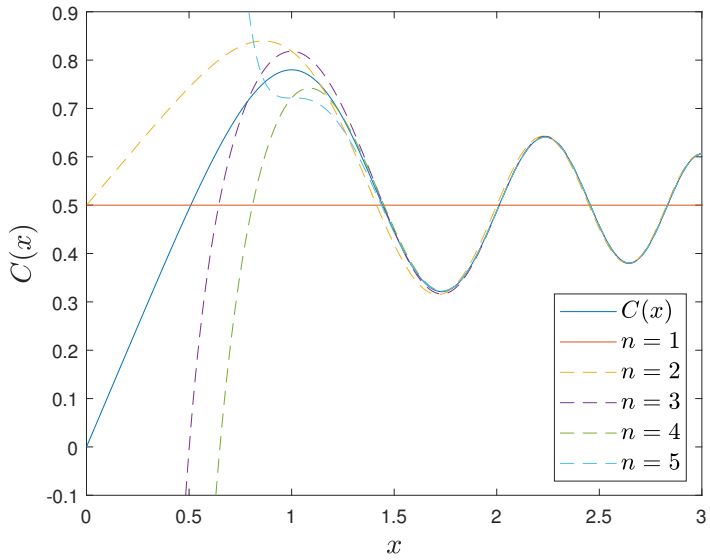

Figure 5.13: Asymptotic expansion of Fresnel sine integral for n number of terms.

5.4 Gaussian LFM Orthogonality

This section investigates the isolation properties of LFM waveforms when a Gaussian amplitude modulation is applied. A general expression of isolation is derived first, as was demonstrated in [Kocjancic et al., 2018]. Then the expression is reduced to the case of up-chirp and down-chirp for which an analytical solution is found. A proof of the Gaussian integral is given before the simulation results are presented and compared to those of a rectangular LFM waveform.

5.4.1 Analytical Derivation of Gaussian LFM Isolation

The Gaussian LFM waveform is defined as

$$s_i(t) = \left(\frac{1}{\pi\lambda^2}\right)^{1/4} \exp\left(-\frac{t^2}{2\lambda^2} + j\left(a_i t + b_i t^2\right)\right) \tag{5.86}$$

where $T = 2\lambda$ is the pulse duration and $b_i = \pi B_i/T$ is the frequency slope of the chirp with bandwidth B_i. The signal model is defined in the same way as in [Cook and Bernfeld, 1993] with an additional term $a_i = 2\pi f_{s,i}$ that defines the starting frequency at $t = 0$.

The derivation starts by inserting (5.86) in the cross-ambiguity function to obtain

$$\begin{aligned}\chi_{i,j}(\tau, f_D) = \sqrt{\frac{1}{\pi\lambda^2}} \int_{-\infty}^{\infty} &\exp\left(-\frac{t^2}{2\lambda^2} - j a_i t - j b_i t^2\right) \\ &\times \exp\left(-\frac{(t+\tau)^2}{2\lambda^2} + j a_j (t+\tau) + j b_j (t+\tau)^2 + j 2\pi f_D t\right) dt\end{aligned} \tag{5.87}$$

which can be rewritten so that the integrand contains only the terms dependent on t

$$\begin{aligned}\chi_{i,j}(\tau, f_D) = \sqrt{\frac{1}{\pi\lambda^2}} &\exp\left(j(b_j\tau^2 + a_j\tau) - \frac{\tau^2}{2\lambda^2}\right) \\ &\times \int_{-\infty}^{\infty} \exp\left(-\left[\frac{1}{\lambda^2} - j(b_j - b_i)\right] t^2\right) \\ &\times \exp\left(-\left[\frac{\tau}{\lambda^2} + j(a_i - a_j - 2\pi f_D - 2b_j\tau)\right] t\right) dt\end{aligned} \tag{5.88}$$

To simplify the expression above, two new functions are introduced

$$\alpha = \frac{1}{\lambda^2} - j(b_j - b_i) \tag{5.89}$$

$$\beta = \frac{\tau}{\lambda^2} + j(a_i - a_j - 2\pi f_D - 2b_j\tau) \tag{5.90}$$

that yield

$$\chi_{i,j}(\tau, f_D) = \sqrt{\frac{1}{\pi\lambda^2}} \exp\left(j(b_j\tau^2 + a_j\tau) - \frac{\tau^2}{2\lambda^2}\right) \times \int_{-\infty}^{\infty} \exp\left(-\alpha t^2 - \beta t\right) dt \tag{5.91}$$

which can be rewritten in the quadratic form as

$$\chi_{i,j}(\tau, f_D) = \sqrt{\frac{1}{\pi\lambda^2}} \exp\left(j(b_j\tau^2 + a_j\tau) - \frac{\tau^2}{2\lambda^2}\right) \times \int_{-\infty}^{\infty} \exp\left(-\alpha\left(t + \frac{\beta}{2\alpha}\right)^2 + \frac{\beta^2}{4\alpha}\right) dt \tag{5.92}$$

and with further rearrangement

$$\chi_{i,j}(\tau, f_D) = \sqrt{\frac{1}{\pi\lambda^2}} \exp\left(j(b_j\tau^2 + a_j\tau) - \frac{\tau^2}{2\lambda^2} + \frac{\beta^2}{4\alpha}\right) \times \int_{-\infty}^{\infty} \exp\left(-\alpha\big(t + \frac{\beta}{2\alpha}\big)^2\right) dt \tag{5.93}$$

The integral in (5.93) can be recognised as Gaussian, which converges to $\sqrt{\pi/\alpha}$ if $\Re[\alpha] > 0$, which is always met, according to (5.89). The detailed treatment of the integral is provided in Section 5.4.3. The final expression therefore reads

$$\chi_{i,j}(\tau, f_D) = \sqrt{\frac{1}{\alpha\lambda^2}} \exp\left(j(b_j\tau^2 + a_j\tau) - \frac{\tau^2}{2\lambda^2} + \frac{\beta^2}{4\alpha}\right) \tag{5.94}$$

The amplitude of the cross-ambiguity function is therefore

$$|\chi_{i,j}(\tau, f_D)| = \frac{1}{\lambda} \exp\left(-\frac{\tau^2}{2\lambda^2}\right) \left|\sqrt{\frac{1}{\alpha}} \exp\left(\frac{\beta^2}{4\alpha}\right)\right| \tag{5.95}$$

and by requiring that $a_i = a_j$ and $b_i = b_j$ the ambiguity function can be obtained as

$$|\chi_{i,i}(\tau, f_D)| = \exp\left(-\frac{\tau^2}{4\lambda^2} - \pi^2\lambda^2\big(f_D + \frac{b_i\tau}{\pi}\big)^2\right) \tag{5.96}$$

which corresponds to the expression given in [Cook and Bernfeld, 1993]. By employing (5.95) the general expression of the isolation can be found as

$$I(\tau, f_D) = \lambda \exp\left(\frac{\tau^2}{2\lambda^2}\right)\left|\sqrt{\frac{1}{\alpha}}\exp\left(\frac{\beta^2}{4\alpha}\right)\right|^{-1} \tag{5.97}$$

The cross-correlation function between two Gaussian chirps with $f_{s,i} = f_{s,j} = 0$ can be derived from (5.94). Therefore, when conditions[2] $f_D = 0$ and $a_i = a_j = 0$ hold, expressions (5.89) and (5.90) are simplified as

$$\alpha = \frac{1}{\lambda^2}\left[1 - j\lambda^2(b_j - b_i)\right] \tag{5.98}$$

$$\beta = \frac{\tau}{\lambda^2}\left[1 - j2\lambda^2 b_j\right] \tag{5.99}$$

and the cross-correlation is

$$R_{i,j}(\tau) = \frac{\exp\left(\frac{\left(1+2jb_i\lambda^2\right)\left(j+2b_j\lambda^2\right)\tau^2}{4\lambda^2\left(\lambda^2(b_i-b_j)-j\right)}\right)}{\sqrt{1 + j\lambda^2(b_i - b_j)}} \tag{5.100}$$

5.4.2 Isolation Between Up-Chirp and Down-Chirp

The isolation between up-chirp and down-chirp of the same bandwidth is the simplest case that can be obtained. By considering opposite chirp rates $b = b_i = -b_j$ and neglecting the frequency offsets $a_i = a_j = 0$ an analytical expression can be obtained. By considering

$$\alpha = \frac{1}{\lambda^2} + j2b \tag{5.101}$$

$$\beta = \tau\alpha \tag{5.102}$$

[2]The derivation of the cross-correlation function follows [Kocjancic et al., 2018], although it has to be noted that the condition for a_i and a_j is stricter then the one given in the citation. The same holds for Section 5.4.2.

and simplifying (5.100) one can obtain

$$R_{i,j}(\tau) = \sqrt{\frac{1}{1+j2b\lambda^2}}\ \exp\left(-\frac{\tau^2}{4}\left(\frac{1}{\lambda^2}+j2b\right)\right) \tag{5.103}$$

The isolation can therefore be determined as

$$I_{i,j}(\tau) = \left|\sqrt{1+j2b_i\lambda^2}\ \exp\left(\frac{\tau^2}{4}\left(\frac{1}{\lambda^2}+2jb\right)\right)\right| \tag{5.104}$$

$$= \sqrt[4]{1+4b^2\lambda^4}\ \exp\left(\frac{\tau^2}{4\lambda^2}\right) \tag{5.105}$$

The minimum value of the isolation given above occurs when $\tau = 0$ and is

$$I_{i,j,min} = \sqrt[4]{1+4b^2\lambda^4} \tag{5.106}$$

Finally, the isolation lower bound can be expressed as a function of B and T as

$$I_{i,j,min} = \sqrt[4]{1+\frac{\pi^2B^2T^2}{4}} \tag{5.107}$$

which can be approximated for $BT \gg 1$ to obtain

$$I_{i,j,min} \approx \sqrt{\frac{\pi}{2}BT} \tag{5.108}$$

Equation (5.108) relates to the isolation approximation (5.44) for rectangular chirps and corroborates the isolation dependence on the time-bandwidth product of the corresponding waveforms.

Figure 5.14 shows the results of a simulation involving a set of up-chirps and down-chirps, both having the same bandwidth and pulse duration $T = 10\,\mu s$. The bandwidth of both waveforms was varied from 1.0 MHz to 500.0 MHz, as marked in the figure, in order to obtain isolation values for different BT-products, as defined with (4.61). The isolation values obtained are comparable to those with the rectangular envelope, although the sidelobes taper off quickly and a constant modulus is not preserved when Gaussian LFM is applied. It can be observed that the minimum isolation values for specific BT-products corroborate the relation in (5.108). The comparison between rectangular and

Gaussian LFM will be further outlined in Section 5.4.4.

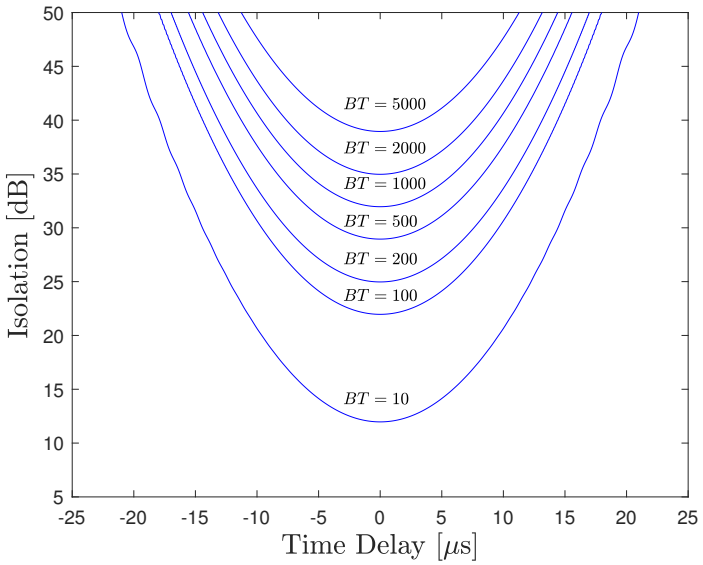

Figure 5.14: Isolation values of a Gaussian up-chirp and a Gaussian down-chirp with $T = 10.0\,\mu s$ and the same bandwidth, varying from 1.0 MHz to 500.0 MHz.

5.4.3 Gaussian Integral

The Gaussian integral is frequently used in statistics and information theory but its complex version is not commonly utilised. In this section, a derivation of the Gaussian integral is given along with its extended version with complex offset [Smith III, 2011]. The theorem for $t \in \mathbb{R}$, $\alpha \in \mathbb{C}$ and $\Re[\alpha] > 0$ states that

$$\int_{-\infty}^{\infty} e^{-\alpha t^2} dt = \sqrt{\frac{\pi}{\alpha}} \tag{5.109}$$

To prove it, we denote the integral as $I(\alpha)$ and calculate

$$I^2(\alpha) = \left[\int_{-\infty}^{\infty} e^{-\alpha x^2} dx\right] \left[\int_{-\infty}^{\infty} e^{-\alpha y^2} dy\right] \tag{5.110}$$

$$= \int_{-\infty}^{\infty}\int_{-\infty}^{\infty} e^{-\alpha(x^2+y^2)} dx dy \tag{5.111}$$

where integrals were replaced by double integration over the entire plane $\mathbb{R}^2$ according to Fubini's theorem [Hubbard and Hubbard, 2009, Page 438]. Now we change to polar coordinates $x = r\cos\theta$ and $y = r\sin\theta$ for which the infinitesimal area element is calculated

as a determinant of the Jacobian matrix

$$dA = dx\,dy = |J|\,dr\,d\theta = \begin{vmatrix} \frac{\partial x}{\partial r} & \frac{\partial x}{\partial \theta} \\ \frac{\partial y}{\partial r} & \frac{\partial y}{\partial \theta} \end{vmatrix} = r\,dr\,d\theta \tag{5.112}$$

Further, after changing the integration limits and introducing a new variable $u = r^2$ with differential $du = 2dr$, we obtain

$$I^2(\alpha) = \int_0^{2\pi}\int_0^{\infty} e^{-\alpha r^2} r\,dr\,d\theta \tag{5.113}$$

$$= 2\pi \int_0^{\infty} e^{-\alpha r^2} r\,dr \tag{5.114}$$

$$= \pi \int_0^{\infty} e^{-\alpha u} du \tag{5.115}$$

$$= -\lim_{\xi\to\infty} \frac{\pi}{\alpha} e^{-\alpha u}\Big|_0^{\xi} \tag{5.116}$$

$$= \frac{\pi}{\alpha} \tag{5.117}$$

where the limit as $\xi \to \infty$ converges when $\Re[\alpha] > 0$. The solution (5.117) holds for the Gaussian integral with an arbitrary complex offset

$$\int_{-\infty}^{\infty} e^{-\alpha(t+\beta)^2} dt = \sqrt{\frac{\pi}{\alpha}} \tag{5.118}$$

where $\alpha, \beta \in \mathbb{C}$ and $\Re[\alpha] > 0$. To prove the relation above, the integrand in (5.118) can be integrated anticlockwise along a closed rectangular contour $\xi(A)$ in a complex plane as depicted in Fig. 5.15. Without any loss of generality, we define $\beta = a + jb \in \mathbb{C}$ and $a, b \in \mathbb{R}$ with $A > |a|$. As the function $f : \mathbb{C} \mapsto \mathbb{C}$ defined as $f(z) = e^{-\alpha z^2} = e^{-\alpha(t+\beta)^2}$

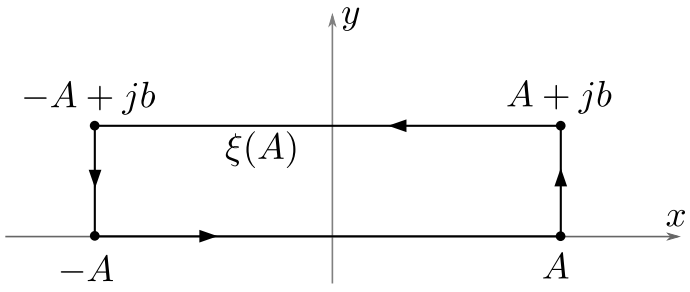

Figure 5.15: Integration path $\xi(A)$ of the Gaussian integral in the complex plane, where x is real axis and y is imaginary axis.

is analytic in $\mathbb{C}$, the Cauchy's theorem for integration along the closed curves applies as follows

$$\oint_{\xi(a)} e^{-\alpha z^2} dz = 0 \tag{5.119}$$

The integration along $\xi(A)$ in the complex plane (x, y) can be split into four contributions

$$\begin{aligned}\oint_{\xi(A)} e^{-\alpha z^2} dz = &\int_{-A}^{A} e^{-\alpha x^2} dx + \int_{0}^{b} e^{-\alpha(A+jy)^2} dy \\ &+ \int_{A}^{-A} e^{-\alpha(x+jb)^2} dx + \int_{b}^{0} e^{-\alpha(-A+jy)^2} dy\end{aligned} \tag{5.120}$$

In the limit as $A \to \infty$, the integrals along the imaginary axis converge to zero

$$\lim_{A\to\infty} \int_{0}^{b} e^{-\alpha(A+jy)^2} dy = 0 \tag{5.121}$$

$$\lim_{A\to\infty} \int_{b}^{0} e^{-\alpha(-A+jy)^2} dy = 0 \tag{5.122}$$

and due to (5.119), when $A \to \infty$, the following holds

$$\int_{-\infty}^{\infty} e^{-\alpha x^2} dx = \int_{-\infty}^{\infty} e^{-\alpha(x+jb)^2} dx \tag{5.123}$$

By taking into account (5.109), replacing $x = a + t$ and $dx = dt$ on the RHS, the proof of the Gaussian integral is concluded

$$\int_{-\infty}^{\infty} e^{-\alpha(t+a+jb)^2} dt = \int_{-\infty}^{\infty} e^{-\alpha(t+\beta)^2} dt = \sqrt{\frac{\pi}{\alpha}} \tag{5.124}$$

5.4.4 Numerical Simulations

Numerical simulations in this section give further insight into the isolation performance of Gaussian LFM waveforms. They are carried out in the same way and with the same parameters as in Section 5.2.5 to allow for a comparison between rectangular and Gaussian amplitude modulations. The frequency modulations of $s_i(t)$ and $s_j(t)$ are defined according to Figure 5.6 and bandwidth difference, as defined in the plots, is $\Delta B = B_j - |B_i|$.

Figure 5.16 shows the cross-correlation functions for different values of ΔB, when $f_{s,i} = f_{s,j} = 0\,\text{MHz}$, $f_D = 0\,\text{MHz}$, and $B_j = 50\,\text{MHz}$. It can be observed that increasing

ΔB decreases the peak maximums and therefore improves the isolation. The effect of changing the starting frequency $f_{s,i}$ is shown in Figure 5.17 when the bandwidth difference and starting frequency of the jth waveform are fixed to $\Delta B = 40\,\text{MHz}$ and $f_{s,j} = 0\,\text{MHz}$, respectively. Plots of the cross-correlation show that the peaks are not invariant to the frequency offset shifts, which is a result of Gaussian amplitude modulation.

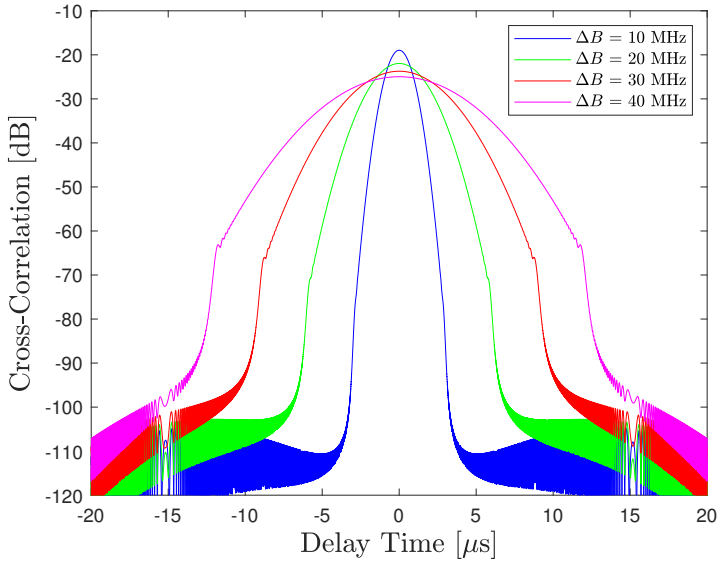

Figure 5.16: Cross-correlation functions of two Gaussian amplitude modulated up-chirps with parametrised bandwidth difference ΔB.

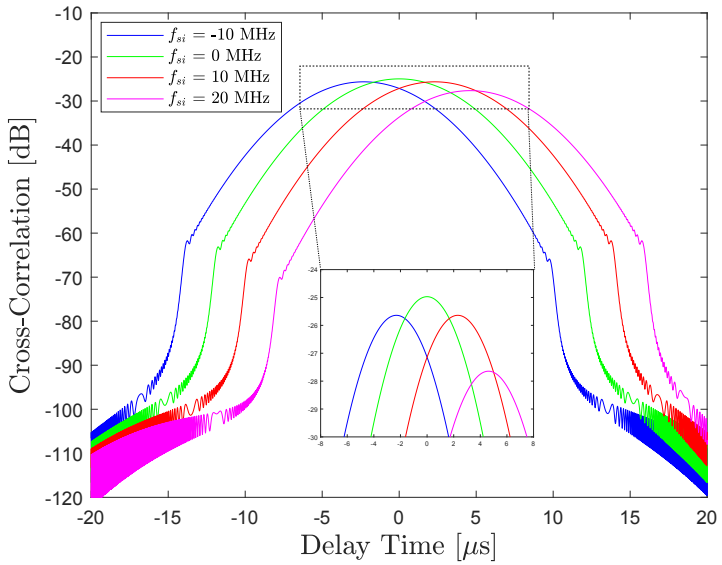

Figure 5.17: Cross-correlation functions of two Gaussian amplitude modulated up-chirps with parametrised starting frequency $f_{s,i}$.

The zoomed area in Figure 5.17 shows that the difference between $f_{s,i} = 0\,\text{MHz}$ and $f_{s,i} = 20\,\text{MHz}$ is around 2.6 dB. The maximum peak is achieved at the zero offset frequency when the frequency spectra of the waveforms are perfectly aligned. Introducing additional frequency shifts to one of the waveforms causes misalignment of the Gaussian shaped spectra, which reduces the energy at zero delay, hence the cross-correlation peak is lower in the time domain.

The comparison between rectangular and Gaussian LFM is shown in Figure 5.18, where combinations of two up-chirps and an up-chirp with down-chirp are shown. The results are shown for $B_j = 50\,\text{MHz}$ and $\Delta B = B_j - |B_i| = 25\,\text{MHz}$. It can be observed that both offer a comparable amount of isolation, although Gaussian LFM achieves 0.5 dB better isolation and better sidelobes roll-off. The advantage of combining LFM waveforms with opposite chirp rates can be noticed as a combination of up-chirp and down chirp with the same bandwidth allocation achieves a 4.7 dB improvement in isolation. The energy is in this case reallocated from the narrower peak in the case of an up-chirp combination to the lower peak with wider sidelobes of an opposite combination.

The comparison of numerical isolation results of the Gaussian and rectangular LFM chirps is given in Table 5.1. The results are obtained for a combination of an up-chirp and down-chirp with the same bandwidth for the BT-products listed in the table. It can be observed that such a modulation, as defined in Figure 5.4, produces isolation values above 30 dB when BT-product increases above 1000. The isolation improvement of Gaussian LFM over rectangular is consistent at approximately 1.5 dB.

Table 5.1: Simulated isolation for up-chirp and down-chirp signal pairs.

BT-Product	Isolation [dB]	
	Rectangular	Gaussian
10	10.45	11.97
100	20.45	21.96
200	23.46	24.97
500	27.44	28.95
1000	30.45	31.96
2000	33.46	34.97
5000	37.44	38.95

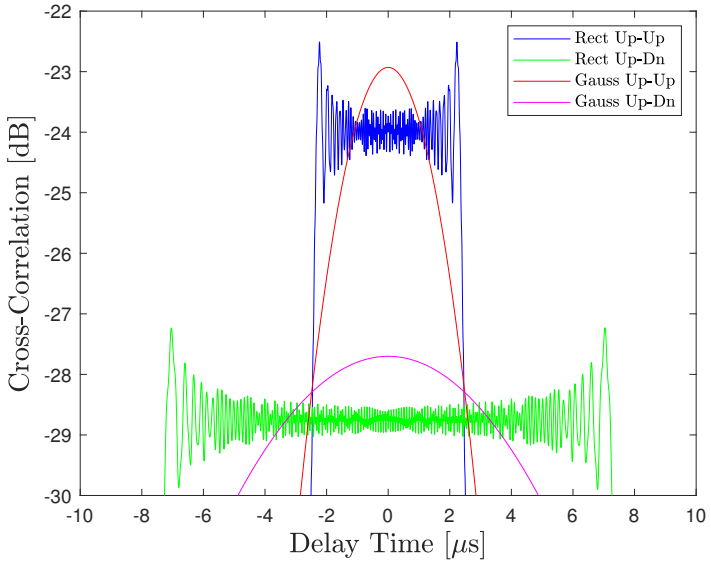

Figure 5.18: Comparison of cross-correlation functions of rectangular and Gaussian amplitude modulation for $B_j = 50\,\text{MHz}$ and $\Delta B = |B_j| - |B_i| = 25\,\text{MHz}$.

5.5 Time-Frequency Approach to Orthogonality

Time-frequency analysis has been an important topic of research when analysing signals in sensing applications related to astronomy [Chassande-Mottin and Flandrin, 1999], earthquakes, optical observations and radar monitoring [Bouchikhi et al., 2014]. It essentially gives an insight into how the energy of a particular signal is distributed jointly in the time and frequency domains. The usual approach in signal processing is to use spectrograms to investigate the properties of a signal in a joint time-frequency domain. But as will be shown, the spectrograms themselves are only one possible representation of a signal in the time-frequency domain [Cohen, 1989]. In this section, an investigation is conducted on how the isolation of signals can be interpreted from the time-frequency distribution point of view. With this in mind, a general theory that is required for the understanding will be given before it is applied to the chirp signals. More on the topic can be found in [Cohen, 1994, Chapter 6].

5.5.1 The Wigner-Ville Distribution and Its Properties

The Wigner-Ville (WVD) distribution was firstly used by Wigner in quantum mechanics and was then utilised for signal processing purposes by Ville [Ville, 1958], hence its long

name Wigner-Ville distribution. It is defined for signal $s(t)$ and its Fourier transform[3] $S(\omega)$ as

$$W_s(t,\omega) = \int_{-\infty}^{\infty} s^*\left(t-\frac{\tau}{2}\right) s\left(t+\frac{\tau}{2}\right) e^{-j\tau\omega} d\tau \tag{5.125}$$

$$= \frac{1}{2\pi}\int_{-\infty}^{\infty} S\left(\omega-\frac{\theta}{2}\right) S^*\left(\omega+\frac{\theta}{2}\right) e^{-jt\theta} d\theta \tag{5.126}$$

where both distributions derived from time or frequency domain are equivalent. It is evident that WVD defined as (5.125) can be viewed as a Fourier transform of $s^*\left(t-\frac{\tau}{2}\right) s\left(t+\frac{\tau}{2}\right)$ and as the signal appears twice in the expression, it belongs to a class of bilinear distributions [Cohen, 1994, Chapter 8]. To prove the equivalence of (5.126), the time domain signal $s(t)$ is expressed in frequency domain as

$$W_s(t,\omega) = \int_{-\infty}^{\infty} \left[\frac{1}{2\pi}\int_{-\infty}^{\infty} S(\omega_1) e^{-j\omega_1\frac{\tau}{2}} e^{j\omega_1 t} d\omega_1\right]^* \left[\frac{1}{2\pi}\int_{-\infty}^{\infty} S(\omega_2) e^{-j\omega_2\frac{\tau}{2}} e^{j\omega_2 t} d\omega_2\right] e^{-j\omega\tau} d\tau \tag{5.127}$$

$$= \frac{1}{2\pi}\int_{-\infty}^{\infty}\int_{-\infty}^{\infty} S^*(\omega_1) e^{-j\omega_1 t} S(\omega) e^{j\omega_2 t} 2\delta(\omega_2+\omega_1-2\omega) d\omega_1 d\omega_2 \tag{5.128}$$

$$= \frac{1}{\pi}\int_{-\infty}^{\infty}\int_{-\infty}^{\infty} S^*(\omega_1) e^{-j\omega_1 t} S(2\omega-\omega_1) e^{j(2\omega-\omega_1)t} d\omega_1 \tag{5.129}$$

$$= \frac{1}{2\pi}\int_{-\infty}^{\infty}\int_{-\infty}^{\infty} S^*\left(\omega+\frac{\omega_3}{2}\right) S\left(\omega-\frac{\omega_3}{2}\right) e^{-j\omega_3 t} \tag{5.130}$$

where in (5.128) the Dirac delta function[4] in integral form (A.27) was used with its sifting property (A.30) and the following scaling equality $\delta(\alpha t) = \frac{1}{|\alpha|}\delta(t)$. In (5.129), the new variable $\omega_3 = 2(\omega_1 - \omega)$ was introduced along with its differential $d\omega_3 = 2d\omega_1$ to obtain the equivalent expression in (5.130).

The most important properties of the distribution are explained below. Time-frequency description of a signal with WVD is highly non-local because at each time t the distribution depends equally on all possible delays τ and a similar observation holds for the frequency

[3]Note that the definitions of Wigner-Ville transform may vary and their final form depends on the definition of the Fourier transform. In mathematical texts it is sometimes normalised symmetrically.

[4]The Dirac delta function is referred to as a function, however it has to be understood as a generalised function or a measure. The reader is pointed to the relevant textbook for more details [Hoskins, 2009].

domain. Time and frequency marginals [Mecklenbräuker and Claasen, 1980] are satisfied

$$\frac{1}{2\pi}\int_{-\infty}^{\infty} W_s(t,\omega)d\omega = |s(t)|^2 \tag{5.131}$$

$$\int_{-\infty}^{\infty} W_s(t,\omega)dt = |S(\omega)|^2 \tag{5.132}$$

which give the information on instantaneous energy and energy density spectrum. WVD is not always positive and its negative values make it difficult to interpret as a physical energy density. The distribution is always real

$$W_s^*(t,\omega) = \int_{-\infty}^{\infty} s\left(t-\frac{\tau_1}{2}\right)s^*\left(t+\frac{\tau_1}{2}\right)e^{j\tau_1\omega}d\tau_1 \tag{5.133}$$

$$= -\int_{\infty}^{-\infty} s\left(t+\frac{\tau_2}{2}\right)s^*\left(t-\frac{\tau_2}{2}\right)e^{-j\tau_2\omega}d\tau_2 \tag{5.134}$$

$$= W_s(t,\omega) \tag{5.135}$$

where the new variable $\tau_2 = -\tau_1$ was introduced and integration limits were switched in (5.134). Time and frequency shifts can be determined for $g(t) = s(t-t_0)e^{j\omega_0 t}$ as

$$W_g(t,\omega) = \int_{-\infty}^{\infty} s^*\left(t-t_0-\frac{\tau}{2}\right)e^{-j\omega_0(t-\tau/2)}s\left(t-t_0+\frac{\tau}{2}\right)e^{j\omega_0(t+\tau/2)}e^{-j\omega\tau}d\tau \tag{5.136}$$

$$= \int_{-\infty}^{\infty} s^*\left(t-t_0-\frac{\tau}{2}\right)s\left(t-t_0+\frac{\tau}{2}\right)e^{-j(\omega-\omega_0)\tau}d\tau \tag{5.137}$$

$$= W_s(t-t_0,\omega-\omega_0) \tag{5.138}$$

and they appear as translations in the time frequency plane. The nonlinearity causes the cross terms to appear when transforming a sum of signals. For the signal defined as $s(t) = s_1(t) + s_2(t)$, the WVD can be expressed as

$$W_s(t,\omega) = W_{s_1}(t,\omega) + W_{s_1,s_2}(t,\omega) + W_{s_2,s_1}(t,\omega) + W_{s_2}(t,\omega) \tag{5.139}$$

where the cross terms are expressed as cross Wigner distributions

$$W_{s_1,s_2}(t,\omega) = \frac{1}{2\pi}\int_{-\infty}^{\infty} s_1^*\left(t-\frac{\tau}{2}\right)s_2\left(t+\frac{\tau}{2}\right)e^{-j\omega\tau}d\tau \tag{5.140}$$

which is not always real and because $W_{s_1,s_2}(t,\omega) = W_{s_2,s_1}^*(t,\omega)$, the distribution of the

sum (5.139) can be rewritten as

$$W_s(t,\omega) = W_{s_1}(t,\omega) + 2\Re\left[W_{s_1,s_2}(t,\omega)\right] + W_{s_2}(t,\omega) \tag{5.141}$$

which demonstrates a drawback of WVD as cross-terms appear when evaluating multi-component signals. Furthermore, cross terms are hard to interpret physically and different distributions need to be applied in such cases. The WVD of the cross-correlation function $R_{h,x}(t) = \int_{-\infty}^{\infty} h^*(\xi)x(t+\xi)d\xi$ can be written as

$$W_{R_{h,x}}(t,\omega) = \int_{-\infty}^{\infty} W_h(\xi,\omega)W_x(t+\xi,\omega)d\xi \tag{5.142}$$

and to prove the relation, the following is stated

$$W_{R_{h,x}}(t,\omega) = \int_{-\infty}^{\infty}\int_{-\infty}^{\infty} h(\xi_1)x^*(t-\frac{\tau}{2}+\xi_1)d\xi_1 \int_{-\infty}^{\infty} h^*(\xi_2)x(t+\frac{\tau}{2}+\xi_2)d\xi_2 e^{-j\omega\tau}d\tau \tag{5.143}$$

and new variables $\xi_1 = u + \frac{\eta}{2}$, $\xi_2 = u - \frac{\eta}{2}$ are introduced. To introduce the new variables, (5.143) is multiplied by the determinant of Jacobian (5.112), in this case $\det(\mathbf{J}) = -1$, to obtain

$$\begin{aligned} W_{R_{h,x}}(t,\omega) = \int_{-\infty}^{\infty}\int_{-\infty}^{\infty}\int_{-\infty}^{\infty} & h^*\left(u-\frac{\eta}{2}\right) h\left(u+\frac{\eta}{2}\right) \\ & \times x^*\left(t-\frac{\tau}{2}+u+\frac{\eta}{2}\right) x\left(t+\frac{\tau}{2}+u-\frac{\eta}{2}\right) e^{-j\omega t}dud\eta d\tau \end{aligned} \tag{5.144}$$

Equivalence in (5.142) is verified by the change of variables $\tau' = \tau - \eta$.

5.5.2 Representation of LFM Waveforms

In this section, the time frequency distributions of LFM waveforms are derived according to the WVD definition. The Cross-correlation rule (5.142) gives an important insight into how the localisation of energy in the time and frequency domains of a waveform $x(\xi)$ propagates through the filter $h(\xi)$. Clearly, the product of the WVD requires the energy coverage to be as low as possible for all the time delays t if a good isolation figure is sought. In the following sections the WVD distributions of an infinite and rectangular chirp signals

are derived. In the following subsections, frequency f is used instead of angular frequency, defined as $\omega = 2\pi f$.

Infinite LFM

The first example is an ideal LFM chirp signal of infinite duration and finite chirp rate. For a signal with starting frequency f_i and chirp rate μ_i it is defined as

$$s_i(t) = e^{j2\pi\left(f_i t + \frac{1}{2}\mu_i t^2\right)} \tag{5.145}$$

and its WVD can be found as

$$\begin{aligned} W_{s_i}(t,f) &= \int_{-\infty}^{\infty} e^{-j2\pi\left[f_i(t-\frac{\tau}{2})+\frac{1}{2}\mu_i(t-\frac{\tau}{2})^2\right]}\, e^{j2\pi\left[f_i(t+\frac{\tau}{2})+\frac{1}{2}\mu_i(t+\frac{\tau}{2})^2\right]}\, e^{-j2\pi f\tau} d\tau && (5.146)\\ &= \int_{-\infty}^{\infty} e^{j2\pi(f_i+\mu_i t-f)\tau} d\tau && (5.147)\\ &= 2\pi\delta\big(2\pi(f_i+\mu_i t-f)\big) && (5.148)\\ &= \delta(f-f_i-\mu_i t) && (5.149) \end{aligned}$$

The instantaneous frequency $f = f_i + \mu_i t$ is therefore perfectly localised and is defined with a delta function. As can be seen in Figure 5.19, the distribution forms an infinite ramp of delta functions wherever $\arg[\delta(x)] = 0$.

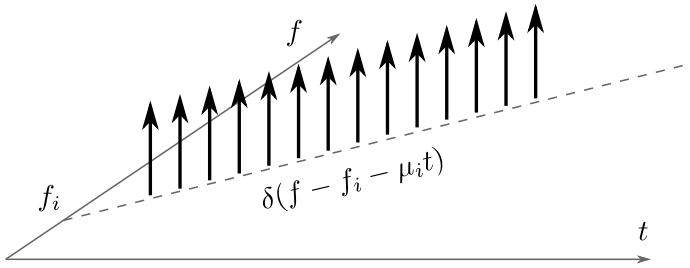

Figure 5.19: WVD of an infinite chirp with starting frequency f_i and slope μ_i.

The cross-correlation between two infinite chirps s_i and s_j in time-frequency space can now be determined. Different chirp rates $\mu_i \neq \mu_j$ are assumed, so that at least one intersection point exists in the joint domain. According to (5.142), the following can be

written for different time delays t'

$$W_{R_{i,j}}(t', f) = \int_{-\infty}^{\infty} W_{s_i}(\xi, \omega) W_{s_j}(t' + \xi, \omega) d\xi \tag{5.150}$$

$$= \int_{-\infty}^{\infty} \delta(f - f_i - \mu_i \xi)\ \delta(f - f_j - \mu_j(t' + \xi)) d\xi \tag{5.151}$$

$$= \int_{-\infty}^{\infty} \delta(f - f_i - \mu_i \xi) \frac{1}{\mu_j} \delta\left(\xi - \left(\frac{f - f_j}{\mu_j} - t'\right)\right) d\xi \tag{5.152}$$

$$= \frac{1}{\mu_j} \delta\left(f - f_i - \frac{\mu_i}{\mu_j}(f - f_j) + \mu_i t'\right) \tag{5.153}$$

To localise the energy in (5.153) for a fixed t', the argument is set to $\arg[\delta(x)] = 0$ and an expression for f is sought. Because the instantaneous frequency is localised exactly, the energy source is represented by a delta impulse function at the location (t', f_E), where $f_E = \frac{1}{\mu_j - \mu_i}(\mu_j f_i - \mu_i f_j - \mu_i \mu_j t)$. Fig. 5.20 depicts a specific case of cross-correlation for a fixed delay $t' = 0$.

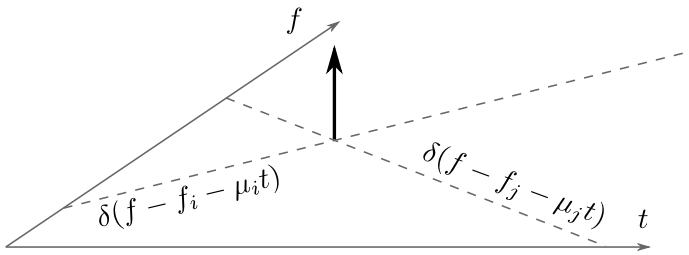

Figure 5.20: WVD of a cross-correlation function for a fixed time delay $t' = 0$ of two infinite chirp signals.

LFM of Finite Duration

The Wigner distribution can be applied to a chirp signal with finite duration. The signal in question is defined as

$$s_i(t) = \text{rect}\left(\frac{t}{T}\right)\ e^{j2\pi\left(f_i t + \frac{1}{2}\mu_i t^2\right)} \tag{5.154}$$

where

$$\text{rect}(t) = \begin{cases} 1, |t| \leq 1/2 \\ 0, \text{elsewhere} \end{cases} \tag{5.155}$$

Inserting (5.154) in (5.125) leads to the expression

$$W_{s_i}(t,f) = \int_{-\infty}^{\infty} \text{rect}\left(\frac{t-\tau/2}{T}\right) e^{-j2\pi\left[f_i(t-\frac{\tau}{2})+\frac{1}{2}\mu_i(t-\frac{\tau}{2})^2\right]} \times \text{rect}\left(\frac{t+\tau/2}{T}\right) e^{j2\pi\left[f_i(t+\frac{\tau}{2})+\frac{1}{2}\mu_i(t+\frac{\tau}{2})^2\right]} e^{-j2\pi f\tau} d\tau \quad (5.156)$$

where the product of the rectangular functions is nonzero for $t \geq 0$ when $-T+2t \leq \tau \leq T-2t$ and $2t \leq T$. The integration limits can therefore be rewritten as

$$W_{s_i}(t,f) = \int_{-T+2t}^{T-2t} e^{j2\pi(f_i-f+\mu_i t)\tau} d\tau \quad (5.157)$$

$$= \frac{1}{j2\pi(f_i-f+\mu_i t)} e^{j2\pi(f_i-f+\mu_i t)\tau}\Big|_{-T+2t}^{T-2t} \quad (5.158)$$

$$= \frac{1}{\pi(f-f_i-\mu_i t)} \sin\big(4\pi(f-f_i-\mu_i t)(T/2-t)\big) \quad (5.159)$$

For $t < 0$, the integral (5.156) is nonzero when the integration variable is $-T-2t \leq \tau \leq T+2t$ and $|2t| \leq T$. The final expression for WVD follows as

$$W_{s_i}(t,f) = \begin{cases} \frac{\sin\left(4\pi(f-f_i-\mu_i t)(T/2-|t|)\right)}{\pi(f-f_i-\mu_i t)}, |t| \leq T/2 \\ 0, \text{elsewhere} \end{cases} \quad (5.160)$$

Figure 5.21 depicts WVD of a rectangular up-chirp signal with $T = 5\,\mu\text{s}$ and $B = 5\,\text{MHz}$. It can be seen that limiting time duration of a chirp signal reduces the localisation accuracy of the WVD and introduces negative values in the distribution.

To demonstrate energy localisation in the process of matched filtering, which is equivalent to the cross correlation, WVD expressions of an up-chirp and down-chirp can be inserted in the cross-correlation expression. Suppose that the energy distribution is sought when received signal and filter are in time alignment $t = 0$. It follows from (5.160) and (5.142) that

$$W_E(\xi,f) = W_{s_i}(\xi,f) W_{s_j}(\xi+t,f)\big|_{t-0} \quad (5.161)$$

$$= \frac{\sin\left(4\pi(f-\mu\xi)(T/2-|\xi|)\right)\sin\left(4\pi(f+\mu\xi)(T/2-|\xi|)\right)}{\pi^2(f-\mu\xi)(f+\mu\xi)} \quad (5.162)$$

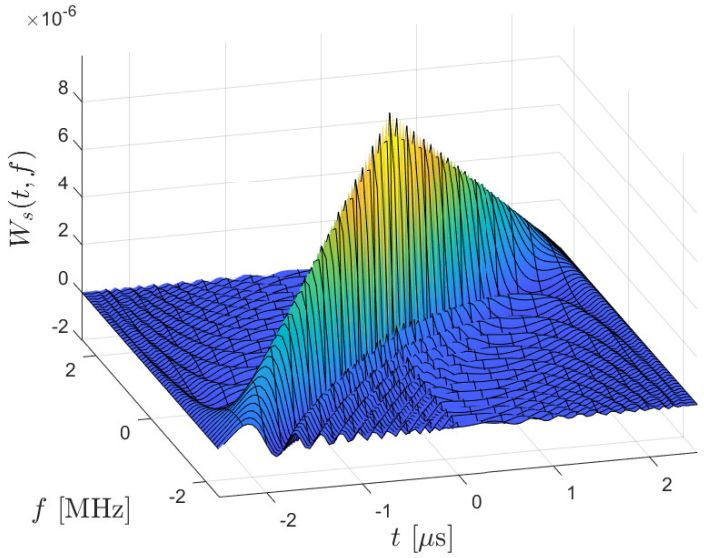

Figure 5.21: WVD of an up-chirp signal with finite rectangular envelope of $T = 5\,\mu s$ and bandwidth of $B = 5\,\text{MHz}$.

which can be rewritten as

$$W_E(\xi, f) = \frac{\sin\left(8\pi\mu\xi(T/2 - |\xi|)\right)}{2\pi^2(\mu^2\xi^2 - f^2)} + \frac{\cos\left(8\pi f(T/2 - |\xi|)\right)}{2\pi^2(\mu^2\xi^2 - f^2)} \tag{5.163}$$

where it was assumed that $\mu = \mu_i = -\mu_i$, $f_i = f_j = 0$ and $|\xi| \leq T/2$. The time-frequency energy distribution $W_E(\xi, f)$ is shown in Figure 5.22, which shows that the energy leakage is sourced from the intersection of time-frequency modulations of the up-chirp and down-chirp, as given with Figure 5.4. The WVD satisfies time and frequency marginals, defined with (5.131) and (5.132), therefore Figure 5.22 accurately presents the localisation of energy in time or frequency domain individually. In this particular case, the energy is concentrated at $f = 0\,\text{MHz}$ and $\xi = 0\,\mu s$.

Gaussian LFM

A similar approach can be undertaken to derive a WVD of an infinite Gaussian AM signal [Cohen, 1994]. To obtain the time-frequency distribution, (5.86) is replaced in (5.125) to

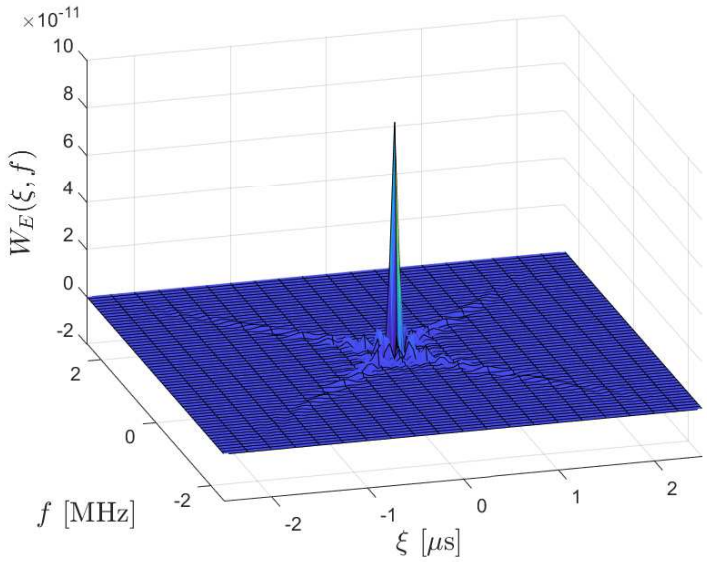

Figure 5.22: Product of an up-chirp WVD and a down-chirp WVD, which shows the energy distribution for a cross-correlation WVD for the time delay $t = 0\,\mu s$.

obtain

$$W_s(t,f) = \frac{1}{\sqrt{\pi}\lambda}\int_{-\infty}^{\infty} e^{-\frac{(t-\tau/2)^2}{2\lambda^2} - j(a(t-\frac{\tau}{2})+b(t-\frac{\tau}{2})^2)} e^{-\frac{(t+\tau/2)^2}{2\lambda^2} - j(a(t+\frac{\tau}{2})+b(t+\frac{\tau}{2})^2)} e^{-j2\pi f\tau} d\tau \tag{5.164}$$

where $\omega = 2\pi f$ and further to

$$W_s(t,f) = \frac{1}{\sqrt{\pi}\lambda} e^{-\frac{t^2}{\lambda^2}} e^{-\lambda^2(a+2tb-2\pi f)^2} \int_{-\infty}^{\infty} e^{-\frac{1}{4\lambda^2}(\tau - 2\lambda^2 j(a+2tb-2\pi f))^2} d\tau \tag{5.165}$$

which is a Gaussian integral and it can be solved as demonstrated in Section 5.4.3 to obtain the final result

$$W_s(t,f) = 2e^{-t^2/\lambda^2} e^{-\lambda^2(a+2tb-2\pi f)^2} \tag{5.166}$$

which is always positive and is therefore physically interpretable. For larger values of λ the energy is being concentrated along the LFM as $f = (a+2tb)/(2\pi)$. The energy localisation property is demonstrated by Figure 5.23, which depicts a Gaussian signal with parameters $T = 5\,\mu s$ and $B = 5\,\text{MHz}$.

The time-frequency distribution of energy for cross-correlation between an up-chirp and a down chirp can now be obtained. According to (5.142) and (5.166), with both

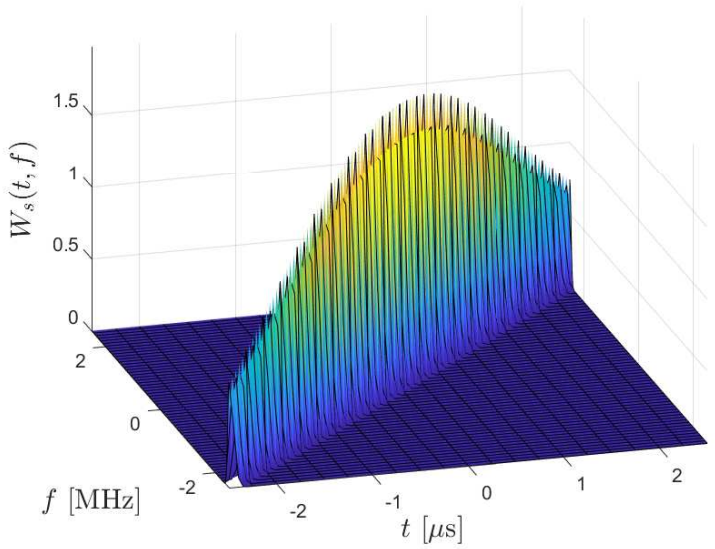

Figure 5.23: WVD of an up-chirp signal with infinite Gaussian envelope and parameters fixed to $T = 5\,\mu\text{s}$ and $B = 5\,\text{MHz}$.

signals perfectly aligned, i.e. $t = 0$, the energy distribution follows from (5.161) as

$$W_E(\xi, f) = 4e^{-2\xi^2/\lambda^2} e^{-8\lambda^2(\xi^2 b^2 + \pi^2 f^2)} \tag{5.167}$$

where ξ is a substitution of the time variable and with $a = 0$ no offset frequency is present. The plot of (5.167) is shown in Figure 5.24 which demonstrates the localisation of energy where up-chirp and down-chirp modulations intersect in the time-frequency domain, which is when $xi = 0$ and $f = 0$. Distribution positivity and correctness of marginals make (5.167), together with the corresponding figure, a valid description of energy source.

The WVD of a cross-correlation function between a Gaussian up-chirp and a Gaussian down-chirp is analytically tractable. By considering signals of the same length, $\lambda = \lambda_i = \lambda_j$, of the same bandwidth but opposite chirp rate, $b = b_i = -b_j$, and no offset frequency, $a_i = a_j = 0$, the derivation is as follows. Inserting the WVD of a Gaussian chirp (5.166) in (5.142), one obtains

$$W_{R_{i,j}}(t, f) = 4e^{-t^2/\lambda^2 - 4\lambda^2(2\pi^2 f^2 + t^2 b^2 + 2tb\pi f)} \int_{-\infty}^{\infty} e^{-(\xi^2 + \xi t)(2/\lambda^2 + 8\lambda^2 b^2)} d\xi \tag{5.168}$$

which is a Gaussian integral that converges when $\Re[2/\lambda^2 + 8\lambda^2 b^2] > 0$, as explained in

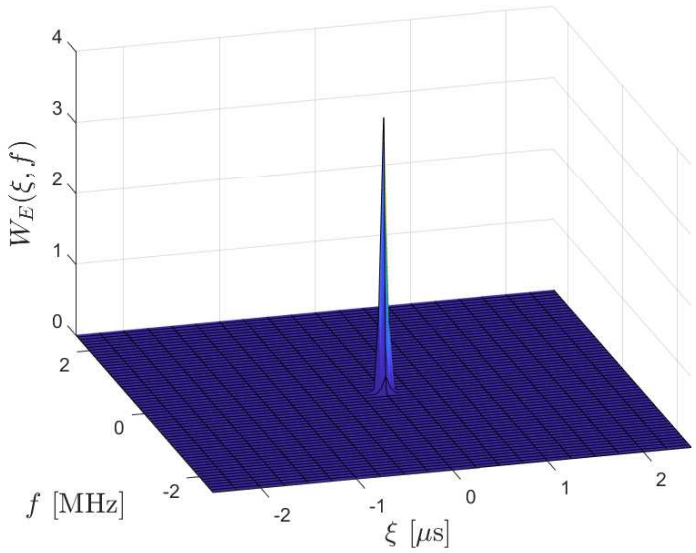

Figure 5.24: WVD of an up-chirp signal with infinite Gaussian envelope and parameters fixed to $T = 5\,\mu\text{s}$ and $B = 5\,\text{MHz}$.

Section 5.4.3. The final expression of WVD is therefore

$$W_{R_{i,j}}(t,f) = \sqrt{\frac{8\pi}{1/\lambda^2 + 4\lambda^2 b^2}} e^{-\frac{t^2}{2\lambda^2} - \lambda^2(8\pi^2 f^2 + 2t^2 b^2 + 8tb\pi f)} \tag{5.169}$$

which is a newly obtained result. For a fixed and arbitrary time delay t_0 between $s_i(t)$ and $s_j(t)$, the energy is localised in the frequency domain, following a Gaussian-like distribution. The WVD is in this case proportional to

$$W_{R_{i,j}}(t,f)\Big|_{t=t_0} \propto \exp\left(-8\lambda^2\pi^2\left(f + \frac{t_0 b}{2\pi}\right)^2\right) \tag{5.170}$$

5.5.3 Generalisation of Time-Frequency Distributions

It was demonstrated that a general expression to define time-frequency distributions can be obtained [Cohen, 1994]. All time-frequency representations can be derived from the general class, defined as

$$G_s(t,\omega) = \frac{1}{4\pi^2}\int_{-\infty}^{\infty}\int_{-\infty}^{\infty}\int_{-\infty}^{\infty} s^*(u - \frac{1}{2}\tau)s(u + \frac{1}{2}\tau)\Phi(\theta,\tau) \times e^{-j\theta t - j\tau\omega + j\theta u} du d\tau d\theta \tag{5.171}$$

where the function $\Phi(\theta, \tau)$ is called the kernel of transformation and defines the properties of the transformation. For the WVD, the kernel function is $\Phi(\theta, \tau) = 1$, which can be proved to lead to the transformation given by (5.125). To obtain the spectrogram, another common time-frequency distribution of the signal energy, one has to set the kernel to

$$\Phi(\theta, \tau) = \int_{-\infty}^{\infty} w^*(u - \frac{1}{2}\tau) w(u + \frac{1}{2}\tau) e^{-j\theta u} du \tag{5.172}$$

with $w(u)$ being the windowing function. The spectrogram distribution is

$$P_s(t, \omega) = |S_s(t, \omega)|^2 = \left| \int_{-\infty}^{\infty} w(\tau - t) s(\tau) e^{-j\omega\tau} d\tau \right|^2 \tag{5.173}$$

where the relation with the short-time Fourier transform (STFT), denoted as $S_s(t, \omega)$, is evident.

If the total energy of a distribution is to be preserved, the kernel must, in general, satisfy $\Phi(0, 0) = 1$. To obtain a real-valued distribution, the following must hold: $\Phi(\theta, \tau) = \Phi^*(-\theta, -\tau)$.

5.6 Summary

In this section, frequency modulated waveforms that are suitable for an MBR were discussed. Firstly, the rectangular LFM waveforms were presented and their properties demonstrated. In particular, the range-Doppler coupling was discussed and the isolation derivation of a combination of an up-chirp and a down-chirp with the same bandwidth was presented. The isolation theory of the LFM signals was then extended to account for the waveforms with arbitrary chirp rates, which demonstrated chirp rate diversity to obtain quasi-orthogonal sets of waveforms. Additionally, an analytical bound on isolation of the rectangular LFM waveforms was shown. The isolation derivations and the cross-correlation bound are novel contributions to the radar field.

The derivations were supported by numerical simulations and derivations of Fresnel integral approximations. Gaussian amplitude LFM were presented as another suitable candidate for waveforms intended for an MBR. In this case, constant amplitude cannot be maintained but the main motivation behind Gaussian AM is the ability to derive isolation

expressions in closed form, another novelty introduced in this work.

Lastly, Wigner-Ville distribution was utilised to examine the time-frequency distributions of LFM waveforms. The approach enabled the proof of the assumption that the interference energy resulting from cross-correlation operation comes from intersections of frequency modulations in time domain.

Chapter 6

Experimental Work

6.1 Introduction

The experimental work that validates the theoretical and simulation results is presented in this chapter. Rectangular chirp suppression results are given in Section 6.2.1 and corroborate the simulation results and theory introduced in Section 5.2. The experiments are thereafter extended to include multiple simultaneous waveforms, primarily to determine inter-channel interference, as demonstrated in Section 6.2.2. The effects of Doppler shifts are investigated in Sections 6.3.3 and 6.3.1, where a rotating and a moving target were used to produce range-Doppler maps and determine waveform isolation properties for specific parameter selections.

6.2 Static Waveform Isolation

This section relates to the experimental work that was conducted to determine waveform isolation properties without the Doppler shift effect. The results of measurements presented below were reported in [Kocjancic et al., 2017, Kocjancic et al., 2018, Kocjancic et al., 2019a].

6.2.1 Suppression of a Rectangular Chirp

The measurement setup consisted of a universal software radio peripheral (USRP) device and two horn antennas, as is depicted in Figure 6.1a. A National Instruments USRP-

2943 was connected to two Narda type 642 antennas, whereby one was connected to the transmitting channel and the second one was connected to the receiving channel. The distance between the antennas, $d = 4.0\,\mathrm{m}$, and the bigger cross section of the antennas, $D = 12\,\mathrm{cm}$, comply with the far field criterion, stating that $d > 2D^2/\lambda$. The carrier frequency was $f_c = 6.0\,\mathrm{GHz}$, while the sampling frequency of the software defined radio was $f_s = 125\,\mathrm{MHz}$.

The parameters of the waveforms used were chosen so that the simulated results given in Section 5.2.5 can be compared to the measurements. The same modulation scheme as given with Figure 5.6 was adopted, where the digital waveform $s_j[n]$ was stored in the receiver and used as a correlating suppression filter and a waveform $s_i[n]$ was transmitted and received via direct microwave link. The isolation was determined according to (4.61) where the cross-correlation was given in the discrete form as

$$R_{i,j}[m] = \begin{cases} \sum_{n=0}^{N-m-1} s_i[n+m]s_j^*[n], \ m \geq 0 \\ R_{j,i}^*[-m], \ m < 0 \end{cases} \tag{6.1}$$

The peak of the autocorrelation function of $s_j[n]$ was determined as a cross-correlation between a digital replica of the waveform and its transmitted version, which was found to be around 0.2 dB lower than the ideal autocorrelation peak of the digital signal. The cross-correlation functions discussed hereafter are normalised to the autocorrelation peak and can be seen as inverted isolation functions $I_{i,j}^{-1}(\tau)$.

The measurements were carried out for two pulse lengths $T = 10\,\mu\mathrm{s}$ and $T = 20\,\mu\mathrm{s}$. The jth waveform was an up-chirp with fixed bandwidth $B_j = 50\,\mathrm{MHz}$ while the bandwidth of the ith waveform was varying with $\Delta B = |B_j| - |B_i|$. Figure 6.3a depicts the cross-correlation value between the ith and jth up-chirp signals. Note that Figure 6.3a corresponds to the Figure 5.8 obtained by simulations and the measurements corroborate the results, as can be determined from the Table 6.1. As discussed previously, increasing the pulse width increases the BT-product of the waveform and therefore improves the isolation between the corresponding signals. This relation can be observed by comparing the isolation values in Table 6.1 and by directly comparing Figures 6.3a and 6.3b. Significant improvements are made by combining chirp signals with opposite slopes. Another

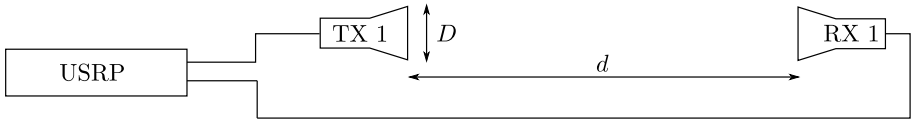

(a) One transmitting channel.

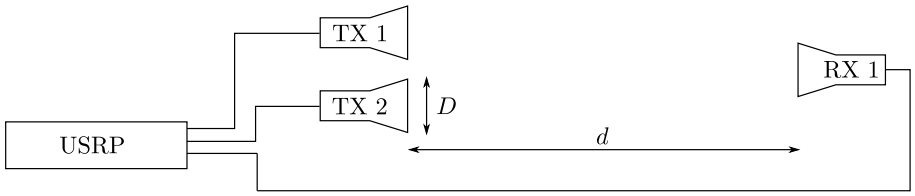

(b) Two transmitting channels.

Figure 6.1: Experimental setup for isolation measurements consisting of a USRP-2943 and horn antennas Narda 642. The largest dimension of antenna aperture is defined as D and the distance between antennas as d.

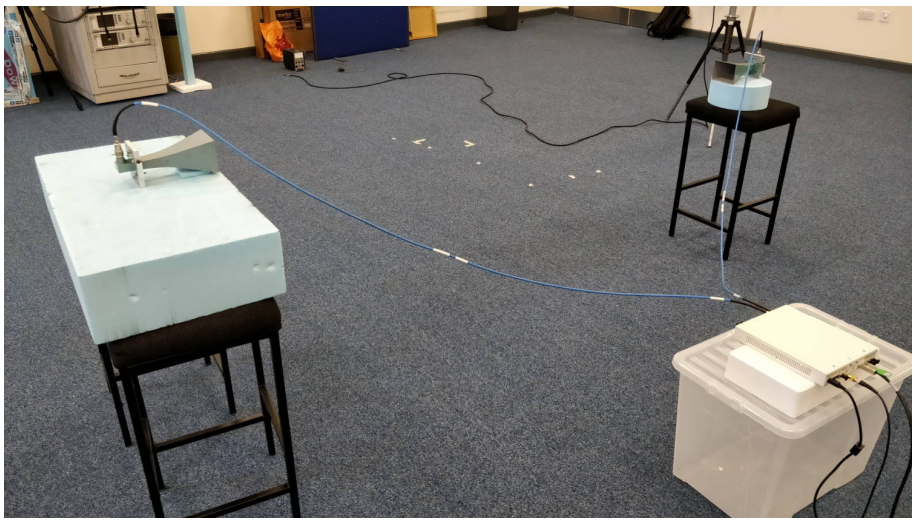

Figure 6.2: Photo of the experimental RF link for stationary channel isolation measurements.

set of measurements was performed where the ith signal was a down-chirp and the results obtained are shown in Figure 6.4. It can be determined that the isolation is in this case increasing with the decreasing bandwidth difference ΔB, as opposed to the case with a combination of up-chirps, where it was decreasing. This is due to the fact that the effective bandwidth difference $\Delta B = B_j - B_i$, as used in isolation equations, is increasing by further decreasing negative B_i. The effects of T and ΔB on isolation are demonstrated in Table 6.1, where measurements are compared with the simulated values, given in brackets.

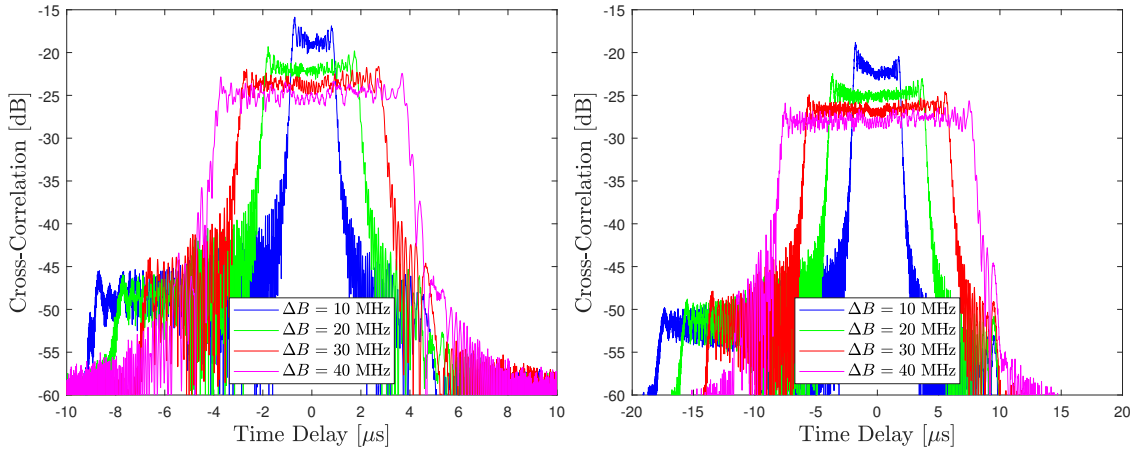

(a) $T = 10\,\mu s$ (b) $T = 20\,\mu s$

Figure 6.3: Measured cross-correlation responses of an up-chirp with $B_j = 50\,\text{MHz}$ and a secondary up-chirp with the bandwidth difference ΔB, while both waveforms having the same duration, for (a) $T = 10\,\mu s$ and for (b) $T = 20\,\mu s$.

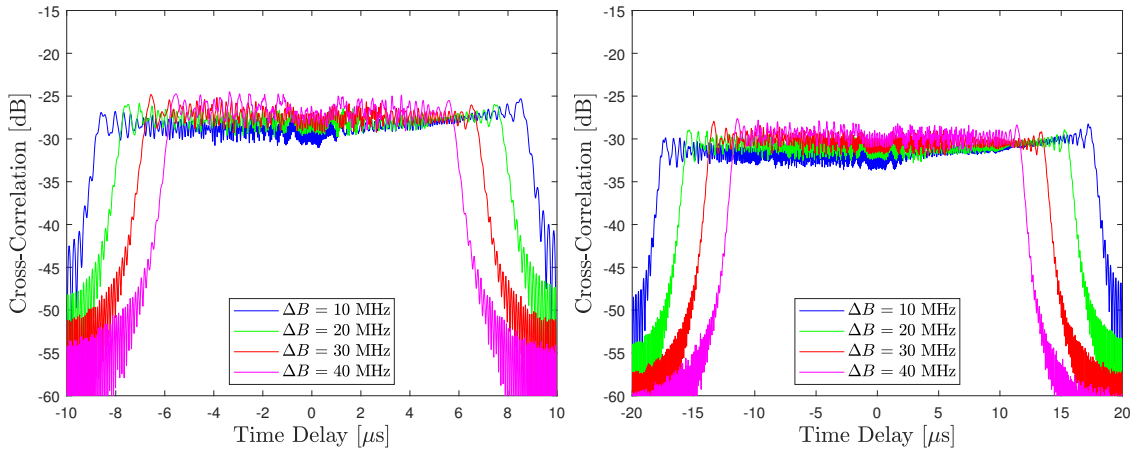

(a) $T = 10\,\mu s$ (b) $T = 20\,\mu s$

Figure 6.4: Measured cross-correlation responses of an up-chirp with $B_j = 50\,\text{MHz}$ and a secondary down-chirp with the bandwidth difference ΔB, while both waveforms having the same duration, for (a) $T = 10\,\mu s$ and for (b) $T = 20\,\mu s$.

6.2.2 Suppression of Superimposed Waveforms

This section presents another set of measurements to exploit the behaviour of multiple waveforms when they are transmitted simultaneously. The data was obtained using the experimental setup presented in Section 6.2.1 to which an additional transmitting antenna was added, as depicted in Figure 6.1b. The sampling frequency was retained as $f_s = 125\,\text{MHz}$ and the carrier frequency as $6.0\,\text{GHz}$. Two waveforms $s_i[n]$ and $s_j[n]$ were transmitted simultaneously by different antennas and the received signal was match

Table 6.1: Measured and simulated isolation values for the rectangular LFM waveforms. Simulated values are given in brackets.

T [μs]	LFM	Isolation [dB]			
		$\Delta B =$ 10 MHz	$\Delta B =$ 20 MHz	$\Delta B =$ 30 MHz	$\Delta B =$ 40 MHz
10	Up-Up	16.90 (18.52)	20.32 (21.55)	22.65 (23.32)	23.46 (24.66)
10	Up-Dn	26.32 (28.14)	26.86 (27.56)	25.86 (26.94)	25.67 (26.51)
20	Up-Up	19.85 (21.55)	23.59 (24.60)	25.63 (26.35)	26.67 (27.61)
20	Up-Dn	29.31 (30.99)	29.82 (30.54)	29.11 (30.08)	28.47 (29.35)

filtered with a copy of the signal $s_j[n]$. The bandwidth of the jth signal was fixed to $B_j = 50\,\text{MHz}$, while the bandwidth of the ith signal was varying so that $\Delta B = |B_j| - |B_i|$ reached 10 MHz, 20 MHz, 30 MHz, and 40 MHz. Note that the measurement parameters were set, so that the starting frequencies of all waveforms were zero. Starting frequency shifts were therefore set to $f_{s,i} = B_i/2$ and $f_{s,j} = B_j/2$, corresponding to the modulation diagram in Figure 5.6.

Figure 6.5 depicts the first set of measurements with the ith and jth signals being both up-chirps. The time duration of the waveforms is fixed to $T = 10\,\mu\text{s}$, which results in ΔBT ranging from 100 to 500. The isolation increases with the bandwidth difference and spans from 13.72 dB to 19.74 dB. As expected, replacing the ith waveform with a down-chirp results in an isolation improvement, as discussed in Section 5.2.4. The measurements obtained with a combination of an up-chirp and a down-chirp are shown in Figure 6.6a. In this case the isolation does not vary significantly and it retains values between 22.16 dB and 22.68 dB. The isolation levels are marked with a dashed line in the plots and show the separation between the matched filter response of the jth waveform and suppression of the adjacent ith waveform. All the isolation results, including those with $T = 20\,\mu\text{s}$, are given in Table 6.2. It can be observed that the pulse length increase does not necessarily improve the isolation, which stems from the fact that the main peak sidelobes are interacting with a suppressed cross-correlation function. In general, when this occurs constructively an increase of amplitude follows, generating a possible false target and effectively reducing

the isolation. To thoroughly test the aforementioned phenomenon, a statistically averaged test over many runs and for different time delays between waveforms $s_i[t]$ and $s_j[t]$ should be evaluated. Note that the measurements presented herein are synchronised in time as the waveforms are transmitted simultaneously.

Figure 6.7 shows the effect of the starting frequency on the isolation. The starting frequency shift $f_{s,i} = 10\,\text{MHz}$ is applied to the ith waveform. The isolation performance shown in Figure 6.7a is directly comparable to Figure 6.5b and Figure 6.7b to Figure 6.5d. It follows from the comparison of the measurements that the isolation difference is minimal and is within 1.5 dB.

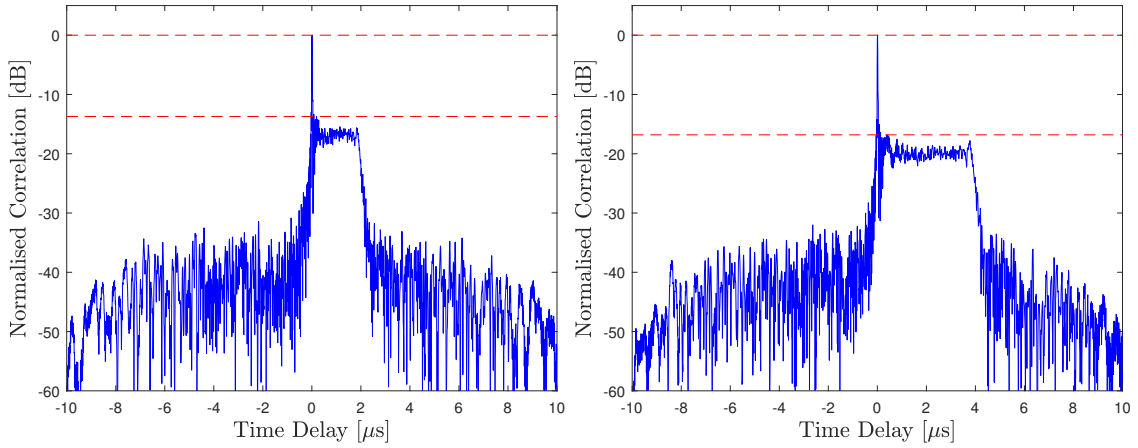

(a) Up-Up: $\Delta B = 10\,\text{MHz}$, $I_{i,j} = 13.72\,\text{dB}$ (b) Up-Up: $\Delta B = 20\,\text{MHz}$, $I_{i,j} = 16.81\,\text{dB}$

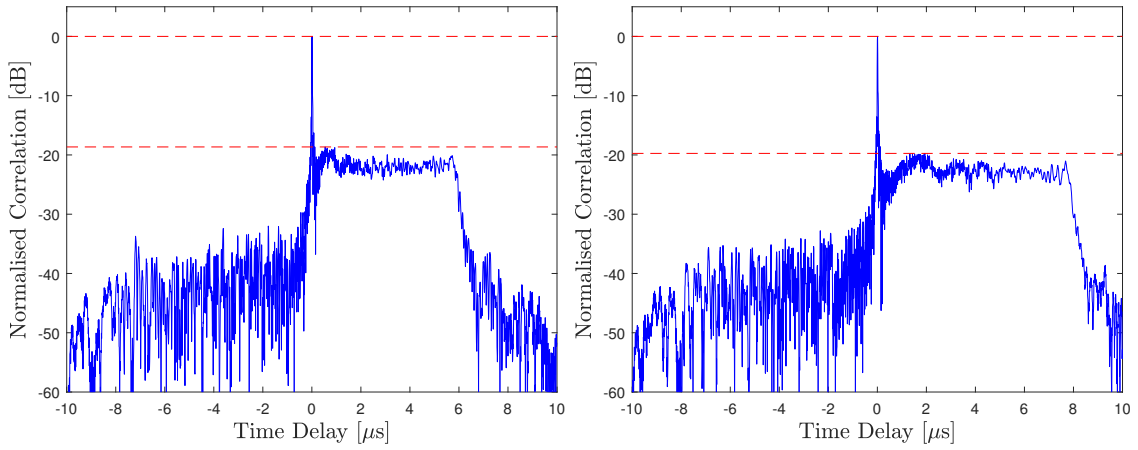

(c) Up-Up: $\Delta B = 30\,\text{MHz}$, $I_{i,j} = 18.65\,\text{dB}$ (d) Up-Up: $\Delta B = 40\,\text{MHz}$, $I_{i,j} = 19.74\,\text{dB}$

Figure 6.5: Measured matched filter responses of an up-chirp with $B_j = 50\,\text{MHz}$ and an up-chirp of varying B_i, when transmitted simultaneously.

The last set of experiments in this section was devised to test suppression of two waveforms $s_i[n]$ and $s_j[n]$ simultaneously by a third waveform $s_k[n]$, which was used as a digital

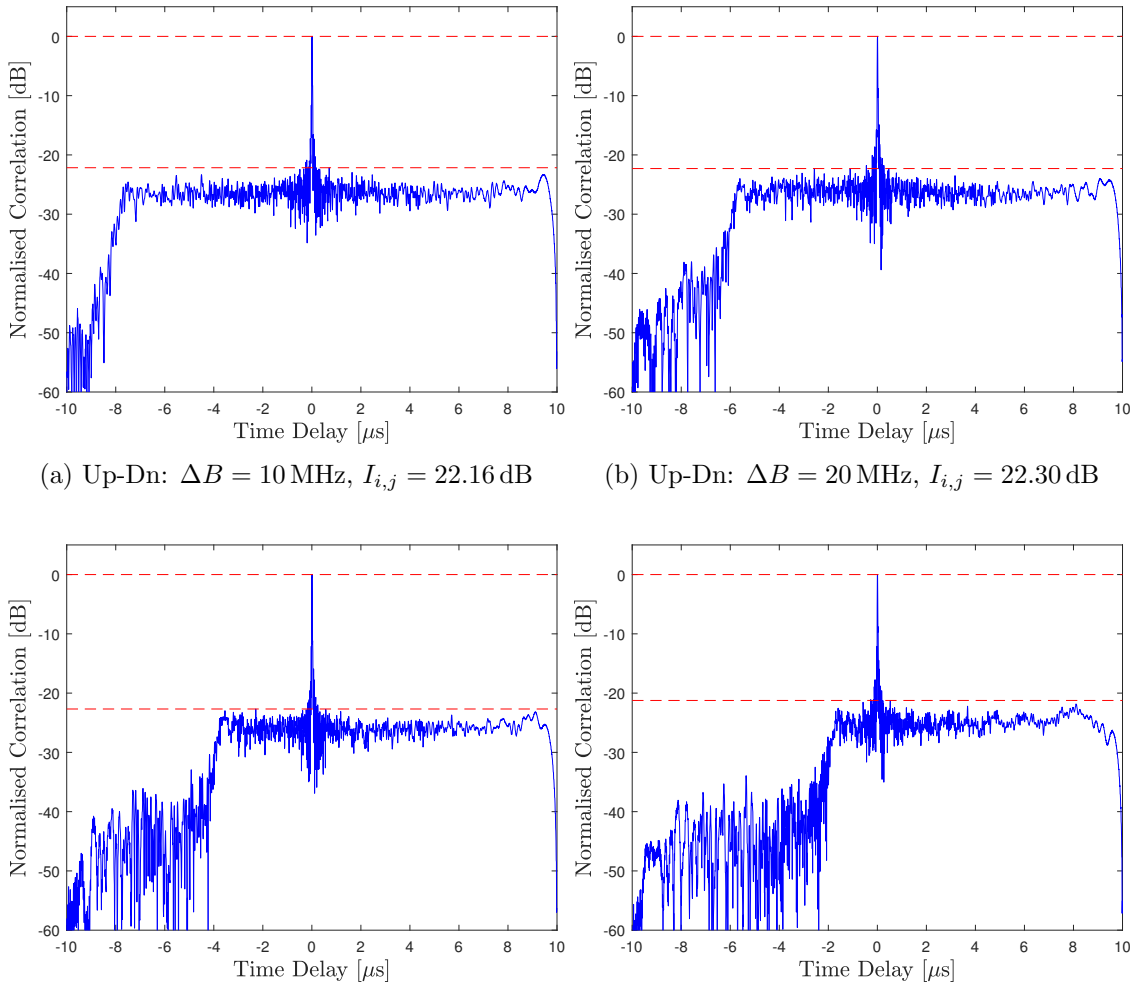

(a) Up-Dn: $\Delta B = 10\,\text{MHz}$, $I_{i,j} = 22.16\,\text{dB}$

(b) Up-Dn: $\Delta B = 20\,\text{MHz}$, $I_{i,j} = 22.30\,\text{dB}$

(c) Up-Dn: $\Delta B = 30\,\text{MHz}$, $I_{i,j} = 22.68\,\text{dB}$

(d) Up-Dn: $\Delta B = 40\,\text{MHz}$, $I_{i,j} = 22.24\,\text{dB}$

Figure 6.6: Measured matched filter responses of an up-chirp with $B_j = 50\,\text{MHz}$ and a down-chirp of varying B_i, when transmitted simultaneously.

correlator at the receiver. The sampling rate and the carrier frequency were the same as in previously described experiments. The ith waveform had a variable bandwidth ΔB, as defined in Table 6.3, and was transmitted as an up-chirp and a down-chirp. The jth

Table 6.2: Measured isolation properties of two rectangular waveforms when transmitted simultaneously.

T [μs]	LFM	Isolation [dB]			
		$\Delta B =$ 10 MHz	$\Delta B =$ 20 MHz	$\Delta B =$ 30 MHz	$\Delta B =$ 40 MHz
10	Up-Up	13.72	16.81	18.65	19.74
10	Up-Dn	22.16	22.30	22.68	21.24
20	Up-Up	13.64	19.04	18.71	22.23
20	Up-Dn	25.60	22.22	21.65	22.77

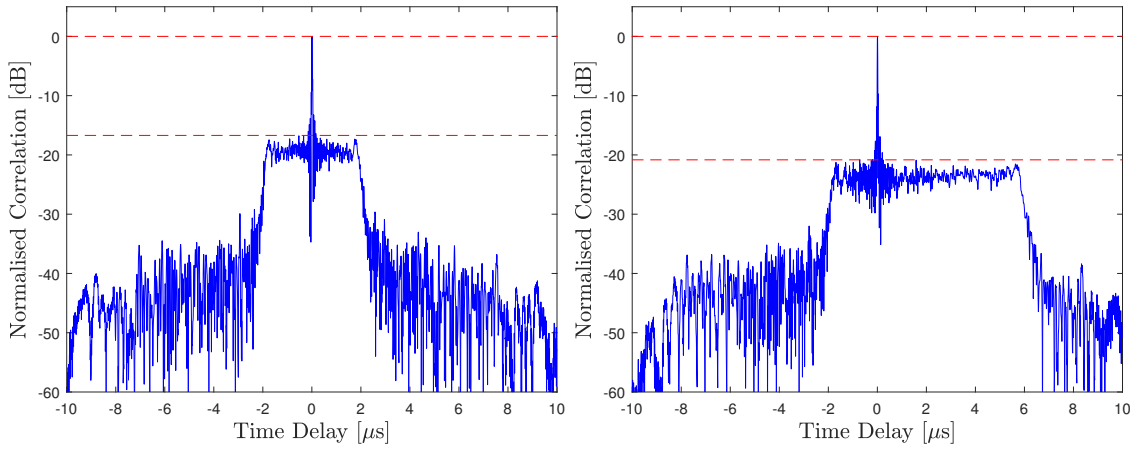

(a) Up-Up: $\Delta B = 20\,\text{MHz}$, $I_{i,j} = 16.71\,\text{dB}$ (b) Up-Up: $\Delta B = 40\,\text{MHz}$, $I_{i,j} = 20.83\,\text{dB}$

Figure 6.7: Matched filter responses of an up-chirp with $B_j = 50\,\text{MHz}$ and an up-chirp of varying B_i and starting frequency $f_{s,i} = 10\,\text{MHz}$, when transmitted simultaneously.

waveform was an up-chirp with constant bandwidth $B_j = 50\,\text{MHz}$, which was simultaneously transmitted with the ith waveform. The kth waveform was digitally implemented as a down-chirp with a bandwidth of $B_k = -50\,\text{MHz}$ and was used to digitally correlate the received sum of ith and jth signal. The isolation results for different ΔB and two values of pulse lengths are shown in Table 6.3 and Figure 6.8. It can be deduced that the superposition of two up-chirp waveforms is better suppressed by the down-chirp correlating waveform, which is shown in Figures 6.8a, 6.8b, and 6.8c. The case when the jth signal is an up-chirp and the ith signal a down-chirp is depicted in Figures 6.8d, 6.8e, and 6.8f, which showes lower figures of isolation, especially when the bandwidth difference $\Delta B = |B_j| - |B_i|$ is smaller. The discrete isolation $I_{i,j,k}[m]$, as used in the evaluation, is defined as

$$I_{i,j,k}[m] = \left| \frac{R_{k,k}[0]}{R_{i,k}[m] + R_{j,k}[m]} \right| \tag{6.2}$$

Table 6.3: Measured isolation properties of two simultaneously transmitted rectangular waveforms when suppressed by a third waveform.

T [μs]	LFM	Isolation [dB]			
		$\Delta B =$ 10 MHz	$\Delta B =$ 20 MHz	$\Delta B =$ 30 MHz	$\Delta B =$ 40 MHz
10	Up-Up	19.00	18.78	18.36	18.74
10	Up-Dn	13.90	16.60	17.35	18.00
20	Up-Up	22.02	21.73	21.88	21.99
20	Up-Dn	16.94	18.62	20.29	21.02

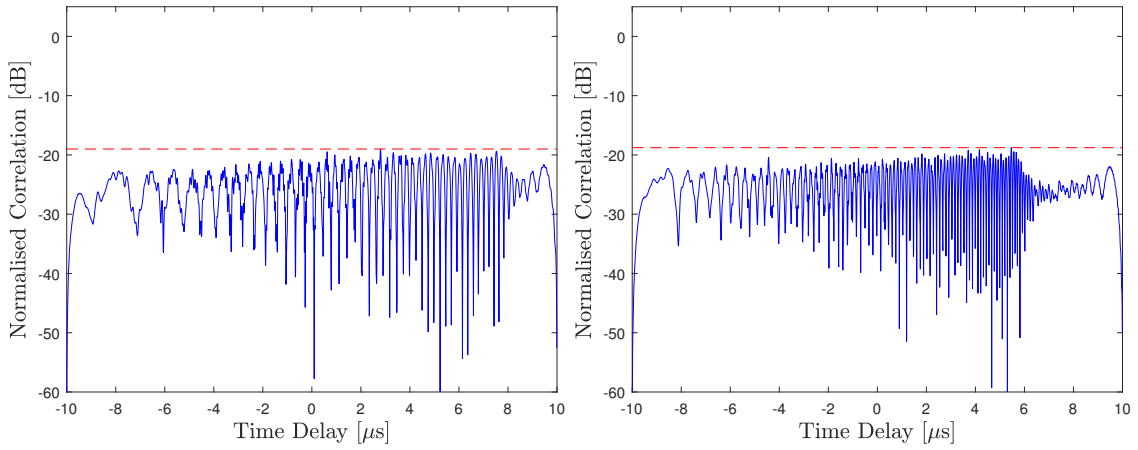

(a) Up-Up: $\Delta B = 10\,\text{MHz}$, $I_{i,j,k} = 19.00\,\text{dB}$ (b) Up-Up: $\Delta B = 20\,\text{MHz}$, $I_{i,j,k} = 18.78\,\text{dB}$

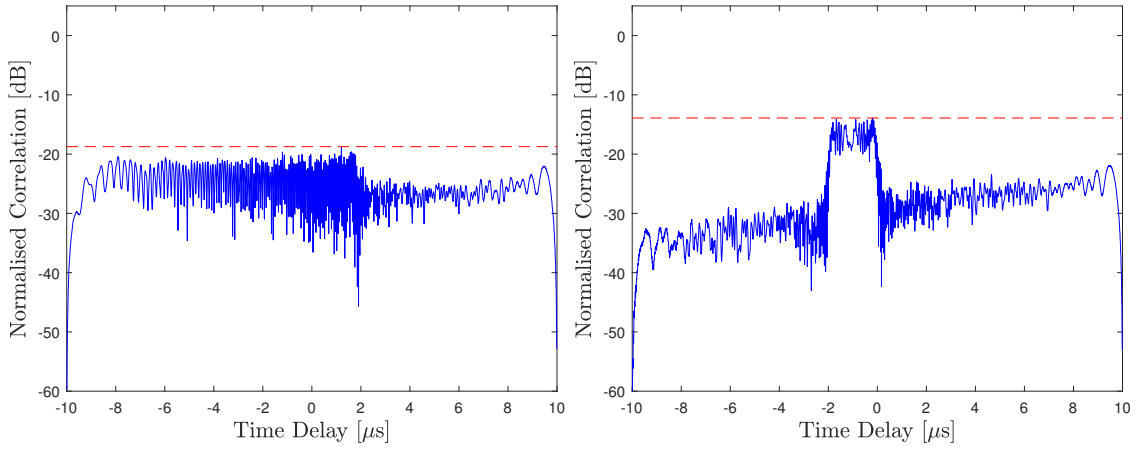

(c) Up-Up: $\Delta B = 40\,\text{MHz}$, $I_{i,j,k} = 18.74\,\text{dB}$ (d) Up-Dn: $\Delta B = 10\,\text{MHz}$, $I_{i,j,k} = 13.90\,\text{dB}$

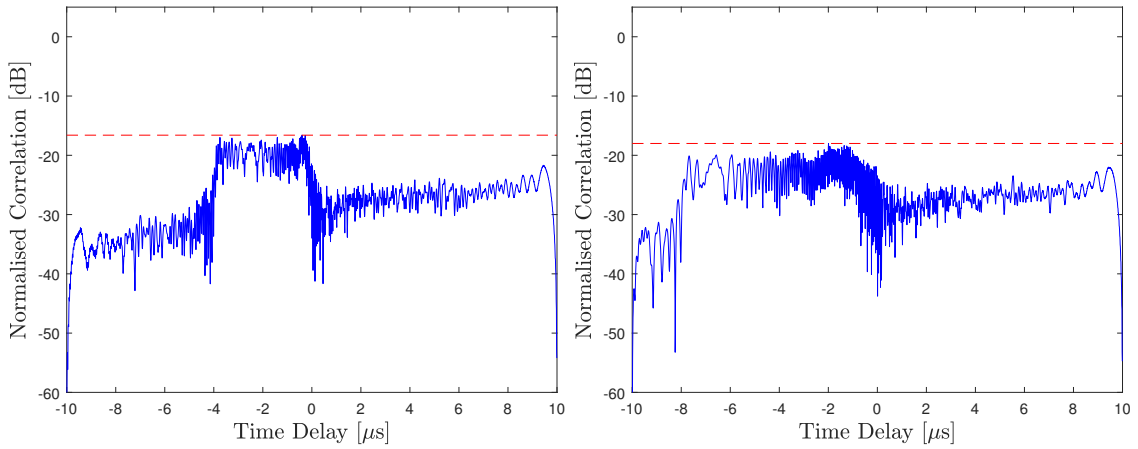

(e) Up-Dn: $\Delta B = 20\,\text{MHz}$, $I_{i,j,k} = 16.60\,\text{dB}$ (f) Up-Dn: $\Delta B = 40\,\text{MHz}$, $I_{i,j,k} = 18.00\,\text{dB}$

Figure 6.8: Measured suppression responses of simultaneously transmitted varying $s_i[n]$ and fixed up-chirp $s_j[n]$ by a filter matched to the $s_k[n]$, which is a fixed down-chirp. $B_j = 50\,\text{MHz}$, $B_k = -50\,\text{MHz}$ and $\Delta B = B_j - |B_i|$, where $s_i[n]$ can be up or down-chirp.

6.2.3 Comparison of Rectangular and Gaussian AM

Additional measurements were carried out to compare the differences between the rectangular and Gaussian amplitude modulation for the pairs of waveforms with different chirp rates. The experimental setup was arranged according to Figure 6.1a and results have been presented in [Kocjancic et al., 2019a]. A USRP with two active channels was used with a sampling frequency $f_s = 75\,\text{MHz}$ and a carrier frequency $f_c = 6.0\,\text{GHz}$. Both channels were connected to two horn antennas (Narda 642) at a distance of $d = 2.6\,\text{m}$ so that a direct RF link was established.

The results of isolation performance between two LFM waveforms with the same bandwidth and opposite chirp rates are shown in Figure 6.9. Waveforms had their bandwidth fixed to $B = 10\,\text{MHz}$ and different BT-products were obtained by changing the pulse width, which resulted in different cross-correlation lengths. Gaussian waveforms, as defined in (5.86), were transmitted until the amplitude fell to $\Delta A = 1/100$ of the maximum value and the total transmission time was determined as

$$T_{max} = 2\lambda\sqrt{-2\log\Delta A} \tag{6.3}$$

where $T = 2\lambda$ is the pulse duration.

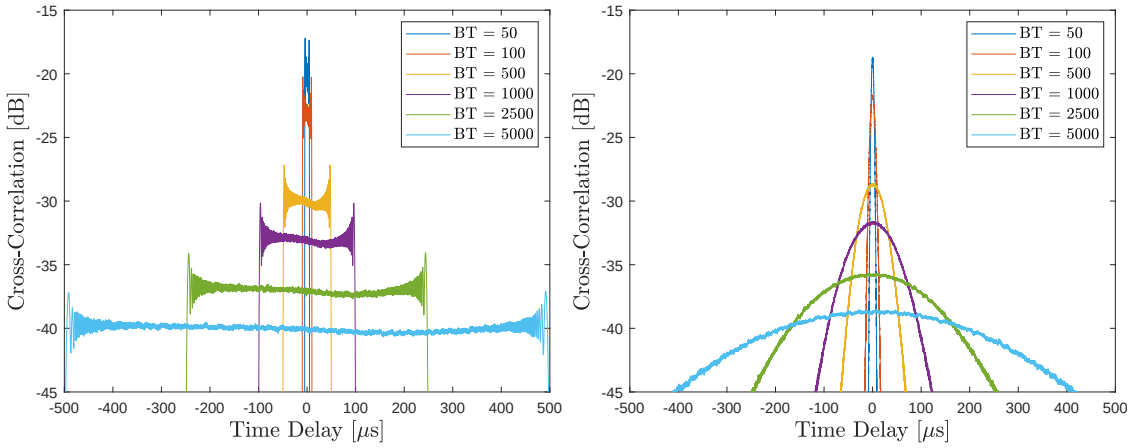

(a) Rectangular AM (b) Gaussian AM

Figure 6.9: Measured cross-correlation responses of rectangular and Gaussian AM waveforms of different BT-products with the bandwidth fixed at $B = 10\,\text{MHz}$.

Isolation values obtained at discrete BT-products are shown in Figure 6.10 with exact numerical values given in Table 6.4. It can be observed that the Gaussian amplitude

modulation implies better isolation values of approximately 1.5 dB, which results from the fact that the Gaussian modulation tapers off the sidelobes of the cross-correlation, including where the maximum peaks of the rectangular AM would occur. Figure 6.10 confirms the correspondence between the measurements and simulations, which appears to be much more accurate than what was obtained in Section 6.2.2. The degradation in the previous section can be attributed to the sampling frequency chosen, as $f_s = 125$ MHz is close to the operational limit of the USRP, which caused amplitude instability of the transmitted waveforms.

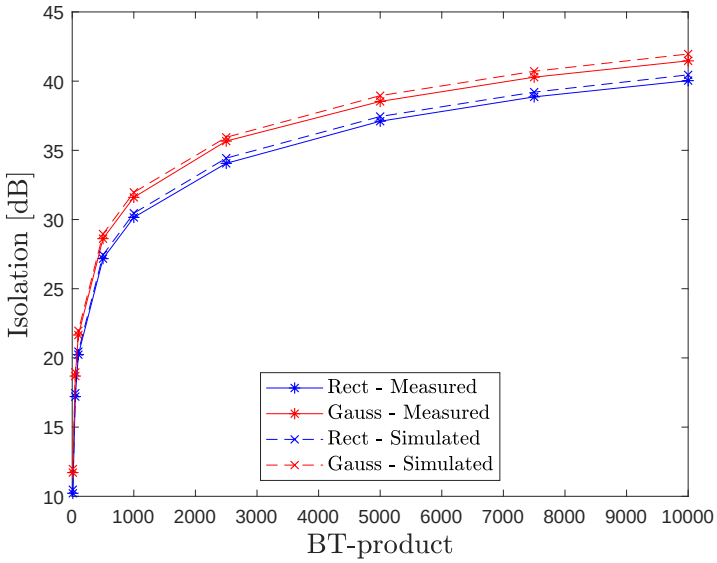

Figure 6.10: Comparison of measured and simulated isolation obtained by LFM waveforms with the same bandwidth and opposite frequency rate as a function of BT-product.

Table 6.4: Measured and simulated isolation between LFM waveforms with the same bandwidth.

AM	Isolation [dB]							
	$BT =$ 50	$BT =$ 100	$BT =$ 500	$BT =$ 1000	$BT =$ 2500	$BT =$ 5000	$BT =$ 7500	$BT =$ 10000
Rect	17.21 (17.45)	20.24 (20.46)	27.17 (27.44)	30.15 (30.45)	34.06 (34.43)	37.10 (37.44)	38.86 (39.20)	40.04 (40.45)
Gauss	18.69 (18.95)	21.65 (21.96)	28.62 (28.95)	31.60 (31.96)	35.67 (35.94)	38.53 (38.95)	40.29 (40.71)	41.47 (41.96)

In order to experimentally assess the isolation performance of waveforms with varying chirp rates, an additional set of measurements was conducted. The experimental setup

and equipment parameters were kept unchanged and only the characteristics of the signals transmitted were modified. The main channel was occupied by a signal of bandwidth $B_j = 10\,\text{MHz}$ and the secondary channel was allocated with a partial bandwidth B_i, which was varied from 1 MHz to 9 MHz. The transmitted waveform associated with the main channel was fixed as an up-chirp and the secondary waveform was tested as an up and a down-chirp. The pulse width parameter was fixed to $T = 250\,\mu\text{s}$, although the Gaussian AM signals were transmitted for 760 µs, which allowed the amplitude to drop to 1/100 at the edges of transmission, as defined with (6.3). All the rectangular waveforms were aligned at the upper frequency band of 10 MHz, as shown in Figure 6.11a, which corresponds to $f_{s,i} = B_j - B_i/2$ and $f_{s,j} = B_j/2$. The Gaussian AM had higher starting frequencies due to the longer transmission time. It follows from (6.3) that $f_{s,j} = \mu_j \lambda \sqrt{-2 \log \Delta A}$ and $f_{s,i} = f_{s,j} + B_j/2 - B_i$, which aligns the signals to the upper frequency limit, as shown in Figure 6.11b. Figure 6.11 shows the equivalence of the allocated bandwidth to rectangular and Gaussian AM, where the bands are marked with the dashed line. During the measurements, the jth signal was used as a digital filter and the ith signal was transmitted and received by a USRP. The isolation results of the experiment described are given in Figure 6.12, which shows the isolation levels as a function of the ΔBT product, where $\Delta B = |B_j| - |B_i|$. The cross-correlation functions comparison between the rectangular and Gaussian LFM is given in Figure 6.13, where the time delay is cropped for the Gaussian chirp. As can be seen in

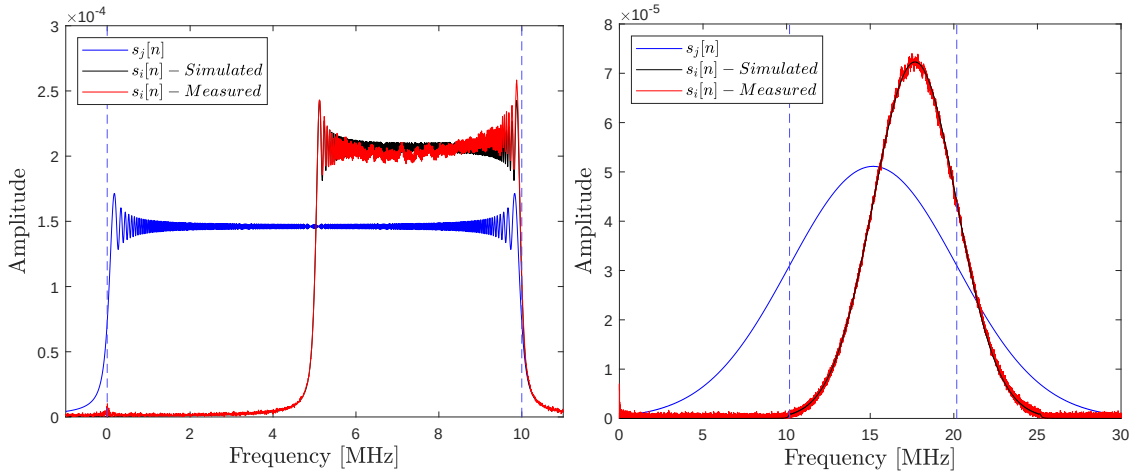

(a) Rectangular AM

(b) Gaussian AM

Figure 6.11: Comparison of amplitude spectra of rectangular and Gaussian AM waveforms when $B_i = 5\,\text{MHz}$ and $B_j = 10\,\text{MHz}$.

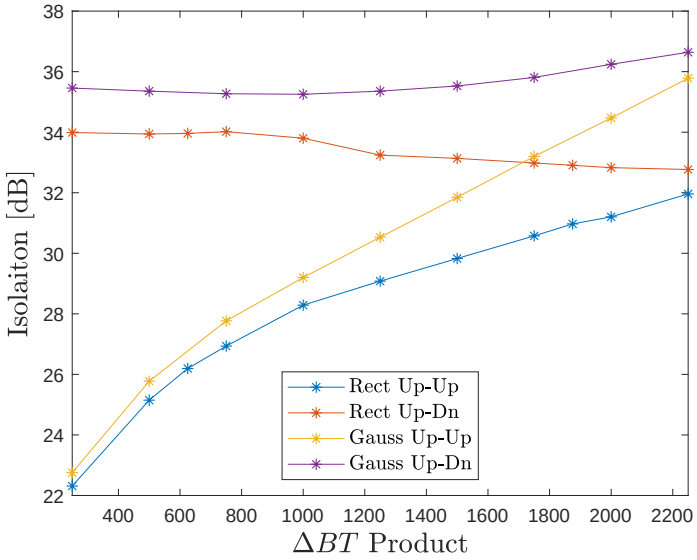

Figure 6.12: Measured isolation values of waveforms with different bandwidths as a function of ΔBT product for rectangular and Gaussian AM of different frequency rates, where the pulse width was set to $T = 250\,\mu s$.

Figure 6.12, the rectangular AM retains expected isolation values while the Gaussian AM improves significantly with the increasing ΔBT product. This is a result of the Gaussian signal spectrum shape, which retains the Gaussian-like amplitude that decreases the energy coverage when the signals are aligned with the lower or upper frequency band, as can be seen in Figure 6.11b. The preceding observations follow from Section 4.4.2 and point to the fact that a Gaussian MBR can achieve better isolation performance if the waveforms are aligned with the limits of dedicated operating bands as opposed to centrally aligned waveforms. The rectangular AM does not exhibit this effect as the amplitude spectrum can be approximated by a rectangular function and the isolation is therefore not sensitive to offset frequencies.

6.3 Isolation Performance with Induced Doppler Shift

This section presents the results of two experiments, which were devised to test the proposed waveforms in the presence of Doppler shifts. Two measurement configurations are described, with a rotating target and with a moving car. The results in this section have been partially published in [Kocjancic et al., 2018, Kocjancic et al., 2019a, Kocjancic et al., 2019c].

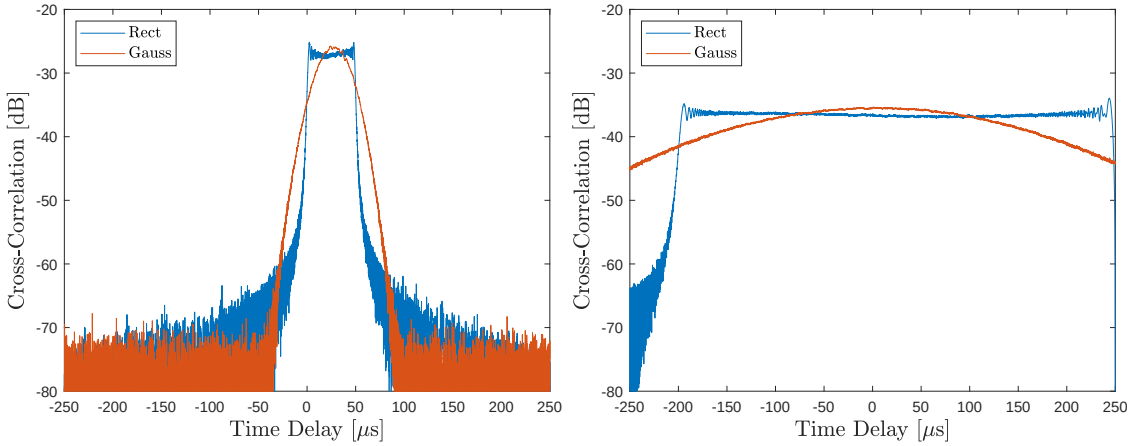

(a) Up-Up: $\Delta B = 2\,\mathrm{MHz}$ (b) Up-Dn: $\Delta B = 2\,\mathrm{MHz}$

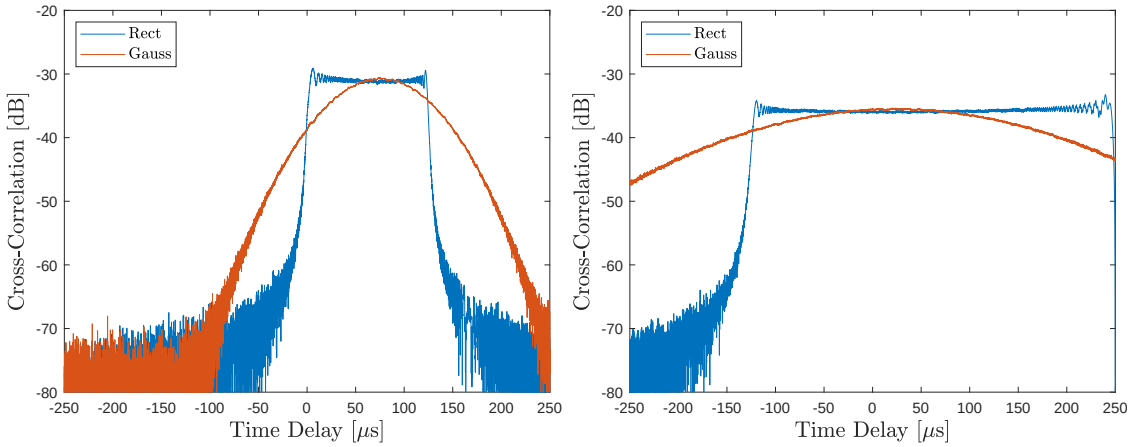

(c) Up-Up: $\Delta B = 5\,\mathrm{MHz}$ (d) Up-Dn: $\Delta B = 5\,\mathrm{MHz}$

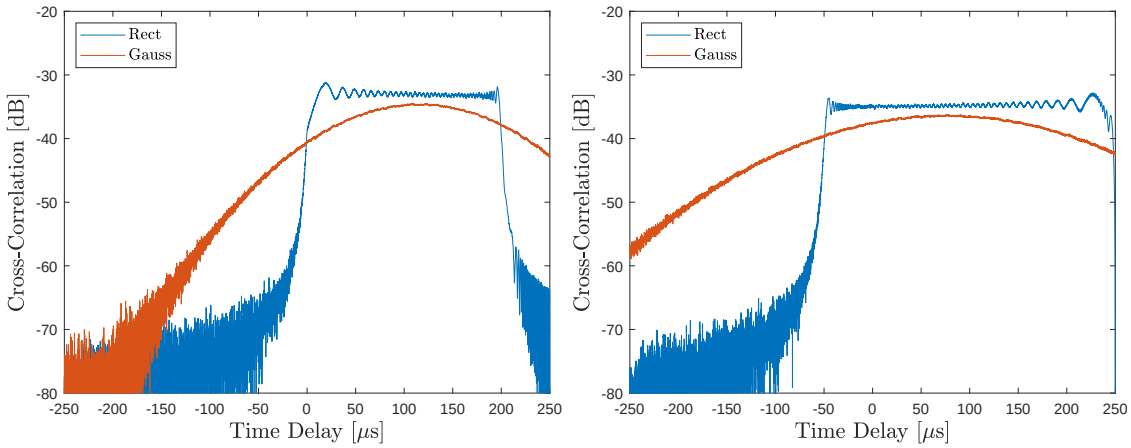

(e) Up-Up: $\Delta B = 8\,\mathrm{MHz}$ (f) Up-Dn: $\Delta B = 8\,\mathrm{MHz}$

Figure 6.13: Measured and normalised cross-correlation functions of waveform combinations with rectangular and Gaussian AM. Up-chirp and down-chirp frequency modulations were applied to signals with $\Delta B = |B_j| - |B_i|$.

Table 6.5: Measured isolation comparison of rectangular and Gaussian AM as a function of varying ΔBT product.

AM	LFM	Isolation [dB]			
		$\Delta BT =$ 500	$\Delta BT =$ 1000	$\Delta BT =$ 1500	$\Delta BT =$ 2000
Rect	Up-Up	25.15 (25.57)	28.29 (28.57)	29.83 (30.36)	31.20 (31.52)
Rect	Up-Dn	33.94 (34.29)	33.80 (34.23)	33.13 (33.55)	32.83 (33.13)
Gauss	Up-Up	25.78 (26.05)	29.20 (29.46)	31.85 (32.06)	34.47 (34.63)
Gauss	Up-Dn	35.36 (35.59)	35.25 (35.48)	35.53 (35.74)	36.24 (36.39)

6.3.1 Isolation with a Rotating Target

An experiment with a rotating target was conducted to test the isolation properties of a set of proposed waveforms in the indoor environment. The isolation was verified in the context of range-Doppler mapping, as we already demonstrated in [Kocjancic et al., 2018]. The transmitted signal consisted of a train of pulses, which were transmitted by a signal generator (Anritsu MS2691). Two horn antennas (Narda 642) were pointing towards a rotating target that was $d = 4\,\text{m}$ away, where the antennas were operating in cross-polarisation, as shown in Figure 6.14. One antenna was connected to the transmitting signal generator and the other one was receiving the reflected signals and conveyed them to the receiving channel of a USRP (National Instruments USRP-2943).

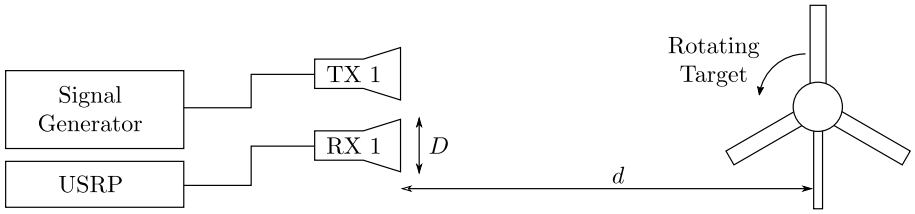

Figure 6.14: Experimental setup for measuring isolation performance in presence of a rotating target.

The sampling frequency of the downconverted signal on the transmitter and receiver side was $f_s = 4\,\text{MHz}$ while the carrier frequency was $f_c = 6\,\text{GHz}$. The pulse width parameter was fixed to $T = 50\,\mu\text{s}$, the pulse repetition frequency to $PRF = 1\,\text{kHz}$ and the bandwidth of the main channel to $B_j = 1\,\text{MHz}$. The selected sampling frequency and

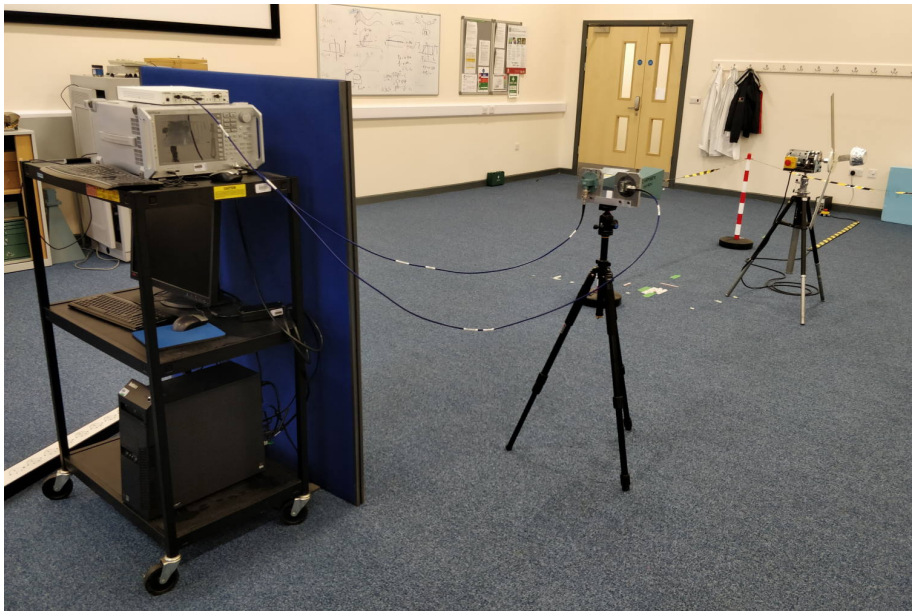

Figure 6.15: Photo of the laboratory setup using a rotating target.

the bandwidth were low due to the sampling limitation of the Anritsu signal generator. The actual pulse length of the Gaussian AM within one PRI of 250 µs was determined so that the amplitude fell to $\Delta A = 10/100$, as defined with (6.3). In this case the length amounted to $T_{max} = 107\,\mu s$. The range-Doppler maps were obtained by integrating 5000 pulses received by the USRP. To obtain the Doppler response, FFT was applied in the slow time dimension with calculation over 8192 points.

Figure 6.16 shows a measurement of the background noise when the rotating target was stationary. The plot is normalised to the compressed rectangular up-chirp with the bandwidth of 1.0 MHz. The dynamic range of the radar system was 49.16 dB, given the compressed peak of 30.76 dB and the noise floor of −18.40 dB.

The measurements of LFM waveforms with the same bandwidth of $B_i = B_j = 1.0\,MHz$ are shown in Figure 6.17a. The main channel signal, used as a digital correlation filter and a transmitting waveform, was an up-chirp, designated as $s_j[n]$. The adjacent channel $s_i[n]$ was a down-chirp of the same bandwidth. Figures 6.17a and 6.17b represent the matched filter response of the main channel for rectangular and Gaussian AM, respectively. It can be seen that the range of Doppler shifts induced by the rotating metal blades extends between −100 Hz and 100 Hz, where the Gaussian AM exhibits lower and smeared sidelobes due to the longer pulse length. The peak response of the rectangular AM was determined

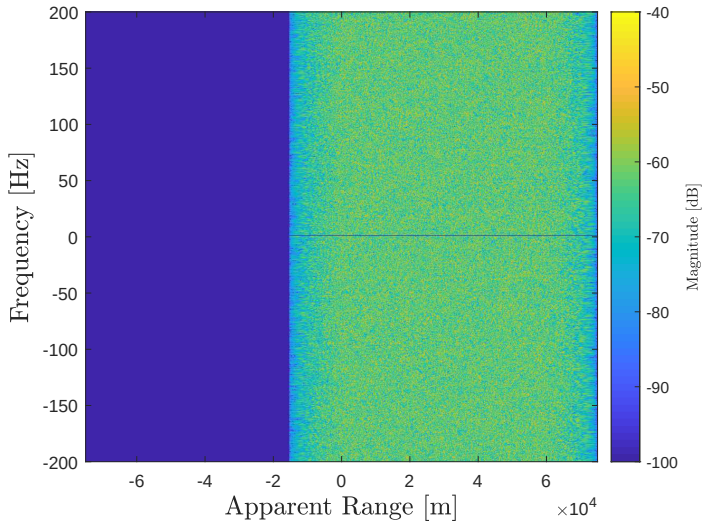

Figure 6.16: A measurement of the background noise with the noise floor of −18.40 dB. The zero frequency components are filtered out and the plot is normalised.

to be 30.76 dB, while the response of the Gaussian AM was 34.43 dB. The suppressions of the adjacent channels $s_i[n]$ with a filter matched to $s_j[n]$ are shown in Figures 6.17c and 6.17d, where the values are normalised to the corresponding peak response levels. The adjacent signal with the rectangular AM was suppressed by 15.94 dB and the Gaussian by 18.46 dB. The simultaneous transmission of $s_i[n]$ and $s_j[n]$ showed that the peak response of the main channel is degraded when only the main channel is extracted with the matched filter. This is because of the interferences caused by the adjacent channel, as can be seen in Figures 6.17e and 6.17f. The peak response degradations amount to 2.40 dB and 3.09 dB for the rectangular and Gaussian AM, respectively.

A similar experiment was repeated, where the adjacent signal occupied half of the allocated bandwidth. The signal $s_i[n]$ was implemented as a down-chirp with $B_i = 0.5$ MHz and centrally aligned bandwidth, with respect to the up-chirp $s_j[n]$ with $B_j = 1.0$ MHz. The resulting measurements are depicted in Figure 6.18, where Figures 6.18a and 6.18b are the matched filter responses. The adjacent signals with rectangular and Gaussian AM were suppressed by 15.61 dB and 16.92 dB, respectively, which is shown in Figures 6.18c and 6.18d. The peak response levels were in this case degraded by 2.05 dB and 3.36 dB, and the simultaneous compression of $s_j[n]$ and suppression of $s_i[n]$ can be seen in Figures 6.18e and 6.18f for the rectangular and Gaussian AM, respectively.

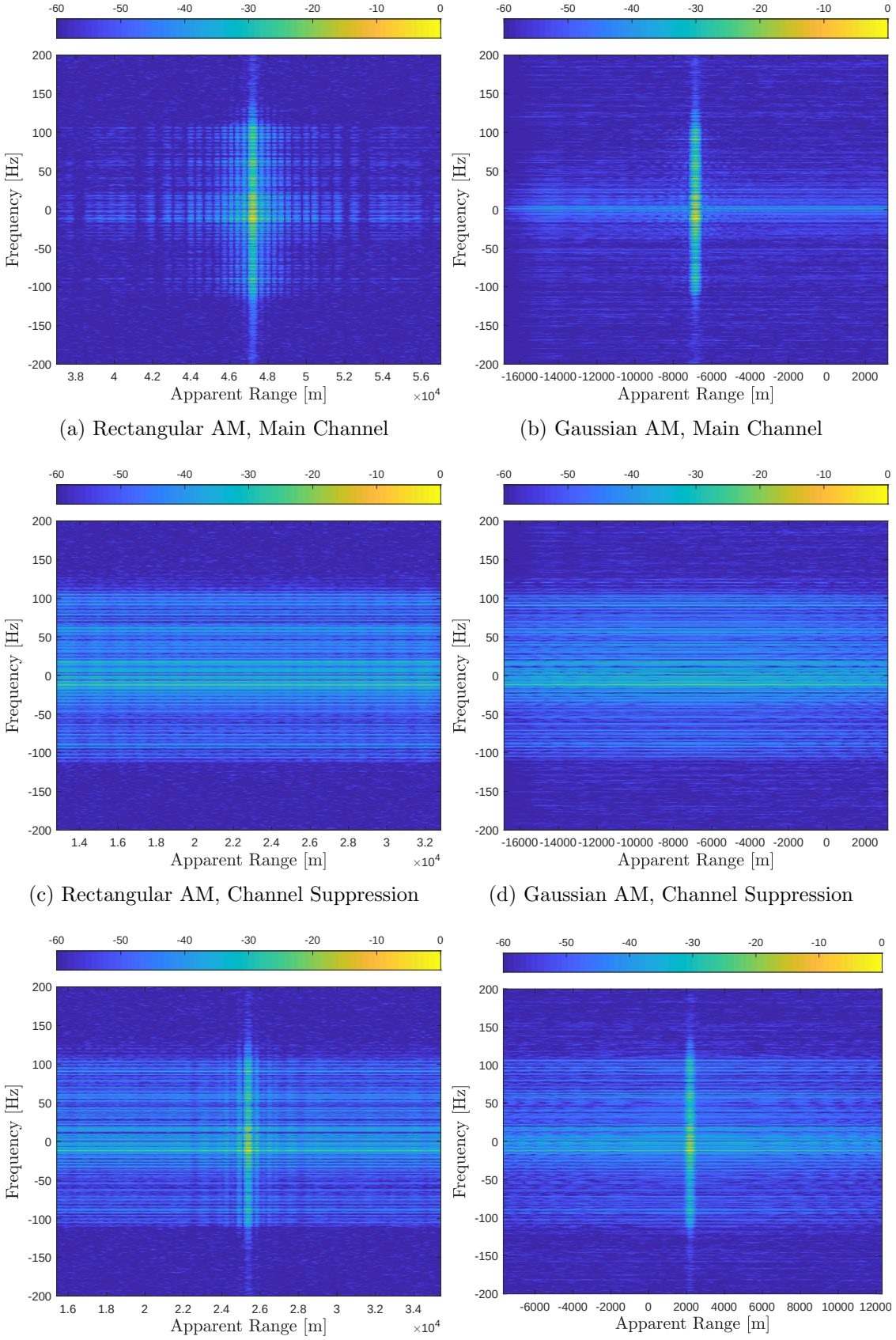

(a) Rectangular AM, Main Channel

(b) Gaussian AM, Main Channel

(c) Rectangular AM, Channel Suppression

(d) Gaussian AM, Channel Suppression

(e) Rectangular AM, Channel Sum

(f) Gaussian AM, Channel Sum

Figure 6.17: Measured range-Doppler maps (in dB) of a rotating target for rectangular and Gaussian AM for a set of an up-chirp (main channel $s_j[n]$) and a down-chirp (adjacent channel $s_i[n]$) with the same bandwidth $B_i = B_j = 1.0\,\text{MHz}$ and pulse width of $T = 50\,\mu\text{s}$.

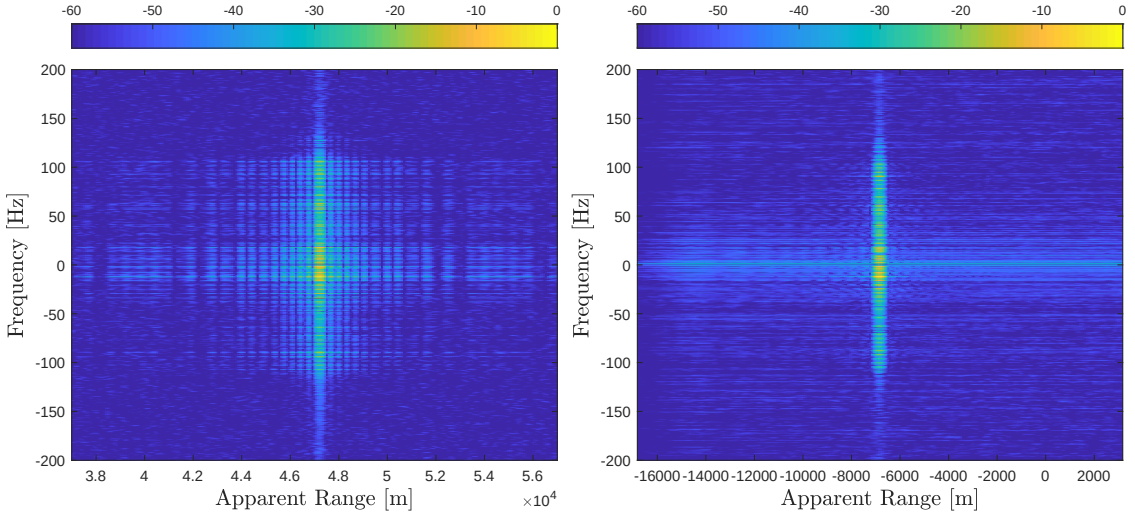

(a) Rectangular AM, Main Channel

(b) Gaussian AM, Main Channel

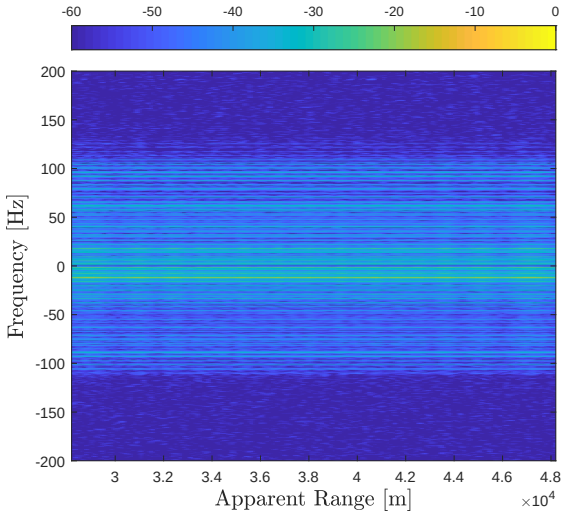

(c) Rectangular AM, Channel Suppression

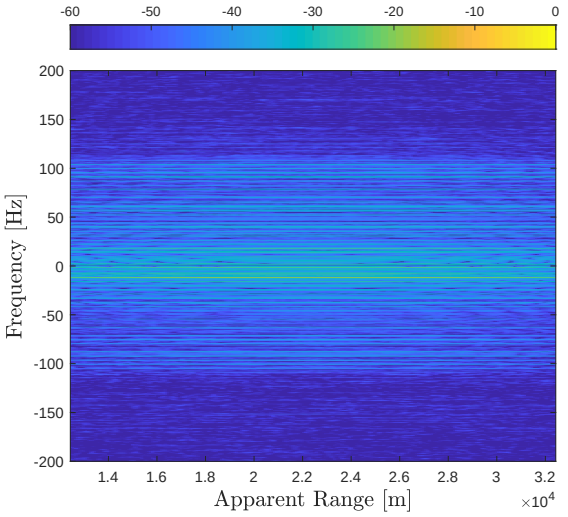

(d) Gaussian AM, Channel Suppression

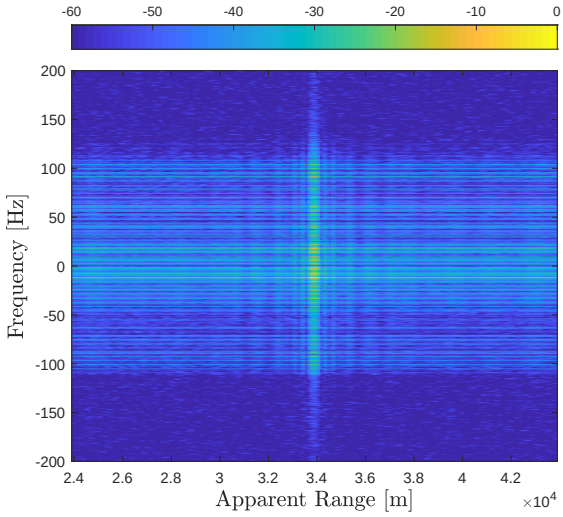

(e) Rectangular AM, Channel Sum

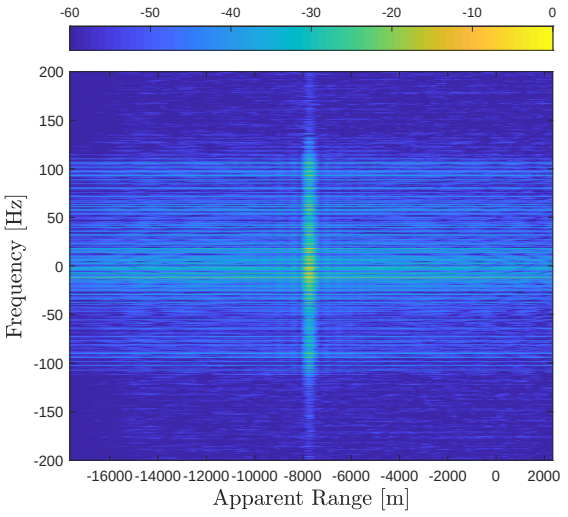

(f) Gaussian AM, Channel Sum

Figure 6.18: Measured range-Doppler maps (in dB) of a rotating target for rectangular and Gaussian AM for a set of an up-chirp (main channel $s_j[n]$) and a down-chirp (adjacent channel $s_i[n]$) with the bandwidth difference $\Delta B = |B_j| - |B_i| = 0.5\,\text{MHz}$ and pulse width of $T = 50\,\mu\text{s}$.

6.3.2 STFT of a Rotating Target

In this section, the results of a two channel MBR radar are presented when STFT is applied to the reflected signals, as already reported in [Kocjancic et al., 2019c]. The measurement setup was the same as introduced in Section 6.3.1 and depicted in Figure 6.14, where the sampling frequency was $f_s = 4.0\,\text{MHz}$ and the carrier frequency $f_c = 5.5\,\text{GHz}$. Two waveforms $s_i[n]$ and $s_j[n]$ were transmitted simultaneously, having the same bandwidth $B_i = B_j = 1.0\,\text{MHz}$ and time duration of $T = 50\,\mu\text{s}$. The pulse repetition frequency was $PRF = 4.0\,\text{kHz}$ and 5000 pulses were received for each measurement. The obtained results are shown in Figure 6.19. The main channel was an up-chirp and the adjacent channel a down-chirp. The performance of rectangular and Gaussian AM modulation was compared for a BT-product of 50, which would theoretically allow for an isolation of 19.0 dB. The Gaussian AM waveform was being transmitted for 108 µs to achieve an amplitude drop of $\Delta A = 10/100$, according to (6.3).

To extract micro-Doppler signatures, STFT was used to produce spectrograms, as given with (5.173). A Hamming window of length $N = 200$ was applied, which is defined as

$$w[n] = 0.54 - 0.46\cos(2\pi\frac{n}{N-1}) \tag{6.4}$$

where $0 \leq n \leq N$ and the window overlapping was 75 samples. FFT was applied in each windowed signal with $n_{FFT} = 16384$ samples after mean value signal components were subtracted. Figure 6.19a depicts the response of a rectangular main channel when a matched filter was used. The peak value of 4.29 dB was obtained after STFT processing. The adjacent channel, a down-chirp suppressed with an up-chirp, is shown in Figure 6.19b, where the maximum value is $-12.58\,\text{dB}$. The isolation performance is, in this case, 16.87 dB. An analogous measurement was conducted for the Gaussian AM. The peak response of the main channel after STFT processing was recorded to be 7.77 dB and the peak response of the suppressed adjacent channel was $-10.83\,\text{dB}$. The isolation in the case of Gaussian AM was therefore 18.60 dB, which is closer to the theoretical value.

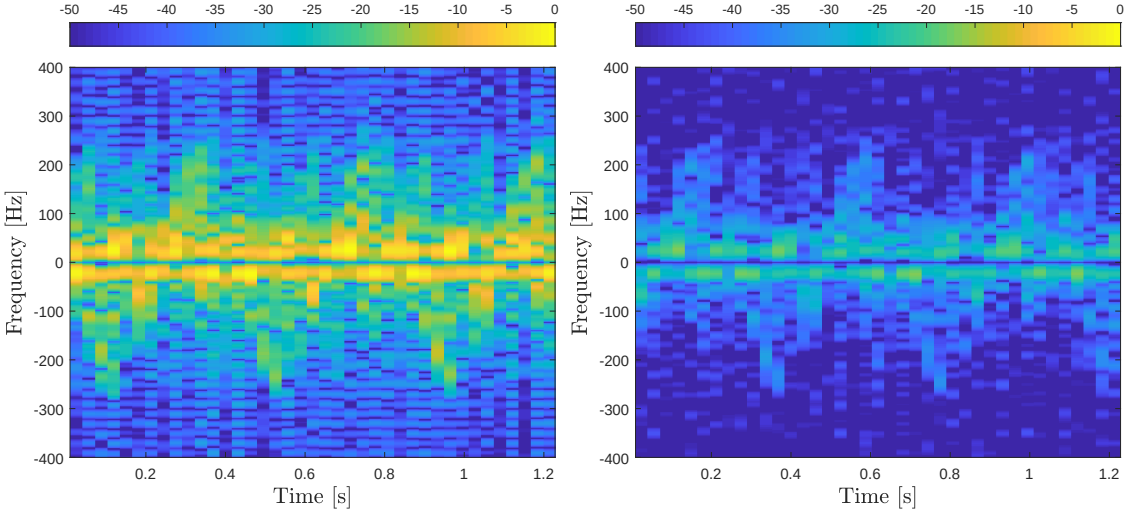

(a) Up-Up: Rectangular AM

(b) Up-Dn: Rectangular AM

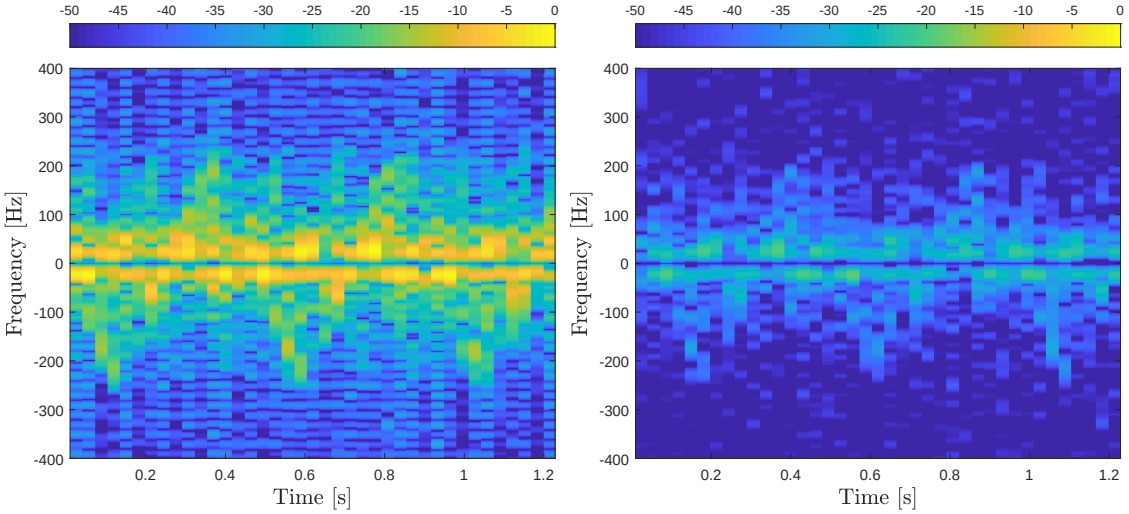

(c) Up-Up: Gaussian AM

(d) Up-Dn: Gaussian AM

Figure 6.19: Measured micro-Doppler signatures of a rotating target for a two-channel MBR with $B_i = B_j = 1.0\,\text{MHz}$ and $T = 50\,\mu\text{s}$. The extraction of the main channel is shown in (a) and (c), whereas suppression of the adjacent channel in (b) and (d).

6.3.3 Isolation with a Moving Target

The experiment in this section was conducted with the same equipment introduced in the previous section, but in the outdoor environment. The signal generator was connected to a transmitting antenna, pointing towards a moving car and the reflected echoes were received by a secondary horn antenna, connected to the USRP, as can be seen in Figure 6.20. Antennas were positioned in a cross-polarisation orientation in order to reduce the mutual coupling. Each measurement was taken whilst a car was approaching the radar

setup in a perpendicular direction with an approximate speed of 9 m/s. Measurements were triggered when the car appeared at a distance $d = 20$ m for the rectangular LFM and 50 m for the Gaussian LFM, as depicted in Figure 6.20.

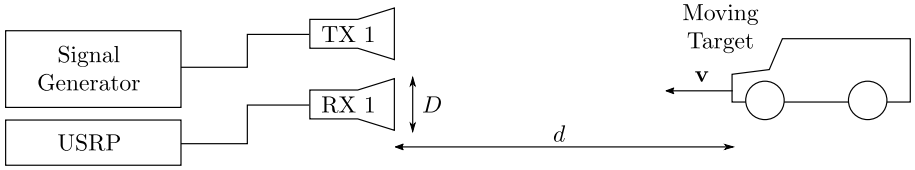

Figure 6.20: Experimental setup for measuring isolation performance in the presence of a moving target, travelling with the speed of $\mathbf{v}$ perpendicular to the radar system.

The carrier frequency for this experiment was $f_c = 6$ GHz and the sampling frequency used for the baseband processing was $f_s = 35$ MHz. All the waveforms in use were LFM, with the main channel occupying a bandwidth $B_j = 5.0$ MHz and the adjacent channel a bandwidth of $B_i = 2.5$ MHz. All the signals were centrally aligned in frequency and therefore $f_{s,i} = f_{s,j} = 0$ Hz. The main channel $s_j[n]$ was an up-chirp and secondary channel $s_i[n]$ a down-chirp, both having a pulse width of $T = 200$ µs so that a ΔBT product of 500 could be achieved. Each range-Doppler diagram was obtained by integrating 100 received pulses in slow time, which were transmitted as a train of pulses with $PRF = 1$ kHz. The FFT, applied in the slow time domain with calculation over 128 points.

Figure 6.21 shows the noise floor measurement, obtained with the filter matched to the rectangular AM waveform $s_j[n]$ and no presence of moving objects. The peak response was -12.50 dB, which determined the dynamic range of the setup as 26.85 dB, provided that the level of the compressed peak was 14.35 dB.

The measurements obtained during the experiment are shown in Figure 6.22. The range-Doppler diagrams resulting from the filter matched to the main channel are shown in Figures 6.22a and 6.22b, which are normalised to the peak levels of the matched filter response. These are responses of the main channel with the full bandwidth coverage, where the non normalised magnitude of the rectangular AM was 19.58 dB and of the Gaussian AM 14.44 dB. It is apparent that the average SNR in the rectangular AM is greater than in the case of Gaussian AM, because of the differences in the triggering distance. The average SNR, when the mean noise level is determined in a range-Doppler submatrix of the size 50×500, is 46.15 dB for the rectangular and 41.82 dB for the Gaussian AM. Figures

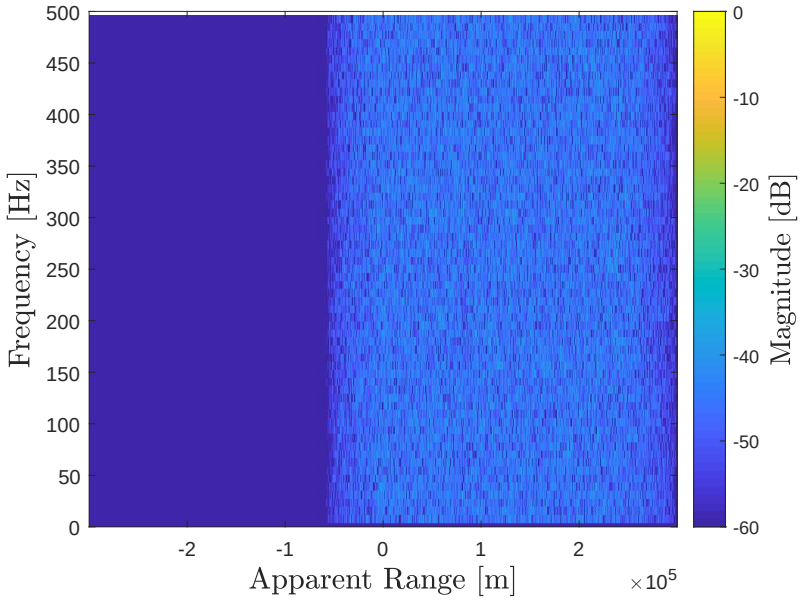

Figure 6.21: A measurement of the background noise when no moving target was present. Plot is normalised to the matched filter peak response.

6.22c and 6.22d are the suppression responses of the adjacent channel $s_i[n]$, where the peak of the correlation filter was obtained as $-6.76\,\text{dB}$ and $-12.16\,\text{dB}$ for the rectangular and Gaussian AM, respectively. Therefore, the resulting isolation values are, respectively, $26.34\,\text{dB}$ and $26.60\,\text{dB}$. Simultaneously transmitting both channels as $s_i[n]+s_j[n]$ reduced the peak response levels after matched filtering to $s_j[n]$ was applied. The compressed signal degraded for $5.23\,\text{dB}$ in the case of rectangular AM and for $1.43\,\text{dB}$ in the case of Gaussian AM.

Statistical analysis of PRIs is demonstrated in Figure 6.23, where the peak response values for each transmission scenario are plotted as a histogram with 40 bins. Each datapoint in every dataset represents a maximum correlation peak in fast time before FFT is applied in the slow time. To compare the mean $\bar{\mu}$ and the variance σ of responses a normal distribution was fitted to every dataset and the results obtained are given in the subcaptions. It can be observed that the variance of matched filter outputs can, in certain cases, reach higher values, which inevitably contributes toward inconsistent isolation values.

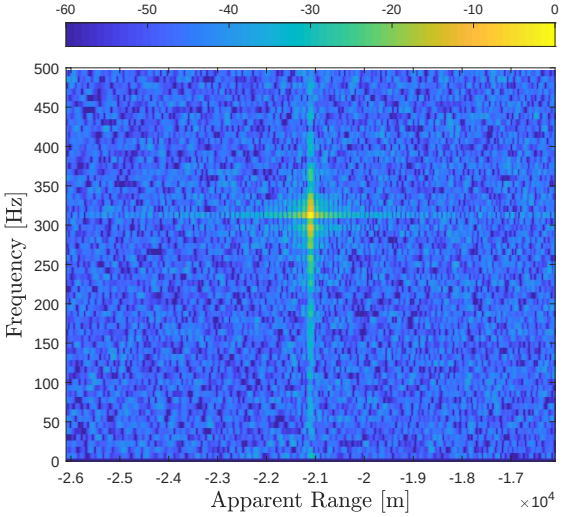

(a) Rectangular AM, Main Channel

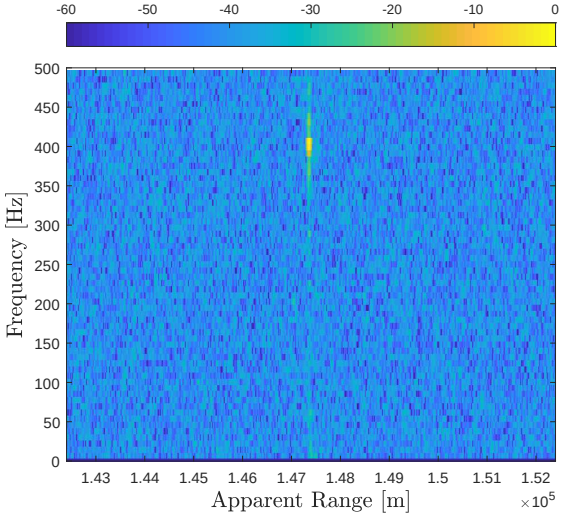

(b) Gaussian AM, Main Channel

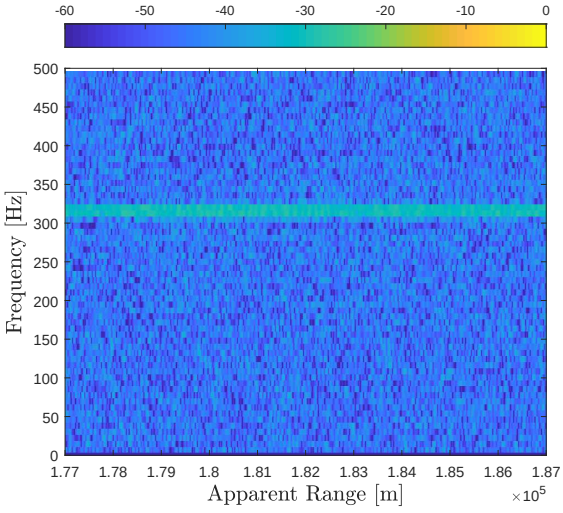

(c) Rectangular AM, Channel Suppression

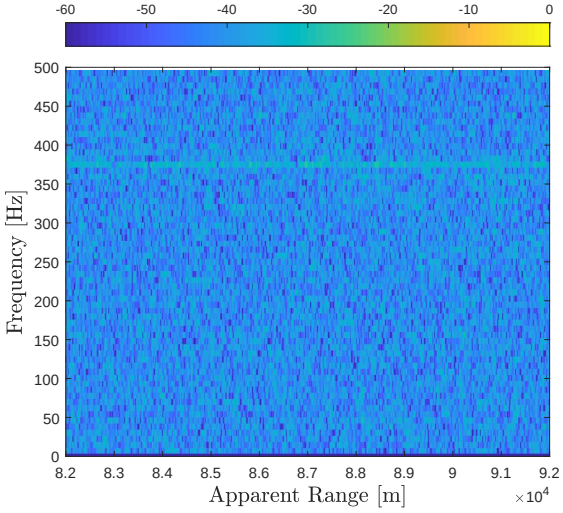

(d) Gaussian AM, Channel Suppression

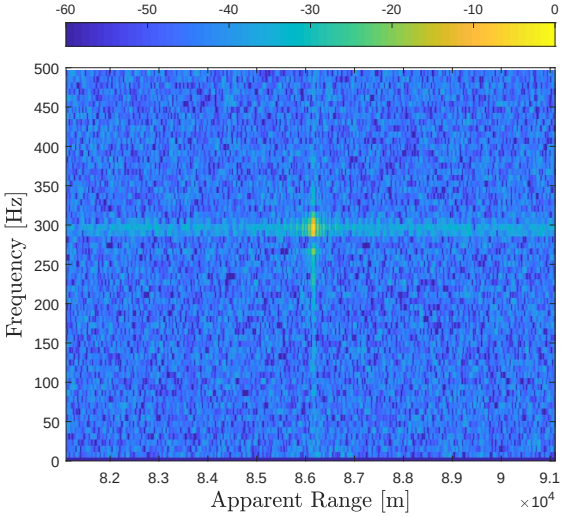

(e) Rectangular AM, Channel Sum

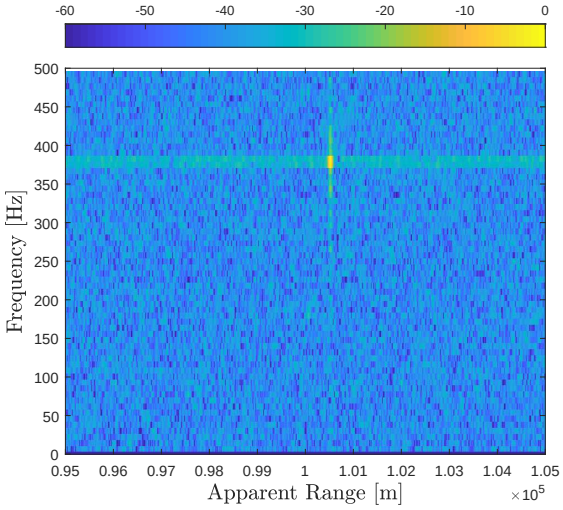

(f) Gaussian AM, Channel Sum

Figure 6.22: Measured range-Doppler maps (in dB) of a moving target with rectangular and Gaussian AM for a set of an up-chirp (main channel $s_j[n]$) and a down-chirp (adjacent channel $s_i[n]$) with the bandwidth difference $\Delta B = |B_j| - |B_i| = 2.5\,\text{MHz}$ and pulse width of $T = 200\,\mu\text{s}$.

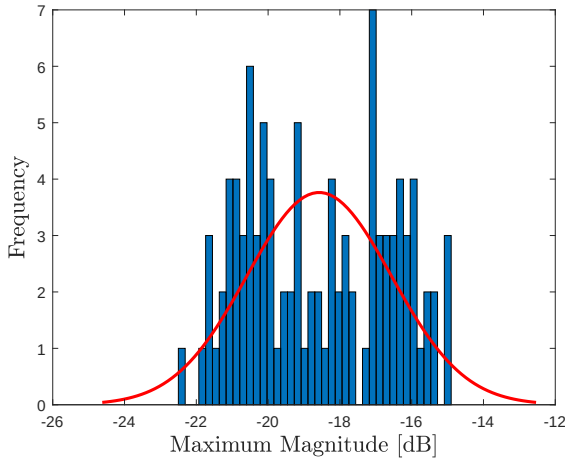

(a) Rectangular AM, Main Channel, Normal Distribution: $\bar{\mu} = -18.58\,\text{dB}$, $\sigma = 2.01\,\text{dB}$

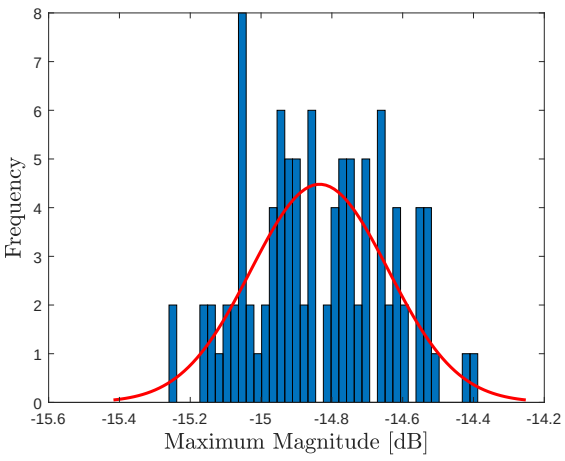

(b) Gaussian AM, Main Channel, Normal Distribution: $\bar{\mu} = -14.83\,\text{dB}$, $\sigma = 0.19\,\text{dB}$

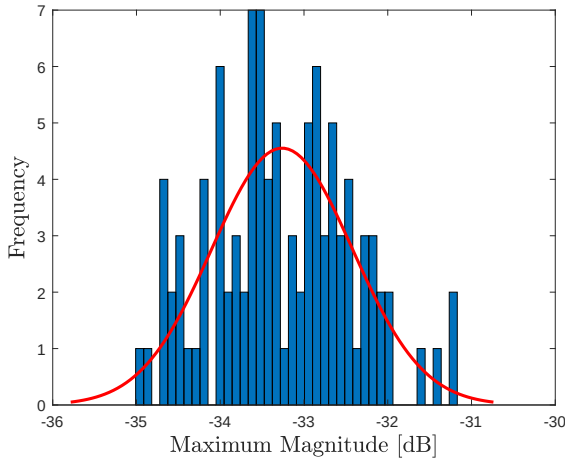

(c) Rectangular AM, Channel Suppression, Normal Distribution: $\bar{\mu} = -33.26\,\text{dB}$, $\sigma = 0.84\,\text{dB}$

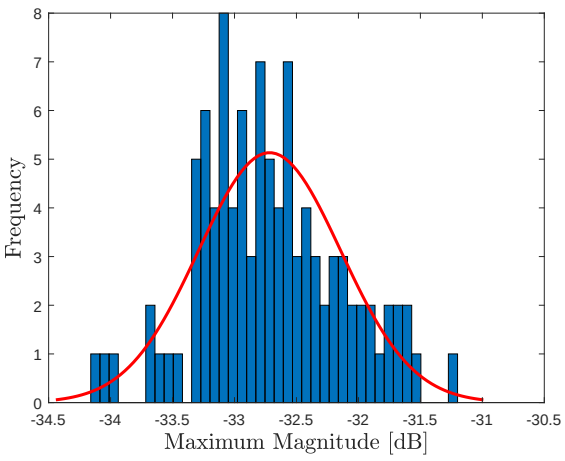

(d) Gaussian AM, Channel Suppression, Normal Distribution: $\bar{\mu} = -32.72\,\text{dB}$, $\sigma = 0.58\,\text{dB}$

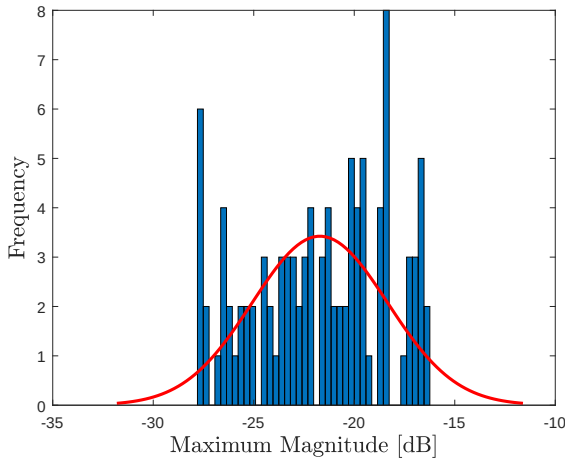

(e) Rectangular AM, Channel Sum, Normal Distribution: $\bar{\mu} = -21.71\,\text{dB}$, $\sigma = 3.37\,\text{dB}$

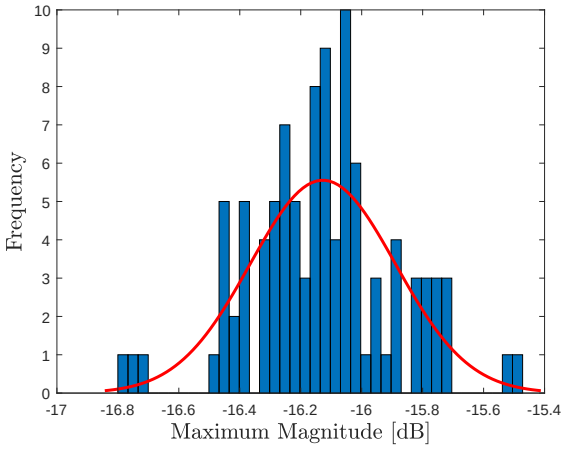

(f) Gaussian AM, Channel Sum, Normal Distribution: $\bar{\mu} = -16.13\,\text{dB}$, $\sigma = 0.24\,\text{dB}$

Figure 6.23: Statistical analysis of PRIs, showing mean $\bar{\mu}$ and variance σ of a fitted normal distribution to the set of all 100 received PRIs, when (a) compression, (c) suppression and (e) summation of rectangular waveforms is applied, likewise for the Gaussian AM.

6.4 Summary

This chapter presented the experimental work that was conducted in relation with the proposed MBR system and analytical isolation results.

Measurements of static waveform isolation presented in Section 6.2 corroborate the analytical work presented in the preceding chapters and show a good alignment with the simulation work that was carried out. Section 6.3 reported more sophisticated experimental tests, which resembled the MBR working environment more closely. It was shown that orthogonal channels can be introduced to a radar system solely based on waveform diversity. Additionally, adjacent channel suppression was found to be able to reduce the interference almost to the level of the noise floor. It was also discovered that multiple waveforms, that are transmitted simultaneously, show some levels of interference, resulting in compressed peak degradation.

The experiments were limited in the sense that accounted for the waveform isolation only when channel isolation was investigated. More sophisticated equipment with multiple independent transmit and receive links would enable an implementation of a phased array with beam steering that would work in conjunction with the waveform isolation in order to improve MBR channel separation. This remains to be investigated in future work.

Figure 6.24: Photo of the experimental setup using MBR and a moving target.

Chapter 7

Conclusion and Future Work

7.1 Conclusion

In the spectrally congested environments, the efficient utilisation of allocated frequency bands has become crucial when new sensing devices are deployed. Spectral radiofrequency (RF) containment and effective use of available bandwidths not only reduces possibility of interference, but also improves on the low probability of detection in adversarial areas. Moreover, airborne sensing platforms have become increasingly compact and complex, as they carry many sensors, including multiple RF based devices. It is therefore important to establish effective and interference-free functioning of such devices, such that isolation between adjacent RF sensors is sufficient. To address the aforementioned challenges, this study proposed a novel radar operating mode, which was designated as multibeam radar (MBR).

An MBR is based on a phased array radar and by employing orthogonal waveforms, multiple operating channels can be enabled. This inherent advantage means that MBR is able to conduct multiple RF sensing functionalities simultaneously without using multiple sensors. As such it becomes suitable for platforms of smaller dimensions, such as drones, missile RF seekers, and autonomous planes. The analytical signal model that has been derived in Section 4.3 demonstrates the feasibility of implementing multiple simultaneous channels in a single RF sensor. In addition, it has been shown that the beam steering complements waveform orthogonality by jointly employing spatial filtering and waveform diversity. Therefore, beam steering and beam shaping techniques can be implemented to

improve on channel isolation.

A key aspect of the proposed MBR is its usage of orthogonal or quasi-orthogonal waveforms. Their properties essentially provide channel isolation for different time delays and Doppler shifts, while using same frequency support. The amount of isolation between the waveforms determines the cross-interference between orthogonal channels, hence the detection and target tracking performance depends on the isolation value.

In the context of waveform design, this research has mainly focused on the linear frequency modulated (LFM) waveforms. This is due to the requirement that the proposed orthogonal waveforms should be Doppler tolerant, which poses a strict design rule on the waveform selection. The proposed LFM waveforms, intended to work in conjunction with the MBR, are well known, but their usage for multifunction and multiple-input multiple-output (MIMO) radars has not been thoroughly addressed in the existing literature. The main contribution of this work is therefore their application to the proposed MBR and analytical investigation of their isolation properties.

In Chapter 5, LFM waveforms with rectangular and Gaussian amplitude modulation have been proposed, where the chirp rate diversity was introduced to implement multiple channels. An isolation expression for both rectangular and Gaussian LFM with different frequency rates was obtained in order to determine the separation between the channels. An analytically derived lower bound on isolation between rectangular LFM waveforms corroborated the performance dependence on the BT-product. Similar relation was derived for the Gaussian chirp, which can exactly predict the amount of the isolation. To the knowledge of the author, both analytical contributions have not been published in the literature before.

One of the main contributions of this work is its experimental part. The literature about MIMO radars and related orthogonal waveform design lacks practical implementations and feasibility demonstrators, which has been addressed by this work. The experimental part has three significant contributions. The first one was a static demonstration of isolation between the sets of proposed waveforms, which corroborated the simulated results. Second experimental instalment was used to induce Doppler shift with a rotating target and produce range-Doppler maps of matched and suppressed channels. It was shown that the separation is possible, although it relates to the limitations imposed by the

equipment. Lastly, the proposed MBR system was replicated as an outdoor setup, emulating a two channel sensing radar. The isolation of the main channel, that was detecting a moving vehicle, and suppression of the adjacent channel showed promising results. As the level of the suppressed signal was comparable to the noise level, the evaluation suggests that the proposed MBR is both possible and feasible in practice.

7.2 Future Work

The research covering MIMO radars and related MBR systems is a relatively new area and much remains to be discovered. The proposed MBR has a great potential to fuse different RF sensors in a single device, yet retain the same underlying technology of the phased arrays currently in use. Furthermore, MBR could be implemented as an additional operating mode whenever the circumstances require simultaneous execution of sensing operations.

The provided derivations of isolation were all calculated in the time domain and frequency approach could be explored as well. Numerical calculations in the frequency domain would therefore be more efficient by employing FFT.

Many aspects of the waveform design can be improved and built upon. As is shown in Appendix B, the proposed combinations of waveforms can be extended to a piecewise linear frequency modulated (PLFM) signal. PLFM waveforms offer more degrees of freedom and can prove more flexible in the context of different optimisation routines.

As was indicated in the experimental section, further investigations of waveform sidelobe interference should be conducted. This is particularly important when three or more channels are in simultaneous operation, a configuration which could potentially produce false targets if the sidelobes were not being suppressed sufficiently.

Additional improvements could be made to the experimental setups, where more channels could be implemented to investigate inter-channel interference. Additionally, equipment which achieves higher bandwidths could be utilised to further improve the isolation performance and therefore dynamic range of the operating radar. Phase steering could be added with a suitable array of antennas as an additional factor contributing to the performance of an MBR.

Appendix A

Mathematical Derivations

A.1 Cauchy-Schwarz Inequality

Suppose that $f(x)$ and $g(x)$ are square-integrable functions over bounded interval so that

$$\int_l^u |f(x)|^2 dx < \infty \tag{A.1}$$

$$\int_l^u |g(x)|^2 dx < \infty \tag{A.2}$$

where $f : \mathbb{R} \mapsto \mathbb{C}$ and $g : \mathbb{R} \mapsto \mathbb{C}$. The Cauchy-Schwarz inequality states that

$$\left| \int_l^u f(t) g^*(x) dx \right|^2 \leq \int_l^u |f(x)|^2 dx \int_l^u |g(x)|^2 dx \tag{A.3}$$

where the integral limits can be expanded to $l \to -\infty$, $u \to \infty$ as long as (A.1) and (A.2) hold. To prove the relation for real functions [Thomas, 1988], the integral is rewritten as

$$\int_l^u \left[\lambda f^*(x) + g^*(x)\right] \left[\lambda f(x) + g(x)\right] dx = A\lambda^2 + (B + B^*)\lambda + C \geq 0 \tag{A.4}$$

where $\lambda \in \mathbb{R}$ and

$$A = \int_l^u |f(x)|^2 dx \geq 0 \tag{A.5}$$

$$B = \int_l^u f^*(x) g(x) dx \tag{A.6}$$

$$C = \int_l^u |g(x)|^2 dx \geq 0 \tag{A.7}$$

RHS of (A.4) is non-negative quadratic function of λ that has only complex roots. According to the quadratic formula, we can write the discriminant as

$$(B + B^*)^2 \leq 4AC \tag{A.8}$$

and inserting the expressions for A, B, C leads to

$$\left[\int_l^u \big(f^*(x)g(x) + f(x)g^*(x)\big)dx\right]^2 \leq 4\int_l^u |f(x)|^2\,dx \int_l^u |g(x)|^2\,dx \tag{A.9}$$

and the Cauchy-Schwarz inequality for real valued functions $f : \mathbb{R} \mapsto \mathbb{R}$ and $g : \mathbb{R} \mapsto \mathbb{R}$ is

$$\left[\int_l^u f(x)g(x)dx\right]^2 \leq \int_l^u f^2(x)dx \int_l^u g^2(x)dx \tag{A.10}$$

Equality in (A.4) holds when

$$\lambda f^*(x) + g^*(x) = \lambda f(x) + g(x) = 0 \tag{A.11}$$

which is true when $f(x)$ and $g(x)$ are linearly related. Alternatively, a real valued λ must exist for which (A.4) reaches value zero at a stationary point. Derivation with respect to λ gives

$$2\lambda A + (B + B^*) = 0 \tag{A.12}$$

and

$$\lambda = -\frac{B + B^*}{2A} \tag{A.13}$$

$$= -\frac{\int_l^u [f^*(x)g(x) + f(x)g^*(x)]dx}{2\int_l^u |f(x)|^2 dx} \tag{A.14}$$

which is true only if

$$g(x) = -\lambda f(x) \tag{A.15}$$

so that the (A.11) and (A.15) are equivalent.

To prove (A.3), we split functions in real and imaginary part so that $f(x) = f_1(x) +$

$jf_2(x)$ and $g(x) = g_1(x) + jg_2(x)$, where $f_1, f_2, g_1, g_2 : \mathbb{R} \mapsto \mathbb{R}$, and write

$$\left| \int_l^u \big(f_1(x) + jf_2(x)\big)\big(g_1(x) + jg_2(x)\big)^* \right|^2 = \tag{A.16}$$

$$= \left| \int_l^u \left[f_1(x)g_1(x) + f_2(x)g_2(x)\right] dx + j\left[f_2(x)g_1(x) - f_1(x)g_2(x)\right] dx \right|^2 \tag{A.17}$$

$$\leq \left[\int_l^u \left[f_1(x)g_1(x) + f_2(x)g_2(x)\right] dx \right]^2 + \left[\int_l^u \left[f_2(x)g_1(x) - f_1(x)g_2(x)\right] dx \right]^2 \tag{A.18}$$

$$\leq \left[\int_l^u f_1(x)g_1(x)dx \right]^2 + \left[\int_l^u f_2(x)g_2(x)dx \right]^2 + \left[\int_l^u f_2(x)g_1(x)dx \right]^2 + \left[\int_l^u f_1(x)g_2(x)dx \right]^2 \tag{A.19}$$

where triangular inequality was applied twice. Now we can apply (A.10) to (A.19) and obtain

$$\left| \int_l^u f(x)g^*(x)dx \right|^2 \leq \left[\int_l^u f_1^2(x)dx + \int_l^u f_2^2(x)dx \right] \left[\int_l^u g_1^2(x)dx + \int_l^u g_2^2(x)dx \right] \tag{A.20}$$

$$= \int_l^u f(x)f^*(x)dx \int_l^u g(x)g^*(x)dx \tag{A.21}$$

$$= \int_l^u |f(x)|^2 dx \int_l^u |g(x)|^2 dx \tag{A.22}$$

which proves the Cauchy-Schwarz inequality for complex functions given by (A.3).

A.2 Parceval's Theorem

Parceval's theorem demonstrates signal energy equivalence in time and frequency domains as

$$\int_{-\infty}^{\infty} |x(t)|^2 dt = \frac{1}{2\pi} \int_{-\infty}^{\infty} |X(\omega)|^2 d\omega = \int_{-\infty}^{\infty} |X(2\pi f)|^2 df \tag{A.23}$$

and follows directly from the Plancharel's theorem

$$\int_{-\infty}^{\infty} g(t)h^*(t)dt = \int_{-\infty}^{\infty} G(\omega)H^*(\omega)d\omega \tag{A.24}$$

when $g(t) = h(t)$ and $G(\omega), H(\omega)$ are respective Fourier transforms. To show the equivalence, inverse Fourier transform is inserted in the LHS of (A.24) to obtain

$$\int_{-\infty}^{\infty} g(t)h^*(t)dt = \int_{-\infty}^{\infty} \left[\frac{1}{2\pi}\int_{-\infty}^{\infty} G(\omega_1)e^{j\omega_1 t}d\omega_1\right]\left[\frac{1}{2\pi}\int_{-\infty}^{\infty} H(\omega_2)e^{j\omega_2 t}d\omega_2\right]^* dt \quad (A.25)$$

and after rearranging the integration terms

$$\int_{-\infty}^{\infty} g(t)h^*(t)dt = \frac{1}{4\pi^2}\int_{-\infty}^{\infty}\int_{-\infty}^{\infty} G(\omega_1)H^*(\omega_2)\left[\int_{-\infty}^{\infty} e^{j(\omega_1-\omega_2)t}dt\right]d\omega_1 d\omega_2 \quad (A.26)$$

where the third integration on the RHS is the Dirac delta function in integral form

$$\delta(\omega_1 - \omega_2) = \frac{1}{2\pi}\int_{-\infty}^{\infty} e^{j(\omega_1-\omega_2)t}dt \quad (A.27)$$

The equality is established after inserting $\delta(\omega_1 - \omega_2) = \delta(\omega_2 - \omega_1)$ in (A.26) to obtain

$$\int_{-\infty}^{\infty} g(t)h^*(t)dt = \frac{1}{2\pi}\int_{-\infty}^{\infty} G(\omega_1)\left[\int_{-\infty}^{\infty} H^*(\omega_2)\delta(\omega_2-\omega_1)d\omega_2\right]d\omega_1 \quad (A.28)$$

$$= \frac{1}{2\pi}\int_{-\infty}^{\infty} G(\omega_1)H^*(\omega_1)d\omega_1 \quad (A.29)$$

where the sifting property of delta function was used

$$f(x_2) = \int_{-\infty}^{\infty} f(x_1)\delta(x_1 - x_2)dx_1 \quad (A.30)$$

Appendix B

Piecewise Linear Frequency Modulation

B.1 Introduction

In this appendix, the numerical characterisation of quasi-orthogonal piecewise linear frequency modulated (PLFM) waveforms is presented. PLFM waveforms are waveforms that are formed from a combination of LFM subchirps and therefore enable more degrees of freedom for optimisation purposes.

Herein, different combinations of PLFM signals are used to produce waveforms with the same time-bandwidth product and optimise them with respect to isolation. The performance of the proposed waveforms are numerically investigated and a comparison between sets is presented. Results confirm that the waveforms have quasi-orthogonal properties and exhibit a degree of Doppler tolerance.

The work presented herein has been previously published in [Kocjancic et al., 2019b]. A review of the research related to the PLFM design has already been discussed in Section 2.4.1.

B.2 Waveform Design

B.2.1 Signal Model

PLFM signals of amplitude A will be considered, that are obtained as the combination of $N = 2$ LFM waveforms, with a complex envelope

$$s_i(t) = A \sum_{n=1}^{N} \text{rect}\left(\frac{t - \tau_{i,n}}{T_{i,n}}\right) e^{2\pi j f_{i,n}(t-\tau_{i,n})} e^{\pi j \mu_{i,n}(t-\tau_{i,n})^2} \tag{B.1}$$

Waveforms with a higher number of subchirps could be considered, but the aim of this research is to determine the impact on isolation for different LFM combinations of the same BT-product.

The frequency offset and chirp rate of the nth subchirp with duration $T_{i,n}$ and bandwidth $B_{i,n}$ are defined as $f_{i,n}$ and $\mu_{i,n} = B_{i,n}/T_{i,n}$, respectively. The bandwidth $B_{i,n}$ is positive for up-chirps and negative for down-chirps and the rectangular function is defined as

$$\text{rect}\left(\frac{t}{T}\right) = \begin{cases} 1, & t \in [0, T] \\ 0, & \text{otherwise} \end{cases} \tag{B.2}$$

The orthogonal properties and Doppler tolerance of five sets of different waveform triplets are studied (that is $i = 1, .., 3$), all of the same energy, with the frequency modulation and design shown in Figure B.5. The related parameters given in Table B.1.

B.2.2 Characterisation Metrics

The level of interference between a pair of waveforms $s_i(t)$ and $s_j(t)$ in the presence of a target inducing a Doppler shift can be described by the cross-ambiguity function

$$\chi_{i,j}(\tau, f_D) = \int s_i^*(t) s_j(t + \tau) e^{j2\pi f_D t} dt \tag{B.3}$$

The isolation is defined as the ratio between the peak of the ambiguity function and the cross-ambiguity function as

$$I_{i,j}(\tau, f_D) = \left|\frac{\chi_{i,i}(0, 0)}{\chi_{i,j}(\tau, f_D)}\right| = \left|\frac{\chi_{j,j}(0, 0)}{\chi_{j,i}(-\tau, f_D)}\right| \tag{B.4}$$

and the minimum level of isolation is

$$\overline{I}_{i,j} = \frac{\chi_{i,i}(0,0)}{\max_{\tau,f_D} |\chi_{i,j}(\tau, f_D)|} \tag{B.5}$$

For each waveform triplet, the lowest isolation between all possible pair combinations is taken as a reference and therefore

$$\overline{I}_{set} = \min_{i,j} \overline{I}_{i,j} \tag{B.6}$$

with $i \in \{1,2,3\}$, $j \in \{1,2,3\}$ and $i \neq j$. The effects of Doppler on orthogonality between waveform pairs is analysed by the zero-delay cut of the cross-ambiguity function

$$\chi_{i,j}(0, f_D) = \int s_i^*(t) s_j(t) e^{j2\pi f_D t} dt \tag{B.7}$$

and the filter mismatch loss due to the Doppler shift can be determined as

$$M_i(f_D) = \frac{\max_\tau |\chi_{i,i}(\tau, f_D)|}{\chi_{i,i}(0,0)} \tag{B.8}$$

As a reference, the Doppler performance of s_i within the Doppler interval $f_D \in [f_{D,min}, f_{D,max}]$ is indicated as

$$\overline{M}_i = \min_{f_D} M_i(f_D) \tag{B.9}$$

Finally, the average power leakage between a pair of waveforms after matched filtering in the interval $\tau \in [\tau_{min}, \tau_{max}]$ is indicated by the peak to average cross-correlation, also known as peak to average power ratio (PAPR), which can be calculated as

$$\overline{P}_{i,j} = (\tau_{max} - \tau_{min}) \frac{\chi_{i,i}(0,0)}{\int_{\tau_{min}}^{\tau_{max}} |\chi_{i,j}(\tau, 0)| d\tau} \tag{B.10}$$

B.3 Numerical Simulations

B.3.1 General Parameters

In this section, a comparison between the five proposed waveform triplets is presented along with their frequency modulation schemes, time delay cuts, Doppler cuts and isolation

figures. The design of the three waveforms forming each triplet is given in the first column of Figure B.5 for the five proposed sets. For clarity, Figure B.5 is indicative and does not take into account the exact design parameters of each waveform given in Table B.1. All waveforms s_i have the same time duration T and bandwidth B and therefore a constant time-bandwidth product of $BT = 5000$ to ensure a fair comparison of the results. For the simulations presented in this appendix, the time duration was fixed to $T = 50\,\mu s$, the bandwidth to $B = 100\,MHz$ and the sampling frequency was $f_s = 400\,MHz$. The maximum Doppler shift considered was $f_{D,max} = 160\,kHz$ which is sufficient to account for targets travelling at Mach 2 for a carrier frequency of 35 GHz. All pair combinations in each of the five sets are characterised by the isolation performance $\overline{I}_{i,j}$, Doppler tolerance $\overline{M}_i$ and PAPR $\overline{P}_{i,j}$. For each set the worst case figure of the isolation $\overline{I}_{set}$ is given as well.

B.3.2 Comments on the Results

Set 1 consists of an up-chirp, a down-chirp and a combination of up and down chirps. Table B.1 shows that the up-chirp and the down-chirp are the combination pair with the best isolation performance. This is in agreement with the results obtained in (5.17) that showed that the isolation improves with the time-bandwidth product as

$$\overline{I}_{i,j} \approx \sqrt{BT}, BT >> 1 \tag{B.11}$$

Furthermore, for chirps with the same duration and different chirp rates, a lower bound on the isolation, derived in (5.43), has been found as

$$\overline{I}_{i,j} > \sqrt{\frac{|\Delta B|T}{2}} \tag{B.12}$$

Note that (B.12) depends on the bandwidth difference between two waveforms with the bandwidth defined as a signed value (i.e. positive for an up-chirp and negative for a down-chirp). As a result, chirp pairs with opposite frequency rates exhibit higher isolation values than chirp pairs with only increasing or decreasing rates. The cross-correlation values shown in Figure B.5b corroborate that up and down-chirps (s_1, s_2) have lower value of interference in comparison to the case with two up-chirps $(s_1, s_{3,1})$. In this case, splitting

s_3 into two subsignals provides chirp rate diversity and results in better orthogonality. The highest value of the cross-correlations $\chi_{3,2}(\tau, 0)$ and $\chi_{1,3}(\tau, 0)$ occurs for negative delays and is due to the contribution of two intersection points in the time-frequency space (see Figure B.5a). According to (B.12), the intersection of the two up-chirps ($s_{3,1}$ and s_1) contributes more energy than the other intersection ($s_{3,2}$ and s_1) that consists of up- and down-chirp.

Set 2 consists of waveforms made of disjoint subchirps and was introduced in [Qazi and Fam, 2015]. The time duration of each subchirp was selected via an optimisation iteration aimed at minimising isolation. Table B.1 shows the best isolation occurs when the first subchirp has a time duration of $T/2 - \Delta T$ and $\Delta T = -0.425\,\mu s$. The best isolation values are obtained when subchirps occupy approximately half of the waveform duration. This can be seen in Figure B.1 showing the value of isolation as a function of ΔT. Decreasing time duration of a chirp effectively decreases the isolation and optimal

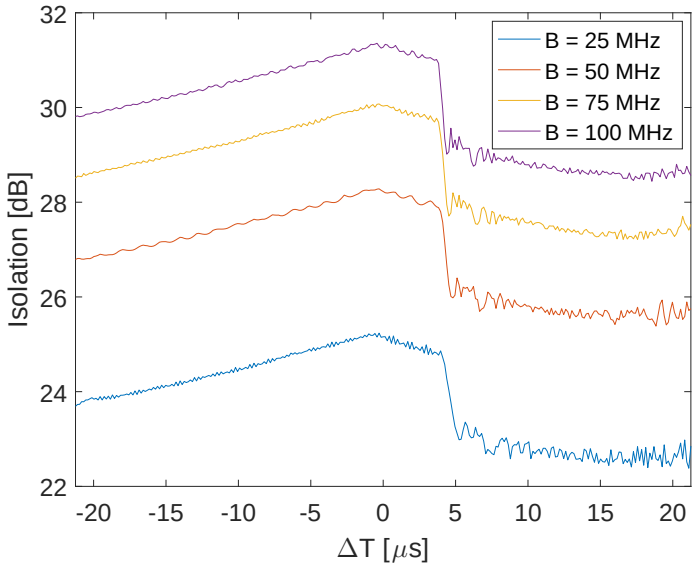

Figure B.1: Optimisation results for the set 2 with parametrised bandwidths. Isolation obtains higher values when time duration of all subsignals is comparable.

isolation values occur when the minimal time duration is maximised. Figure B.5e shows that the cross-correlations $\chi_{2,1}(\tau, 0)$ and $\chi_{3,2}(\tau, 0)$ have the highest value in the centre, where single intersections in the time-frequency modulation plots contribute the most. The aforementioned intersections correspond to the pairs of up-chirps ($s_{1,1}, s_{2,1}$ at positive delays) and down-chirps ($s_{1,2}, s_{2,2}$ at negative delays) both of which have the same $|\Delta B|T$

and therefore comparable level of isolation. Similar reasoning holds for $\chi_{3,2}(\tau, 0)$.

Set 3 was previously used for time-synchronised multichannel communications systems [Shen and Papandreou-Suppappola, 2006], hence its isolation values are worse when the waveforms are transmitted with different time delays. The waveforms were defined according to the frequency modulations shown in Figure B.5g. Optimisation results were obtained for a fixed s_2 and by varying the other two waveforms so to change the starting frequencies $f_{1,2}$ and $f_{3,2}$ whilst adjusting the bandwidths $B_{1,1}$, $B_{3,1}$ accordingly. Figure B.2 shows that isolation increases when the intermediate frequencies have opposite signs and that the plot is symmetric around the axis $f_{1,2} = f_{3,2}$. Results indicate two optimal solutions and one of them is defined in Table B.1. It shows that the first subchirp $s_{2,1}$ has a constant frequency value. This confirms the results in Figure B.2 as the optimal solutions are located at the edges of the frequency distribution. The optimisation variables were bounded within the interval $f_{1,2}, f_{3,2} \in [-50\,\text{MHz}, 50\,\text{MHz}]$.

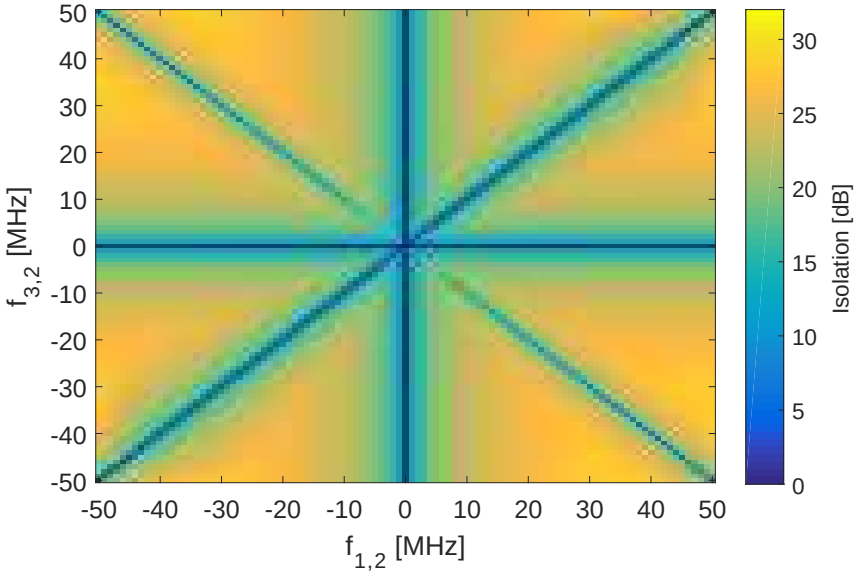

Figure B.2: Optimisation results for the waveform set 3. Isolation of the the entire set is shown as a function of optimisation parameters $f_{1,2}$ and $f_{3,2}$.

Sets 4 and 5 were obtained by fixing s_2 and optimising s_1 and s_3. The bandwidth of each subchirp was fixed whilst the time duration was varied according to $T_{i,1} = T/2 + \Delta T_i$. In this case, the optimisation variables were bounded within the intervals $\Delta T_1, \Delta T_3 \in [-22.5\,\mu\text{s}, 22.5\,\mu\text{s}]$. Figure B.3 and Figure B.4 show that the optimal regions are those where ΔT_1 and ΔT_3 have opposite signs with the optimal values being in the corners. In the

case of set 4, the highest values of cross-ambiguity function $\chi_{3,2}(\tau, 0)$ (Figure B.5k) are a contribution of intersections of chirp pairs $s_{s_2,1}, s_{3,1}$ and $s_{s_2,2}, s_{3,2}$ for positive delays. This contribution can be minimised by employing chirp rate diversity and therefore increasing the chirp rate difference between corresponding pairs. The difference is maximised by increasing the values of $|\Delta T_3|$ which leads to the optimal figures noted in Table B.1 and shown in Figure B.3. Similar reasoning is suitable for set 5. The difference in this case is that the chirp pairs $s_{2,1}, s_{3,1}$ and $s_{2,2}, s_{3,2}$, contributing to the maximum value of $\chi_{3,2}(\tau, 0)$ for positive delays, have opposite slopes. This improves isolation performance as shown in Figure B.4 and corroborates (B.12).

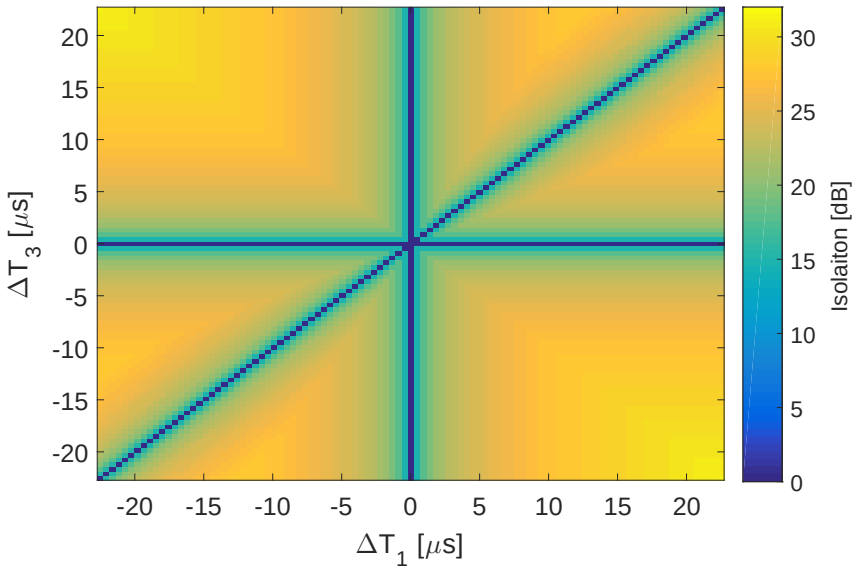

Figure B.3: Optimisation results for the waveform set 4. Isolation of the the entire set is shown as a function of optimisation parameters ΔT_1 and ΔT_3.

Doppler tolerance of each waveform depends on the longest LFM subchirp of the waveform. In general, if the time duration of the longest subchirp is increased, the filter mismatch due to Doppler shift will reduce. Doppler tolerance is not optimal as the filter mismatch for most waveforms decreases to $-6\,\text{dB}$ but it still has an advantage over polyphase codes [Deng, 2004]. This can be observed in the third column of Figure B.5 that shows filter mismatch $M_i(f_D)$ for each set.

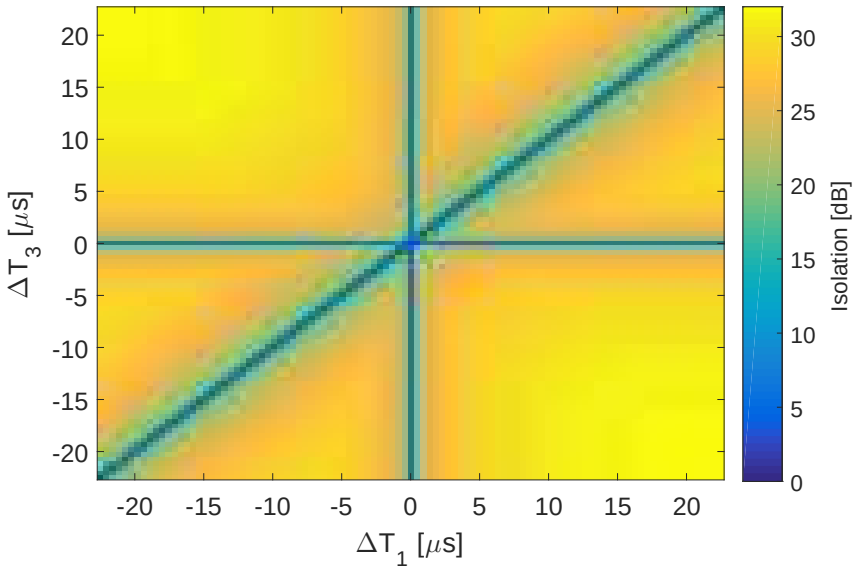

Figure B.4: Optimisation results for the waveform set 5. Isolation of the the entire set is shown as a function of optimisation parameters ΔT_1 and ΔT_3.

Table B.1: Waveform parameters and isolation figures for the proposed waveform sets.

	s_i	s_j	$\tau_{i,1}$ [µs]	$T_{i,1}$ [µs]	$f_{i,1}$ [MHz]	$B_{i,1}$ [MHz]	$\tau_{i,2}$ [µs]	$T_{i,2}$ [µs]	$f_{i,2}$ [MHz]	$B_{i,2}$ [MHz]	$\overline{I}_{i,j}$ [dB]	$\overline{M}_i$ [dB]	$\overline{P}_{i,j}$ [dB]	$\overline{I}_{set}$ [dB]
Set 1	s_1	s_2	-25.000	25.000	-50.0	50.0	0.000	25.000	0.0	50.0	37.44	-0.23	40.07	32.18
	s_2	s_3	-25.000	25.000	50.0	-50.0	0.000	25.000	0.0	-50.0	32.18	-0.23	50.40	
	s_3	s_1	-25.000	25.000	-50.0	100.0	0.000	25.000	50.0	-100.0	32.18	-7.19	50.40	
Set 2	s_1	s_2	-25.000	24.575	-50.0	25.0	-0.425	25.425	50.0	-75.0	31.36	-6.20	58.93	31.36
	s_2	s_3	-25.000	24.575	-50.0	50.0	-0.425	25.425	50.0	-50.0	31.37	-6.11	59.72	
	s_3	s_1	-25.000	24.575	-50.0	75.0	-0.425	25.425	50.0	-25.0	32.23	-6.07	55.52	
Set 3	s_1	s_2	-25.000	25.000	-50.0	50.0	0.000	25.000	0.0	50.0	32.53	-0.23	70.02	28.77
	s_2	s_3	-25.000	25.000	-50.0	0.0	0.000	25.000	-50.0	100.0	29.17	-7.19	71.96	
	s_3	s_1	-25.000	25.000	-50.0	87.0	0.000	25.000	37.0	13.0	28.77	-6.06	72.42	
Set 4	s_1	s_2	-25.000	47.500	-50.0	100.0	22.500	2.500	50.0	-100.0	31.12	-0.72	42.70	31.12
	s_2	s_3	-25.000	25.000	-50.0	100.0	0.000	25.000	50.0	-100.0	31.12	-7.19	42.70	
	s_3	s_1	-25.000	2.500	-50.0	100.0	-22.500	47.500	50.0	-100.0	35.24	-0.72	40.90	
Set 5	s_1	s_2	-25.000	47.500	-50.0	100.0	22.500	2.500	50.0	-100.0	32.01	-0.73	51.53	32.01
	s_2	s_3	-25.000	25.000	-50.0	100.0	0.000	25.000	50.0	-100.0	32.01	-7.19	51.53	
	s_3	s_1	-25.000	2.500	-50.0	100.0	-22.500	47.500	50.0	-100.0	35.25	-0.73	40.90	

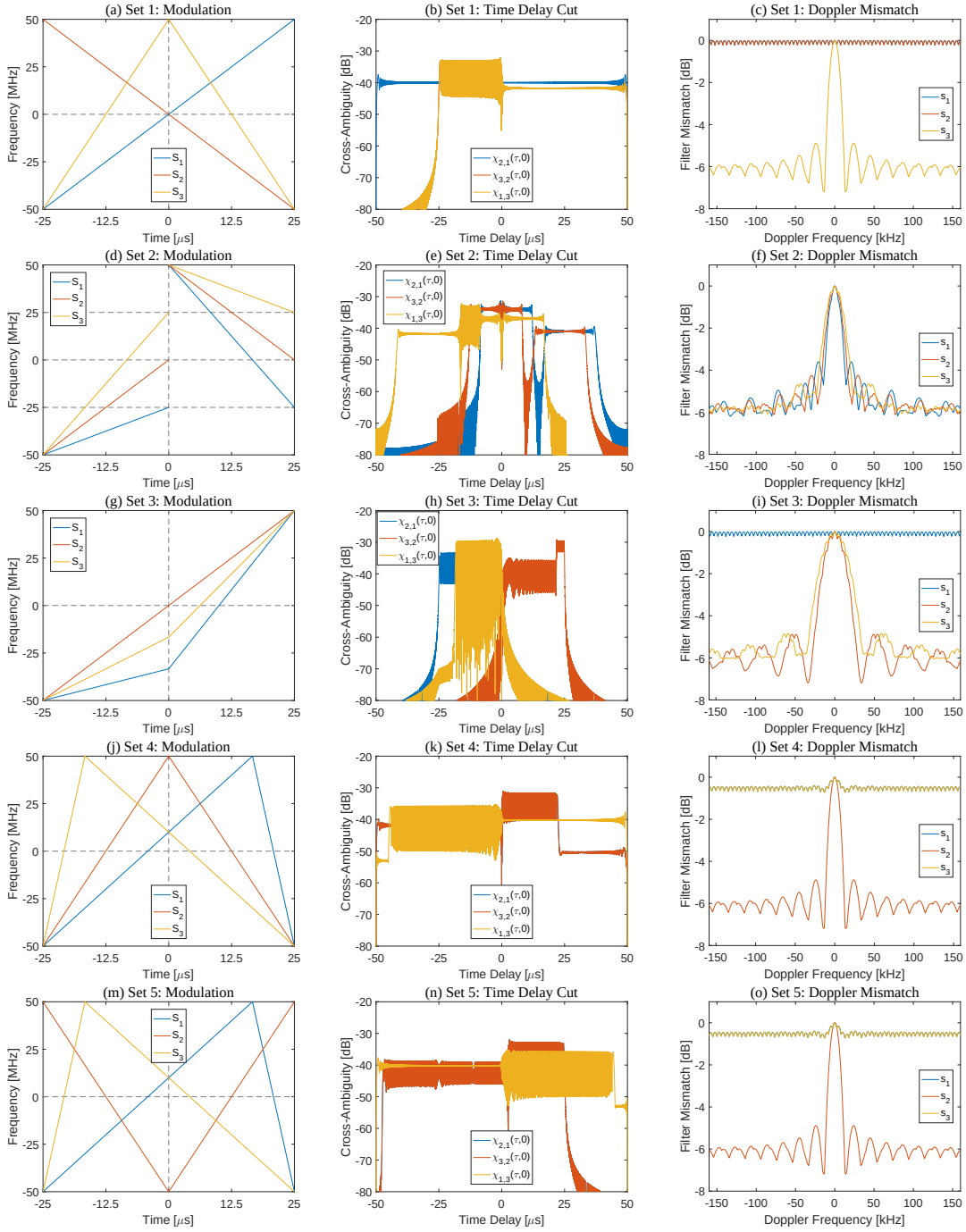

Figure B.5: First column depicts frequency modulations, second column shows zero Doppler cuts of normalised cross-ambiguity functions $\chi_{i,j}(\tau, 0)$ and third one filter mismatch losses due to Doppler shift $M_i(f_D)$.

B.4 Summary

In this appendix, the orthogonal properties of piecewise LFM waveforms were investigated. It was shown that increasing time-bandwidth product increases the isolation between the waveforms. The use of linear subchirps ensures that the waveforms show Doppler tolerant properties to a certain degree. Additionally, it was demonstrated that the isolation figures do not vary significantly when the bandwidth and time duration of a set of waveforms is fixed. The insights presented herein can be used to employ more complex optimisation techniques for waveform generation.

References

[Abramowitz and Stegun, 1965] Abramowitz, M. and Stegun, I. (1965). *Handbook of Mathematical Functions*. Dover Publications Inc.

[Ahmed and Alouini, 2014] Ahmed, S. and Alouini, M.-S. (2014). MIMO-Radar Waveform Covariance Matrix for High SINR and Low Side-Lobe Levels. *IEEE Transactions on Signal Processing*, 62(8):2056–2065.

[Antonik and Wicks, 2007] Antonik, P. and Wicks, M. C. (2007). Waveform diversity: Past, present, and future. *IET Conference Publications*, (530 CP).

[Aubry et al., 2014] Aubry, A., De Maio, A., Piezzo, M., and Farina, A. (2014). Radar waveform design in a spectrally crowded environment via nonconvex quadratic optimization. *IEEE Transactions on Aerospace and Electronic Systems*, 50(2):1138–1152.

[Axelsson, 2003] Axelsson, S. (2003). Noise radar for range/doppler processing and digital beamforming using low-bit adc. *IEEE Transactions on Geoscience and Remote Sensing*, 41(12):2703–2720.

[Bender and Orszag, 1999] Bender, C. M. and Orszag, S. A. (1999). *Advanced Mathematical Methods for Scientists and Engineers*. Springer New York.

[Bernaschi et al., 2012] Bernaschi, M., Di Lallo, A., Farina, A., Fulcoli, R., Gallo, E., and Timmoneri, L. (2012). Use of a graphics processing unit for passive radar signal and data processing. *IEEE Aerospace and Electronic Systems Magazine*, 27(10):52–59.

[Bliss and Forsythe, 2004] Bliss, D. and Forsythe, K. (2004). Multiple-input multiple-output (MIMO) radar and imaging: degrees of freedom and resolution. In *The Thrity-*

Seventh Asilomar Conference on Signals, Systems & Computers, 2003, pages 54–59. IEEE.

[Blunt et al., 2014a] Blunt, S., Jakabosky, J., Cook, M., Stiles, J., Seguin, S., and Mokole, E. (2014a). Polyphase-coded FM (PCFM) radar waveforms, part II: optimization. *IEEE Transactions on Aerospace and Electronic Systems*, 50(3):2230–2241.

[Blunt et al., 2014b] Blunt, S. D., Cook, M., Jakabosky, J., De Graaf, J., and Perrins, E. (2014b). Polyphase-Coded FM (PCFM) radar waveforms, part I: Implementation. *IEEE Transactions on Aerospace and Electronic Systems*, 50(3):2218–2229.

[Blunt and Mokole, 2016] Blunt, S. D. and Mokole, E. L. (2016). Overview of radar waveform diversity. *IEEE Aerospace and Electronic Systems Magazine*, 31(11):2–42.

[Bouchikhi et al., 2014] Bouchikhi, A., Boudraa, A.-O., Cexus, J.-C., and Chonavel, T. (2014). Analysis of multicomponent LFM signals by Teager Huang-Hough transform. *IEEE Transactions on Aerospace and Electronic Systems*, 50(2):1222–1233.

[Brandfass et al., 2018] Brandfass, M., Dallinger, A., and Weidmann, K. (2018). Modular, scalable multifunction airborne radar systems for high performance ISR applications. *Proceedings International Radar Symposium*, 2018-June:1–10.

[Brookner, 2003] Brookner, E. (2003). Phased arrays around the world - progress and future trends. In *IEEE International Symposium on Phased Array Systems and Technology*, volume January, pages 1–8. IEEE.

[Burger and Nickel, 2008] Burger, W. and Nickel, U. (2008). Space-time adaptive detection for airborne multifunction radar. In *2008 IEEE Radar Conference*, pages 1–5. IEEE.

[Chang et al., 2018] Chang, G., Liu, A., Yu, C., Ji, Y., Wang, Y., and Zhang, J. (2018). Orthogonal Waveform With Multiple Diversities for MIMO Radar. *IEEE Sensors Journal*, 18(11):4462–4476.

[Chapling, 2016] Chapling, R. (2016). Asymptotic Methods A Course in Part II of the Mathematical Tripos. Technical report, Cambridge University, Camridge, UK.

[Chassande-Mottin and Flandrin, 1999] Chassande-Mottin, E. and Flandrin, P. (1999). On the Time–Frequency Detection of Chirps. *Applied and Computational Harmonic Analysis*, 6(2):252 – 281.

[Chen, 2014] Chen, B. (2014). *Synthetic Impulse and Aperture Radar (SIAR).* Wiley-Blackwell.

[Chen Baixiao et al., 2001] Chen Baixiao, Liu Hongliang, and Zhang Shouhong (2001). Long-time coherent integration based on sparse-array synthetic impulse and aperture radar. In *CIE International Conference on Radar Proceedings*, pages 1062–1066. IEEE.

[Chen Baixiao et al., 2002] Chen Baixiao, Zhang Shouhong, Wang Yajun, and Wang Jun (2002). Analysis and experimental results on sparse-array synthetic impulse and aperture radar. In *2001 CIE International Conference on Radar Proceedings (Cat No.01TH8559)*, pages 76–80. IEEE.

[Cherniakov, 2008] Cherniakov, M. (2008). *Bistatic Radar: Emerging Technology.* John Wiley & Sons, USA.

[Cohen, 1989] Cohen, L. (1989). Time-Frequency Distributions a Review. *Proceedings of the IEEE*, 77(7):941–981.

[Cohen, 1994] Cohen, L. (1994). *Time Frequency Analysis: Theory and Applications.* Prentice Hall.

[Commin and Manikas, 2012] Commin, H. and Manikas, A. (2012). Virtual SIMO radar modelling in arrayed MIMO radar. In *Sensor Signal Processing for Defence (SSPD 2012)*, pages 34–34. Institution of Engineering and Technology.

[Conn et al., 2004] Conn, M., Koenig, F., Goldman, G., and Adler, E. (2004). Waveform generation and signal processing for a multifunction radar system. In *Proceedings of the 2004 IEEE Radar Conference (IEEE Cat. No.04CH37509)*, number Mmic, pages 161–165. IEEE.

[Conway et al., 2018] Conway, M. D., Russel, D. D., Morris, A., and Parry, C. (2018). Multifunction phased array radar advanced technology demonstrator nearfield test results. In *2018 IEEE Radar Conference (RadarConf18)*, pages 1412–1415. IEEE.

[Cook and Bernfeld, 1993] Cook, C. E. and Bernfeld, M. (1993). *Radar Signals: An Introduction to Theory and Application*. Artech House Publishers, Boston, USA.

[Davis et al., 2014] Davis, M., Showman, G., and Lanterman, A. (2014). Coherent MIMO radar: The Phased Array and Orthogonal Waveforms. *IEEE Aerospace and Electronic Systems Magazine*, 29(8):76–91.

[Deng, 2004] Deng, H. (2004). Polyphase Code Design for Orthogonal Netted Radar Systems. *IEEE Transactions on Signal Processing*, 52(11):3126–3135.

[Dorey et al., 1984] Dorey, J., Blanchard, Y., and Christophe, F. (1984). Le project 'RIAS': une approche nouvelle du radar des surveillance aerienne. In *Colloque International sur le Radar*, pages 505–510, Paris, France.

[Dorey, J. and Garnier, G. and Auvray, G., 1989] Dorey, J. and Garnier, G. and Auvray, G. (1989). RIAS, radar à impulsion et antenna synthetique. In *Colloque International sur le Radar*, pages 556–562, Paris, France.

[Drentea, 2010] Drentea, C. (2010). *Modern Communications Receiver Design and Technology*. Artech House.

[Esmaeili Najafabadi et al., 2017] Esmaeili Najafabadi, H., Ataei, M., and Sabahi, M. F. (2017). Chebyshev chaotic polynomials for MIMO radar waveform generation. *IET Radar, Sonar & Navigation*, 11(2):330–340.

[Farina et al., 2017] Farina, A., De Maio, A., and Haykin, S. (2017). *The Impact of Cognition on Radar Technology*. Electromagnetics and Radar. Institution of Engineering and Technology.

[Fenn, 2007] Fenn, A. J. (2007). *Adaptive Antennas and Phased Arrays for Radar and Communications*. ARTECH HOUSE INC.

[Fishler et al., 2004] Fishler, E., Haimovich, A., Blum, R., Chizhik, D., Cimini, L., and Valenzuela, R. (2004). MIMO radar: An idea whose time has come. In *Proceedings of the 2004 IEEE Radar Conference (IEEE Cat. No.04CH37509)*, pages 71–78. IEEE.

[Fishler et al., 2006] Fishler, E., Haimovich, A., Blum, R., Cimini, L., Chizhik, D., and Valenzuela, R. (2006). Spatial Diversity in Radars—Models and Detection Performance. *IEEE Transactions on Signal Processing*, 54(3):823–838.

[Frankford, 2011] Frankford, M. T. (2011). *Exploration of Mimo Radar Techniques With a Software-Defined Radar*. PhD thesis.

[Fuhrmann and San Antonio, 2008] Fuhrmann, D. and San Antonio, G. (2008). Transmit Beamforming for MIMO radar systems using signal cross-correlation. *IEEE Transactions on Aerospace and Electronic Systems*, 44(1):171–186.

[Galati and Pavan, 2009] Galati, G. and Pavan, G. (2009). Design Criteria for a Multifunction Phased Array Radar integrating Weather and Air Traffic Control Surveillance. In *2009 European Radar Conference (EuRAD)*, number October, pages 294–297, Rome, Italy.

[Galati and Pavan, 2011a] Galati, G. and Pavan, G. (2011a). On the Signal Design for Multifunction/Multi-parameter Radar. In *2011 MICROWAVES, RADAR AND REMOTE SENSING SYMPOSIUM*, number c, pages 28–34. IEEE.

[Galati and Pavan, 2011b] Galati, G. and Pavan, G. (2011b). Orthogonal and Complementary Radar Signals for Multichannel Applications. In *8th European Radar Conference*, number October, pages 178–181, Manchaster, UK.

[Galati and Pavan, 2013] Galati, G. and Pavan, G. (2013). Waveforms design for modern and MIMO radar. In *Eurocon 2013*, number July, pages 508–513, Zagreb, Croatia. IEEE.

[Gao et al., 2016] Gao, C., Teh, K. C., Liu, A., and Sun, H. (2016). Piecewise LFM waveform for MIMO radar. *IEEE Transactions on Aerospace and Electronic Systems*, 52(2):590–602.

[Gini et al., 2012] Gini, F., Maio, A. D., and Patton, L. K. (2012). *Waveform Design and Diversity for Advanced Radar Systems*. IET, London, UK.

[Godrich et al., 2011] Godrich, H., Petropulu, A. P., and Poor, H. V. (2011). Power Allocation Strategies for Target Localization in Distributed Multiple-Radar Architectures. *IEEE Transactions on Signal Processing*, 59(7):3226–3240.

[Gogineni and Nehorai, 2010] Gogineni, S. and Nehorai, A. (2010). Polarimetric MIMO Radar With Distributed Antennas for Target Detection. *IEEE Transactions on Signal Processing*, 58(3):1689–1697.

[Gogineni and Nehorai, 2011] Gogineni, S. and Nehorai, A. (2011). Target Estimation Using Sparse Modeling for Distributed MIMO Radar. *IEEE Transactions on Signal Processing*, 59(11):5315–5325.

[Gray and Capria, 2008] Gray, D. A. and Capria, A. (2008). MIMO noise radar - matched filters and coarrays. In *2008 IEEE Radar Conference*, pages 1–6. IEEE.

[Grossi et al., 2011] Grossi, E., Lops, M., and Venturino, L. (2011). Robust waveform design for MIMO radars. *IEEE Transactions on Signal Processing*, 59(7):3262–3271.

[Haimovich et al., 2008] Haimovich, A., Blum, R., and Cimini, L. (2008). MIMO Radar with Widely Separated Antennas. *IEEE Signal Processing Magazine*, 25(1):116–129.

[Haimovich, 2008] Haimovich, A. M. (2008). MIMO Radar: A Multi-Sensor Spatially Diverse Radar Architecture. Technical report, New Jersey Institute of Technology, Newark, USA.

[Hampton, 2013] Hampton, J. R. (2013). *Introduction to MIMO Communications*, volume 9781107042. Cambridge University Press, Cambridge.

[Han and Nehorai, 2016] Han, K. and Nehorai, A. (2016). Jointly optimal design for mimo radar frequency-hopping waveforms using game theory. *IEEE Transactions on Aerospace and Electronic Systems*, 52(2):809–820.

[Hansen, 2009] Hansen, C. R. (2009). *Phased Array Antennas*. John Wiley & Sons.

[Hassanien et al., 2015] Hassanien, A., Amin, M. G., Zhang, Y. D., and Ahmad, F. (2015). A dual function radar-communications system using sidelobe control and waveform diversity. In *2015 IEEE Radar Conference (RadarCon)*, pages 1260–1263. IEEE.

[Hassanien et al., 2016] Hassanien, A., Amin, M. G., Zhang, Y. D., and Ahmad, F. (2016). Phase-modulation based dual-function radar-communications. *IET Radar, Sonar & Navigation*, 10(8):1411–1421.

[Hassanien et al., 2017] Hassanien, A., Himed, B., and Rigling, B. D. (2017). A Dual-Function MIMO Radar-Communications System Using Frequency-Hopping Waveforms. In *Radar Conference (RadarConf), 2017 IEEE*, volume 1, pages 1721–1725.

[Haykin, 1994] Haykin, S. (1994). *Communication Systems*. Wiley.

[He et al., 2012] He, H., Li, J., and Stoica, P. (2012). *Waveform Design for Active Sensing Systems - A Computational Approach*. Cambridge University.

[He et al., 2009] He, H., Stoica, P., and Li, J. (2009). Designing Unimodular Sequence Sets With Good Correlations—Including an Application to MIMO Radar. *IEEE Transactions on Signal Processing*, 57(11):4391–4405.

[He et al., 2010a] He, Q., Blum, R. S., Godrich, H., and Haimovich, A. M. (2010a). Target Velocity Estimation and Antenna Placement for MIMO Radar With Widely Separated Antennas. *IEEE Journal of Selected Topics in Signal Processing*, 4(1):79–100.

[He et al., 2010b] He, Q., Lehmann, N. H., Blum, R. S., and Haimovich, A. M. (2010b). MIMO Radar Moving Target Detection in Homogeneous Clutter. *IEEE Transactions on Aerospace and Electronic Systems*, 46(3):1290–1301.

[Herd et al., 2010] Herd, J., Carlson, D., Duffy, S., Weber, M., Brigham, G., Rachlin, M., Cursio, D., Liss, C., and Weigand, C. (2010). Multifunction Phased Array Radar (MPAR) for Aircraft and Weather Surveillance. In *2010 IEEE Radar Conference*, pages 945–948. IEEE.

[Horton, 1959] Horton, B. (1959). Noise-Modulated Distance Measuring Systems. *Proceedings of the IRE*, 47(5):821–828.

[Hoskins, 2009] Hoskins, R. F. (2009). *Delta Functions: Introduction to Generalised Functions*. Elsevier Science.

[Hubbard and Hubbard, 2009] Hubbard, J. H. and Hubbard, B. B. (2009). *Vector Calculus, Linear Algebra, and Differential Forms: A Unified Approach.* Matrix Editions.

[Huizing, 2008] Huizing, A. G. (2008). Scalable multifunction RF system: Combined vs. separate transmit and receive arrays. In *2008 IEEE Radar Conference*, pages 1–6. IEEE.

[Jin et al., 2013] Jin, Y., Wang, H., Jiang, W., and Zhuang, Z. (2013). Complementary-based chaotic phase-coded waveforms design for MIMO radar. *IET Radar, Sonar & Navigation*, 7(4):371–382.

[Jorge Nocedal, 2006] Jorge Nocedal, S. W. (2006). *Numerical Optimization.* Springer-Verlag.

[Kangrun Chen et al., 2015] Kangrun Chen, K. C., Yang Liu, Y. L., and Wei Zhang, W. Z. (2015). Study on integrated radar-communication signal of OFDM-LFM based on FRFT. In *IET International Radar Conference 2015*, pages 6 .–6 . Institution of Engineering and Technology.

[Khan et al., 2006] Khan, H., Zhang, Y., Ji, C., Stevens, C., Edwards, D., and O'Brien, D. (2006). Optimizing Polyphase Sequences for Orthogonal Netted Radar. *IEEE Signal Processing Letters*, 13(10):589–592.

[Khan et al., 2018] Khan, Z., Lehtomaki, J. J., Hossain, E., Latva-Aho, M., and Marshall, A. (2018). An FPGA-Based Implementation of a Multifunction Environment Sensing Device for Shared Access With Rotating Radars. *IEEE Transactions on Instrumentation and Measurement*, 67(11):2561–2578.

[Kocjancic et al., 2017] Kocjancic, L., Balleri, A., and Merlet, T. (2017). Study of the frequency slope effect on the chirp waveform orthogonality. In *International Conference on Radar Systems (Radar 2017)*, pages 1–6.

[Kocjancic et al., 2018] Kocjancic, L., Balleri, A., and Merlet, T. (2018). Multibeam radar based on linear frequency modulated waveform diversity. *IET Radar, Sonar Navigation*, 12(11):1320–1329.

[Kocjancic et al., 2019a] Kocjancic, L., Balleri, A., and Merlet, T. (2019a). Experiments of quasi-orthogonal linear frequency modulated waveforms for multibeam radar. In *2019 IEEE Radar Conference (RadarConf)*, pages 1–6.

[Kocjancic et al., 2019b] Kocjancic, L., Balleri, A., and Merlet, T. (2019b). Numerical characterisation of quasi-orthogonal piecewise linear frequency modulated waveforms. In *2019 Sensor Signal Processing for Defence Conference (SSPD)*, pages 1–5.

[Kocjancic et al., 2019c] Kocjancic, L., Balleri, A., and Merlet, T. (2019c). STFT target analysis with quasi-orthogonal LFM waveforms. In *2019 International Conference on RADAR Systems*.

[Kota et al., 2016] Kota, J., Jacyna, G., and Papandreou-Suppappola, A. (2016). Non-stationary signal design for coexisting radar and communications systems. In *2016 50th Asilomar Conference on Signals, Systems and Computers*, number 3, pages 549–553, Pacific Grove, CA, USA. IEEE.

[Krieger, 2014] Krieger, G. (2014). MIMO-SAR: Opportunities and Pitfalls. *IEEE Transactions on Geoscience and Remote Sensing*, 52(5):2628–2645.

[Kulpa, 2013] Kulpa, K. (2013). *Signal Processing in Noise Waveform Radar*. Artech House.

[Labreuche et al., 2017] Labreuche, C., Barbaresco, F., Nguyen, D., Guenais, T., and Gosselin, F. (2017). Multi-criteria Aggregation for Adaptive multifunction Radar Resource Management Performances Evaluation. In *2017 18th International Radar Symposium (IRS)*, pages 1–10. IEEE.

[Lai and Narayanan, 2010] Lai, C.-P. and Narayanan, R. M. (2010). Ultrawideband Random Noise Radar Design for Through-Wall Surveillance. *IEEE Transactions on Aerospace and Electronic Systems*, 46(4):1716–1730.

[Lehmann et al., 2007] Lehmann, N. H., Fishler, E., Haimovich, A. M., Blum, R. S., Chizhik, D., Cimini, L. J., and Valenzuela, R. A. (2007). Evaluation of Transmit Diversity in MIMO-Radar Direction Finding. *IEEE Transactions on Signal Processing*, 55(5):2215–2225.

[Lesturgie, 2011] Lesturgie, M. (2011). Some relevant applications of MIMO to radar. In *2011 12th International Radar Symposium (IRS)*, pages 714–721.

[Levanon, 2004] Levanon, M. (2004). *Radar Signals*. John Wiley & Sons.

[Li et al., 2017] Li, H., Zhao, Y., Cheng, Z., and Feng, D. (2017). OFDM Chirp Waveform Diversity Design With Correlation Interference Suppression for MIMO Radar. *IEEE Geoscience and Remote Sensing Letters*, 14(7):1032–1036.

[Li and Stoica, 2007] Li, J. and Stoica, P. (2007). MIMO Radar with Colocated Antennas. *IEEE Signal Processing Magazine*, 24(5):106–114.

[Li and Stoica, 2009] Li, J. and Stoica, P. (2009). *MIMO Radar Signal Processing*. John Wiley & Sons, Hoboken, New Jersey.

[Li and Wang, 2012] Li, S. and Wang, Y. (2012). The design of radar signal processor based on fpga. In Zhang, Y., editor, *Future Wireless Networks and Information Systems*, pages 283–288, Berlin, Heidelberg. Springer Berlin Heidelberg.

[Liggins et al., 2017] Liggins, M., Hall, D., and Llinas, J. (2017). *Handbook of Multisensor Data Fusion: Theory and Practice, Second Edition*. Electrical Engineering & Applied Signal Processing Series. CRC Press.

[Liu et al., 2006] Liu, B., He, Z., Zeng, J., and Liu, B. (2006). Polyphase Orthogonal Code Design for MIMO Radar Systems. In *2006 CIE International Conference on Radar*, number M, pages 1–4. IEEE.

[Liu et al., 2012] Liu, D., Liu, Y., and Cai, H. (2012). Orthogonal polyphase code sets design for MIMO radar using Tabu Search. In *2012 IEEE International Conference on Intelligent Control, Automatic Detection and High-End Equipment*, pages 123–127. IEEE.

[Liu Guosui et al., 1999] Liu Guosui, Gu Hong, and Su Weimin (1999). Development of random signal radars. *IEEE Transactions on Aerospace and Electronic Systems*, 35(3):770–777.

[Luce et al., 1992] Luce, A. S., Molina, H., Muller, D., and Thirard, V. (1992). Experimental results on RIAS digital beamforming radar. In *92 International Conference on Radar*, pages 74–77.

[McCormick et al., 2017] McCormick, P. M., Blunt, S. D., and Metcalf, J. G. (2017). Simultaneous radar and communications emissions from a common aperture, Part I: Theory. *2017 IEEE Radar Conference, RadarConf 2017*, pages 1685–1690.

[Mecklenbräuker and Claasen, 1980] Mecklenbräuker, W. and Claasen, T. A. C. M. (1980). The Wigner distribution—A tool for time-frequency signal analysis—Part I: Continuous time signals. *Philips Journal of Research*, 35(3-6):217–250.

[Moo and DiFilippo, 2018] Moo, P. W. and DiFilippo, D. J. (2018). Overview of Naval Multifunction RF Systems. In *2018 15th European Radar Conference (EuRAD)*, pages 178–181. IEEE.

[Papoulis, 1962] Papoulis, A. (1962). *The Fourier Integral and Its Applications*. McGraw-Hill Education.

[Petrolati et al., 2012] Petrolati, D., Angeletti, P., and Toso, G. (2012). New piecewise linear polyphase sequences based on a spectral domain synthesis. *IEEE Transactions on Information Theory*, 58(7):4890–4898.

[Qazi and Fam, 2012] Qazi, F. A. and Fam, A. T. (2012). Good code sets based on Piecewise Linear FM. *IEEE National Radar Conference - Proceedings*, pages 0522–0527.

[Qazi and Fam, 2014] Qazi, F. A. and Fam, A. T. (2014). Doppler detection capable good polyphase code sets based on Piecewise Linear FM. *IEEE National Radar Conference - Proceedings*, pages 212–217.

[Qazi and Fam, 2015] Qazi, F. A. and Fam, A. T. (2015). Doppler tolerant and detection capable polyphase code sets. *IEEE Transactions on Aerospace and Electronic Systems*, 51(2):1123–1135.

[Ren et al., 2019] Ren, W., Zhang, H., Liu, Q., and Yang, Y. (2019). Greedy Code Search Based Memetic Algorithm for the Design of Orthogonal Polyphase Code Sets. *IEEE Access*, 7:13561–13576.

[Richards, 2005] Richards, M. A. (2005). *Fundamentals of Radar Signal Processing*. Tata McGraw-Hill.

[Richards et al., 2009] Richards, M. A., Holm, W. A., and Scheer, J. A. (2009). *Principles of Modern Radar: Basic Principles*. SciTech Publishing Inc.

[Schikorr et al., 2016] Schikorr, M., Fuchs, U., and Bockmair, M. (2016). Radar Resource Management Study for Multifunction Phased Array Radar. *2016 European Radar Conference (EuRAD)*, pages 213–216.

[Searle et al., 2008] Searle, S., Howard, S., and Moran, B. (2008). The use of complementary sets in MIMO radar. In *2008 42nd Asilomar Conference on Signals, Systems and Computers*, number 6, pages 510–514. IEEE.

[Shen and Papandreou-Suppappola, 2006] Shen, H. and Papandreou-Suppappola, A. (2006). Diversity and channel estimation using time-varying signals and time-frequency techniques. *IEEE Transactions on Signal Processing*, 54(9):3400–3413.

[Skolnik, 2008] Skolnik, M. (2008). *Radar Handbook*. McGraw-Hill Education Ltd.

[Smith III, 2011] Smith III, J. O. (2011). *Spectral Audio Signal Processing*. W3K Publishing.

[Soltanalian et al., 2013] Soltanalian, M., Naghsh, M. M., and Stoica, P. (2013). A fast algorithm for designing complementary sets of sequences. *Signal Processing*, 93(7):2096–2102.

[Stailey and Hondl, 2016] Stailey, J. E. and Hondl, K. D. (2016). Multifunction Phased Array Radar for Aircraft and Weather Surveillance. *Proceedings of the IEEE*, 104(3):649–659.

[Stimson, 2014] Stimson, G. W. (2014). *Stimson's Introduction to Airborne Radar*. SciTech Publishing Inc.

[Sturm et al., 2009] Sturm, C., Zwick, T., and Wiesbeck, W. (2009). An OFDM System Concept for Joint Radar and Communications Operations. In *VTC Spring 2009 - IEEE 69th Vehicular Technology Conference*, number 4, pages 1–5. IEEE.

[Thomas, 1988] Thomas, J. B. (1988). *An Introduction to Communication Theory and Systems*. Springer, New York.

[Torres et al., 2014] Torres, S., Adams, R., Curtis, C., Forren, E., Forsyth, D., Ivic, I., Priegnitz, D., Thompson, J., and Warde, D. (2014). A demonstration of adaptive weather surveillance and multifunction capabilities on the National Weather Radar Testbed Phased Array Radar. In *2014 International Radar Conference*, pages 1–6. IEEE.

[Tuzlukov, 2017] Tuzlukov, V. (2017). *Signal Processing in Radar Systems*. CRC Press.

[Ville, 1958] Ville, J. (1958). Theory and Applications of the Notion of Complex Signal. Technical report, RAND Corporation, Santa Monica, CA, USA.

[Wang, 2015] Wang, W.-Q. (2015). MIMO SAR OFDM Chirp Waveform Diversity Design With Random Matrix Modulation. *IEEE Transactions on Geoscience and Remote Sensing*, 53(3):1615–1625.

[Wang and Cai, 2012] Wang, W.-Q. and Cai, J. (2012). MIMO SAR using Chirp Diverse Waveform for Wide-Swath Remote Sensing. *IEEE Transactions on Aerospace and Electronic Systems*, 48(4):3171–3185.

[Willis, 2004] Willis, N. J. (2004). *Bistatic Radar*. SciTech Publishing Inc, USA.

[Willis and Griffiths, 2007] Willis, N. J. and Griffiths, H. (2007). *Advances in Bistatic Radar*. SciTech Pub., USA.

[Willsey et al., 2011a] Willsey, M. S., Cuomo, K. M., and Oppenheim, A. V. (2011a). Quasi-Orthogonal Wideband Radar Waveforms Based on Chaotic Systems. *IEEE Transactions on Aerospace and Electronic Systems*, 47(3):1974–1984.

[Willsey et al., 2011b] Willsey, M. S., Cuomo, K. M., and Oppenheim, A. V. (2011b). Selecting the Lorenz Parameters for Wideband Radar Waveform Generation. *International Journal of Bifurcation and Chaos*, 21(09):2539–2545.

[Winter and Lupinski, 2006] Winter, E. and Lupinski, L. (2006). On Scheduling the Dwells of a Multifunction Radar. In *2006 CIE International Conference on Radar*, pages 1–4. IEEE.

[Wirth, 2013] Wirth, W.-D. (2013). *Radar Techniques Using Array Antennas*. Institution of Engineering and Technology.

[Wu et al., 2019] Wu, Z.-J., Xu, T.-L., Zhou, Z.-Q., and Wang, C.-X. (2019). Fast Algorithms for Designing Complementary Sets of Sequences Under Multiple Constraints. *IEEE Access*, 7:50041–50051.

[Xu et al., 2008] Xu, L., Li, J., and Stoica, P. (2008). Target detection and parameter estimation for MIMO radar systems. *IEEE Transactions on Aerospace and Electronic Systems*, 44(3):927–939.

[Xu and Shi, 2018] Xu, Z. and Shi, Q. (2018). Interference Mitigation for Automotive Radar Using Orthogonal Noise Waveforms. *IEEE Geoscience and Remote Sensing Letters*, 15(1):137–141.

[Yang et al., 2013] Yang, J., Qiu, Z., Jiang, W., and Li, X. (2013). Poly-phase codes optimisation for multi-input – multi- output radars. (November 2012):93–100.

[Zeng et al., 2011] Zeng, X., Zhang, Y., and Guo, Y. (2011). Polyphase coded signal design for MIMO radar using MO-MicPSO. *Journal of Systems Engineering and Electronics*, 22(3):381–386.